Single biomolecule studies using optical tweezers

Inauguraldissertation

zur
Erlangung der Würde eines Doktors der Philosophie
vorgelegt der
Philosophisch-Naturwissenschaftlichen Fakultät
der Universität Basel

von
Sudhir C. Husale
aus Basel

Basel, 2005

Genehmigt von der Philosophisch-Naturwissenschaftlichen Fakultät
auf Antrag von

Herrn Prof. H.-J. Güntherodt (Fakultätsverantwortlicher)

Herrn PD Dr. M. Hegner (Thesis advisor)
Herrn Prof. Dr. Bert Hecht (Korreferent)
Herrn Prof. Dr. Marcel Mayor (Chair)

Basel, den 5. Juli 2005

Prof. Dr. Hans-Jakob Wirz

Dekan der Philosophisch-
Naturwissenschaftlichen Fakultät

Single biomolecule studies using optical tweezers

Thesis submitted to the University of Basel for the Degree of Doctor of Philosophy

Husale Sudhir Charudatta

June 2005

Contents

Name of the topic **Page numbers**

Abbreviations

OT = Optical tweezers

DNA = Deoxyribonucleic acid

dsDNA = double stranded DNA

ssDNA = single stranded DNA

OTAB = Octadecyl-trimethyl ammonium bromide

DTAB = Dodecyl-trimethyl ammonium bromide

CTAB = Cetyl-trimethyl ammonium bromide

DMDTAB = Dimethyl-ditetradecyl ammonium bromide

SDS = Sodium dodecyl sulphate

SOS = Sodium octyl sulphate

CMC = critical micelle concentration

EtBr = Ethidium bromide

DOPE = dioleoyl-phosphatidyl ethanolamine

WLC = worm like chain model

CoHex = Hexaammine cobalt trichloride

NaOH = Sodium hydroxide

PCR = Polymerase Chain Reaction

SMF = Single-molecule fluorescence detection

FRET = Fluorescence resonance energy transfer

GFP = Green fluorescent protein

ATP = Adenosine triphosphate

dATP = Deoxyadenosine triphosphate

dCTP = Deoxycytidine triphosphate

dGTP = Deoxyguanosine triphosphate

dNTPs = Deoxynucleoside triphosphates

dUTP = Deoxyuridine 5'-triphosphate

Synopsis

Single biological molecule studies enable to probe and visualize exciting details of the events in physiological *in vivo* processes. The basic underlying question of this dissertation is to understand biological processes at a single molecule level. In contrast to ensemble techniques, advances in single molecule manipulation (e.g. optical and magnetic tweezers, atomic force microscopy) and / or fluorescence techniques allow to investigate the properties of individual molecules in real time with a possibility to change external conditions (buffers) *in situ* and modulate inter- and intra-molecular interactions.

This thesis reports the application of a single molecule technique, dual beam optical tweezers, for the study of single biomolecules. A range of single molecule systems was investigated such as i)VirE2 protein DNA machinery, ii) DNA-surfactant, EtBr (ethidium bromide), SYBR® Green-DNA interactions and iii) dsDNA denaturation studies. In addition the development of the present experimental setup is described to enable combined force measurement as well as single molecule fluorescence studies. The presented biomolecular results provide new and complementary information on the different biological systems demonstrating the diversity of experiments that can be performed on single DNA molecules using optical tweezers.

Chapter one gives a brief introduction to optical tweezers, describes how optical tweezers work, the physics behind it, details of the experimental setup and the method of force calibration required in micromanipulation. Optical tweezers have opened exciting avenues of research, especially in biology. Biologists will be able to investigate the nature of molecular machines one by one, and infer from their behavior those properties common to the population.

In chapter 2, we show how optical tweezers were employed to study the change in the mechanical properties of single DNA molecules upon binding of small agents. The first part of this chapter reports on the changes in mechanics of single dsDNA in the presence of cationic and anionic surfactants (used as non-viral vectors in gene therapy). The second part describes the interaction of DNA binding ligands (SYBR® Green, EtBr) with individual DNA strands.

Agrobacterium tumefaciens (AT), a Gram-negative bacterium, evolved a complex and unique mechanism to transfer a long single stranded DNA (ssDNA) molecule from its cytoplasm to the eukaryotic host plant cell nucleus. Central to this mechanism, chapter 3 discusses the results of the measurements on VirE2 protein interacting with single stranded DNA (ssDNA). VirE2 protein is a multifunctional protein from AT that coat the transferred-ssDNA (T-DNA), interacts with host factors assisting nuclear import of the complex, forms channels in lipid bilayers and displays a highly cooperative binding to ssDNA. The biological findings are presented in a new generic model which can be used to explain how generation of forces helps bacterial DNA to enter the plant cell based on our single molecule data.

Single molecule dsDNA denaturation, relevant in many molecular biological experiments, induced by NaOH and mechanical pulling are studied in chapter 4. Here optical tweezers experiments give access to the 'melting' of hydrogen bonds by mechanical forces or alkali denaturation (NaOH) of dsDNA in real time. The mechanical stability and the transition of dsDNA to ssDNA is investigated at different ionic strength as well as in buffers. Fluorescent images of single λ DNA labeled with SYBR® Green were observed up to forces ≥ 65 pN and indicate a B-DNA to S –DNA transition.

Chapter 5 describes the implementation of single-molecule fluorescence detection (SMF) in optical tweezers. The design and instrumental capabilities of optical tweezers combined with SMF are discussed in detail. The development of this instrument provides a worldwide unique experimental setup and opens up new possibilities in the studies of complex biological systems.

Finally chapter 6 summarizes the results of this thesis and discusses future experimental applications. The appendices provide further details for DNA sample preparation, molecular biology and chemical surface activation recipes, an instruction manual for the setup and the list of currently published papers.

OPTICAL TWEEZERS

1.1 Introduction

The last two decades have witnessed different new techniques such as optical tweezers (OT) (photon fields), magnetic tweezers (magnetic fields), atomic force microscopy (cantilevers), microfibres (microneedles) and flow fields for single biomolecule manipulation studies. Among these OT are the most suited technique for the specific manipulation (~ 5 nm displacements) and high force resolution (0.1 pN to 200 pN) and defined as an instrument (technique) in which the forces exerted by a strongly focused beam of laser light is used to trap and move dielectric objects or biological cells ranging in the size of micrometers (1).

In the early 1970, Ashkin was the first to show the use of radiation pressure to trap dielectric objects and levitation of glass spheres in air and vacuum (2). In 1986 Ashkin and his colleagues showed the first demonstration of single beam optical trapping of particles ranging from the sizes of 10 μm to 40 μm in liquid (3). After their invention, they successfully demonstrated the trapping of biological objects. Since then the advent of this new biophysical technique (OT) has made a large number of significant breakthroughs in the manipulation of single biological molecules. About 12 years ago, single kinesin molecules (motor proteins) were observed for the first time to have a step-size of 8 nm (4), two years later, further demonstration came from the experiment of overstretching of double stranded DNA (dsDNA) as a force versus extension curve (5). These results proved that optical trapping techniques have great potential in biology to probe the molecular mechanisms of motor proteins as well as mechanics of single biomolecules. Nowadays single beam or dual beam optical tweezers are predominately used and became an important tool for research in the fields of biology, physical chemistry and soft condensed matter physics. Recent advances promise to take optical tweezers out of the laboratory and into the mainstream of manufacturing and diagnostics (6).

1.2 Working principle of optical tweezers

There are two different regimes suitable for the explanation of the possibility to manipulate particles by OT. 1. The Mie regime is valid for the particles having sizes larger than the wavelength of light. 2. The Rayleigh regime for the particles having sizes smaller than the wavelength of light.

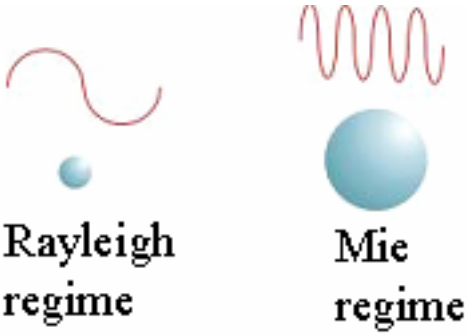

The basic principle behind optical tweezers is the momentum transfer associated with bending of light rays. Light carries momentum which is proportional to its energy in the direction of propagation. Figure 1 explains the working of an OT with the help of a ray optic diagram (Mie regime).

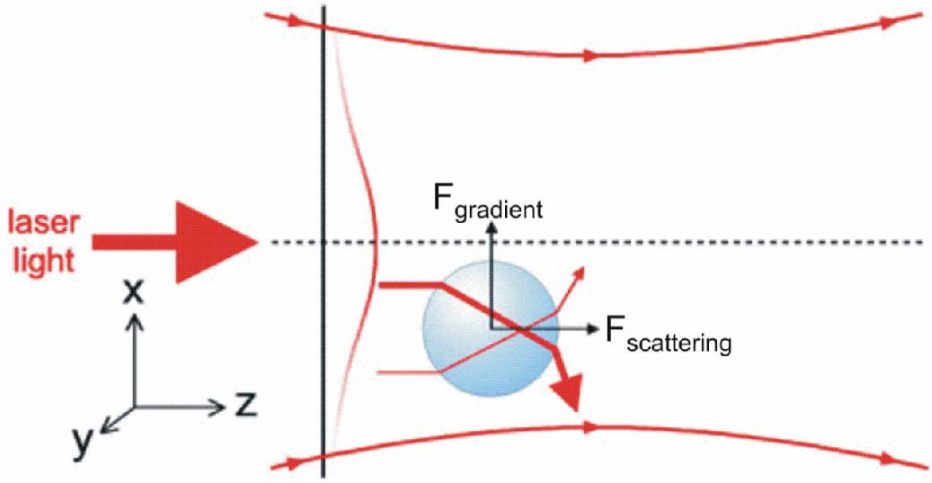

Figure 1. Schematic of working of optical tweezers.

The light coming from a laser is brighter at the centre of the beam as compared to the light at the edges (Gaussian profile). When this light interacts with a bead (dielectric object), the incident light rays on the sphere are deviated according to the laws of reflection and refraction. Each ray is refracted at the surface of the bead so that its direction of propagation changes according to Snell's law, which states that $n_1 \sin(\theta_1) = n_2 \sin(\theta_2)$ where n_1 is the index of refraction of the medium surrounding the sphere (usually water) and n_2 is the index of refraction of the sphere. Here θ_1 is the angle of incidence of the ray with respect to a line perpendicular to the surface of the sphere and θ_2 is the angle with respect to the same line at which the ray propagates within the sphere. Before entering into the bead, the rays travel horizontally with zero vertical momentum. After deflection, they pick up vertical momentum because any

change in the direction of light, by reflection or refraction, will result in a change of the momentum of the light. Thus to any change in its momentum, conservation of it requires that the affected object must undergo an equal and opposite momentum change. This gives rise to a force acting on the bead. However, the asymmetry in the light intensity (i.e. gradient) gives rise to an imbalance in the reaction forces and the object is pulled towards the brighter side. This is why, the sphere experiences an equal and opposite force – back towards the centre of the laser beam.

The sum of the forces from all such rays can be split into two components: $F_{scattering}$, the scattering force, pointing in the direction of the incident light (z, see axes in Fig 1), and $F_{gradient}$, the gradient force, arising from the gradient of the Gaussian intensity profile and pointing in the direction of the x-y plane towards the centre of the beam (dotted line). The gradient force is a restoring force that pulls the bead into the centre of the beam. If the contribution to $F_{scattering}$ of the refracted rays is larger than that of the reflected rays (e.g. by focusing the light) then a restoring force is also created along the z-axis, and a stable trap will exist.

The second explanation (i.e. Rayleigh regime) applies to particles that are much smaller than a wavelength of light, and can thus be treated as Rayleigh scatterers possessing a polarizability, α. The electric field E from a light source induces a dipole moment αE in the particle which then experiences a force $\vec{\mathbf{F}} = \alpha/2 \nabla\vec{\mathbf{E}} \cdot \vec{\mathbf{E}}$ attracting it to the focus of the light. Since α is proportional to the particle volume, the force holding the particle in the trap is proportional to the particle size, as well as the beam intensity gradient (7).

1.3 Physics behind optical tweezers

Light has the ability to exert radiation pressure on matter whereas radiation pressure is the force per unit area on an object due to the change in momentum of light. All light consists of photons, each having a momentum $\vec{P}$ (8). For light of specific wavelength λ, the magnitude of the momentum of a single photon is given by

$$\left|\vec{P}\right| = \frac{h}{\lambda} \qquad [1]$$

The intensity of the light is determined by the number of photons passing through a given area per unit time. The momentum flux of photons from light of a given intensity is given by the poynting vector $\vec{S}$:

$$d\left(d\vec{P}/dt\right)=\left(n/c\right)\vec{S}\,dA \qquad [2]$$

where n is the index of refraction, c is the speed of light, P is the total momentum of the photons, and dA is an element of area normal to S (7)**.**

Since the force on a dielectric object is given by the change in momentum of light induced due to refraction of the light by the object, the total force on the object is the difference between the momentum flux entering the object and that leaving the object. The total force on an object due to refraction of light is therefore

$$\vec{F} = d\vec{P}_{in}/dt - d\vec{P}_{out}/dt = (n/c)\iint(\vec{S}_{in} - \vec{S}_{out})dA \qquad [3]$$

Thus, if the light, coming into a dielectric object from a medium of index n, is deflected, changing the direction of S when it exits the dielectric material, then there is a finite force exerted on the object.

The index n in equation 3 represents the medium surrounding the sphere. The change in direction of the light due to refraction is all contained within the integral.

1.4 Dual beam optical tweezers

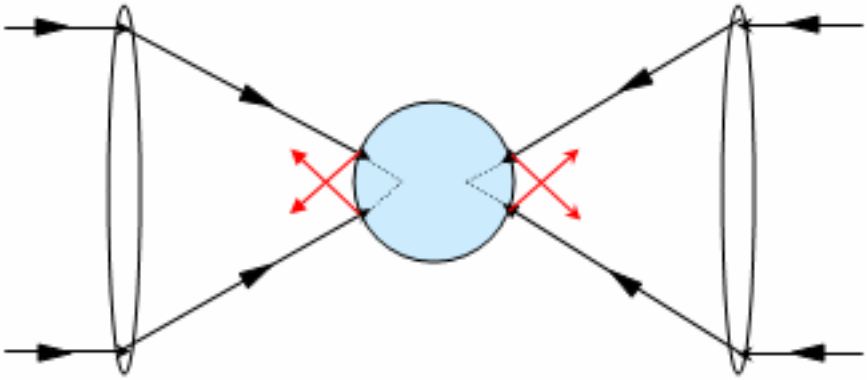

Figure 2. Schematic diagram of a dual beam optical tweezers.

Fig. 2 shows the design of dual beam optical tweezers. The red lines represent light reflected at the surface of the sphere. In this design, two microscope objectives face each other and focus two separate laser beams to the same spot. Since the force due to reflection is approximately the same for each laser (providing equal laser power), these reflection forces cancel and the trap can be stabilized (8). Dual beam optical tweezers instruments are therefore able to generate higher trapping forces for a given laser power of each laser and can be constructed with lower numerical aperture microscope objectives. In addition, the two laser beams must be aligned to within less

than a bead diameter and the resulting measurements must be corrected for errors due to drifts in the relative alignment of the laser beams (9).

1.5 Experimental setup

Figure 3 shows the experimental setup used for this study required for the injection and detection of the two counter-propagating laser beams (9). It consists of two identical water immersion lenses L1, L2 [UPLAPO 60X/W/IR, Olympus, Zürich, Switzerland (NA=1.2, d_{BA}=7.2 mm, 285 μm working distance)] that form an afocal optical system. The two counter-propagating lasers A and B are superimposed (*i.e* focus nearly at the same point) to allow a high trapping efficiency. For this reason, the lens L_2 is placed onto a XYZ flexure stage (MDT631, Thorlabs, Newton, NJ) operated by a 3-axis piezocontroller (MDT690, Thorlabs, Newton, NJ), PBS: polarized beam splitter, QW: quarter-wave plate and F: low-pass filter. The imaging part consist of a light-emitting diode (LED) ~ 380 nm, a dichroic mirror (DM) and a

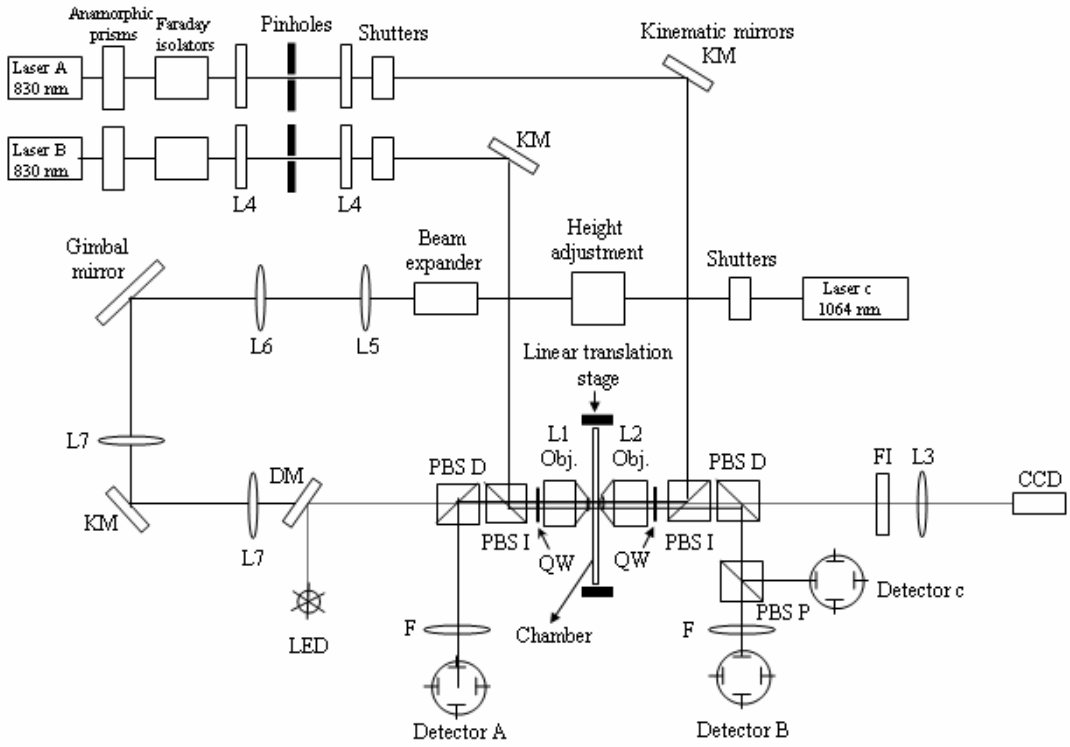

Figure 3*. Schematics of the experimental setup of dual beam optical tweezers.*

low-pass filter (FI) for imaging. L3 is a planoconvex lens used to image the focal plane of L2 on to a CCD camera. The chamber is placed on an independent piezoelectric element (517.3CL, Physik Instrumente, Waldbronn, Germany). Since this setup is fully symmetric, the laser B can be also injected and detected without any significant loss of power on detector B. Each single-mode diode laser [5431-G1, SDL,

San Jose, CA (λ=830 nm, maximum power 200 mW)] is driven with an external module (laser diode driver model 505, Newport, Irvine, CA) and is temperature controlled (temperature controller model 325, Newport, Irvine, CA). The collimated delivered beam is Gaussian TEM_{00} mode and rectangular shaped (~ 5.2×1.7 mm). Beam shaping is required to provide circular beam cross-section and is achieved using anamorphic prisms (06GPA004, Melles Griot, Irvine, CA) that produce a square-shaped beam (~ 5.2 mm, full length). To prevent back reflections and reduce mode-hopping of the laser, we used optical isolators (IO-5-830-LP, Optics for Research, Caldwell, NJ). Finally, the beam is spatial filtered using two identical achromat doublets (focal length: 100 mm, Newport) and a 40 μm pinhole [mounted on a XYZ positioner (LP-1-XYZ, Newport, Irvine, CA)]. After this filtering, the laser beam exhibits a clean Gaussian profile with an isotropic circular shape (ϕ = 5 mm) and can be finally injected into the microscope lenses.

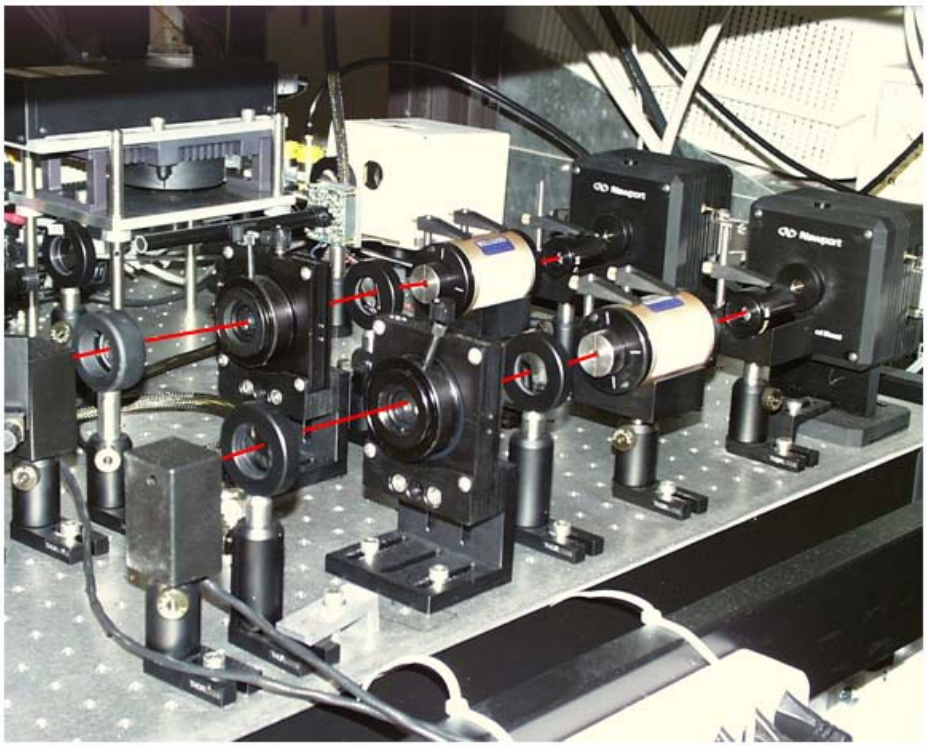

Figure 4. *The laser beam shaping path of dual beam optical tweezers.*

1.6 Third trap (steerable trap)

For the third beam, we use a diode laser emitting at 1064 nm (LCS-DTL-322, Laser 2000, Wessling, Germany) (9). The beam has a TEM_{00} beam diameter of ~ 1.5 mm and is linear polarized (maximum output power: 1 W). The laser beam is first brought

to a correct height (similar to that of lasers A and B) using a X-beam-steerer, composed of two 45 degree -mirrors (height adjustment).

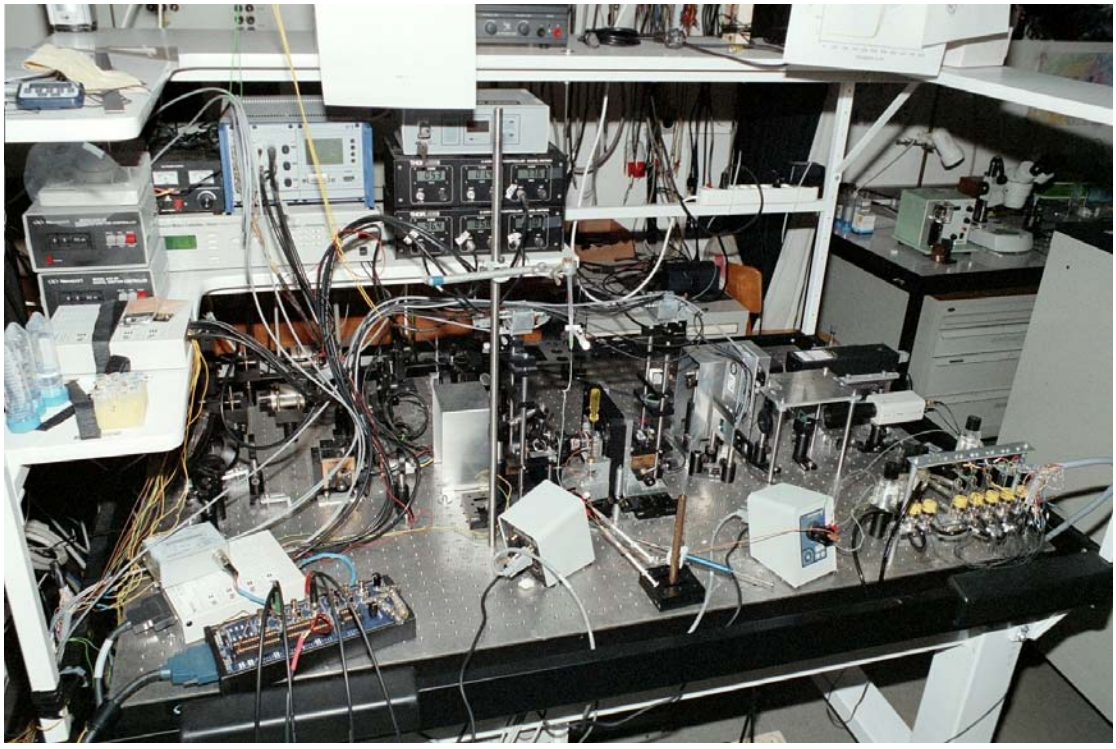

Figure 5*. Photograph of the instrument.*

To achieve proper overfilling of the microscope back aperture (lens L_1, required for efficient single beam trapping), a 6X beam expander (S6ASS0106, Sill Optics, Wendelstein, Germany) is then implemented within the path. For Z-steering, we use two lenses L_5 (focal length: 80 mm) and L_6 (focal length: 62.9 mm). These two lenses form an afocal arrangement and L_5 is placed onto a piezoelectric element (MDT631, Thorlabs, Newton, NJ), which is operated by a piezocontroller (MDT690, Thorlabs, Newton, NJ) and an additional DC-stepper motor. The XYZ flexure stage (used only in the Z direction) has a piezoelectric translation of 15 μm and a manual DC translation of 2 mm. This results in a maximum possible change in depth of focus of ~ 35 nm and ~ 4.6 μm for the piezoelectric and DC operations, respectively. Beam steering along the X and Y directions (in the specimen plane) is achieved by pivoting a gimbal mount (U200-G, Newport, Irvine, CA) which is optically at the same plane as the back aperture L1 of the microscope lens. For precise movements of the gimbal, we use closed-loop DC actuators (CMA-12CCL, Newport, Irvine, CA) driven by a ESP300 platform (Newport, Irvine, CA). With such a configuration, the minimal incremental angular motion of the gimbal is 7×10^{-6} radians, yielding a minimal incremental motion of ~ 42 nm in the specimen plane, and allows beam steering

without loss of incident rays. The XY-steering lenses (labelled L_7, focal length: 175 mm) also are placed in an afocal arrangement.

After proper conditioning of the laser, the laser beam passes through a dichroic mirror and enters the microscope lens L_1. At the entrance back aperture of L_1, we measured a diameter of ~ 7.1 mm. It is important to note that the PBS used to inject lasers A and B transmits most of the 1064 nm laser beam. However, parasitic back reflections of the 1064 nm laser beam can interfere with the output readings of the detectors A and B. To prevent this, we implemented low-pass filters [labelled F in Fig.3 (Schott, Feldbach, Switzerland)].

1.7 Chamber, imaging, flow system

The chamber consists of two parafilm layers sealed on two microscope coverglass (no.1) (9). Prior to sealing, the parafilm layers are cut to define a channel (50×3.5×0.3 mm) for fluid injection and a ~ 100 µm glass tube (inner diameter) (WPI, CMF 346) is inserted between the parafilm layers.

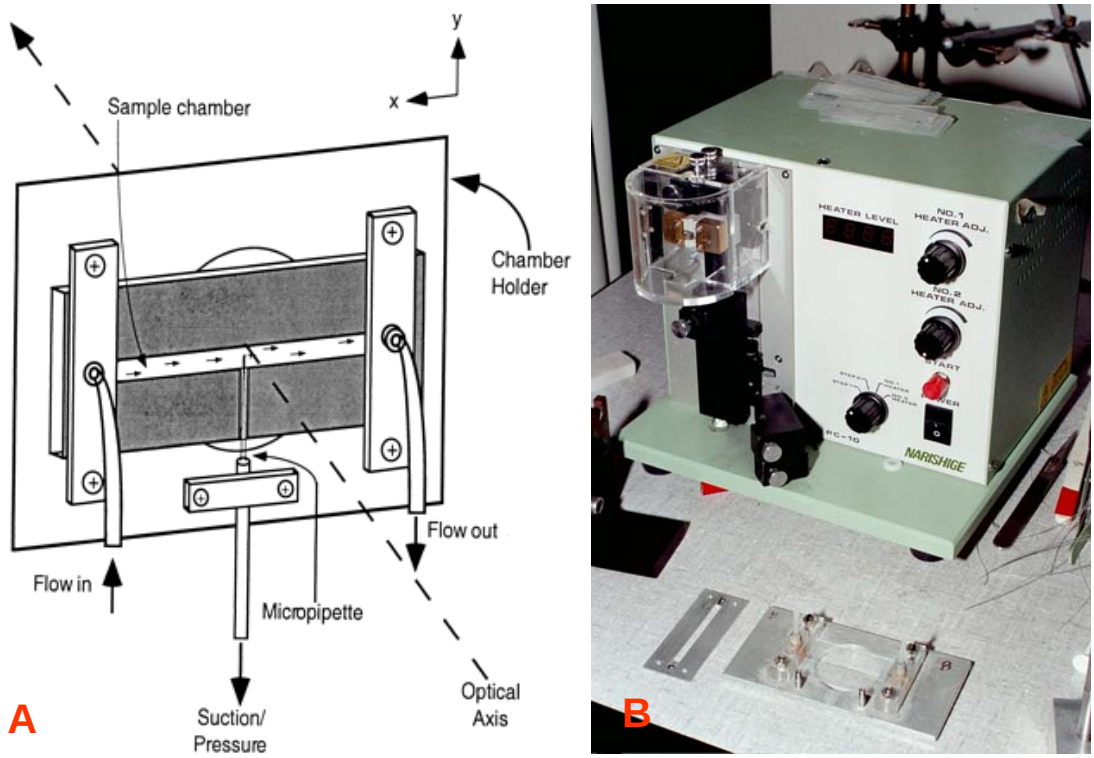

Figure 6. *A) schematics of a fluid chamber and B) micropipette puller.* Two holes are drilled within the chamber to define an inlet and an outlet for liquid. The ~ 300 µm-thick chamber is then placed on an aluminium holder. A glass

micropipette is pulled from a custom made glass capillary (outer diameter ~ 80 μm) (KG-33, Garner Glass, Claremont, CA) to obtain a < 1 μm diameter on one side. The micropipette is finally inserted inside the ~ 100 μm tube and connected to a manual syringe to allow suction of micron-sized beads. An important point is that the nearly-coincident focus of the two counter-propagating laser beams defines a fixed location in space. For this reason, the chamber has to be placed on an element that allows movements in 3-dimensions, independently of the XYZ flexure stage used to align the lasers. This element is composed of two 1-dimensional translation stages (TSX-1D, Newport, Irvine, CA) that have a 25 mm travel range in the optical Z direction. These stages hold a 3-axis piezoelectric flexure scanner (517.3CL, Physik Instrumente, Waldbronn, Germany) that has a maximum range of 100 μm for the X and Y directions and 20 μm along the Z axis, respectively. Each axis is operated by a voltage signal (0-100 V) provided by an amplifier module (E-503.00, Physik Instrumente, Waldbronn, Germany). This voltage is controlled by an analog signal (0-10 V) applied to the BNC inputs of the amplifier. For accurate movements (closed-loop operation), a servo controller (E-509.C3, Physik Instrumente, Waldbronn, Germany) is used. For a typical experiment, the pipette and the trapped bead have to be imaged onto a CCD camera. A plano-convex lens L_3 is therefore used to image the specimen plane (the focus of the objective lenses) onto the chipset of a CCD camera (VCB-3424, MSM Trading, Basel, Switzerland). Illumination light is provided by a light emitting diode (LED, Marubeni, CA) (λ=380 nm) which is first reflected by a dichroic mirror (760DCLP, Omega Optical, Brattleboro, VT) and then injecting into L_1 (Fig.3). The pipette is brought into the specimen plane using both manual translation stages and a piezoelectric device. Note that finally additional low-pass filters [labelled FI in Fig.3 (Schott, Feldbach, Switzerland)] are used to eliminate unwanted IR radiation on the CCD.

Fluid delivery is controlled using pressure bottles and an automatic valve system (MVP, Hamilton, Reno, NV). Pressure bottles are used either to contract or expand the air on the different buffer solutions, which are afterwards injected in the chamber by the value system.

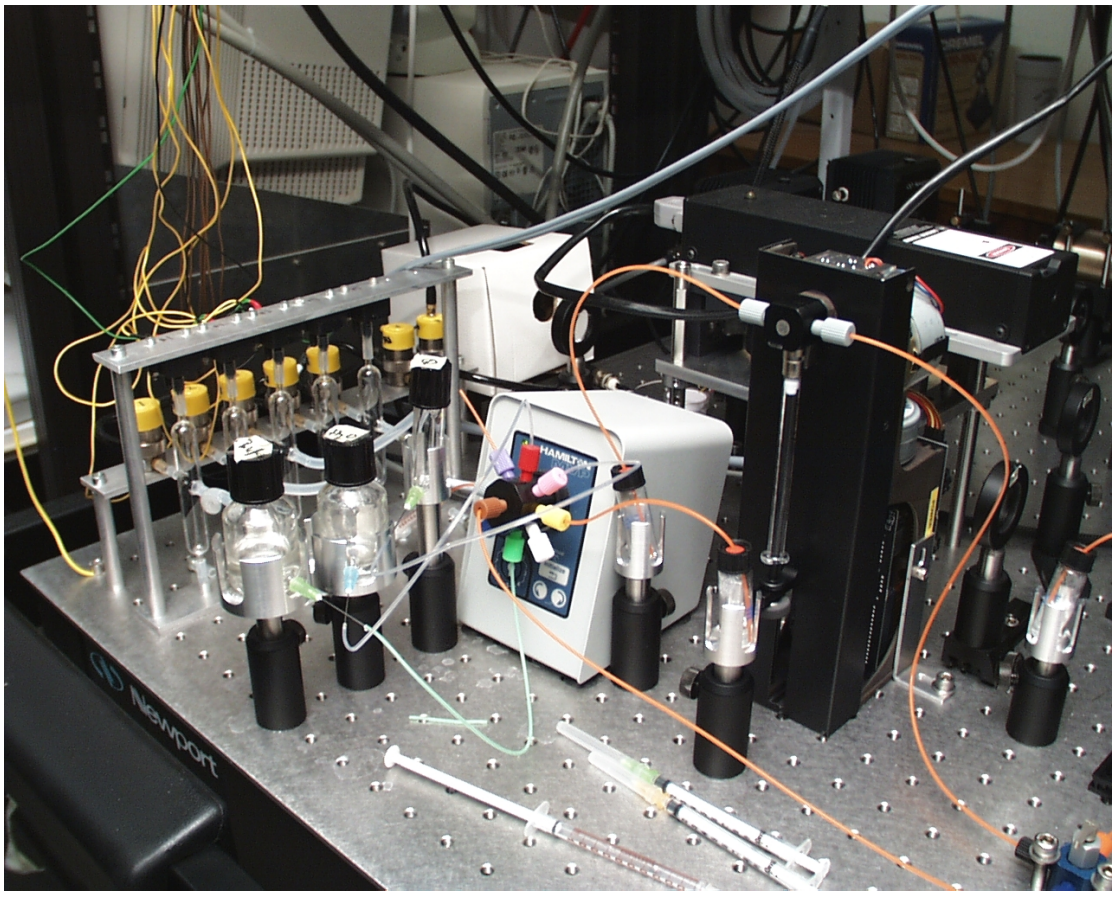

Figure 7. *Photograph of the fluid delivery system.*

The flow rate in the chamber is directly proportional to the applied pressure (vacuum) or the difference in height between the liquid in the buffer solution during manual injections and the waste solution (connected to the outlet of the chamber).

1.8 Force measurement with optical tweezers

Optical tweezers can be used to directly measure forces which act on trapped objects and are described by the equation:

$$\mathbf{F} = -k\mathrm{x} \qquad [4]$$

Thus, if we can determine the constant *k*, referred to as the trap stiffness, measuring the position of the bead in the trap determines the force on the bead in the trap.

In a dual-beam optical tweezers instrument, the trapping laser itself can be used to measure the bead position. Laser light entering and exiting a polystyrene sphere has its momentum changed by the presence of the bead, and this momentum change determines the force exerted on the bead by the light. This change in momentum is equivalent to a change in the direction of propagation of the light, which can in principle be directly measured by imaging the beam position. When a force is applied to the bead, the deflection of the laser beam itself can then be directly measured using

a position sensitive photodiode detector which is previously described in detail by Grange *et al.* (9). For each laser, a 2-dimensional linear PSD detector is used to readout the light intensities and its displacements which are relevant to determine the force. To reduce noise, the electronic circuit (needed for proper signal conditioning) is placed in a shielded box next to the detector.

1.9 Force–power and bead size dependence

Fig.8 shows the force acting on a polystyrene microsphere (3.10 μm in diameter) as a function of the speed of flow.

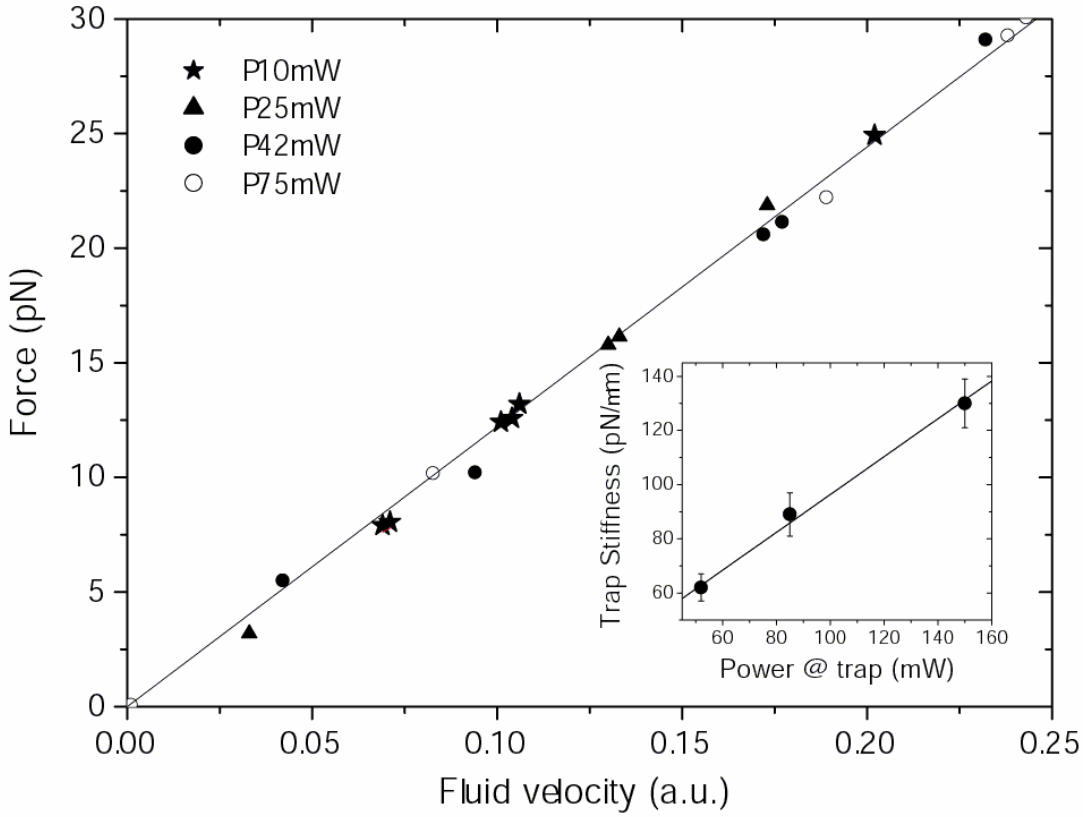

Figure 8. *Force as a function of the fluid velocity (3.10 μm-diameter-bead). Empty circles, 150 mW; filled circles, 84 mW; triangles, 50 mW; stars, 20 mW. Solid line, linear fit to the data. In the inset is shown the dependence of the trap stiffness as a function of the total laser power (i.e. for the two laser beams).*

For a total power of 150 mW, the force shows - as expected - a linear behavior as a function of the applied pressure (9). Decreasing the total power of the laser should not affect the force acting on the trapped particle but should dramatically decrease the trapping efficiency. In other words, the stiffness of the light lever is modified when the power of the lasers is changed (see inset of Fig.8). In a regular single-beam OT a

new calibration should be performed to accurately determine the force acting on the trapped particle in each and every experiment. In contrast to our instrument, we however directly measure the change in light momentum flux. Therefore, the force *versus* applied pressure plots measured for different laser powers show a unique linear dependence (9).

1.10 Trap stiffness calibration

The most popular method for the calculation of the trap stiffness is by recording a power spectrum measurement. Every object in solution is bombarded constantly by surrounding molecules. As a result, a spring-like device such as a bead in an optical trap experiences a mean-square displacement noise, $<\Delta x^2>$, proportional to the temperature, T, which is inversely related to spring stiffness, k ($<\Delta x^2> = k_B T / k$, where k_B is the Boltzmann constant), the so-called equipartition theorem. If the device is linear, its corresponding mean-square force noise is $<\Delta F^2> = k \cdot k_B T$. The spectrum of fluctuations of an object is determined by the proportionality that exists between its ability to absorb thermal energy and its ability to dissipate it by friction. This result is embodied in the 'fluctuation-dissipation theorem' (1).

Thus the stiffness of an optical trap can be estimated from the power spectral density $S_{FF}(f)$ of the thermal force fluctuations (9):

$$S_{FF}(f) = \frac{2k_B T \beta f^2}{\pi\left(f^2 + f_c^2\right)} \qquad [5]$$

This gives the frequency dependence of fluctuations, or the power spectrum, of the force fluctuations in an optical trap (9), where $\beta = 6\pi\eta a$, hydrodynamic drag coefficient of the object where a is the radius of the bead and η is the viscosity of the medium. $S_{ff}(f)$ is the spectral density in pN^2/Hz, $k_B T = 4.1$ pN·nm at room temperature, k_B is Boltzmann's constant, T is the absolute temperature, f_c the corner frequency which is related to the stiffness of the trap by the relation $f_c = (2\pi\beta)^{-1} k$. The 'corner frequency', f_c is the frequency above which the system cannot respond to an external stimulus. The corner frequency sets a limit to the rate at which processes can be observed and measured experimentally. For our experiment (dual beam OT), spherical particles are used and are trapped far away from the chamber walls. Therefore, the viscous drag is easily computable. Once stiffness of trap is known then the force F applied on trapped object can be measured with the displacement of it

from the equilibrium position using equation 4. An example of an ideal (experimental) power spectrum is shown in figure 9.

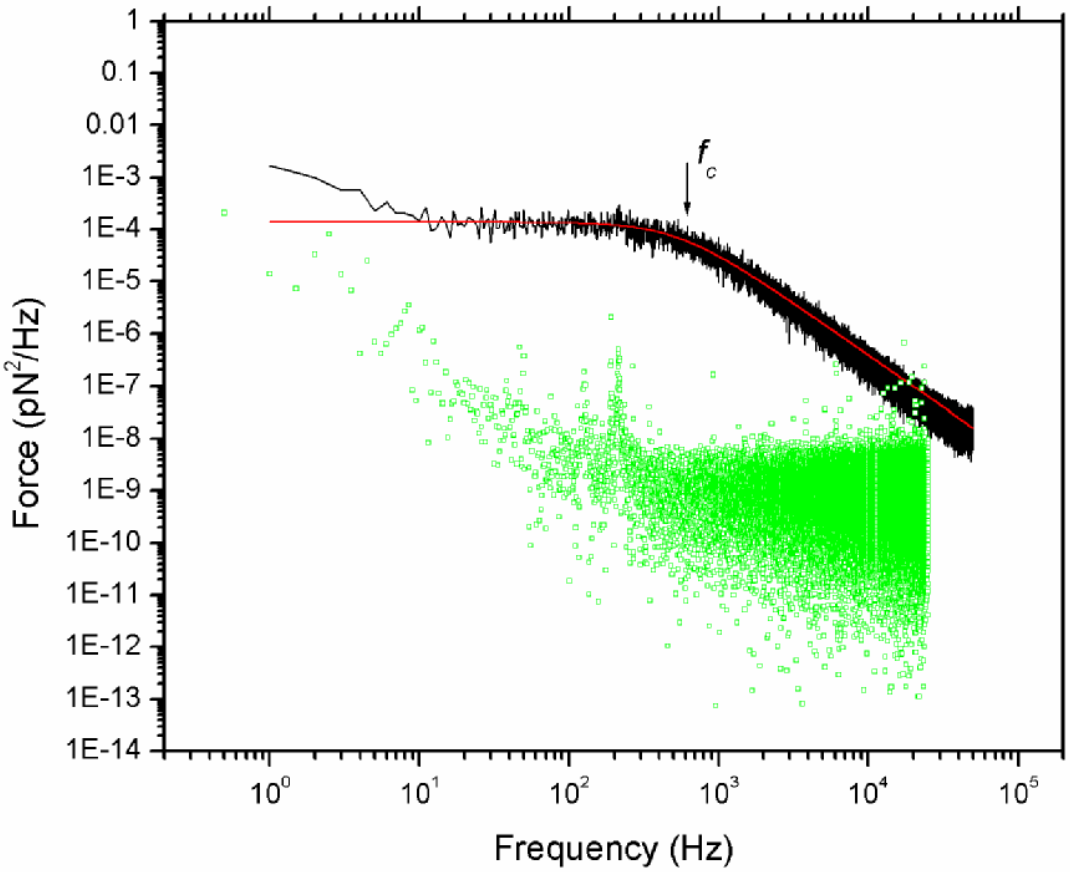

Figure 9. *Measured power spectrum for a 3.1 µm bead in an optical trap (black curve) and Lorentzian fit (red curve). Green curve shows the noise of the laser beam without an object (bead) in the focal region.*

The power spectrum has been obtained for a 3.10 µm-diameter-bead over a large bandwidth (10-50 kHz). The force fluctuations are approximately constant at low frequencies until f_c (785 Hz) is reached, at which point the slope of the power spectrum changes significantly. Thus, measurement of the fluctuations in the force of a bead in an optical trap due to Brownian motion can be used to determine f_c. Therefore, from equation 4 this is a measurement of the trap stiffness, k, which allows us to determine the force on a bead in the trap directly from its change in position.

1.11 Applications of Optical tweezers in Biology

Many studies have been reported to study the mechanical and kinetic properties of single macromolecules using optical tweezers as a force transducer. In biology, OT

offers a non-invasive and precise micromanipulation of a specimen in a closed and native environment. Mainly the research work done on the measurement of mechanical (elasticity, torque, rigidity, stiffness) properties of cell membranes, single dsDNA or ssDNA molecules, filamentous proteins and the study of single motor molecules is listed here.

1.11.1 First biological applications of optical tweezers

In 1987, Ashkin was the first to report the use of optical tweezers for manipulating biological objects (10). Bacteria and viruses were trapped using an argon laser at a wavelength of 514 nm, however this visible laser light caused substantial damage to the biological objects even at very low powers. In his second paper, he described the use of an IR laser (Nd: YAG laser of wavelength 1064 nm) to trap and manipulate a variety of living cells and organelles. The authors found that the IR laser did not cause any visible damage to the investigated cells (11).

1.11.2 Single biomolecule measurements

The use of OT allows direct access to nanomechanical properties of single biomolecules. Such investigations allow to get fundamental knowledge upon the building blocks which provide genome data storage (DNA, RNA) and the components of the cytoskeleton. For instance the buckling and rigidity of a single microtubules was found to be dependent on their length (12). These microtubules were manipulated and at same time their shape (flexural rigidity) was observed (13). Folding-Unfolding transitions in a single giant muscle protein (i.e. Titin molecules) were measured as a force extension curve (14) and their elasticity was measured (15,16). The stiffness of the essential molecules of the connective tissue, procollagen molecules, studied by stretching (17), and the elasticity of the cytoplasm was measured by optical tweezers technique (18). OT were developed to allow cell sorting for the creation of cell patterns for drug screening (19).

1.11.3 Measurements involving DNA

Steve Chu *et al.* reported the first manipulation and elasticity studies of single DNA molecules. They attached polystyrene spheres to the ends of long DNA molecule and pulled the two spheres apart using optical tweezers (20). Their single molecule manipulation allowed observations of the relaxation of a single DNA molecule by optical microscopy (21). In addition they attached DNA to the latex spheres which were trapped and increased the length of this biopolymer with the help of flow and directly visualized these processes with fluorescence microscopy (22). Carlos

Bustamante and his group were the first who investigated elastic responses of single and double stranded DNA molecules by applying a known external force. They observed conformational changes in dsDNA during the overstretching at approximately 65 pN (5). More detailed studies into the mechanics of single dsDNA were conducted (23-25) and provided not only mechanical information on RNA folds but also torsional information (26). Polymerization and mechanical properties of individual RecA-DNA filaments, containing either single-stranded or double-stranded DNA were characterized by Hegner *et al.* (27) and others (28,29). The kinetics and mechanism of DNA uptake into the cell nucleus could be investigated by measuring the extension of a dsDNA molecule between a bead and the nucleus (30). Single molecule optical tweezers experiments allow also to follow the assembly and unfolding of individual nucleosomes by stretching chromatin fibers (31). OT have been used to determine the thermodynamic properties of DNA molecules and the effect on the overstretch transition at various pH from 6 to 10.6 and temperatures from 11° C to 55° C (32,33). The first experiment on stretching of RNA and the thermodynamics of RNA folding was performed in 2003 by the Bustamante group (34). Many regulatory biological processes in the cell such as the progress of a messenger RNA through the ribosome, the action of RNA helicases in initiation of translation and spliceosome activity all involve controlled mechanical deformation and unfolding of RNA strands.

1.11.4 Nucleic acid-based enzymes

RNA polymerase, a molecular motor capable of moving through thousands of base pairs without detaching from the DNA template, has also been investigated and was found capable of generating at least 14 pN of force. Measurements of velocity and stall forces were carried out investigating the prokaryotic *E. coli* RNA polymerase (35,36).

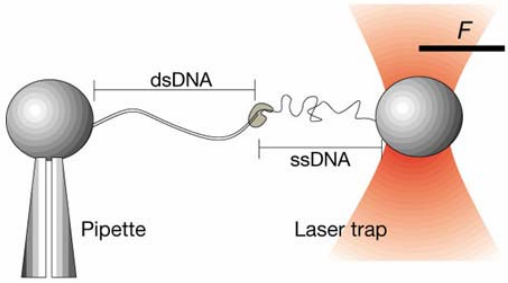

Figure 10. *The force-induced exonuclease activity of T7 DNAp to remove any desired length of the non-template strand* (37).

Single dye labeled molecules of RNA polymerase sliding on dsDNA which was suspended in between two beads (38) and direct observation of DNA rotation during transcription by E. coli RNA polymerase could be visualized using advanced optical microscopy setups (39). The DNA packaging into the viral head of phi 29 bacteriophage was directly studied by applying forces on the DNA (40). The ability of topoisomerase enzymes to release a single supercoil in a DNA molecule was studied (41) and the protein synthesis by single ribosomes could be examined using magnetic, optical tweezers respectively (42).

1.11.5 In cell biology, intracellular materials such as organelles and chromosomes have been investigated with OT. Single kinesin molecules which carry out the transport of cargo within the cell along microtubules was subjected to forces in different directions. Forward and lateral forces showed only little effect on the molecule processivity but backward forces significantly slowed the speed of molecule (43). The cytoplasmic viscoelasticity in plant cells was measured by manipulations within the cell (44). Chromosome movement during cell division was studied by applying optical forces (45), and the microdissection of chromosomes and microcloning was performed by Greulich *et al.* (46). The elasticity and conformations of the red blood cell membrane skeleton which provide a important insights into cellular movement within veins was studied by Svoboda *et al.* (47). Precise manipulations of chromosomes arms and fragments in mitotic newt lung cells (48) and optically controlled collisions of viruses with cell membranes inducing adhesion and molecular recognition were demonstrated (49). The lateral mobility of membrane proteins within membranes (50) and the Young's modulus of the bacterial cell wall could be investigated (51). Controlled micromanipulation of sperm in three dimensions was achieved by Colon *et al.* (52) and drilling by UV laser and sperm insertion into egg cells was demonstrated (53) allowing future manipulations in the field of *in vitro* fertilization. An important issue is the influence of the high-intensity light used for manipulations regarding the damage of complete cells within the wavelength range of 790-1064 nm. It was found that the rotation rates of *Escherichia coli* tethered to glass (54) were affected by the longer wavelength (i.e. 1064 nm) and lasers that uses wavelengths of 830 and 970 nm were recommended for future use.

1.11.6 Biological motors

Many enzymes are involved in the production of work and movement within cells. Their ability to convert chemical energy into mechanical energy named them as

molecular motors. Molecular motors move along linear substrates and can be divided into two subsections: 1. 'Porters' are processive enzymes, such as kinesin, which walk along their filament, carrying a cargo contained in a vesicle, without diffusing off from the microtubule track. 2. 'Rowers' which are non-processive enzymes and produce just a single tug on the filament (e.g. actin) and then dissociate, such as myosin in muscle.

The first measurement of motor forces using optical tweezers was published in 1993 by Svoboda *et al.* (4). A single kinesin molecule was attached to a polystyrene bead which was held in optical tweezers. Then the sphere was brought close to a microtubule which was fixed to a microscope slide. Upon interaction, the kinesin molecule pulled the bead (its cargo) along the microtubule track.

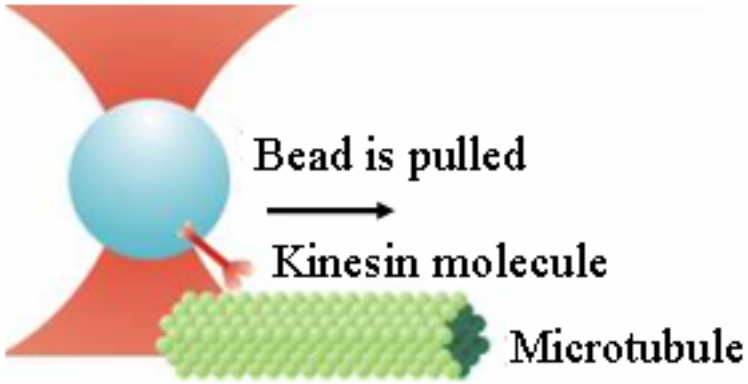

Figure 11*. Force measurement of kinesin (or dynein) as it moves along microtubules (attached to the surface of a coverslip). The molecule kinesin is attached to a sphere which is held in an optical trap* (4).

The position of the sphere was monitored using a four-quadrant detector and discrete 8 nm steps taken by the kinesin molecule were identified. One year later, force and velocity of kinesin were reported (55) and the bead movement by single kinesin molecules was observed (56). The unbinding force of kinesin attached to microtubules under various nucleotide conditions was measured (57) and the load dependent forward motion of kinesin could be elucidated (58).

Dynein which travel on microtubule in the opposite direction to kinesin were observed to be an oscillating force generator (59) and a stepwise movement of single 22S dynein molecules found to take place only at low concentration of ATP (60).

Movement and force produced by single myosin head arising from stochastic interaction of it (myosin) with actin was measured (61), its unbinding force was found to be 9 pN which was independent of its angle relative to the interacting actin filament

(62). The force of single myosin molecule pulling against an actin filament was determined by Finer *et al.* in the early nineties (63).

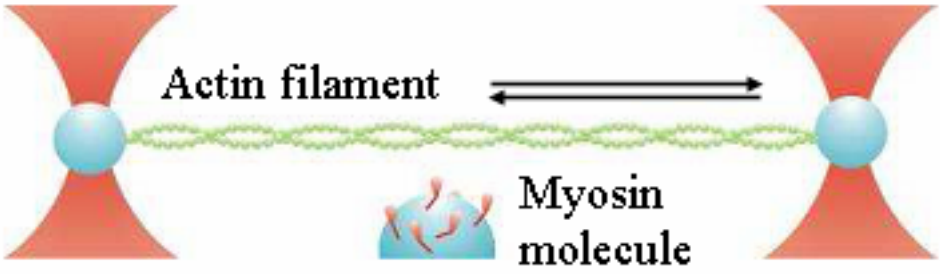

Figure 12. *The force measurement of myosin as it moves along actin filaments* (63).

Another group of motor proteins exists that rotate (rotary motors) and are found to be embedded in biomembranes. They are driven by the flow of ions due to transmembranes of electrochemical gradients. One such rotary motor is the bacterial flagellar motor which Steven Block and others have studied using optical traps (64). Berry and Berg performed a more detailed study of the forward and reverse rotation of the bacterial flagella rotary motor protein (65,66).

1.12 Conclusion

Here a short overview of optical tweezers is given since their developments have driven much of the current single molecule research and have opened exciting avenues of research, especially in biology. With the advent of sophisticated optical tweezers instruments it is possible to look at complex molecular systems at a single molecule level and reveal behavior which would be averaged out in traditional biochemistry experiments. Ultimately, the goal of single-molecule manipulation with OT is to access the machinery of a living cell. Although the task of characterizing molecular machines and organelles seems daunting, there has been exciting progress. In the near future, scientists may come to see each cell as an individual with its own set of molecular machinery. By using methods like OT for manipulating single molecules, biologists will be able to investigate the nature of molecular machines one by one, and infer from their behavior those properties common to the population (1).

1.13 References

1. Bustamante, C., Macosko, J.C. and Wuite, G.J.L. (2000) Grabbing the cat by the tail: Manipulating molecules one by one. *Nat. Rev. Mol. Cell. Biol.*, **1**, 130-136.

2. Ashkin, A. and Dziedzic, J.M. (1971) Optical levitation by radiation pressure. *Applied Physics Letters*, **19**, 283-285.
3. Ashkin, A., Dziedzik, J.M., Bjorkholm, J.E. and Chu, S. (1986) Observation of a single-beam gradient force optical trap for dielectric particles. *Opt. Lett.*, **11**, 288-290.
4. Svoboda, K., Schmidt, C.F., Schnapp, B.J. and Block, S.M. (1993) Direct observation of kinesin stepping by optical trapping interferometry. *Nature*, **365**, 721-727.
5. Smith, S.B., Cui, Y. and Bustamante, C. (1996) Overstretching B-DNA: the elastic response of individual double-stranded and single-stranded DNA molecules. *Science*, **271**, 795-799.
6. Grier, D.G. (2003) A revolution in optical manipulation. *Nature*, **424**, 810-816.
7. Smith, S.B., Cui, Y. and Bustamante, C. (2003) Optical-Trap Force Transducer that Operates by Direct Measurement of Light Momentum. *Methods in Enzymology*, **361**, 134-162.
8. Williams, M.C. (2002) Optical Tweezers: Measuring Piconewton Forces. *Single Molecule Techniques*, **volume of the Biophysics Textbook Online**, http://www.biophysics.org/btol/.
9. Grange, W., Husale, S., Güntherodt, H.-J. and Hegner, M. (2002) Optical tweezers system measuring the change in light momentum flux. *Rev. Sci. Instr.*, **73**, 2308 - 2316.
10. Ashkin, A. (1987) Optical trapping and manipulation of viruses and bacteria. *Science*, **235**, 1517-1520.
11. Ashkin, A., Dziedzic, J.M. and Yamane, T. (1987) Optical trapping and manipulation of single cells using infrared-laser beams. *Nature*, **330**, 769-771.
12. Kurachi, M., Hoshi, M. and Tashiro, H. (1995) Buckling of a Single Microtuble by Optical Trapping Forces: Direct Measurement of Microtuble Rigidity. *Cell Motil. Cytoskeleton*, **30**, 221-228.
13. Felgner, H., Frank, R. and Schliwa, M. (1996) Flexural rigidity of microtubules measured with the use of optical tweezers. *J. Cell. Sci.*, **109**, 509-516.
14. Kellermayer, M.S.Z., Smith, S.B., Granzier, H.L. and Bustamante, C. (1997) Folding-Unfolding Transitions in Single Titin Molecules Characterized with Laser Tweezers. *Science*, **276**, 1112-1116.
15. Tskhovrebova, L., Trinick, J., Sleep, J.A. and Simmons, R.M. (1997) Elasticity and unfolding of single molecules of giant muscle protein titin. *Nature*, **387**, 308-312.
16. Kellermayer, M.S.Z., Smith, S.B., Bustamante, C. and Granzier, H.J. (1998) Complete unfolding of the titin molecule under external force. *J. Struct. Biol.*, **122**, 197-205.
17. Sun, Y.L., Luo, Z.P. and An, K.N. (2001) Stretching Short Biopolymers Using Optical Tweezers. *Biochem. Biophys. Res. Commun.*, **286**, 826-830.
18. Tomishigie, M., Sako, Y. and Kusumi, A. (1998) Regulation mechanism of the lateral diffusion of band 3 in erythrocyte membranes by the membrane skeleton. *Journal of Cell Biology*, **142**, 989-1000.
19. Zahn, M., Renken, J. and Seeger, S. (1999) Fluorimetric multiparameter cell assay at the single cell level fabricated by optical tweezers. *FEBS Letters*, **443**, 337-340.

20. Chu, S. (1991) Laser manipulation of atoms and particles. *Science*, **253**, 861-866.
21. Perkins, T.T., Quake, S.R., Smith, D.E. and Chu, S. (1994) Relaxation of a single DNA molecule observed by optical microscopy. *Science*, **264**, 822-826.
22. Perkins, T.T., Smith, D.E., Larson, R.G. and Chu, S. (268) Stretching of a single tethered polymer in a uniform folw. *Science*, **268**, 83-87.
23. Wang, M.D., Yin, H., Landick, R., Gelles, J. and Block, S.M. (1997) Stretching DNA with optical tweezers. *Biophys. J.*, **72**, 1335-1346.
24. Bustamante, C., Smith, S.B., Liphardt, J. and Smith, D. (2000) Single-molecule studies of DNA mechanics. *Curr. Op. Struct. Biol.*, **10**, 279-285.
25. Baumann, C.G., Bloomfield, V.A., Smith, S.B., Bustamante, C., Wang, M.D. and Block, S.M. (2000) Stretching of single collapsed DNA molecules. *Biophys. J.*, **78**, 1965-1978.
26. Bustamante, C. (2004) Of torques, forces, and protein machines. *Protein Science*, **13**, 3061-3065.
27. Hegner, M., Smith, S.B. and Bustamante, C. (1999) Polymerization and mechanical properties of single RecA-DNA filaments. *Proc. Natl. Acad. Sci. USA*, **96**, 10109-10114.
28. Bennink, M.L., Scharer, O.D., Kanaar, R., Sakata-Sogawa, K., Schins, J.M., Kanger, J.S., Grooth, B.G.d. and Greve, J. (1999) Single-molecule manipulation of double-stranded DNA using optical tweezers: Interaction studies of DNA with RecA and YOYO-1. *Cytometry*, **36**, 200-208.
29. Shivashankar, G.V., Feingold, M., Krichevsky, O. and Lîbchaber, A. (1999) RecA polymerization on double-stranded DNA by using single-molecule manipulation: The role of ATP hydrolysis. **96**, Proc. Natl. Acad. Sci. USA.
30. Salman, H., Zbaida, D., Rabin, Y., Chatenay, D. and Elbaum, M. (2001) Kinetics and mechanism of DNA uptake into the cell nucleus. *Proc. Natl. Acad. Sci. U S A*, **98**, 7247-7252.
31. Bennink, M.L., Leuba, S.H., Leno, G.H., Zlatanova, J., deGrooth, B.G. and Greve, J. (2001) Unfolding individual nucleosomes by stretching single chromatin fibers was studied with optical tweezers. *Nat. Struct. Biol.*, **8**, 606-610.
32. Williams, M.C., Wenner, J.R., Rouzina, L. and Bloomfield, V.A. (2001) Effect of pH on the overstretching transition of double-stranded DNA: Evidence of force-induced DNA melting. *Biophys. J.*, **80**, 874-881.
33. Williams, M.C., Wenner, J.R., Rouzina, L. and Bloomfield, V.A. (2001) Entropy and heat capacity of DNA melting from temperature dependence of single molecule stretching. *Biophys. J.*, **80**, 1932-1939.
34. Liphardt, J., Onoa, B., Smith, S.B., Tinoco, I.J. and Bustamante, C. (2001) Reversible unfolding of single RNA molecules by mechanical force. *Science*, **292**, 733-737.
35. Yin, H., Wang, M.D., Svoboda, K., Landick, R., Block, S.M. and Gelles, J. (1995) Transcription against an applied force. *Science*, **270**, 1653-1657.
36. Davenport, R.J., Wuite, G.J., Landick, R. and Bustamante, C. (2000) Single-molecule study of transcriptional pausing and arrest by E. coli RNA polymerase. *Science*, **287**, 2497-2500.
37. Wuite, G.J.L., Smith, S.B., Young, M., Keller, D. and Bustamante, C. (2000) Single-molecule studies of the effect of template tension on T7 DNA polymerase activity. *Nature*, **404**, 103-106.

38. Harada, Y., Funatsu, T., Murakami, K., Nonoyama, Y., Ishihama, A. and Yanagida, T. (1999) Single-Molecule Imaging of RNA Polymerase-DNA Interactions in Real Time. *Biophys. J.*, **76**, 709-715.
39. Harada, Y., Ohara, O., Takatsuki, A., Itoh, H., Shimamoto, N. and Kinosita, K. (2001) Direct observation of DNA rotation during transcription by Escherichia coli RNA polymerase. *Nature*, **409**, 113-115.
40. Smith, D.E., Tans, S.J., Smith, S.B., Grimes, S., Anderson, D.L. and Bustamante, C. (2001) The bacteriophage phi 29 portal motor can package DNA against a large internal force. *Nature*, **413**, 748-752.
41. Strick, T.R., Croquette, V. and Bensimon, D. (2000) Single-molecule analysis of DNA uncoiling by a type II topoisomerase. *Nature*, **404**, 901-904.
42. Vanzi, F., Vladimirov, S., Knudsen, C.R., Goldman, Y.E. and Cooperman, B.S. (2003) Protein synthesis by single ribosomes. *RNA*, **9**, 1174-1179.
43. Block, S.M., Asbury, C.L., Shaevitz, J.W. and Lang, M.J. (2003) Probing the kinesin reaction cycle with a 2D optical force clamp. *Proc. Natl. Acad. Sci. U S A*, **100**, 2351-2356.
44. Ashkin, A. and Dziedzic, J.M. (1989) Internal cell manipulation using infrared laser traps. *Proc. Natl. Acad. Sci. U S A*, **86**, 7914-7918.
45. Berns, M.W., Wright, W.H., Tromberg, B.J., Profeta, G.A., Andrews, J.J. and Walter, R.J. (1989) Use of a laser-induced optica force trap to study chromosome movement on the mitotic spindle. *Proc. Natl. Acad. Sci. U S A*, **86**, 4539-4543.
46. Greulich, K.O. (1992) Chromosome microtechnology: microdissection and microcloning. *Trends. Biotechnol.*, **10**, 48-51.
47. Svoboda, K., Schmidt, C.F., Branton, D. and Block, S.M. (1992) Conformation and elasticity of the isolated red blood cell membrane skeleton. *Biophys. J.*, **63**, 784-793.
48. Liang, H., Wright, W.H., Cheng, S., He, W. and Berns, M.W. (1993) Micromanipulation of chromosomes in PTK-2 cells using laser miccrosurgery (optical scalpel) in combination with laser-induced optical force (optical tweezers). *Exp. Cell Res.*, **204**, 110-120.
49. Mammen, M., Helmerson, K., Kishore, R., Choi, S.K., Phillips, W.D. and Whitesides, G.M. (1996) Optically controlled collisions of biological objects to evaluate potent polyvalent inhibitors of virus-cell adhesion. *Chem. Biol.*, **3**, 757-763.
50. Winckler, B., Forscher, P. and Mellman, I. (1999) A diffusion barrier maintains distribution of membrane proteins in polarized neurons. *Nature*, **397**, 698-701.
51. Mendelson, N.H., Sarlls, J.E., Wolgemuth, C.W. and Goldstein, R.E. (2000) Chiral self-propulsion of growing baterial marofibers on a solid surface. *Phy. Rev. Lett.*, **84**, 1627-1630.
52. Colon, J.M., Sarosi, P., McGovern, P.G., Ashkin, A., Dziedzic, J.M., Skurnick, J., Weiss, G. and Bonder, E.M. (1992) Controlled micromanipulation of human sperm in three dimensions with an infrared laser optical trap:effect on sperm velocity. *Fertil. Steril.*, **57**, 695-698.
53. Schutze, K., Clement-Sengewald, A. and Ashkin, A. (1994) Zona drilling and sperm insertion with combined laser microbeam and optical tweezers. *Fertil. Steril.*, **61**.

54. Neuman, K.C., Chadd, E.H., Liou, G.F., Bergman, K. and Block, S.M. (1999) Characterization of photodamage to Escherichia coli in optical traps. *Biophys. J.*, **77**, 2856-2863.
55. Svoboda, K. and Block, S.M. (1994) Force and velocity measured for single kinesin molecules. *Cell*, **77**, 773-784.
56. Block, S.M., Goldstein, L.S. and Schnapp, B.J. (1990) Bead movement by single kinesin molecules studied with optical tweezers. *Nature*, **348**, 348-352.
57. Kawaguchi, K. and Ishiwata, S. (2001) Nucleotide-dependent single-to double-headed binding of kinesin. *Science*, **291**, 667-669.
58. Coppin, C.M., Pierce, D.W., Hsu, L. and Vale, R.D. (1997) The load dependence of kinesins mechanical cycle. *Proc. Natl. Acad. Sci. U.S.A.*, **94**, 8539-8544.
59. Shingyoji, C., Higuchi, H., Yoshimura, M., Katayama, E. and Yanagida, T. (1998) Dynein arms are oscillating force generators. *Nature*, **393**.
60. Hirakawa, E., Higuchi, H. and Toyoshima, Y.Y. (2000) Processive movement of single 22S dynein molecules occurs only at low ATP concentrations. *Proc. Natl. Acad. Sci. U.S.A*, **97**.
61. Molloy, J.E., Burns, J.E., Kendrick-Jones, J., Tregear, R.T. and White, D.C. (1995) Movement and force produced by a single myosin head. *Nature*, **378**, 209-212.
62. Nishizaka, T., Miyata, H., Yoshikawa, H., Ishiwata, S. and Kinosita, K.J. (1995) Unbinding force of a single motor molecule of muscle measured using optical tweezers. *Nature*, **377**, 251-254.
63. Finer, J.T., Simmons, R.M. and Spudich, J.A. (1994) Single myosin molecule mechanics: piconewton forces and nanometre steps. *Nature*, **368**, 113-119.
64. Block, S.M., Blair, D.F. and Berg, H.C. (1989) Compliance of bacterial flagella measured with optical tweezers. *Nature*, **338**, 514-518.
65. Berry, R.M. and Berg, H.C. (1997) Absence of a barrier to backwards rotation of the bacterial flagellar motor demonstrated with optical tweezers. *Proc. Natl. Acad. Sci. U S A*, **94**, 14433-14437.
66. Ryu, W.S., Berry, R.M. and Berg, H.C. (2000) Torque-generating units of the flagellar motor of Escherichia coli have a high duty ratio. *Nature*, **403**, 444-451.

Small molecules binding to DNA

2.1 Effect of surfactant molecules binding to single dsDNA investigated by optical tweezers

2.1.1 Abstract

Cationic surfactants are widely used as nonviral vectors in gene therapy. The mechanics of single dsDNA in presence of cationic and anionic surfactants was measured at physiological conditions. The average compaction force induced by the cationic surfactants DTAB, CTAB and DMDTAB was ~ 25 pN, 22 pN and 30 pN respectively. The binding kinetics of the molecules (real time changes in condensing force) indicates a highly cooperative binding and compaction of single dsDNA. Binding of short cationic molecules (e.g. OTAB) to DNA did not induce any condensation. Force clamp experiments revealed that the collapsing speed – transition of elongated helical coiled dsDNA to a collapsed globular or toroidal state – of dsDNA increased depending on the length of the hydrophobic tail of the surfactant molecules. Anionic surfactants bound to dsDNA, but these molecules had a minimal effect on the mechanics of naked DNA. Our experiments suggest that concentrations below the critical micelle concentration (CMC) are recommended for reproducible DNA compaction for gene therapy.

Abbreviations: dsDNA = double stranded DNA, OTAB = Octadecyl-trimethyl ammonium bromide, DTAB = Dodecyl-trimethyl ammonium bromide, CTAB = Cetyl-trimethyl ammonium bromide, DMDTAB = Dimethyl-ditetradecyl ammonium bromide, SDS = Sodium dodecyl sulfate, SOS = Sodium octyl sulfate, CMC = critical micelle concentration.

2.1.2 Introduction

Genetic information is stored as individual sequences along double stranded DNA (dsDNA) molecules. External influences such as radiation, chemical, mechanical etc. can alter and damage the encoded sequence which thereafter looses its normal information. Besides the natural cellular repair machinery which is able to fix such damages at the gene level, gene therapy is thought to have the potential to provide a treatment to solve such defects. The treatment of inherited gene defects by either replacing or supplementing nonfunctional genes by ‘healthy’ genes might be within reach. It is believed that the transfer of selected genes into a host will ameliorate a

disease in a patient. Great hopes are that gene therapy will be a technique routinely used in the future to treat inherited diseases.

Cell membrane and DNA both are negatively charged. Thus due to electrostatic repulsion the cell membrane acts as a barrier and it is highly improbable that 'naked' DNA transfers through a cell membrane without modifications. Transfer vectors such as viral or nonviral are able to mask the newly added DNA and provide a means to circumvent the electrostatic repulsion in between DNA and cell membrane.

There are different types of viral vectors such as retrovirus, adenovirus, adeno-associated virus, herpex simplex virus, papilloma virus etc. (1). The safety of their use in humans is still matter of debate and the application of non-viral vectors (e.g. cationic lipids and liposomes) are more favorable due to their simplicity, low cost production on a large scale and lack of specific immune responses (2). Usually the modification of DNA as cationic complexes is tuned such that it has excess positive charge which is allowing efficient interaction with the negatively charged membranes. Neutral or anionic liposomes require entrapment of DNA inside vesicles. Cationic surfactants do not need such entrapment as it can easily bind to the negatively charged DNA through charge interaction. It is believed that the compaction of DNA due to the interaction with surfactant complexes may offer some means of protection against subsequent enzymatic degradation within the cell.

The first success of cationic lipid mediated *in vitro* transfection was achieved in 1987 (3). It was shown that the complex formation of condensed DNA with cationic lipids and fusogenic lipids are very efficient for the transfection into eukaryotic cells. Since then many liposomal formulations have been subjected to clinical evaluations as a nonviral vectors for gene therapy in cancer and cystic fibrosis (4,5). Rädler *et al.* reported that complexes containing DNA and cationic surfactants (lipid bilayers) can form a biological system having a potential in gene delivery (6). During the last 15 years there is solid progress in the development and application of nonviral vectors in gene therapy.

However non-viral gene transfection faced many obstacles. Limitations are mainly arising from its toxicity, low efficiency or failure cases reported due to the degradation of the transferred dsDNA inside a cell (7). Almost all cationic surfactants are toxic for cells. Specially single chain surfactant such as cetyl-trimethyl ammonium

bromide (CTAB) and dodecyl-trimethyl ammonium bromide (DTAB) show higher cellular toxicity. Their toxicity can be decreased by an addition of dioleoyl-phosphatidyl ethanolamine (DOPE) which was previously reported in the literature (8). To date *in vivo* gene transfer with single chain lipids was not reported because of its low efficiency.

Overall the success in gene therapy is totally depending on the selection and development of a vector system which can transfect genes with high efficiency exhibiting low or no toxicity. The development of such 'magic' lipids represents the first challenge to achieve successful gene therapy. Numerous studies reported on the development of more efficient structures of cationic lipids (9-12). Binding of cationic surfactants to DNA is the first step during the development of such lipids. The optical tweezers technique provides an efficient way to study such interactions on a single molecule level with high precision. Our findings on the mechanical properties of these complexes provide additional insights to future design and synthesis of new non-viral vectors and can help to understand their mechanism of interaction which is largely unknown (6).

Apart from biotechnological or biomedical applications, cationic surfactants have a variety of other applications in basic research. In nature, dsDNA is found in compact forms e.g. in chromosomes. Condensation is achieved by positively charged proteins like histones or naturally occurring polyamines such as spermidine^{3+}, spermine^{4+} etc. (13-15). A couple years ago the condensation of DNA due binding of cationic alkyl-ammonium was reported using isothermal titration calorimetry (16). Some groups studied the stretching and condensation of DNA by naturally occurring polyamines spermidine^{3+}, spermine^{4+} and the inorganic cation CoHex with optical tweezers (17,18). Study of condensation, compaction and decompaction are important in the field of biophysics, biochemistry and molecular biology to learn more about packaging and protection of DNA. Charge neutralization and phase behavior processes have been investigated earlier (19-23).

Forty years ago the use of cationic surfactants was reported, CTAB was then used for the precipitation and counting of small quantities of DNA. This precipitation method is still in use with some newer modifications (24-26). Some interactions of cationic surfactants such as CTAB or DTAB with DNA were studied by different methods such as fluorescence microscopy, dynamic light scattering and modeled by Monte Carlo simulations etc.. The condensation of single molecules of T4 DNA and discrete

transition between the coil and globule state was observed in the presence of the cationic surfactant CTAB. The decompaction of the DNA-cationic surfactant complex was studied by addition of salts. At the single molecule level this unfolding transition was observed to occur in a discrete manner. The globule to coil transition can be achieved with the help of anionic surfactants or synthetic polyacid and the condensation induced by CTAB was observed to be a reversible process (22,23,27,28). It has been recently shown that one CTAB molecule binds to one phosphate group of DNA (monomers) (29). Grosberg's theory predicted that a DNA collapse would show an abrupt phase transition but experiments with fluorescence microscopy and optical tweezers showed that it is discontinuous at the single molecule level (18,30,31). Decompaction of the DNA-cationic surfactant does not depend on the hydrophobicity of the compacting amphiphile such as CTAB, DTAB and tetradecyl-trimethyl ammonium bromide (TTAB) (32). The binding of cationic surfactant molecules to DNA enhanced strongly with an increase in the surfactants alkyl chain length (33).

Even though a lot of work has been done on surfactant DNA complexes there is still lack of information on the mechanical properties at the single molecule level such as compaction force, binding kinetics, transition speed of the coiled DNA to globule or toroidal form etc. The coil to globule transition is studied by fluorescence microscopy technique but no mechanical information of the molecule itself can be extracted.

The presented studies provide detailed information on the binding of cationic surfactants with different aliphatic chain lengths at single molecule level under physiological conditions. We elucidate the effect of binding of cationic surfactant to DNA, condensation forces involved in DNA compaction and can directly measure the collapse speed of individual DNA molecules (coil to globule transition).

Our results will help to clarify discrepancies observed in the interaction of DTAB with DNA which was investigated by other methods like isothermal microcalorimetry, UV spectrophotometry, potentiometric technique. They showed that interaction of DTAB with DNA did not cause any condensation (27) while according to research work published by Matulis *et al.* condensation of DNA was detected (16).

OTAB is a surfactant with a small aliphatic chain length of 8 and it has been reported that there is no visible interaction between DNA and OTAB (16,34). An increase in the turbidity of the system was observed but OTAB was unable to form a precipitate as predicted previously (34), our single molecule experiments provide new insights.

2.1.3 Materials and methods

Chemicals and materials: Surfactants – OTAB, DTAB, CTAB, DMDTAB, SOS, SDS and Sulfo SMCC were purchased from Sigma-Aldrich (Schnelldorf, Germany). Polystyrene beads, amino and streptavidin modified beads were available from Spherotech Co. (Libertyville, IL). Plasmid DNA pTYB1 and Klenow exo$^-$ (New England Biolabs, Bioconcept Basel), Biotin dATP, Biotin dCTP (Invitrogen, Bioconcept, Basel), Expand long template PCR (Roche, Mannheim), Biotin dUTP (Fermentas, Leon-Rot).

Preparation of DNA: Modified DNA (tethered in between two polystyrene beads) was prepared by PCR amplification. The initial DNA plasmid pTYB1 (7477 bp) which provides a template for amplification was purchased from New England Biolabs. According to our design the following forward primer 5' Thiol TGT AAC TCG CCT TGA TCG TTG GGA 3' (start at position 607) and the reverse primer 5' AGC GGA TAC ACC AGG ATT TGT CGT 3' (start at 7194) were purchased from Microsynth, Balgach. The PCR reaction was performed as follows: 94° C, 10 seconds, annealing at 57° C for 30 sec., elongation at 68 °C for 6 minutes (25 cycles). A final elongation step of the reaction at 68° C for 7 minutes was performed to complete all the newly generated 6587 base pairs dsDNA strands. Approximately 7 µg of modified dsDNA were generated by this PCR reaction. After amplification of the DNA it was cut asymmetrically at one end with Hind III restriction enzyme [generates 4 base pair overhangs (AGCT)]. Klenow exo$^-$ enzyme was used to fill in the overhangs with biotinylated nucleotides dUTP, dCTP, dATP and dGTP. The final length of the product was 5623 bp. The introduced thiol group at the 5' prime end served as specific group for covalent coupling of the dsDNA to amino modified polystyrene beads mediated by sulfo-SMCC cross linkers (35).

This study was performed on a dual beam optical tweezers setup consisting of two counter propagating diode lasers focused inside a liquid chamber cell. The fluid cell is made from two layers Nescofilms® sandwiched in between two cover glass plates (No.1). The depth of the chamber is approximately 240 µm, with a volume of ~ 18 µl. The experiment is set-up as follows: first a streptavidin coated polystyrene bead (diameter 2.17 µm) is optically trapped which then was transferred onto a glass micro-pipette by applying suction (36). Next dsDNA modified polystyrene beads (diam. 2.2 µm) (35) were injected. One end of the dsDNA was covalently coupled to the

interface of the trapped bead whereas another end was free exposing a biotin label. Thus the pipette bead was approached to 'fish' the biotinylated free end of the dsDNA. After successful hook up to the streptavidin functionalized sphere the DNA was stretched by moving the pipette away from the trapped bead. The force versus extension was recorded as reported in earlier studies (36). 150 mM NaCl, 10 mM HEPES pH 7.5, 1 mM EDTA and 1 mM NaN_3 was used as a standard buffer throughout all experiments. Cationic surfactants were injected at an average flow speed of ~ 25 µl per minute by gravity flow. To automatically exchange buffers a controlled pressure on buffer bottles was applied which was used to expand or contract the volume of the air on top of the liquid using an automatic valve system (MVP, Hamilton, Reno NV) (36).

2.1.4 Results

2.1.4.1 Basic considerations

Binding of cationic surfactant can be described as follows. First binding of alkyl-ammonium bromide (cationic surfactant) to the negatively charged phosphate backbone of dsDNA by electrostatic interactions is considered *i.e.* replacement of sodium cation with the surrounding counterion of the cationic surfactant. Then the condensation of the complex starts due to subsequent displacement of the other Na^+ ligands (16).

$$DNAP^- \bullet Na^+ + RNMe_3^+ + Br^- \leftrightarrow DNAP^- \bullet RNMe_3^+ + Na^+ + Br^- \quad [1]$$

$$nDNAP^- \bullet RNMe_3^+ \leftrightarrow (DNAP^- \bullet RNMe_3^+)_n \downarrow \quad [2]$$

where '*Me*' is the methyl (CH_3–) part and ↓ describes the precipitation of the last product. Both these electrostatic and hydrophobic interactions occur simultaneously in a highly cooperative manner.

The net charges on the DNA can be neutralized by the association of the counterion and charged surfactant molecules. The overall Helmholtz free energy (E_{tot}) is given as:

$$E_{tot} = E_{complex} + E_{solvation} + E_{mixing} \quad [3]$$

Where $E_{complex}$ is the energy needed to form an isolated complex, $E_{solvation}$ is the solvation energy (combination of electrostatic interaction between the complexes plus

the interactions between the complexes and the free counterions and surfactants), the last term E_{mixing} describes the free energy of mixing different species.

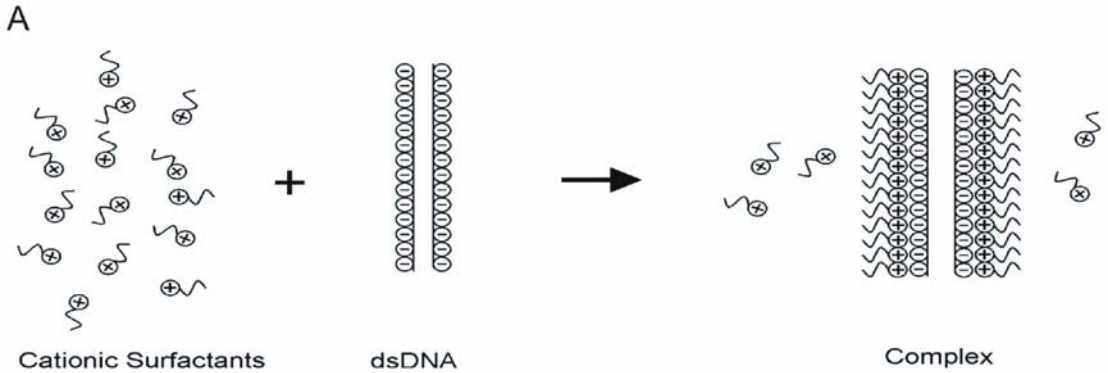

Figure 1A. *Schematic representation of cationic surfactants interacting with DNA.*

The hydrophobic interactions between the hydrocarbon tails of the cationic surfactant molecules and the core of the DNA on the basis of Fig.1A has been previously reported by Kuhn *et al.* (37) and can be given as

$$E^{v}{}_{DNA\_complex} = \chi_{DNA} \sum_{i,l}^{z,l_{max}} l\sigma_l(i) \qquad [4]$$

where χ_{DNA} describes the attraction between the hydrocarbon tails and the DNA core, z the charged phosphate groups on the DNA, i number of sites, l number of cationic surfactant, σ occupation variables of each site i. Figure 1B provides an overview of the chemical structures of different surfactant used in this study.

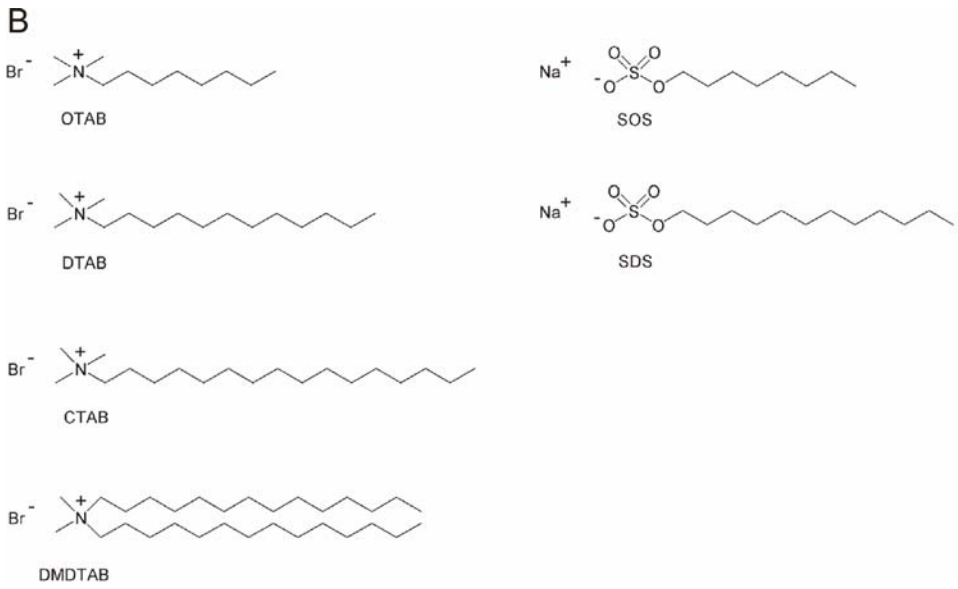

Figure 1B. *Chemical structures of the surfactants.*

2.1.4.2 Mechanics of naked (native) DNA

DNA is a highly charged polymer and attains a random coil like structure in solution to maximize its entropy. The elastic response of single DNA to an external applied load was first reported by Smith *et al.* (38). The mechanics of naked DNA under external load can be well explained with the worm like chain model (WLC) (39). An interpolation formula that describes the extension of DNA with contour length L_0 under an applied force is given by

$$\frac{FP}{k_B T} = \frac{1}{4}\left[1 - \frac{x}{L_0}\right]^{-2} - \frac{1}{4} + \frac{x}{L_0} \qquad [5]$$

where the flexibility of the DNA chain is described by the persistence length P which is defined as the distance over which two segments of DNA chain remain directionally correlated. F is the applied force, x/L_0 is the fractional extension of the DNA, L_0 is the contour length, k_B the Boltzmann constant and T is the absolute temperature. Stretched naked DNA exhibits two distinct mechanical regimes, one is the entropic elasticity regime dominated by the thermal energy up to ~ 6 pN (40). The above equation [5] describes an entropic elasticity of the molecule over the extension $x/L_0 < 0.97$. Plotting this data as a square root of force versus extension, allows to extract *P* directly from the *y*-axis intercept as $(4P\cdot(k_BT)^{-1})^{-1/2}$.

If the molecule is stretched beyond its contour length then deviations from the WLC model at forces higher than 6 pN occur. Here the second regime starts which is termed as enthalpic elasticity and is dominated by base pair stacking interactions. The DNAs resistance (change in slope) to stretching beyond its counter length can be characterized by a term S (stretch modulus). Equation [5] is expanded by S and is then described as an extensible WLC (18).

$$\frac{FP}{k_B T} = \frac{1}{4}\left[1 - \frac{x}{L_0} + \frac{F}{S}\right]^{-2} - \frac{1}{4} + \frac{x}{L_0} - \frac{F}{S} \qquad [6]$$

The force increases rapidly over a small extension as soon as the molecule reaches its contour length. At standard buffer condition DNA molecule show stretch modulus of ~1000 pN and contour length is attained at ~ 26 pN. At ~ 65 pN overstretching of naked DNA is observed which allows extension to 1.7 times the contour length over a very small range of force ~ 2 pN. This indicates the conversion of B form DNA to S form (38). The origin of this overstretching of dsDNA at ~65 pN is still discussed controversial. Some models describe the transition arising from melting of the base

pairs, others as a structural transition and is still open for additional research. A typical stretching experiment on naked dsDNA (force versus extension) is shown in fig. 2 (black squares) and helps to guide the eye as a mechanical 'ruler' for naked dsDNA in standard chamber.

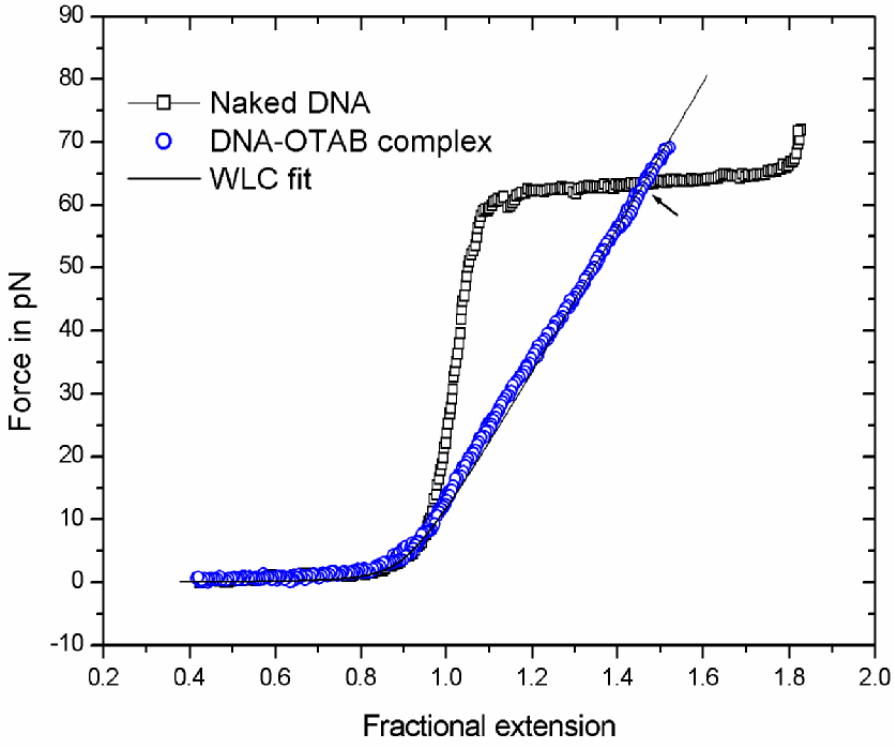

Figure 2. *Elastic response of naked dsDNA with persistence length of 50 nm and a stretch modulus of 1000 pN (black squares), stretching of the dsDNA-OTAB complex (blue circles). To evaluate the persistence length (15 nm) and the stretch modulus (135 pN) a fit with the extensible WLC model is performed (black line). The force versus distance behavior of the complex (in-between 10 and 46 pN) shows an asymptotic approach to the extensible WLC model (black line) at both the low force (<10 pN) and the high force regime (>45 pN).*

To check the elastic response of DNA interacting with cationic surfactants, the naked dsDNA was kept at ~ 80% of its contour length and the solution surrounding the DNA was exchanged according to the subsequent experiments. For this whole study, we used aliphatic cationic or anionic surfactants of which some are used in first trials of gene transfer applications (e.g. CTAB, DTAB). Different length of the hydrophobic tail of the cationic surfactant and variations of the charge of the counter ion were investigated.

Double stranded DNA exposed to short single chain OTAB molecules was modified in both its entropic and enthalpic elastic regime. In figure 2, the curve with the black squares displays naked B-form DNA with a persistence length of 50 nm and a stretch modulus of approximately 1000 pN. The blue curve shows the force versus extension behavior of the DNA - OTAB complex. The complex exhibits a reduced stretch modulus of 135 pN only and the persistence length is shorter ~ 15 nm. Upon extension, the DNA-OTAB complex is giving slack at a force of ~35 pN. Fits with the extensible WLC module yields stretch modulus of 180 pN for lower forces ($F \leq$ 25 pN) and 135 pN for higher forces ($F \geq 40$ pN) (asymptotic behavior). The contour length of the complex molecule is not changed but the coating of the dsDNA is rendering a softer molecule for longitudinal elongation. The intercept of the force versus extension curve of the DNA-OTAB complex (shown by an arrow in fig. 2) with the plateau of the naked DNA remains at 1.42 with high reproducibility. Previous studies have shown that groove binders show hysteresis and intercalators show an increase in contour length upon extension of the molecule by external forces (41,42). OTAB molecules (aliphatic chain length of 8 CH_2) interact with dsDNA in a different manner since the contour length is not changing and no hysteresis or overstretching is measurable. The force extension pulling curves reveal that OTAB is not condensing but is clearly binding to DNA (change in stretch modulus). Since no condensation was observed, small chain molecules (chain length 8 CH_2) do not induce any phase transfer (coil to globule). Such transfers are shown later in this study using longer chain molecules.

When naked DNA was exposed to DTAB molecules of aliphatic chain length 12, condensation of the DNA complex was readily observed as shown in figure 3 (curve with blue triangles). As compared to the naked form of dsDNA (black squares) which does not show any significant force upon extension to ≤ 90% of its contour length, here an additional offset force was needed to elongate the molecule from its final complex state. A constant increase of ~ 25 pN ($\pm$ 2.5 pN) in force was observed during initial elongation up to 90% of its contour length. The black line represents an overlay of the extensible WLC model adapted with a force offset of ~25 pN and ~7% ($\pm$ 2 %) elongation of the contour length. Again an asymptotic behavior of the curve in the force regime in-between 35 pN to 55 pN was observed with a stretch modulus of 210 pN ($\pm$ 50 pN) and 145 pN ($\pm$ 15 pN) respectively as shown in figure 3. The

inset shows the force versus extension response up to contour length of the complexed molecule.

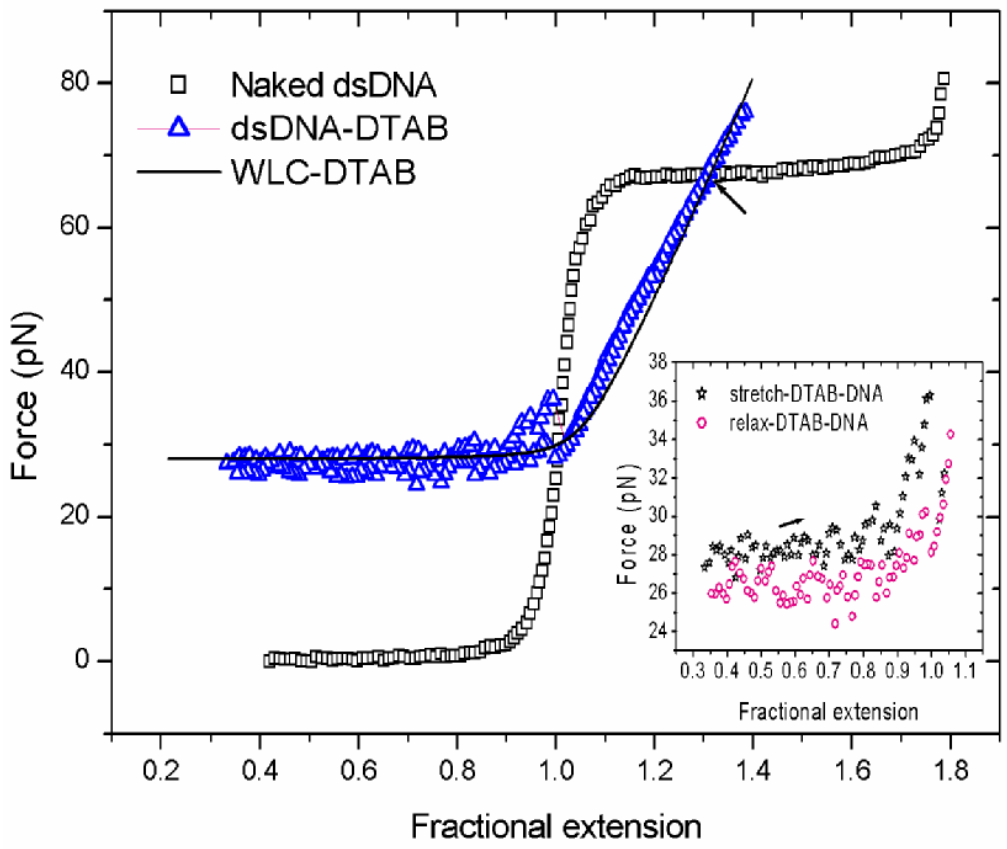

Figure 3. *Black curve shows the pulling of naked dsDNA as a reference force versus distance experiment while the blue triangle show the response of the complex of dsDNA - DTAB upon pulling. Black line represents the extensible WLC overlay with stretch modulus of ~145 pN. Inset shows a stick release phenomenon (black star curve) while stretching, the arrow indicates the pulling direction. The pink circles curve shows some hysteresis during relaxation.*

The extension of the molecule (black stars) is occurring with a stick release pattern of about 2 pN and starts to increase to ~ 5 pN (± 2 pN) when the molecule reaches 0.9 fractional extension. This could be attributed to an unpacking of coiled structure or opening of loops of the DNA-DTAB complex, assuming that DTAB condenses DNA into a toroidal or globule form. The curve with pink circles reveals that during relaxation of the molecule some hysteresis occurs. The jitter in the measured data is similar to the one observed during elongation over the respective extensions. A small hysteresis was always observed throughout the different experiments despite changes in pulling speed (16 nm /sec up to 800 nm/sec). We postulate that the whole process during extension and relaxation (unraveling and raveling of interdigitate tertiary

structure) is fast enough with our pulling speeds. Here condensation of naked dsDNA with monovalent cations was observed. Earlier studies have reported that it is necessary to have cation valence +2 or more to condense dsDNA e.g. Mn^{2+}, Mg^{2+}, polyamines–spermidine^{3+}, spermine^{4+}, $Co(NH_3)_6^{3+}$, diaminoalkane series, polylysine, or basic histones etc. (43). Pulling DNA-DTAB complexes to forces higher than 80 pN did reveal some repeatable but non reproducible overstretching transitions at forces higher than observed in naked B-DNA (i.e. @ 65 pN).

CTAB (aliphatic chain length of 16) formed also a condensing complex with the nucleic acid strands. The force versus extension plot is shown in fig. 4A.

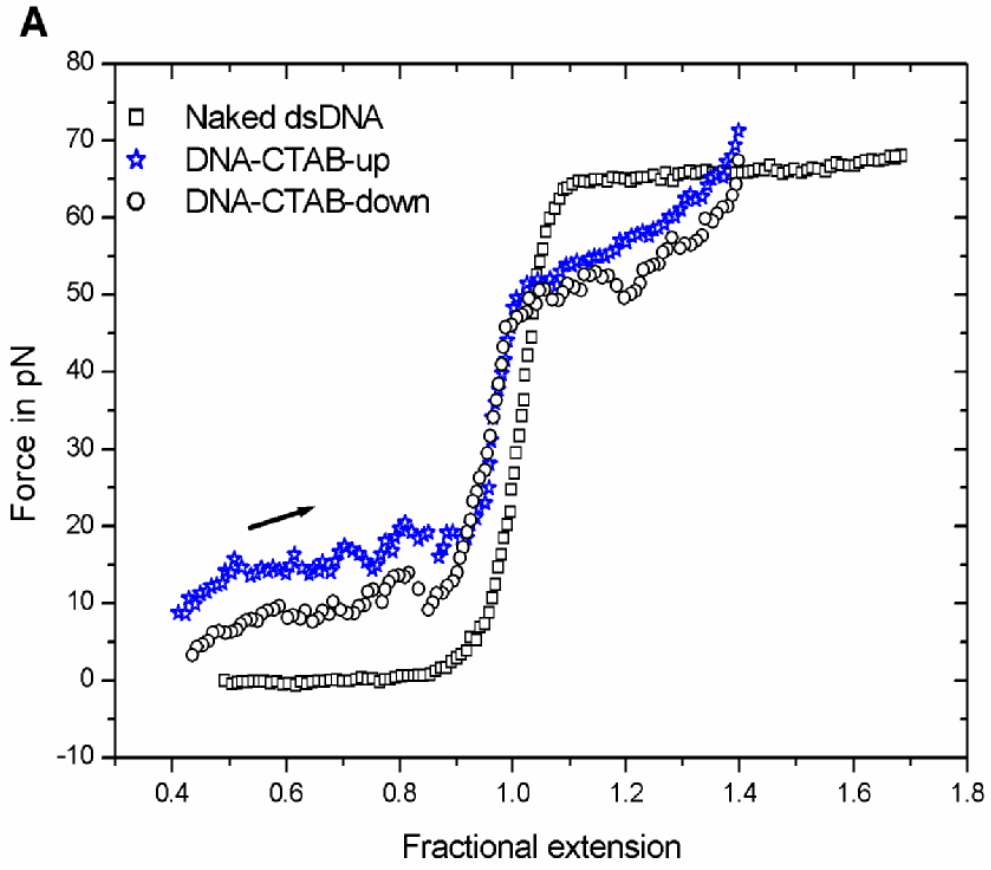

Figure 4A. *Black squares indicate the pulling of naked dsDNA. Stretching of the DNA-CTAB complex is shown by blue star curves (black arrow indicates the direction of stretching). Empty circle curve shows the relaxation of the DNA-CTAB complex.*

During stretching an increase in the pulling force with a sawtooth like extension pattern up to 0.9 fractional extension was observed. This could suggest that the DNA-CTAB complex was made up of unevenly packed DNA or that the longer aliphatic chains were able to interdigitate in a tertiary structure (loops). Such type of extension

– relaxation pattern was less prominent in complexes with chain length 12 (DTAB). Interestingly the complexation of the dsDNA with the long chain CTAB molecules is lowering the overstretch transition which is dominated and induced by the underlying dsDNA molecule. A possible scheme of the extension of this complex is shown in figure 4B.

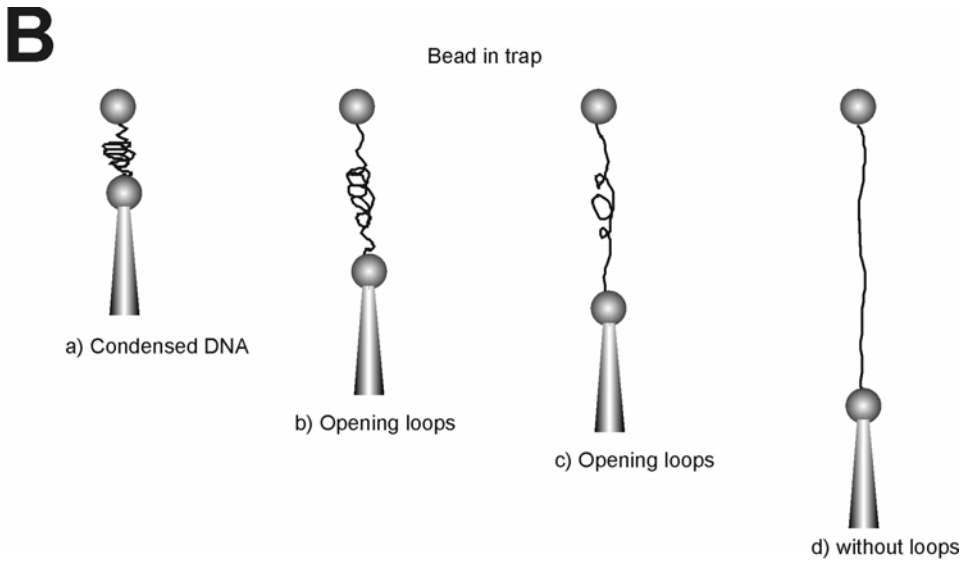

Figure 4B. *Schematic representation of pulling of condensed form of DNA. The direction of stretching of condensed form of DNA– a). Opening of possible loops induced by the cationic surfactant is shown in b) and c) providing sawtooth like relaxation upon stretching. Fully stretched form of the complex is shown in d).*

Opening of individual loops might require higher forces towards the complete extension of the complex molecule. During relaxation again hysteresis of 7 pN (± 1 pN) (i.e. difference between pulling cycle and relaxation up to the fractional extension of 0.9) was observed indicating that compaction forces of DNA molecules were different from those during stretching. To enable equilibrium conditions the DNA-CTAB complex was pulled with a slow speed ~10 nm/sec, again hysteresis was observed. An overlay with the extensible WLC model revealed a much higher stretch modulus ~1200 pN than previously observed with shorter surfactant molecules, which indicates a stronger interaction of the hydrophobic tails in the complexing molecules than with the shorter ones presented before.

A pulling experiment of DNA tethered with double tailed chain DMDTAB molecules is shown in fig. 5 (blue curve). The average condensing force was observed at 30 pN (± 5 pN). DNA-DMDTAB complex showed no hysteresis during extension and

relaxation, with this double chain compound the observed hysteresis was less than 1 pN.

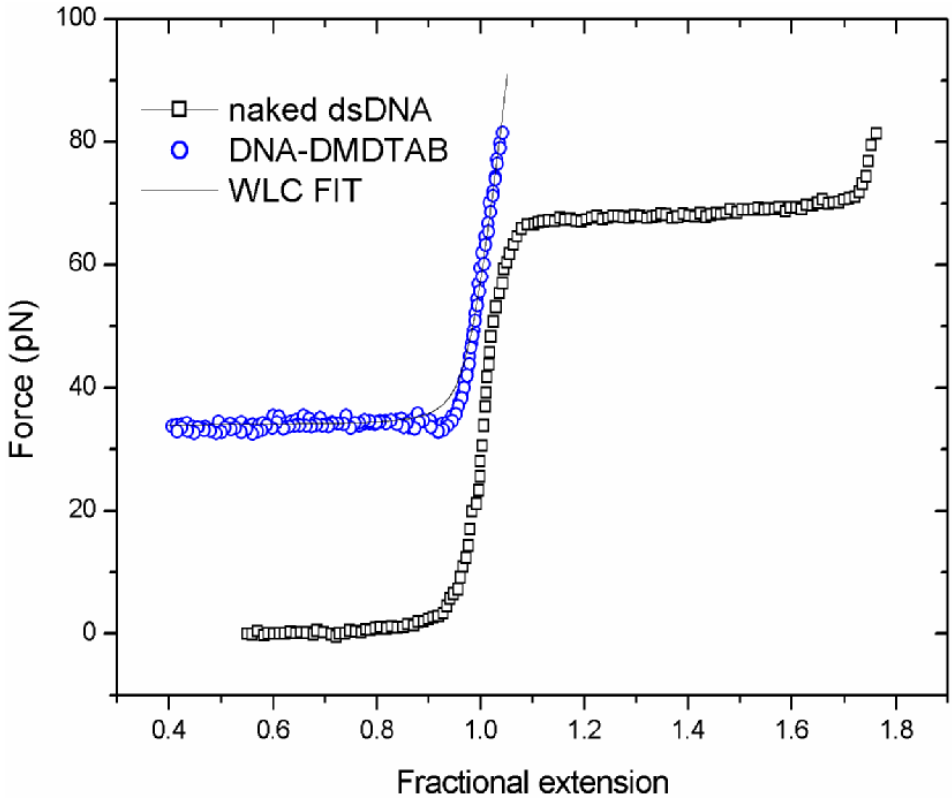

Figure 5. *Mechanics of DMDTAB-DNA complex is shown by blue circles, dsDNA reference curve (black squares) and extensible WLC fit for the DNA-DMDTAB complex (black line).*

To obtain extensible WLC fit (black line), we just added the offset value of the condensation force to equation 6. The stretch modulus of the complex was of 1100 pN (± 100 pN) comparable to the previously investigated CTAB complexes. The homogeneity of the force versus distance experiments led to the conclusion that the compaction efficiency of these double tailed DMDTAB molecules is higher than the one of single tailed cationic surfactant molecules. Again, short characteristic plateaus in the force experiments were repeatable (at forces > 80 pN, data not shown) in successive cycles, but the features were not reproducible.

2.1.5 Magnitude of condensation force

Depending on the molecules investigated we observed condensation of the DNA molecules with variable condensation forces representing the force needed to stretch

the molecule from globule to coil form. We calculated the magnitude of force over the range Δx from x_1 to x_2. The work done can be given as (18)

$$W_c = \int_{x_1}^{x_2} F \cdot dx = F_c \cdot \Delta x \qquad [7]$$

Where F_c is the force of condensation and Δx is the range over which the molecule stretched (from x_1 to x_2). The difference in work done by stretching the condensed DNA to its contour length gives an extra energy required by elongation of the cationic surfactant-DNA complex. This excess work represents the energy of attraction between molecule segments because the force observed to collapse the dsDNA is due to increased elastic entropy and the minimization of hydrophobic contacts of the coated molecule with the surrounding water (hydrophobic collapse) (17). Thus it can be represented by the following equations. $W_{ex} = W_c - W_n$.

$$W_{ex} = \int_{x_1}^{x_2} \left(F_c - F_n\right) \cdot dx = W_c - W_n \qquad [8]$$

Where F_n is the force required to stretch the naked DNA (uncollapsed state). W_n is the work done by the naked DNA. The elastic response of naked DNA can be fitted with extensible wormlike chain model. Data of naked DNA pulled over same Δx (the distance over which both state coincides) and it is used for the calculation of excess work done performed by complex structure. The values obtained for W_{ex} with the above compounds are found to be in the order of 1.3 – 2.7 k_BT/bp [DTAB ~2.3 k_BT/bp; CTAB ~1.27 k_BT/bp; DMDTAB ~2.69 k_BT/bp]. These energies are comparable and reveal that there is enough energy provided by binding the charged hydrophobic cations to collapse the complexed dsDNA stably into a globule at room temperature.

2.1.6 Kinetics of Binding of cationic lipids

The binding of these molecules to DNA in real time was investigated next. Constant distance experiments allow to reveal changes in force at different (relaxed or stretched) configurations of DNA. The response of dsDNA upon surfactant counterion binding was observed. In these set of experiments we held center to center distance in between two beads constant. Changes in force in the milli second time scale were monitored. Figure 6A shows the kinetics of binding of DTAB molecules to DNA (black squares). Typically a sigmoidal curve indicated that the binding occurs as a

highly cooperative process. Pink line on black curve in figure 6A represents the Boltzmann fit. The binding curve or the changes in magnitude of force can be fitted and described by the following equation:

$$F = A_2 + (A_1 - A_2) \Big/ \left[1 + \exp\left((x - x_0) \Big/ dx \right)\right] \qquad [9]$$

Where A_1 is the initial external force on the naked DNA molecule (extended conformation of DNA i.e. helical form), A_2 is the final value of the condensed force (saturation force of a globule or toroidal form), x is the time in sec, x_0 is the time scale at which molecule is precisely in the mid point of transition and dx is slope factor or time constant and can be given by $y^{(1)} = (A_2 - A_1) \Big/ 4dx$.

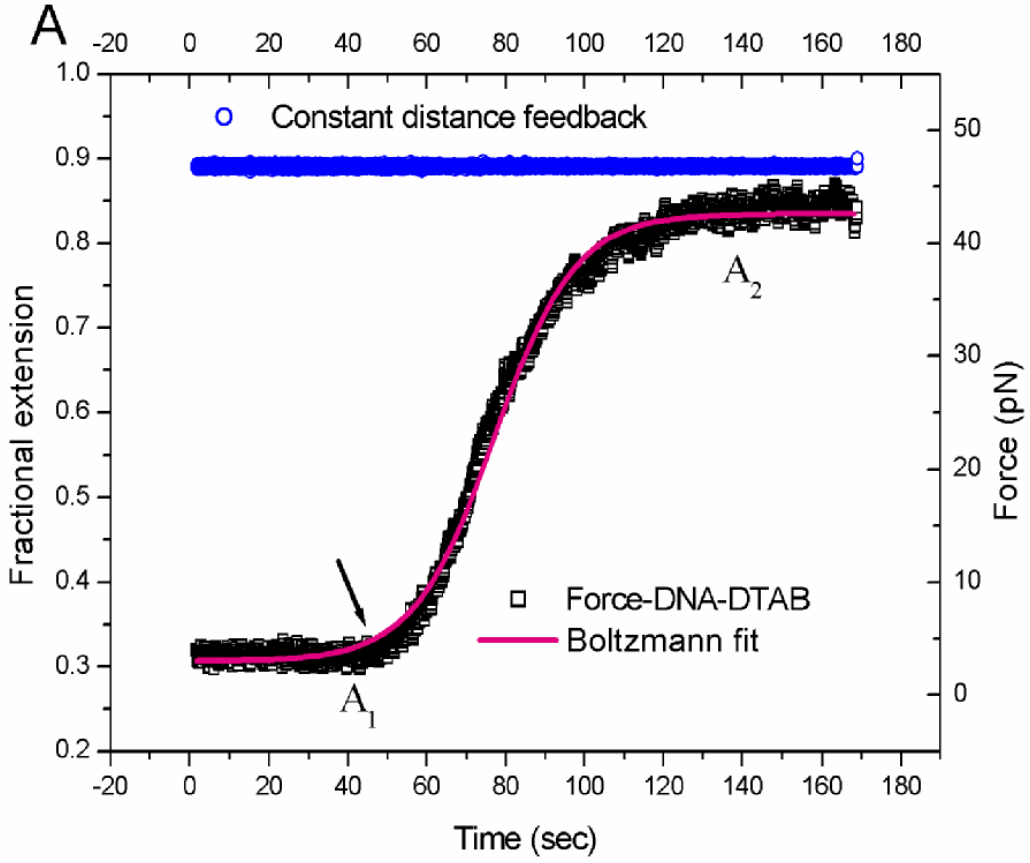

Figure 6A. *Force versus time of DTAB binding to naked DNA (black curves). Blue circles represent the constant fractional extension over same time of interval. The black arrow is the indicator of the start of the interaction of DTAB molecules with DNA and the pink line represent the Boltzmann fit.*

The arrow in fig 6A indicates the arrival and start of interaction of DTAB molecules with the naked dsDNA. The subsequent increase in force indicates the binding of cationic surfactant molecules to dsDNA. The surfactant molecules continuously

exchange with the native counter-ions present on the backbone surface of DNA. The transition reaches an end at point A_2 (~ 42 pN) and remains constant suggesting that there are no more binding sites available on the DNA. Comparable results of binding of cationic surfactant DTAB to DNA was reported at concentration well below the CMC (critical micelle concentration) of the surfactant. The shape of binding isotherms was also sigmoidal demonstrating cooperative binding (44).

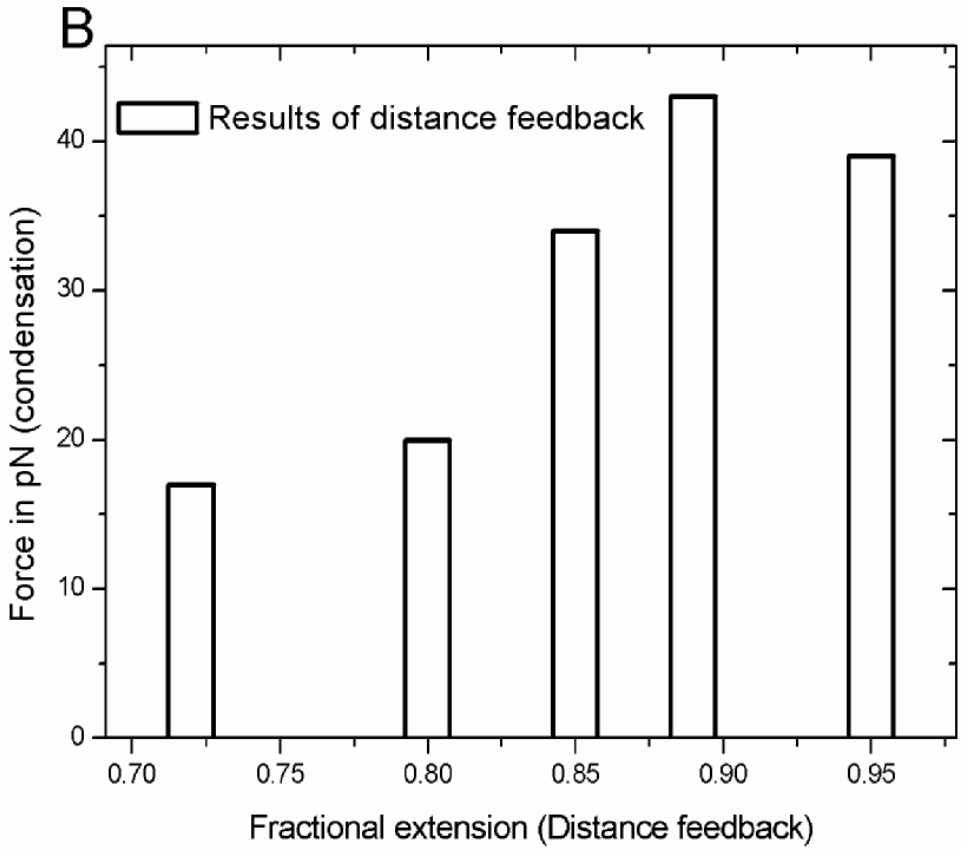

Figure 6B. *Columns show the magnitude of condensation force obtained at different constant fractional extension.*

The histogram in figure 6B shows the magnitude of condensing force obtained by holding DNA molecules at different fractional extensions. A maximum condensation at ~ 0.9 fractional extension of dsDNA was observed. This coincided with the raise of entropic forces of naked dsDNA in solution and indicates a full extension of the initial naked DNA as a target for the interacting molecules. As the molecule remains fully stretched during complexation, the hydrophobic forces which arise due to surfactant adsorption reach a maximum of ~ 40 pN. More relaxed dsDNA at 0.7 fractional extension could form DNA loops and therefore enable intramolecular hydrophobic contacts. Such contacts are more favorable for flexible segments. Obviously interacting intramolecular will reduce hydrophobic contact with the surrounding water

and requires less energy and could also mechanically compensate external forces in the formation of loops (DNA in a relaxed conformation). Increasing the fractional extension decreases the probability of intramolecular contacts.

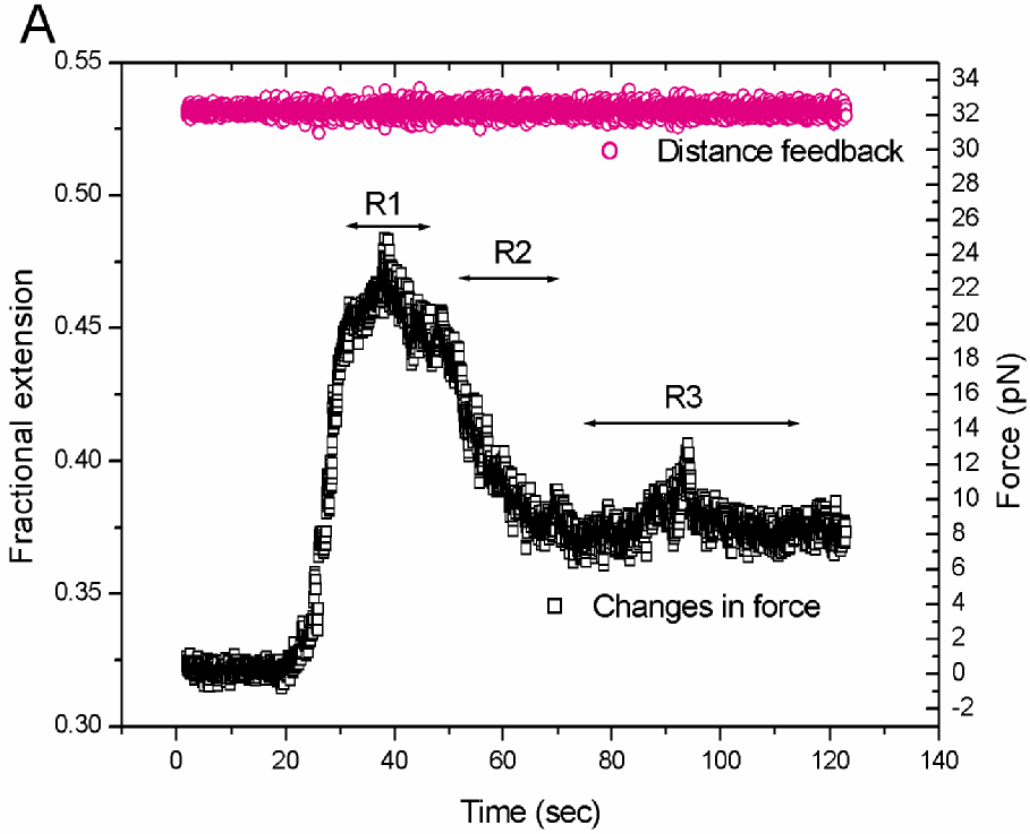

Figure 7A. *Constant fractional extension over time in seconds (pink circles). Simultaneous evolution of force over same time period is shown by black squares. The R1, R2 and R3 represent the changes in force over different regions.*

Fig.7A shows the binding kinetics of CTAB having an aliphatic CH_2 chain length of 16. We observed changes in force in three steps R1, R2 and R3 as indicated in the above figure. In region R1 we observed an abrupt increase in force from a relaxed molecule at 0.5 pN to ~22 pN within approximately 20 sec. During the next period R2, the force started to drop and reached ~ 9 pN with comparable speed. Then the force stabilized in region R3. This indicated that binding of CTAB occurred in a cooperative manner but discontinuous (discrete). Our results show that after some period of the initial formation of the CTAB-DNA complex the force started to drop and reached a stable value. This suggests that there is one metastable state (coexistence of coil and globule state) for few seconds. This type of variable states previously was observed and is consistent with our result (22). First the force started to rise due to complex compaction and subsequent drop in force indicate either some

decompaction or formation of intramolecular contacts of the complex. First CTAB molecules bind to DNA and secondly compact the complex and then the penetration of the hydrophobic tails relaxes the complex (22). Optical tweezers experiments done with 200 mM spermidine revealed also an abrupt increase in force from 0.2 pN to 1.7 pN within 3 seconds followed by a decrease in force to 0.5 pN (17).

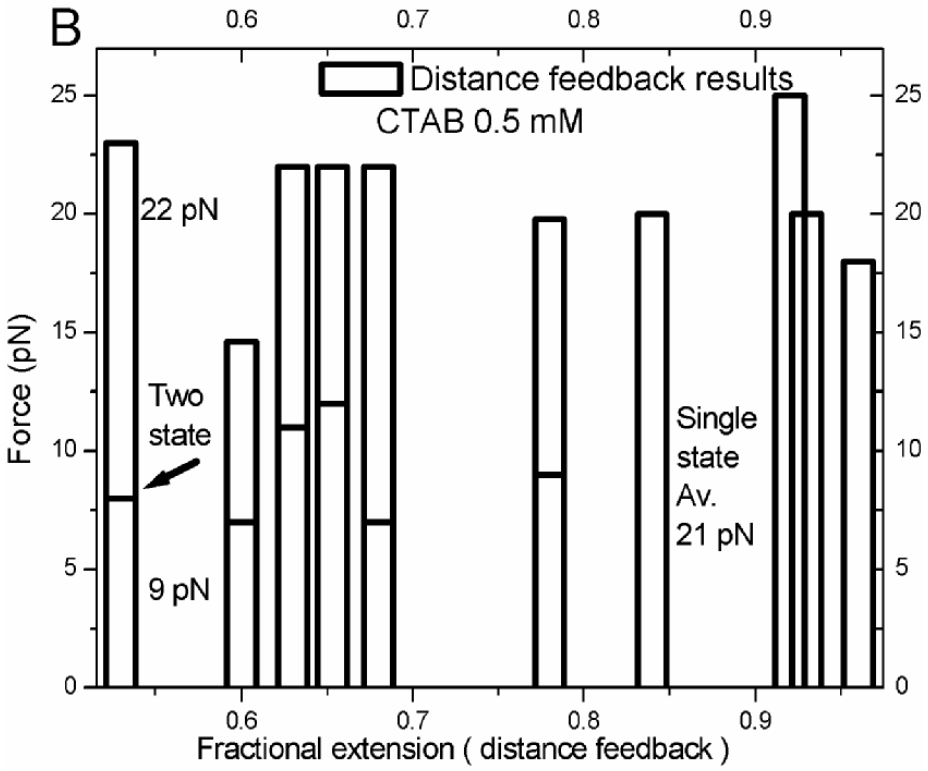

Figure 7B. *Histograms of the magnitude of condensing forces performed at different fractional extensions. Experiments up to fractional extension 0.8 show a segmentation indicated by a black line (as indicated by an arrow) representing a drop in force from its first state (high force value) to a second relaxed state.*

Figure 7B shows the force values observed during CTAB-DNA complex formation at different fractional extensions. We observed a two state kinetics indicated by an abrupt force increase to a certain value and then some relaxation. We postulate a metastable state which we observed up to a fractional length of 0.8. At longer fractional extension we measured sigmoidal binding curves as with DTAB. An average force of 22 pN for the metastable state and a second stable state at an average of 9 pN was measured. Interestingly the final force value at fractional extension longer than 0.8 provides the same high value like during the metastable transition. The arrow in figure 7B indicates the two regimes where first a high force of 22 pN is

observed (metastable transition) and then a drop to a second stable state at ~9 pN is revealed.

Binding double aliphatic chain cations of length $(CH_2)_{14}$ induced a faster and stronger complex formation as compared to DTAB and CTAB. Figure 8A shows the results of the experiment where the DNA molecule was kept at constant distance of 0.82 fractional extension and changes in forces were evaluated.

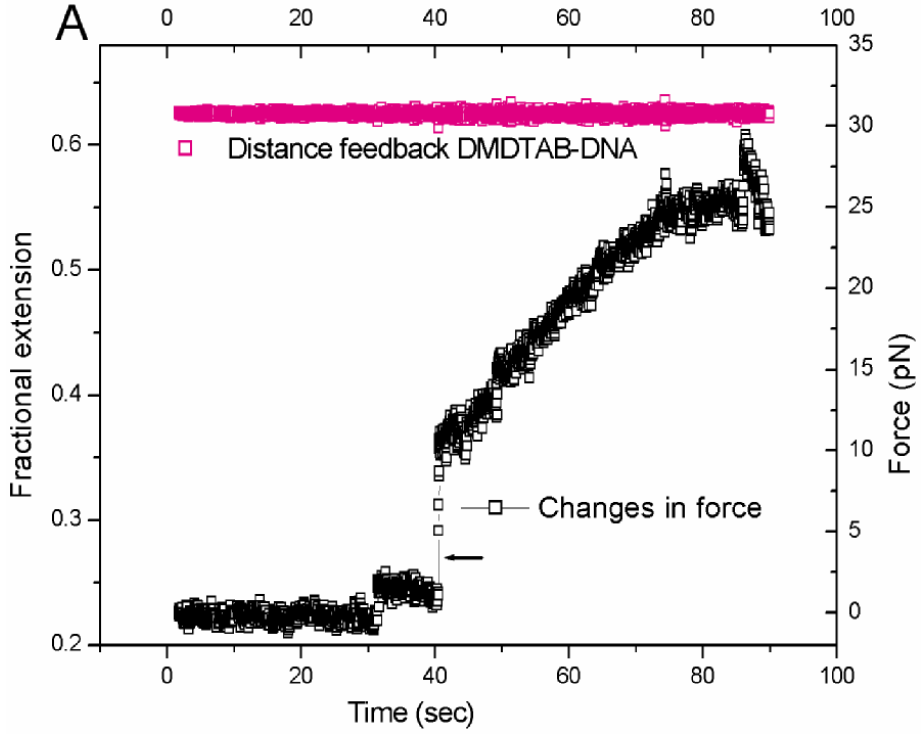

Figure 8A. *Black squares indicate the changes in force with time upon an exposure of dsDNA to DMDTAB molecules. Constant fractional extension versus time in seconds (pink squares).*

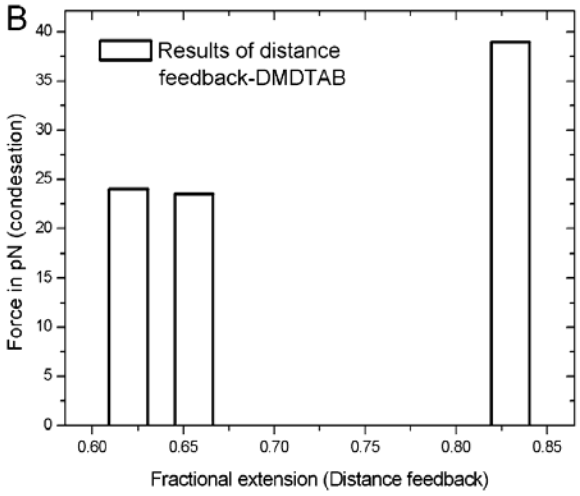

Figure 8B. *Saturation force obtained at different constant fractional extension with DMDTAB molecules (black columns).*

Abrupt rises in force within a very short time scale of few seconds were observed and we indicated here by an arrow in figure 8A. This suggests an initial fast exchange of counterions, whereas during the experiment the rise in force was not constant. The force reached a maximum value but fluctuations up to ~ 5 pN revealed a highly dynamic process. These fluctuations were observed only with the double tailed DMDTAB compound during complex formation. The overall increase in force resembles a sigmoidal curve. Figure 8B summarizes experiments carried out at different fractional extension. The final condensation force was again higher when the DNA molecule was clamped close to its contour length as observed with the other surfactant compounds.

2.1.7 Transition speed of elongated DNA clamped at different forces to globule or toroidal form of DNA (DNA collapse)

Here we define, collapsing of dsDNA as a transition of helical coiled form of DNA into a toroidal or globular from. These experiments which investigate the phase transfer speed will give additional insights into DNA polymer physics and polyelectrolyte research. To extract the values of collapse speed of DNA in real time we clamp the molecule in between two spheres and apply a constant external force. Subsequently the DNA interacts with the cationic surfactants which convert its structure at a given force. To get the collapse speed, we monitored the changes in distance in real time evolution during buffer exchange.

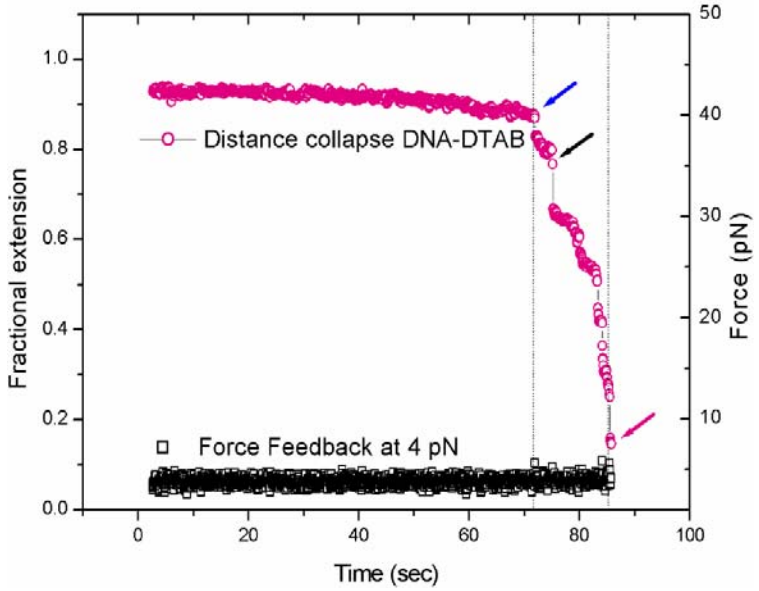

Figure 9. *Pink circles show the fractional extension response of the dsDNA during the transition into a globular complex when it was exposed to DTAB molecules.*

Simultaneous force feedback at clamped 4 pN is shown by the black squares. Start of the collapse of DNA (blue arrow). Stepwise fast decrease of the fractional extension (loop formation) (black arrow). The black dotted lines indicate the region where the molecule is undergoing the transition from coil to globule. The final form of collapsed DNA is reached after ~ 13 seconds, the constant force value of 4 pN (pink arrow).

The experiments were performed with 1.9 μm long dsDNA. With this experimental setup we achieved a maximum compaction factor of 20. Longer DNA approximately 100 μm in length would provide a higher fractional compaction factor but such experiments are difficult to perform with optical tweezers. As shown in figure 9 first we clamped a naked dsDNA molecule at a force of 4 pN. A decrease in distance was observed when the DNA buffer started to exchange with surfactant buffer (~72 sec). The distance decrease indicated binding of DTAB molecules to naked DNA. The blue arrow shows the point where actual cation displacements started. Then we could follow in real time the transition of naked DNA into the compacted form of the DNA-surfactant complex. The total collapse of the molecule to the small compact globules like form occurred within ~ 13 sec. A sharp decrease in distance indicated a highly cooperative process. In figure 9, small jumps indicated abrupt changes in distance as marked by a black arrow. Several processes could happen at the same time such as loop formation and linear compaction of the globule structure. We suggest that the collapse transition induced by DTAB is discrete and loops of different sizes were intermediately formed. Nucleation sites could be present which allow fast loop formation as jumps were observed during the transition process. The curve in between the dotted lines represents the partial states of the DNA-DTAB complex. The final fractional compacted length of the DNA-DTAB complex is highlighted by the pink arrow.

DTAB F (pN)	2.5	3.8	7	9.5	12.5
DTAB T (sec)	19	17.3	6	21.7	58
CTAB F (pN)	1.5	3	4	9	12
CTAB T (sec)	2.1	1.6	1.8	2.7	2.8
DMDTAB F (pN)	2	6	11	24	42
DMDTAB T (sec)	0.48	0.36	0.46	0.72	6

Table I *shows a summary of the time scale for the transition from a coil to a globule form at different force clamp experiment.*

We observed that the collapsing speed or speed of the transition decreased with increase in clamping force (Table I). Incomplete collapse of the molecule at forces above 25 pN was observed. Above this threshold force, the molecule will not be able to make lateral intramolecular contacts resulting in incomplete compaction.

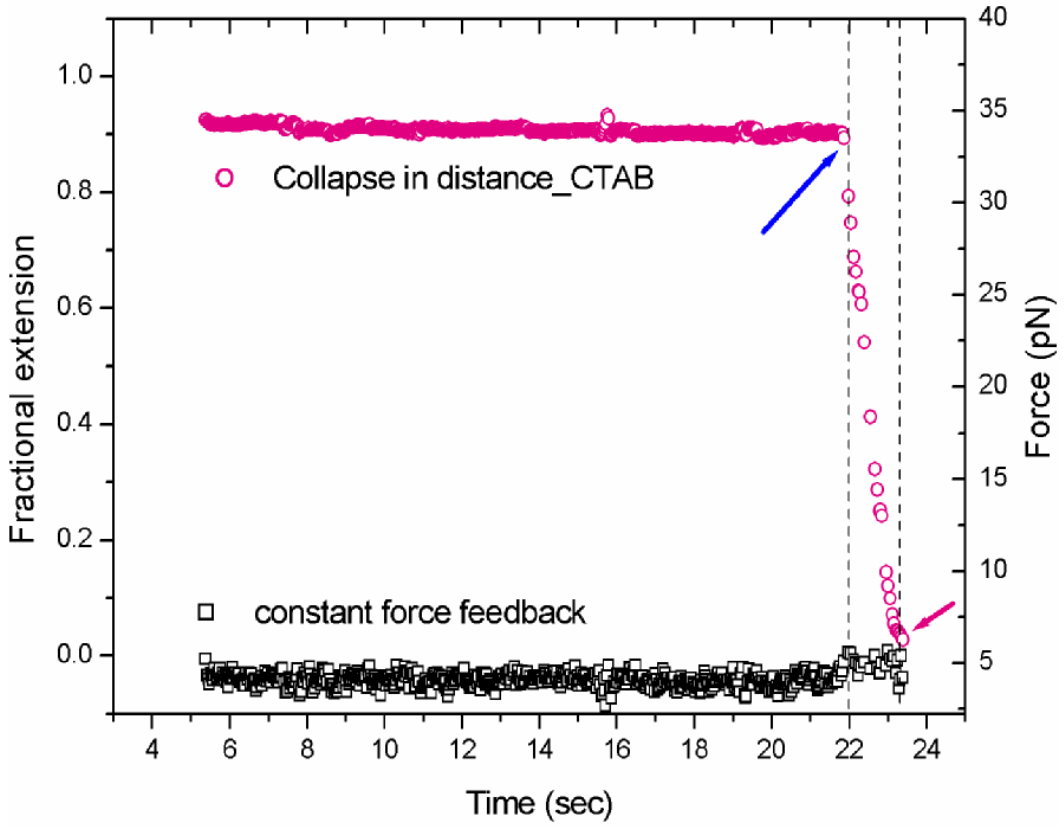

Figure 10. *Pink empty circles indicate the transition induced by CTAB molecules shown as fractional extension versus time. Black squares show the simultaneous value of the clamped force. The start point of the transition (blue arrow) and (pink arrow) are clearly detected by black dotted line. At end point, the molecule reaches its final compacted form at the given value of clamped force.*

The collapsing speed of DNA was also monitored during the interaction of CTAB molecules with DNA at 4 pN (Fig. 10). The transition from coil to globule occurred in ~1.8 sec which was ~ 10 times faster than with DTAB. Again the collapsing speed increased while decreasing the clamping force (Table I). CTAB molecules compacted dsDNA faster when molecule was kept at a relaxed position. At certain value of 22 pN clamp force close to contour length, no collapsing of DNA was monitored even if CTAB bound to it. The transition time to collapse DNA into a globular form during different force clamp experiments is shown in Table I.

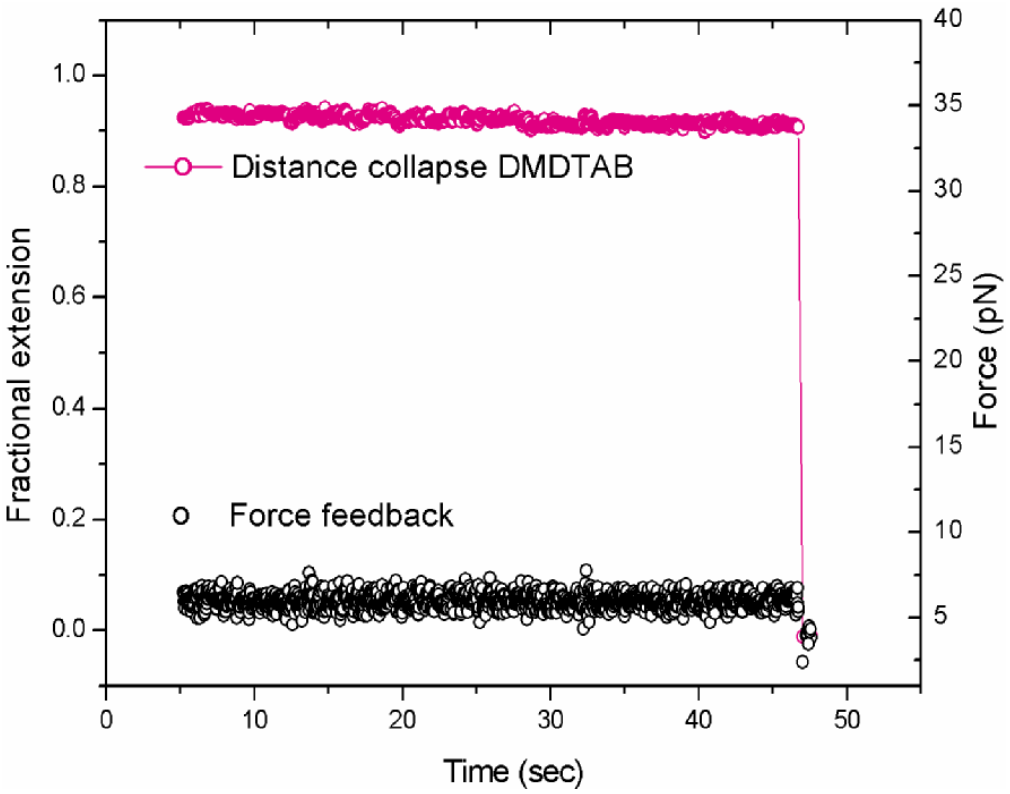

Figure11. *Curve with pink circles shows the sharp collapse of DNA by DMDTAB molecules (fractional extension versus time). Black circles represent the constant clamped value of force (force versus time).*

The double tail DMDTAB molecules with an individual chain length of 14 provided a transition speed of ~ 2µm/sec exhibiting a strong binding affinity (Fig. 11). The pink curve indicates the DNA collapse induced by the DMDTAB molecules. No partial or coexistence state was measured. Only a very sharp collapse of DNA was observed. Different collapsing speeds induced by the DMDTAB molecules at different force feedback are presented in Table I. One striking feature was that we observed collapse of the dsDNA even when it was elongated beyond the contour length (at ~25 pN). No collapse was seen when the DNA was stretched to ~ 63 pN close to the value of ~ 65 pN (B-S transition) (38). Our results indicate that compaction speed is depending on the length and the density of the aliphatic chains of the surfactant.

2.1.8 dsDNA stretching in presence of anionic surfactants

We have carried out some experiments with anionic surfactants (sometimes used for gene transfer experiments) to explore its effect on the mechanics of DNA. As shown in figure 12, naked DNA was exposed to the anionic surfactant SDS. As expected we

didn't measure any condensation but there was slight change in stretch modulus of the molecule from 1000 pN to 800 pN.

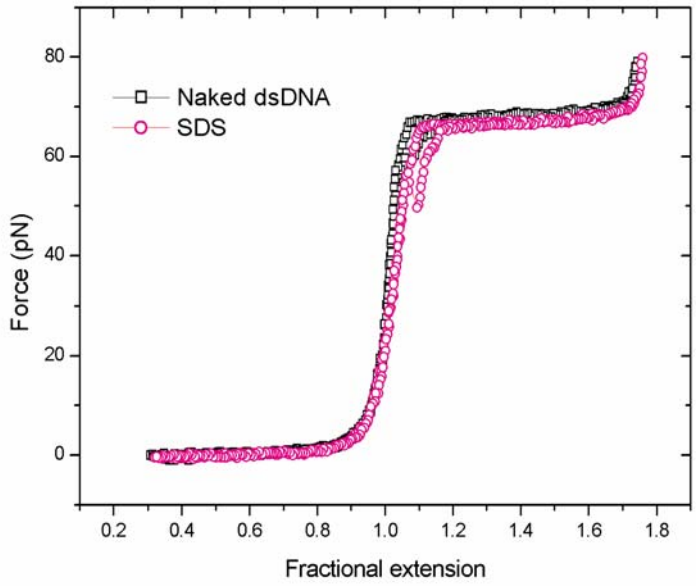

Figure 12. *The black curve shows the mechanics of naked dsDNA while pink curve indicates the mechanical response of naked DNA in presence of the anionic surfactant SDS.*

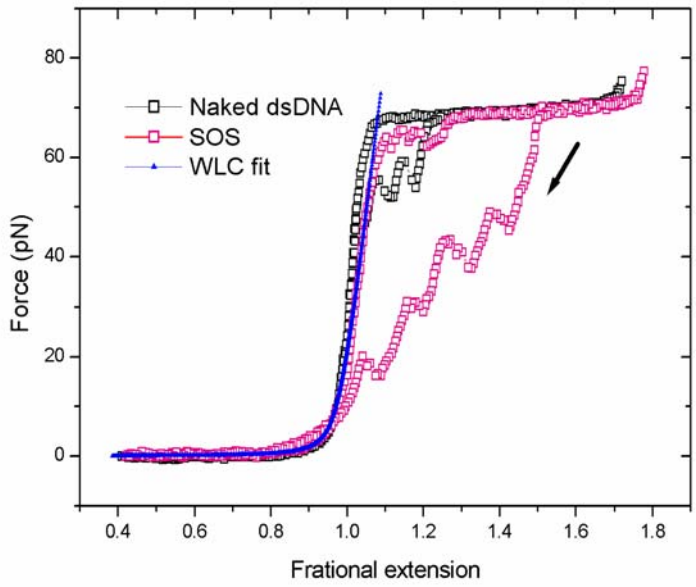

Figure 13. *Black square curve represents the naked B form of DNA. Pink squares show the stretching of naked DNA in presence of anionic surfactant SOS. The black*

arrow indicates the relaxation of the DNA molecule. Blue curve is the fit by the extensible WLC model.

Figure 13 shows stretching of naked DNA in presence of SOS. During the relaxation we observed more hysteresis as compared to previous experiments with SDS but the molecule was able to reanneal. During the next extension it was again double stranded DNA with a measured stretch modulus of 700 pN. It is difficult to interpret these results with the longer anionic surfactant. Since the bases of DNA are hydrophobic, the presence of anionic surfactants could lower the melting temperature and induce some dehybridization during stretching which then revealed some hysteresis on the relaxation path. After refilling of our chamber with normal DNA buffer, the mechanics of the naked form of DNA was observed again.

2.1.9 Discussion

Here we described the mechanical extension of single dsDNA by force measuring optical tweezers. The DNA molecule is covalently anchored at its 5' end and by molecular recognition at 3' end (biotin–streptavidin). We investigated the condensation force of ionic surfactant-DNA complexes, the kinetics of binding at different extensions and the speed of collapse of DNA at different force clamp values. For instance the pulling of the condensed form of a DTAB-DNA complex is shown in figure 3. Figures 6A, B indicate that it binds and condenses dsDNA molecules. This result shows similarities with the condensation of DNA experimentally performed by isothermal titration calorimetry (16). But other thermodynamic and binding experiments reported that interaction of DTAB molecules with DNA did not cause any condensation of DNA (27). Our results strengthen the calorimetric ensemble experiments (16). Earlier studies showed a maximum condensation force for DNA-Hexaammine cobalt trichloride (CoHex) complexes at ~ 4pN and DNA-spermidine complex at ~1 pN (17,18). Our results demonstrate that the condensation force (an average for DTAB, CTAB and DMDATB) is at least ~5 times greater than the maximum observed in binding studies of CoHex. This indicates that the condensation forces measured with cationic surfactant are higher than any other previous study and are heavily influenced by the fact that these cations are directly linked to an aliphatic chain which favor also a minimization of the hydrophobic interfaces by collapsing into a globule structure. Certainly the length of the hydrophobic tails plays an

important role since DMDTAB which has two tails (14 CH_2) is providing comparable condensation forces as the shorter DTAB (12 CH_2). The longer tails might be subjected to some steric hindrance when interacting with the hydrophobic grooves of dsDNA and the intramolecular interactions might be affected by such features as observed with the longer CTAB molecules. The compounds with chain lengths of 12 or 14 are therefore recommended for the condensation of DNA.

The speed of the transition from stretched DNA to collapsed DNA-surfactant complex as obtained on the basis of force clamp measurements (fig. 9-11) indicates that free DNA polymer ends are not necessary for the collapse of the molecule. The theory of Ostrovsky and Bar-Yam predicted that nucleation of collapse in a single heteropolymer (DNA) will occur starting from an end (45). We performed all experiments by attaching the ends of single DNA molecule on bead surfaces. This suggests that for collapse of DNA just the formation of loops is needed. Such loops are provided with the help of lateral contacts between two or more adjacent segments. Our results are consistent with the previous experimental work performed with optical tweezers (CoHex) (18).

We observed a immediate collapse of DNA induced by double tailed DMDTAB molecules as shown in figure 11. The total time needed for the transition from a coil form of DNA to a compact (globule) was ~0.35 sec only and no discontinuity during the collapse of DNA was observed. Previously Grosberg and Khokhlov theoretically predicted that DNA collapse will involve an abrupt phase transition (31), only DMDTAB experiments confirm these predictions. It has been reported that the two tailed surfactants compact DNA more efficiently than single tailed ones (46). The values presented in table I also suggest that the collapse speed (transition time) induced by double tails are at least 2x faster than with single chain surfactants. A transition was observed even when the molecule was clamped at ~40 pN which suggests that it was still able to make intramolecular contacts or loops at such high external loads. Thus we can say that mechanism of DNA collapse at the single molecule level depends on the chain length of single tailed or double tailed monovalent cationic surfactants and our finding of mechanical parameters maybe helpful for biochemists or molecular biologists for the design of future gene transfer compounds.

The collapse transition of DNA can be interpreted as first positively charged head groups of cationic surfactants interact and bind to the negative charges of the

phosphate groups of the DNA backbone (electrostatic interactions). The second step is initiated by hydrophobic interactions which show to be cooperative. These hydrophobic interactions provide the driving force responsible for a conformational change of the DNA into a collapsed globule. The initial random coil of the dsDNA in solution which is dominated by entropic forces is converted into a hydrophobic compact globule due to surface minimization.

2.1.9.1 Speed of transition and the effect of CH_2 tail lengths

The speed of collapse as a function of aliphatic hydrocarbon CH_2 chain lengths is shown in figure 14.

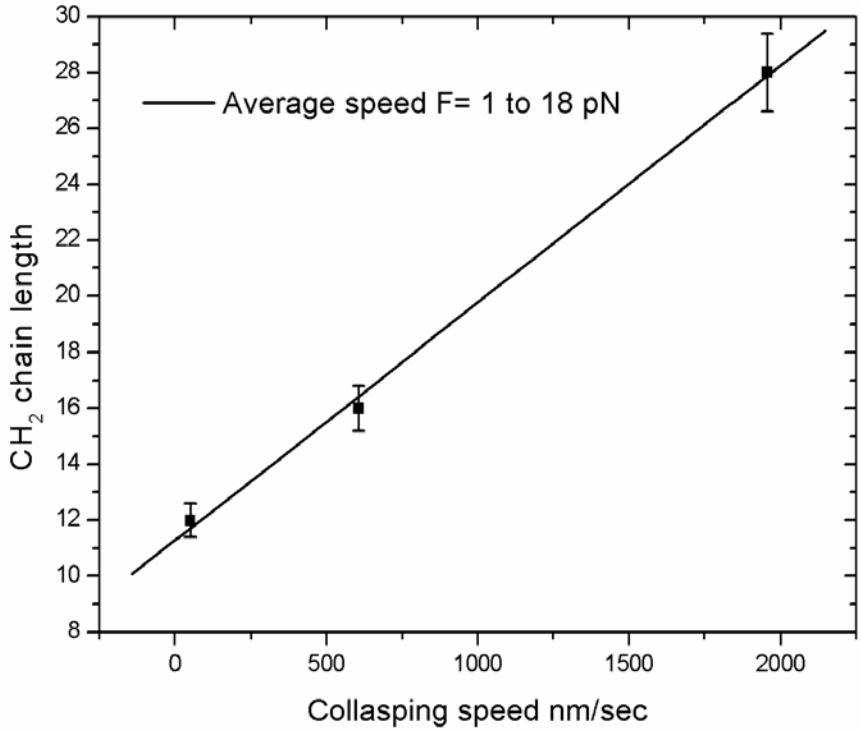

Figure 14. *Black squares indicate the values of the average collapsing speed in between 1 to 18 pN in force clamp experiments. The black line represents the linear fit to the number of CH_2 within the hydrophobic chain (total CH_2 tail length in cationic compounds) versus collapsing speed.*

We averaged the speed of collapse in our force clamp experiments up to 18 pN. With the addition of methylene groups (CH_2) to the chain length, the speed increased, and showed to follow in a linear manner which is given as y = a+bx where parameters a = 11.27 (± 0.45239), b = 0.00849 (± 3.82525E-4).

For this study, only the chain length, hydrophobic part of cationic surfactant was changed and hydrophilic part remained unaltered (see figure 1 B). Thus the increase of collapse speed only depended on the hydrocarbon chain length and indicated as expected that the hydrophobic interactions became stronger by increasing the length of the hydrophobic tail, representing the driving force to change the local conformation and thereafter the collapse of the DNA. Earlier potentiometric studies revealed comparable findings in an ensemble, they observed that binding isotherms were strongly dependent on the chain length of the surfactant (47). Again our studies confirm that chain length longer than 11 CH_2 are required to induce compaction.

2.1.9.2 Reversibility of cationic surfactant-dsDNA complex bindings to naked B form of DNA

The mechanism of cationic surfactant mediated gene delivery is still unclear. It is important to know whether the induced structural changes from a naked coil form to a DNA globule complex are reversible or not. Transfected DNA becomes active only when the cationic lipid complex will be released after successful transfer through the lipid bilayer. In previous studies it was shown that the release of DNA can be achieved by addition of anionic surfactants (21). We found that anionic surfactants affected the mechanics of dsDNA slightly and that different anionic polyelectrolytes might mimic the processes in the cell nucleus. We expected a change in state from the globule back to the coil form if the transition is reversible (equation 2). From our constant distance feed back experiments we found that the condensation saturation force was reached when the ratio of positive charges cationic surfactant molecules to negative charges of dsDNA was ≥ 1.

By exchanging the surrounding buffer and depleting the concentration of the surfactant molecules it was possible to get back to the naked state of DNA (B–form). This reversibility was achieved for DNA complexes with OTAB, CTAB and DTAB but failed with double chain length DMDTAB-DNA complexes. This result provides also information for biochemical studies since some cationic surfactants are used as precipitation or counting agents in DNA extraction procedures (24). The DNA surfactant globule formed by CTAB molecules could be transformed back to a coiled form of DNA by addition of polyacrylic acid (48) or extra NaBr (23). In fact these

results suggest that binding and collapse induced by cationic surfactant molecules is a reversible process.

2.1.9.3 Concentrations of cationic surfactants

The concentration of cationic surfactants is an important parameter for future gene transfer studies and optical tweezers experiments are ideal to follow the binding of surfactant to a single DNA molecule. By probing many surfactant concentrations from short to longer alkyl chains, we concluded that the half of the critical micelles concentration (1/2 x CMC) of respective compounds represented the optimal experimental concentration. Previously it has been reported that the short molecules didn't produce any heat in calorimetry studies therefore there was no significant binding between short aliphatic molecules and DNA (16). An increase in the turbidity of the system was observed by others but no precipitate formation was possible in OTAB bulk studies (34). When we lowered the concentration below 0.1 x CMC in DNA buffer at 150 mM NaCl no binding of OTAB molecules to dsDNA was observed. But we observed clear binding of short, OTAB molecules to DNA at a particular concentration in our sensitive force measurement studies. Binding of OTAB molecules was prominent when the concentration was at ~ 0.5 x CMC. Here we report that OTAB binds to DNA but without condensing it. Thus such a result could be important for DNA transfections without the condensation of DNA.

2.1.9.4 Structural Formations

It is important to elucidate what is happening on the local scale since the structure of the DNA lipid complex is still unclear. Both, optical tweezers investigations and ensemble experiment provide indirect insights. On the basis of isothermal titration calorimetry study Matulis *et al.* interpreted the three distinct structural models of binding of DNA alkyl-ammonium complex (16). They favored the model which suggests that hydrophobic tails are lying down on the DNA surface and cationic head groups could localize within several Å from DNA phosphate groups. They disfavored the model which suggests that there is a possibility of cationic surfactants (DTAB) binding to DNA by forming large micelles like structures on the DNA surface (49). We carried out some experiments to elucidate the binding effect of micelles structures on DNA at the single molecule level.

Experiments with micelles (concentration of cationic surfactant was above the CMC value) were carried out and one experiment is shown in figure 15. The black triangles show the stretching of DNA-OTAB complex formation above CMC value (i.e. usually 1.5xCMC or 2xCMC). The black arrow indicates peaks during pulling of the condensed complex induced by the micelles structures.

Below the CMC of OTAB no peaks were observed. These experiments showed repeatable force peaks from pulling experiment to experiment but variations in the location of these shorter range force peaks was observed.

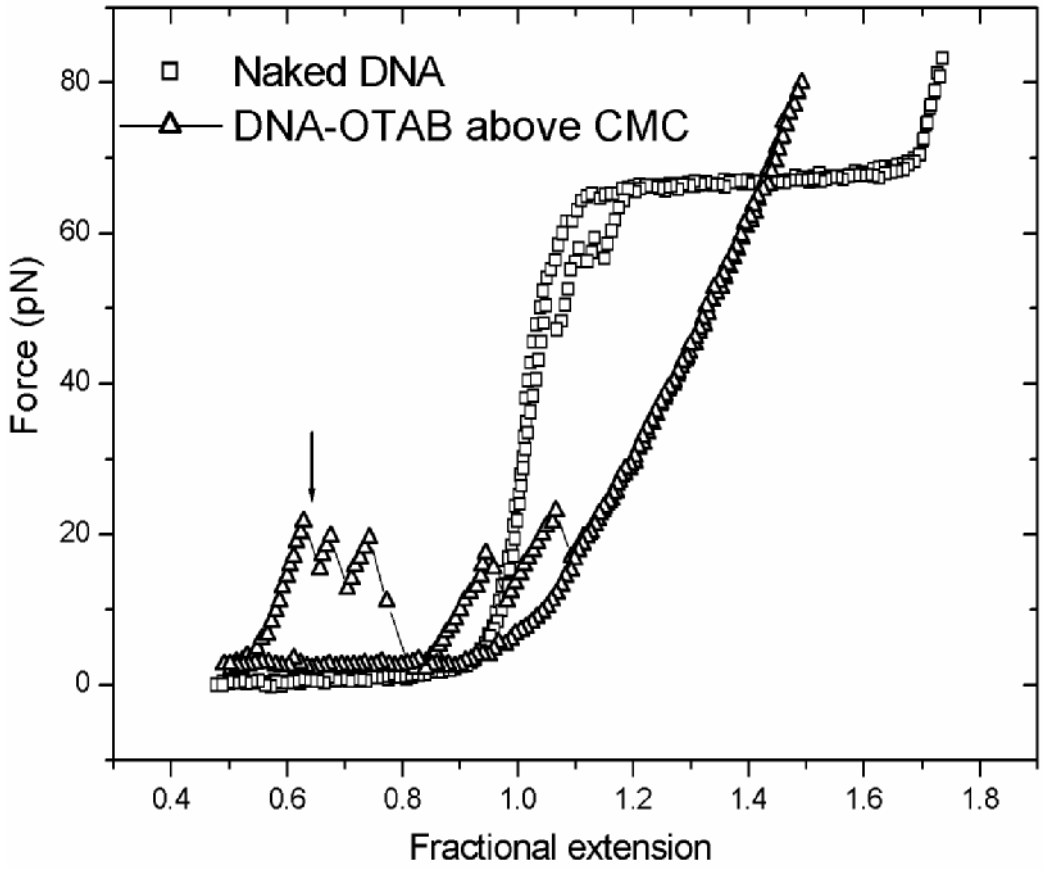

Figure 15. *Stretching of naked form of DNA is shown with black squares. Curve with triangles represents the stretching of OTAB-DNA complex. The concentration of OTAB was more than the value of its CMC.*

We found that interactions of micelle like structures or molecular aggregates with dsDNA were measurable at concentrations above CMC. These results disagree with structure predicted by Buckin *et al.* (49) at lower concentration of cationic surfactants

but they would be feasible at concentration above the CMC. Thus the reproducibility of our curves at values of ½ x CMC agree with the model described by Matulis *et al*. (16). At concentrations many times higher than CMC with CTAB molecules, we found that at these concentrations one strand of the naked DNA was detached and showed a transition to ssDNA mechanics (data not shown). It's difficult to elucidate the possibility of penetration or intercalation of hydrophobic tail inside the DNA structure with optical tweezers experiments.

2.1.10 Conclusion

In conclusion short and long cationic surfactant molecules bound to DNA but only surfactants with longer chains [12, 16 and 2x14] condensed dsDNA.

Binding of double tailed cationic surfactants was at least two times more efficient than the one with single tailed chains.

Though DATB is shorter than CTAB, measured condensation forces of dsDNA induced by DTAB molecules were stronger. Our mechanical experiments with DTAB-DNA complexes indicate that these complexes are more stable and can be recommend for the construction nonviral vectors.

Binding of cationic surfactants to DNA represent a reversible process and can easily be induced by exchange of the surrounding cationic surfactant solution with normal DNA buffer. The DMDTAB molecules are difficult to remove completely by using buffer only.

The CH_2 chain length is a key parameter and plays an important role during binding, condensing and collapsing of dsDNA. The speed of collapse of DNA increased linearly with an increase in CH_2 chain length (applicable to the CH_2 length ≥ 12).

We recommend (½ x CMC) as a concentration for the binding of cationic surfactant to DNA. Optical tweezers experiments provide an additional insight to the mechanical properties of DNA-surfactant complexes. The binding strength and optimal concentrations for compaction and shielding can be evaluated and be compared with cytotoxicity of the corresponding compounds.

Acknowledgement

Financial support is acknowledged from the Swiss National Foundation (SNF) grant (3152-67919.02) and by the National Center of Competence in Research 'Nanoscale Science' (NCCR).

2.1.11 References

1. Verma, I.M. and Somia, N. (1997) Gene therapy-promises, problems and prospects. *Nature*, **389**, 239-242.
2. Song, L. and Zheng, M. (2001) Nonviral Gene Therapy. *Curr. Gene Ther.*, **1**, 201-226.
3. Felgner, P.L., Gadek, T.R., Holm, M., Roman, R., Chan, H.W., Wenz, M., Northrop, J.P., Ringgold, G.M. and Daniesen, M. (1987) Lipofection: A Highly Efficient, Lipid-Mediated DNA-Transfection Procedure. *Proc. Natl. Acad. Sci. U S A*, **84**, 7413-7417.
4. Caplen, N.J., Alton, E.W.F.W., Middleton, P.G., Dorin, J.R., Stevenson, B.J., Gao, X., Durham, S.R., Jeffery, P.K., Hodson, M.E., Coutelle, C. *et al.* (1995) Liposome-mediated CFTR gene transfer to the nasal epithelium of patients with cystic fibrosis. *Nature Med.*, **1**, 39-46.
5. Nabel, G.J., Nabel, E.G., Yang, Z.Y., Fox, B.A., Plautz, G.E., Gao, X., Huang, L., Shu, S., Gordon, D. and Chang, A.E. (1993) Direct gene transfer with DNA-liposome complexes in melanoma: expression, biological activity, and lack of toxicity in humans. *Proc. Natl. Acad. Sci. U S A*, **90**, 11307-11311.
6. Rädler, J.O., Koltover, I., Salditt, T. and Safinya, C.R. (1997) Structure of DNA-Cationic Liposome Complexes: DNA intercalation in multilamellar membranes in distinct interhelical packing regimes. *Science*, **275**, 810-814.
7. Li, S. and Huang, L. (2000) Nonviral gene therapy: promises and challenges. *Gene Therapy*, **7**, 31-34.
8. Pinnaduwage, P., Schmitt, L. and Huang, L. (1989) Use of a quaternary ammonium detergent in liposome mediated DNA transfection of mouse L-cells. *Biochim. Biophys. Acta.*, **985**, 33-37.
9. Farhood, H., Bottega, R., Epand, R.M. and Huang, L. (1992) Effect of cationic cholesterol derivatives on gene transfer and protein kinase C activity. *Biochim. Biophys. Acta*, **1111**, 239-246.
10. Felgner, J.H., Kumar, R., Sridhar, R., Wheeler, C., Tsai, Y.J., Border, R., Ramsay, P., Martin, M. and Felgner, P.L. (1994) Enhanced gene delivery and mechanism studies with a novel series of cationic lipid formulations. *J. Biol. Chem.*, **269**, 2550-2561.
11. Lee, E.R., Marshall, J., Siegel, C.S., Jiang, C., Yew, N.S., Nichols, M.R., Nietupski, J.B., Ziegler, R.J., Lane, M.B., Wang, K.X. *et al.* (1996) Detailed analysis of structures and formulations of cationic lipids for efficient gene transfer to the lung. *Hum. Gene. Ther.*, **7**, 1701-1717.
12. Wheeler, C.J., Felgner, P.L., Tsai, Y.J., Marshall, J., Sukhu, L., Doh, S.G., Hartikka, J., Nietupski, J., Manthorpe, M., Nichols, M. *et al.* (1996) A novel cationic lipid greatly enhances plasmid DNA delivery and expression in mouse lung. *Proc. Natl. Acad. Sci. U S A*, **93**, 11454-11459.
13. Laundon, C.H. and Griffith, J.D. (1988) Curved helix segments can uniquely orient the topology of supertwisted DNA. *Cell*, **52**, 545-549.
14. Gosule, L.C. and Schellman, J.A. (1976) Compact form of DNA induced by spermidine. *Nature*, **259**, 333-335.
15. Chattoraj, D.K., Gosule, L.C. and Schellman., J.A. (1978) DNA condensation with polyamines. II. Electron microscopic studies. *J. Mol. Biol.*, **121**, 327-337.
16. Matulis, D., Rouzina, I. and Bloomfield, V.A. (2002) Thermodynamics of Cationic Lipid Binding to DNA and DNA Condensation: Roles of Electrostatics and Hydrophobicity. *J. Am. Chem. Soc.*, **124**, 7331 - 7342.

17. Murayama, Y., Sakamaki, Y. and Sano, M. (2003) Elastic response of single DNA molecules exhibits a reentrant collapsing transition. *Phys. Rev. Lett.*, **90**, 018102 - 018104.
18. Baumann, C.G., Bloomfield, V.A., Smith, S.B., Bustamante, C., Wang, M.D. and Block, S.M. (2000) Stretching of single collapsed DNA molecules. *Biophys. J.*, **78**, 1965-1978.
19. He, S., Arscott, P.G. and Bloomfield, V.A. (2000) Condensation of DNA by multivalent cations: experimental studies of condensation kinetics. *Biopolymers*, **53**, 329-341.
20. Kuhn, P.S., Levin, Y. and Barbosa, M.C. (1999) Charge inversion in DNA-amphiphile complexes: possible application to gene therapy. *Physica A*, **274**, 8-18.
21. Dias, R.S., Lindman, B. and Miguel, M.G. (2002) Compaction and decompaction of DNA in the presence of cationic amphiphile mixtures. *J. Phys. Chem. B*, **106**, 12608-12612.
22. Mel'nikov S M, Sergeyev, V.G. and Yoshikawa, K. (1995) Discrete coil-globule transition of large DNA induced by cationic surfactant. *J. Am. Chem. Soc.*, **117**, 2401-2408.
23. Mel'nikov, S.M., Sergeyev, V.G., Yoshikawa, K., Takahashi, H. and Hatta, I. (1997) Cooperativity or phase transition? Unfolding transition of DNA cationic surfactant complex. *J. Chem. Phys.*, **107**, 6917-6923.
24. Sibatani, A. (1970) Precipitation and counting of minute quantities of labeled nucleic acids as cetyltrimethylammonium salt. *Analytical Biochemistry*, **33**, 279-285.
25. Francino, O., Piol, J. and Cabré, O. (1987) Precipitation of DNA by cetyltrimethylammonium bromide to avoid coprecipitation of salts. Application of the method of recovery of Drosophila DNA following adsorption to hydroxyapatite. *J. Biochem. Biophy. Meth.*, **14**, 177-180.
26. Ishaq, M., Wolf, B. and Ritter, C. (1990) Large-Scale Isolation of Plasmid DNA Using Cetylrimethylammonium. *BioTechniques*, **9**, 19-24.
27. Bathaie, S.Z., Moosavi-Movahedi, A.A. and Saboury, A.A. (1999) Energetic and binding properties of DNA upon interaction with dodecyl trimethylammonium bromide. *Nucleic Acids Res.*, **27**, 1001-1005.
28. Xu, Y. and Szoka, F.C.J. (1996) Mechanism of DNA Release from Cationic Liposome/DNA Complexes Used in Cell Transfection. *Biochemistry*, **35**, 5616-5623.
29. Bonincontro, A., Marchetti, S., Onori, G. and Rosati, A. (2005) Interaction cetyltrimethylammonium bromide-DNA investigated by dielectric spectroscopy. *Chemical Physics*, **315**, 55-60.
30. Ueda, M. and Yoshikawa, K. (1996) Phase Transition and Phase Segregation in a single Double-stranded DNA Molecule. *Phys. Rev. Lett.*, **77**, 2133-2136.
31. Grosberg, A.Y. and Khokhlov, A.R. (1994) Polyelectrolytes. Trans. Atanov, Y. A. *Statistical Physics of Macromolecules*, **5**, 217-220.
32. Miguel, M.G., Pais, A.A.C.C., Dias, R.S., Leal, C., Rosa, M. and Lindman, B. (2003) DNA-cationic amphiphile interactions. *Coll. and Surf. A: Phys. Eng. Asp.*, **228**, 43-55.
33. Dias, R., Mel'nikov, S., Lindman, B. and Miguel, M.G. (2000) DNA Phase Behavior in the Presence of Oppositely Charged Surfactants. *Langmuir*, **16**, 9577-9583.

34. Dias, R., Antunes, F., Miguel, M., Lindman, S. and Lindman, B. (2002) DNA-lipid system. A physical chemistry study. *Braz. J. Med. and Bio. Res.*, **35**, 509-522.
35. Hegner, M. (2000) DNA Handles for Single Molecule Experiments. *Single Mol.*, **1**, 139-144.
36. Grange, W., Husale, S., Güntherodt, H.-J. and Hegner, M. (2002) Optical tweezers system measuring the change in light momentum flux. *Rev. Sci. Instr.*, **73**, 2308 - 2316.
37. Kuhn, P.S., Barbosa, M.C. and Levin, Y. (2000) Effects of hydrophobicity in DNA surfactant complexation. *Physica A*, **283**, 113-118.
38. Smith, S.B., Cui, Y. and Bustamante, C. (1996) Overstretching B-DNA: the elastic response of individual double-stranded and single-stranded DNA molecules. *Science*, **271**, 795-799.
39. Bouchiat, C., Wang, M.D., Allemand, J.F., Strick, T., Block, S.M. and Croquette, V. (1999) Estimating the Persistence Length of a Worm-Like Chain Molecule from Force-Extension Measurements. *Biophys. J.*, **76**, 409-413.
40. Odijk, T. (1995) Stiff chains and filaments under tension. *Macromolecules*, **28**, 7016 -7018.
41. Husale, S., Grange, W. and Hegner, M. (2002) DNA mechanics affected by small DNA interacting ligands. *Single Mol.*, **3**, 91-96.
42. Sischka, A., Toensing, K., Eckel, R., Wilking, S.D., Sewald, N., Ros, R. and Anselmetti, D. (2005) Molecular Mechanisms and Kinetics between DNA and DNA-binding ligands. *Biophys. J.*, **88**, 404-411.
43. Bloomfield, V.A. (1996) DNA condensation. *Curr. Op. Stru. Bio.*, **6**, 334-341.
44. Gorelov, A.V., Kudryashov, E.D., Jacquier, J.C., McLoughlin, D.M. and Dawson, K.A. (1998) Complex formation between DNA and cationic surfactant. *Physica A*, **249**, 216-225.
45. Ostrovsky, B. and Bar-Yam, Y. (1995) Motion of polymer ends in homopolymer and heteropolymer collapse. *Biophys. J.*, **68**, 1694-1698.
46. Karlsson, L., Eijk, M.C.P.v. and Söderman, O. (2002) Compaction of DNA by Gemini Surfactants: Effects of Surfactant Architecture. *J. Coll. Int. Sci.*, **252**, 290-296.
47. Hayakawa, K., Santerre, J.P. and Kwak, J.C.T. (1983) The binding of cationic surfactants by DNA. *Biophysical Chemistry*, **17**, 175-181.
48. Mel'nikov, S.M., Sergeyev, V.G. and Yoshikawa, K. (1995) Transition of Double-Stranded DNA Chains between Random Coil and Compact Globule States Induced by Cooperative Binding of Cationic Surfactant. *J. Am. Chem. Soc.*, **117**, 9951-9956.
49. Buckin, V., Kudryashov, E., Morrissey, S., Kapustina, T. and Dawson, K. (1998) Do surfactants form micelles on the surface of DNA? *Pro. Coll. Poly. Sci.*, **110**, 214-219.

2.2 DNA Mechanics Affected by Small DNA Interacting Ligands

2.2.1 Abstract

We have investigated the mechanics of individual DNA strands exposed to DNA binding ligands. The interaction of these agents with individual dsDNA strands measured by optical tweezers clearly indicates the ligand-DNA binding mode. As expected, if the compound is intercalating then an increase of contour length is detected. Groove binders affect the overstretching capabilities of the formerly "naked" dsDNA strand. We interacted SYBR® Green I with naked dsDNA. The binding mode of this compound, which is used for nucleic acid gel staining, is not known. The mechanics of the interaction of SYBR® is revealed by optical tweezers experiments. The force extension curves on single dsDNA fragments show a groove-binding mode, which does not affect the contour length of the molecule but significantly alters the overstretching behavior of the dsDNA.

2.2.2 Introduction

Small nucleic acid binding agents are used as DNA staining reagents in molecular biological techniques (1). These agents bind to the DNA in different manners: intercalation between the base pairs, within the minor or major grooves, and by non-classical modes (2). For typical DNA staining experiments (e.g. gel electrophoresis), the binding properties of these compounds affect the fluorescence signal to noise ratio significantly. For instance, it is known that Ethidium Bromide (MW 394.32; CAS 1239-45-8), which has to intercalate between the individual stacked base pairs, cannot be used if the amount of DNA is typically less than tens of nanograms. In contrast, other compounds such as SYBR® Green I (Molecular Probes, Eugene, OR), which bind to dsDNA with great specificity, are able to reveal DNA amounts of two orders of magnitudes lower weight.

In addition, small DNA binding ligands have great importance in treatment of genetic, oncogenic and viral diseases (3). They can for instance act as probes for nucleic acid damage and structure (4). The activity of a variety of naturally occurring and man-made antibiotics has been linked to their ability to bind the minor groove of DNA. Sequence-specific DNA-binding small molecules that can permeate human cells potentially could regulate transcription of specific genes. For instance Dickinson *et al.* (5) showed that these synthetic ligands specifically inhibit DNA-binding of transcription factors, and therefore provide a general approach for regulation of gene expression, as well as a mechanism for the inhibition of viral replication. There are different approaches to get insight into the binding interaction, affinity and specific amount of molecules bound per base pair among which are x-ray diffraction and NMR studies (6,7).

In a recent study, Coury *et al*. (8) presented a procedure to detect these properties by measuring the contour length of the dsDNA molecule by scanning force microscopy. They incubated the bare DNA molecules with the specific agent and subsequently deposited the modified molecules onto a mica surface and investigated the amount of extension relative to the contour length. For their studies it was shown that the fraction of bound molecules could be estimated and an affinity could be determined by subjecting the DNA to various amounts of ligands. Such an approach reveals some of these parameters, but has the drawback that molecules have to be placed onto a surface in order to be accessible to the SFM imaging. It was shown (9,10) that the deposition of DNA onto mica is allowing the dsDNA molecule to adhere to the surface in a equilibrated manner, but in the subsequent study (10) it was experimentally explored that the dsDNA is partially changing its conformation from B-form DNA to A-form. A significant influence of the surface vicinity onto the binding behavior of the small reagents to DNA has to be included, and therefore, such measurements using the SFM can only reveal general trends upon reagent binding. If agents are investigated which bind to the grooves of the DNA, then an increase of contour length is not occurring. The specific binding of the groove-binding compound has to be examined by competition experiments with intercalating agents to prove an interaction.

Also, force spectroscopy was performed with SFM to discriminate small molecule DNA binding mode (11). It was shown that the mechanical properties are greatly affected when small molecules interact with DNA. The force versus extension curves show typical and different behaviours for cross-linking (cisplatin), minor groove binder (bernil), and intercalating [ethidium bromide (EtBr)] molecules. Thus, it was emphasized that force spectroscopy could be used as a fast and reliable tool for screening purposes. To further investigate the binding mode of such small interacting molecules, we present in this paper OT experiments. While SFM is best suited when overall mechanical properties have to be investigated, OT is a technique of choice to reveal small changes in mechanics (persistence length, stretch modulus). In this study, we show experiments performed on both EtBr and SYBR® green (i.e. a compound of which the binding mode is not clearly indicated). In agreement with SFM (11), we observe characteristic changes for each DNA binding molecule. Both the persistence length and the stretch modulus of DNA show a significant decrease upon interaction with such agents. Moreover, by applying a constant force feedback while injection of the agents, we were able to determine binding kinetics.

2.2.3 Experimental Section

Modification of dsDNA and Coupling to Beads

For typical optical tweezers experiments, a micron-sized bead (BangsLabs, Fishers IN) is generally coated with some receptor (e.g. antibodies or streptavidin) and placed onto a micropipette that can be moved using a piezoelectric element. Then a second set of microspheres is injected in the fluid chamber and one of them is trapped. These spheres have single dsDNA molecules attached with one end to the chemically activated surface, exposing on the other dsDNA end a ligand (e.g. biotin) into the solution. The experiment then just consists of approaching the pipette close enough to the bead in the trap till some force is felt onto a detector (Fig. 1 A and B). Due to the high affinity of biotin-streptavidin ($KD > 10^{-14}\ M^{-1}$) the molecular recognition of this ligand-receptor interaction is easy to achieve. In contrast, an site directed coupling of single molecules to beads is generally more efficient demanding.

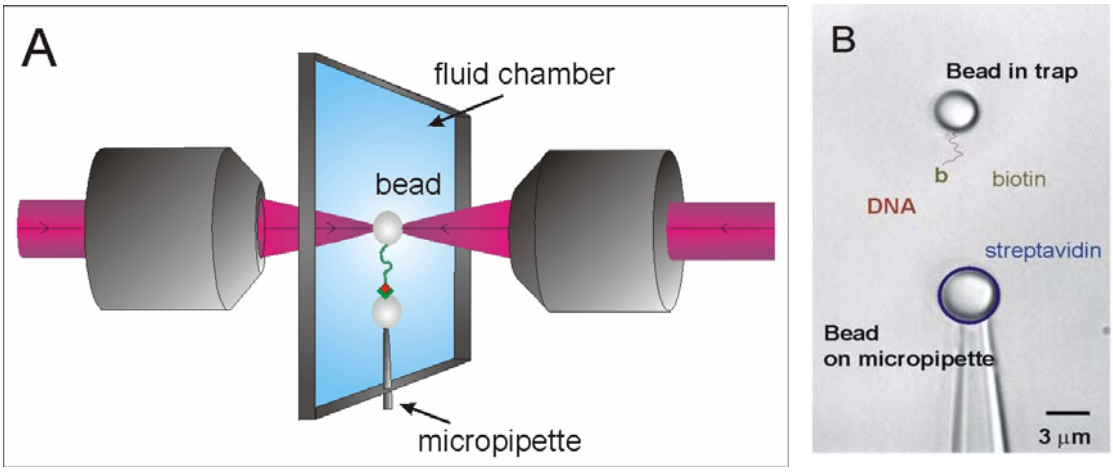

Figure 1. A) *Scheme of the double beam optical tweezers showing the counter propagating laser beams (λ= 830 nm) and the beads held by the micropipette and the OT within the fluid chamber.* ***B)*** *A typical picture obtained during the optical tweezers experiment. A bead (3.1 microns in diameter) coated with streptavidin receptors is held by suction on a micropipette. A second bead (in the center of the image, 2.9 microns in diameter) is trapped in three dimensions using two counter propagating laser beams. Single dsDNA molecules are covalently attached to this latter bead and have a free biotinylated 3' end (schematically shown (not to scale)). For a typical experiment, the micropipette is moved with nanometer accuracy close to the streptavidin bead till some deflection of the laser beam on a position detector is observed. In this case, the dsDNA single molecule is linked to the streptavidin receptor through a streptavidin-biotin bridge.*

Although there are different approaches to attach DNA molecules to chemically modified beads, the best is certainly to use a site directed covalent coupling for one end only because it allows making stock solutions of material and to reach high forces while applying external tension. For instance, an antigen-antibody bridge will rupture at forces above ~50 pN (in typical slow pulling tweezers experiments). Site directed covalent coupling of dsDNA to amino beads was performed using a procedure similar to the one described in (12). In brief, we use a commercial dsDNA circular plasmid (pTYB1, 7477 base pairs (NEB, Beverly, MA)). The plasmid DNA was then digested with a restriction enzyme (BSA1), which cuts only once in a non symmetrically manner. In other words, two different non-palindromic overhangs are obtained after a single enzymatic digestion

that can be subsequently modified in two different ways. At one end of the digested plasmid DNA, biotinylated nucleotides (Invitrogen, Basel CH) were incorporated using the Klenow exo$^-$ polymerase enzyme (NEB, Beverly, MA). On the other end small thiol modified dsDNA extensions (Microsynth, Balgach CH) were ligated. After intensive cleaning, we end up with modified dsDNA molecules with biotin groups at their 3' end and a thiol group at the 5' end. Covalent coupling of as-modified dsDNA molecules to amino-beads (BangsLabs, Fishers IN) was achieved through a standard SMCC cross linker (Pierce, Rockford, IL) as described in (12).

Optical Tweezers

The implementation and description of the optical tweezers instrument used to perform the experiments have been presented in details in (13). Basically, it consists of a dual beam apparatus, i.e. two counter propagating laser beams which share coincident foci. In contrast to single beam optical tweezers,- our instrument directly measures the change in light momentum flux when a trapped object experiences a force. This instrument, therefore, has to be calibrated once since local parameters do not affect the force readings. In addition the dual beam optical tweezers has a high trapping efficiency, which is typically three times larger than in a conventional single beam optical tweezers setup.

2.2.4 Results

Although AFM based techniques have been applied in the past to investigate mechanical properties of single polymers (14,15), intrinsic relevant parameters such as the persistence length are not accessible to this technique, mainly because of the large thermal noise of commercial AFM cantilever. Optical tweezers have, however, typical force resolution of about 0.3 pN and overcome limitations of standard AFM devices. This is of prime importance in our study since only slight changes are expected while interacting small DNA binding molecules.

2.2.4.1 Mechanics of dsDNA

To check the integrity of our bare dsDNA, we show in Fig. 2 a typical force F versus extension x curve (150 mM NaCl, Hepes buffer pH 7.5). As expected, the dsDNA

(circles) shows an overstretching plateau at 68 pN (S-transition), in excellent agreement with previous studies (16). Although the origin of the transition is subject of some debate (16,17), the force versus extension curve for forces below 60 pN can be well described by an extensible worm like chain model (WLC) (18), using:

$$x / L = 1 - 0.5(k_B T / FA)^{1/2} + F / S \qquad [1]$$

where A is the persistence length, S the stretch modulus of the molecule, L the contour length, and kBT = 4.1 pN·nm at room temperature. At small forces (typically smaller than 5 pN), only entropy should contribute to the observed mechanics of DNA and we can - to a good approximation - neglect any enthalpic elastic terms (S) in Eq. 1. In this case, a linear fit of F-1/2 (Fig. 3) as a function of the extension gives a robust estimate of the persistence length A. We find an A value of 50 nm, consistent with previous studies (16,18). Knowing this latter parameter and the contour length of the molecule, the stretch modulus of the dsDNA can be easily obtained from a fit of the force versus fractional extension using Eq. 1. We obtain an S value of 1500 pN using our standard chamber buffer.

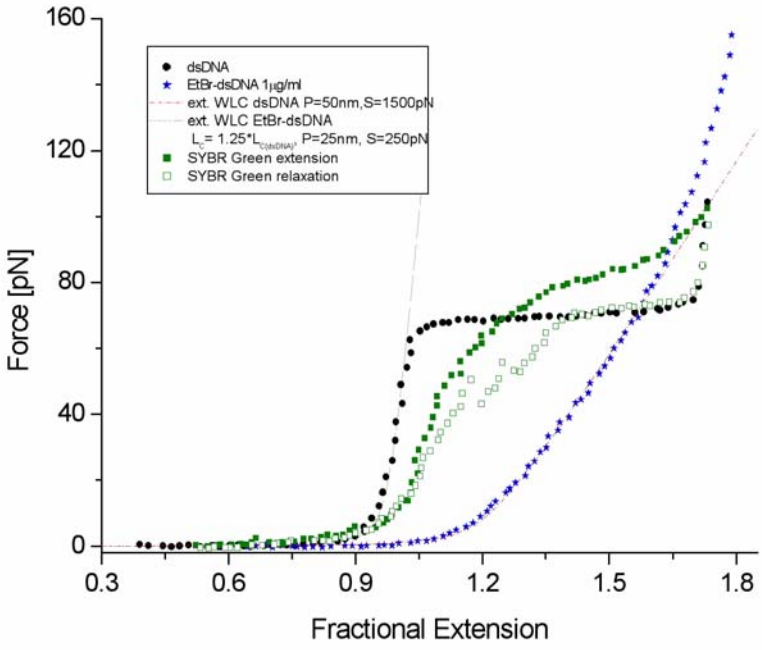

Figure 2. *Typical force versus fractional extension x/L curves obtained for bare dsDNA (circles); and EtBr (stars). SYBR® Green I dsDNA (squares, full square extension, hollow*

squares relaxation), Also shown is the fit to the data using an extensible worm like chain model (Eq. 1) (dashed lines). From this fit; relevant enthlapic parameters (stretch modulus) are obtained.

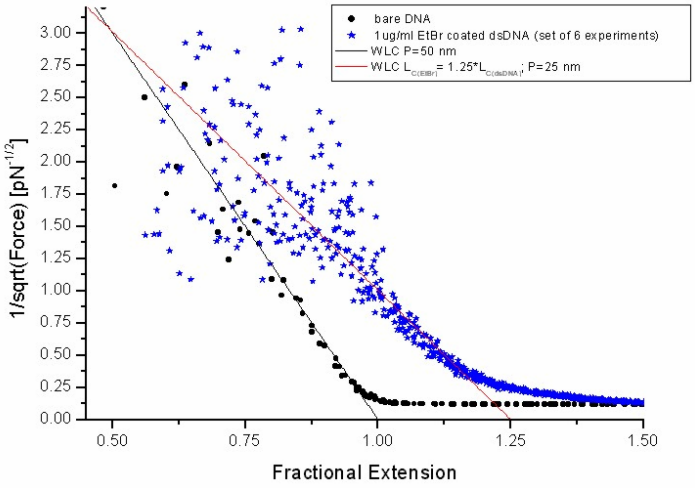

Figure 3. *The inverse of the square root of the force F as function of the fractional extension x/L (squares, bare dsDNA. circles; dsDNA after EtBr intercalation). The linear dependence observed for forces below ~10 pN is typical of a non-extensible worm like chain (WLC) behavior. The persistence length (contour length) is deduced from an extrapolation a zero extension (force). Because the point where the DNA is attached onto the streptavidin bead is unknown; the contour length has to be adjusted according to the length of the linearized dsDNA plasmid. The jittering observed above ~1.5 indicates where thermal noise fluctuations dominate the signal.*

2.2.4.2 Mechanics of dsDNA Interacting with Small Molecules

In the previous paragraph we measured the individual properties of "naked" dsDNA in order to have a molecular "ruler", to which we can compare the subsequent experiments. Next, we investigated the interaction of the bare dsDNA with ethidium bromide (EtBr). For such agents that directly intercalate between adjacent base pairs we expect to observe great changes in the mechanical properties. Therefore, by measuring the end-to-end distance of the molecule, while maintaining a constant force, we can directly follow the uptake kinetics of DNA binding agents. This way we ensure that the DNA molecule is

covered to its maximum binding capabilities at a specific concentration of reagent. We present in figure 4 the results of such a force feedback experiment at ~50 pN. The flow force of EtBr for this experiment was 15 pN in the orthogonal direction [2.5 mM], not affecting the force feedback on the dsDNA molecule.

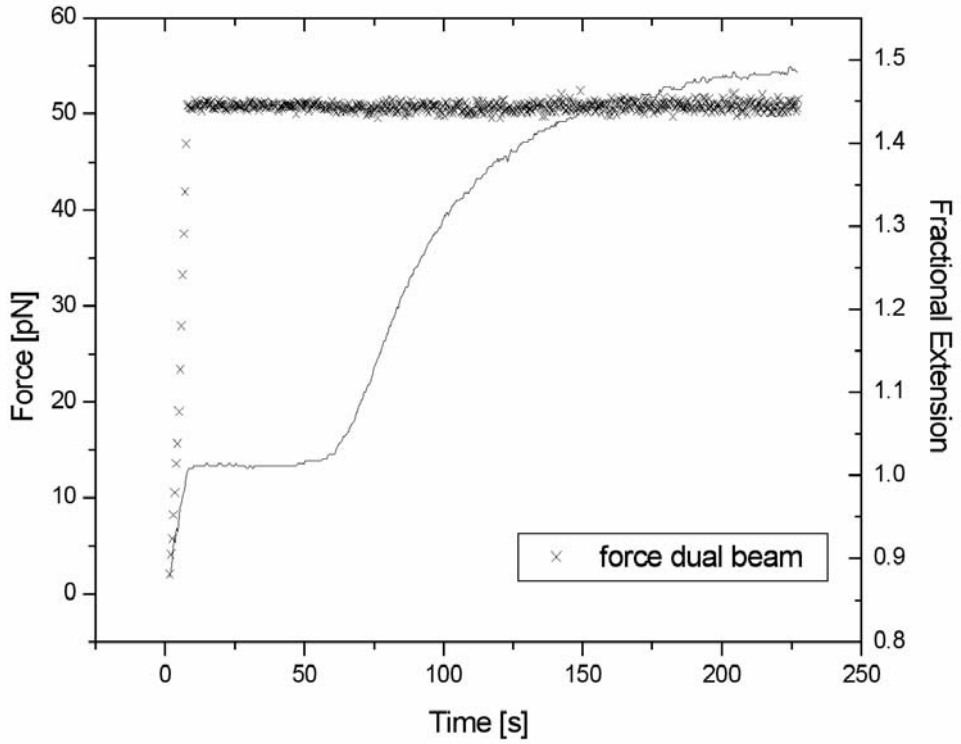

Figure 4. *Incorporation of EtBr into a dsDNA single molecule followed in real time. For this experiment, a bare dsDNA was first pulled beyond its entropically regime up to 50 pN (0 to 5 seconds) along the X-axis (as defined in our experiment). Then, a flow of EtBr (2.5 M) was applied in the chamber (15 pN along the Y direction, i.e. perpendicular to the pulling direction) and the force along the X-axis was kept constant at 50 pN. When EtBr arrives in the vicinity of the single dsDNA molecule (after 50 seconds), the bead end to end distance starts to increase, indicating intercalation of EtBr into adjacent DNA base pairs. After 150 seconds, the bead end-to-end distance does not show any significant dependence, which reveals maximum incorporation of EtBr. Crosshairs, force (pN); line, fractional extension. Incorporation of EtBr is completed after ~150 s for 2.5 μM at the chosen flow rate.*

In figure 2 the mechanical properties of such an EtBr intercalated dsDNA molecule is shown (stars). A fitting procedure identical to the one describe above reveals values of 25 nm and 250 pN for the persistence and stretch modulus respectively. In addition, we observe a change of contour length of about 25 % due to the intercalation of EtBr.

According to (19), the increase of length per EtBr molecule is 0.34 nm. Observing the increase of length directly from the measurement, we can conclude that, on average, every fourth base pair has intercalated EtBr, which can be difficult to access using scanning force spectroscopy measurement. Furthermore, from the parameters extracted, we see that the intercalation of dyes is greatly affecting the mechanics of bare dsDNA. Namely the decrease of persistence length by factors two and the reduction of the stretch modulus of six. We should mention that an applied tension on the double strand DNA during the intercalation did not bias the amount of uptake of binding agents. For instance, feedback on the force at 50 pN or at 0 pN does not change any mechanical properties.

Additionally, in figure 2 the force versus extension of a dsDNA coated with SYBR® Green I is shown (squares). As visible in the graph, the interaction of the SYBR® Green I with dsDNA doesn't alter the contour length of the molecule, but slightly decreases the persistence length (40 nm) and the stretch modulus (500 pN) of the DNA molecule during the extension cycle. During the relaxation of the molecules in presence of SYBR®, we repeatedly observe hysteresis of the force versus extension experiment. The overstretching plateau of the interacting dsDNA is affected during extension and during relaxation. Extension of the molecule shows a short overstretch plateau occurring at higher force values ~80 pN but almost no cooperativity as in the S-transition of bare dsDNA is observed. The force extension curve is then "merging" with the one from bare dsDNA after the S-transition. During relaxation of the SYBR® -dsDNA complex, again an overstretch plateau is observed which indicates either that some SYBR® molecules unbound during the high force applied to the dsDNA molecule or that intermolecular forces in-between SYBR® molecules have been ruptured, which frees parts of the bare backbone of the underlying dsDNA molecule. During the next pulling cycle, the force versus extension curve follows on a comparable path and shows the same hysteresis.

2.2.5 Conclusion

Using optical tweezers experiments, we were able to measure directly the kinetics of binding of small ligands to dsDNA. By recording a force versus distance experiment, we are able to extract the mechanical parameters of the modified dsDNA molecule directly. The parameters obtained indicate the way of binding, if intercalation occurs, then the contour length is affected. Additionally, we can determine the occupancy of the ligand on the DNA from such measurements and see how the native mechanics of the molecule is altered. If compounds bind to dsDNA which aren't intercalating, then the binding is directly revealed in the way the modified dsDNA is going through its overstretch transition. Such experiments can give direct insight into the binding of small ligands to DNA and can be of great importance for a general only screening of other compounds.

Acknowledgement

This work was supported by grants from the Swiss National Science Foundation and the support from the NCCR Nanoscale Science is gratefully acknowledged.

2.2.6 References

1. Haugland, R.P. (1996) Handbook of fluorescent probes and research chemicals. *Molecular Probes Inc. Eugene OR*.
2. Lipscomb, L.A., Zhou, F.X., Presnell, S.R., Woo, R.J., Peek, M.E., Plaskon, R.R. and Williams, L.D. (1996) Structure of a DNA-Porphyrin Complex. *Biochemistry*, **35**, 2818 - 2823.
3. Haskell, C.M. (1990) Cancer Treatment. *Saunders Philadelphia*.
4. Williams, L.D. and Goldberg, I.H. (1988) Selective strand scission by intercalating drugs at DNA bulges. *Biochemistry*, **27**, 3004 - 3011.
5. Dickinson, L.A., Gulizia, R.J., Trauger, J.W., Baird, E.E., Mosier, D.E., Gottesfeld, J.M. and Dervan, P.B. (1998) Inhibition of RNA polymerase II transcription in human cells by synthetic DNA-binding ligands. *Proc. Natl. Acad. Sci. U S A*, **95**, 12890-12895.
6. Coste, F., Malinge, J.M., Serre, L., Shepard, W., Roth, M., Leng, M. and Zelwer, C. (1999) Crystal structure of a double-stranded DNA containing a cisplatin interstrand cross-link at 1.63 A resolution: hydration at the platinated site. *Nucleic Acids Res.*, **27**, 1837 - 1846.
7. Gelasco, A. and Lippard, S.J. (1998) NMR Solution Structure of a DNA Dodecamer Duplex Containing a cis-Diammineplatinum(II) d(GpG) Intrastrand

Cross-Link, the Major Adduct of the Anticancer Drug Cisplatin. *Biochemistry*, **37**, 9230 - 9239.

8. Coury, J.E., McFail-Isom, L., Williams, L.D. and Bottomley, L.A. (1996) A novel assay for drug-DNA binding mode, affinity, and exclusion number: Scanning force microscopy. *Proc. Natl. Acad. Sci. U S A*, **93**, 12283-12286.
9. Rivetti, C., Guthold, M. and Bustamante, C. (1996) Scanning Force Microscopy of DNA Deposited onto Mica: EquilibrationversusKinetic Trapping Studied by Statistical Polymer Chain Analysis. *J. Mol. Biol.*, **264**, 919-932.
10. Rivetti, C. and Codeluppi, S. (2001) Accurate length determination of DNA molecules visualized by atomic force microscopy: evidence for a partial B- to A-form transition on mica. *Ultramicroscopy*, **87**, 55-66.
11. Krautbauer, R., Pope, L.H., Schrader, T.E., Allen, S. and Gaub, H.E. (2002) Discriminating small molecule DNA binding modes by single molecule force spectroscopy. *FEBS Lett.*, **510**, 154-158.
12. Hegner, M. (2000) DNA Handles for Single Molecule Experiments. *Single Mol.*, **1**, 139-144.
13. Grange, W., Husale, S., Güntherodt, H.-J. and Hegner, M. (2002) Optical tweezers system measuring the change in light momentum flux. *Rev. Sci. Instr.*, **73**, 2308 - 2316.
14. Rief, M.H., Clausen–Schaumann, H. and Gaub, H.E. (1999) Sequence-dependent mechanics of single DNA molecules. *Nat. Struct. Biol.*, **6**, 346-349.
15. Fisher, T.E., Marszalek, P.E., Oberhauser, A.F., Carrion-Vazquez, M. and Fernandez, J.M. (1999) The micro-mechanics of single molecules studied with atomic force microscopy. *J. Physiol. (Lond.)*, **520**, 5-14.
16. Smith, S.B., Cui, Y. and Bustamante, C. (1996) Overstretching B-DNA: the elastic response of individual double-stranded and single-stranded DNA molecules. *Science*, **271**, 795-799.
17. Rouzina, I. and Bloomfield, V.A. (2001) Force-Induced Melting of the DNA Double Helix 1. Thermodynamic Analysis. *Biophys. J.*, **80**, 882-893.
18. Hegner, M., Smith, S.B. and Bustamante, C. (1999) Polymerization and mechanical properties of single RecA-DNA filaments. *Proc. Natl. Acad. Sci. USA*, **96**, 10109-10114.
19. Lerman, L.S. (1964) Acridine mutagens and DNA structure. *J. Cell. Comp. Physiol.*, **64**, 1-18.

3. Mechanical properties and molecular machinery of VirE2–ssDNA filament investigated by optical tweezers

3.1 Abstract

Agrobacterium tumefaciens is a plant pathogen that evolved a unique mechanism of interkingdom gene transfer. Central to this mechanism, the VirE2 protein is a multifunctional protein that coats the ssDNA transferred, interacts with host factors assisting nuclear import of the complex and also forms channels in lipid bilayers. We investigated the formation and the mechanics of single VirE2-ssDNA complex by optical tweezers. Known characteristics of the ssDNA-VirE2 complex (electron microscopy studies) such as the formation of blocks of regularly coating protein and reduction of length of the ssDNA molecule upon VirE2 binding were observed with optical tweezers. New details such as the kinetics showed that VirE2 proteins act as powerful machinery, capable of producing work up to 50 pN load while coating ssDNA at a rate larger than 500 VirE2 per second.

In addition, we show that ssDNA-binding VirE2 proteins could be solely responsible for pulling ssDNA into the host cell cytoplasm. In contrast to other types of molecular machineries (motors) where chemical energy *(*ATP) is necessary to exert a force on DNA, pulling of ssDNA by VirE2 into the host cytoplasm does not require any external energy. Instead, the generation of forces is governed by: (i) the cooperative binding of VirE2 proteins on ssDNA in the host cell cytoplasm, (ii) local conformational changes in the protein induced by binding to ssDNA, (iii) the ability of VirE2 proteins to effectively condense ssDNA into highly rigid structures.

Keywords

The abbreviations used are: ssDNA, single-stranded DNA; T-DNA, transferred-DNA; ssT-DNA, single-stranded transferred-DNA.

3.2 Introduction

Agrobacterium tumefaciens, a Gram-negative bacterium, evolved a complex and unique mechanism to transfer a long single stranded DNA (ssDNA) molecule from its cytoplasm to the eukaryotic host plant cell nucleus. There, the transferred DNA molecule finally integrates stably in the genome. The expression of the genes located on this ssDNA leads to the formation of tumors, the symptoms of the crown gall disease caused by *Agrobacterium* (1).

Most of the genetic information required for this interkingdom transfer process to occur is located on the large tumor inducing plasmid (Ti plasmid) of *Agrobacterium* (2-4). There, the transferred ssDNA (T-DNA) sequence is delineated by 24bp long imperfect repeats (called the border sequences) and the proteins needed for the T-DNA transfer to occur are encoded by seven operons. As these proteins are necessary for virulence, they were called the virulence (Vir) proteins (VirA to VirG). The formation of the T-DNA is obtained upon VirD1/VirD2 cleavage of the border sequence in a site- and strand-specific manner. Concomitantly VirD2 becomes covalently attached to the 5' end of the nicked DNA (5-8). The nicked DNA is then displaced 5' to 3' from the plasmid, producing single-stranded T-DNA covalently bound to VirD2 (9). The VirD2 protein will then serve as a pilot for the T-DNA all along the transfer to the plant cell nucleus.

The export of the ssDNA through the two bacterial membranes relies on a multiprotein machinery (the type IV secretion system) composed of eleven VirB proteins and VirD4. These 12 proteins span the inner and outer membrane of the bacterium and form a multiprotein machine necessary for secretion of the T-DNA. This machinery shares homology to bacterial conjugation and one of its components, the coupling protein (VirD4), is proposed to supply the ATP-dependant power to pump the T-DNA from the bacterium to the recipient host cell (10).

The length of ssDNA transferred can be up to 150 000 bases, hence there is a strong requirement for a mechanism to protect the ssDNA from nucleases present in the host cell. This role is likely to be fulfilled by the VirE2 protein, as it is a ssDNA binding protein (11) and was shown *in vitro* to protect ssDNA from nucleases (12). Image processing of negatively stained VirE2-ssDNA complexes revealed structural characteristics at low resolution of the complexes (13,14). 4.25 molecules of VirE2

coat the ssDNA per turn of the solenoid. Each VirE2 molecule shields 19 nucleotide of ssDNA under equilibrium conditions. The ssDNA is totally shielded by the VirE2 protein and hence protected from nuclease degradation. This way, the T-complex can more easily pass the cytosol and the nuclear pore complex than uncoated ssDNA that would form hairpins and thus not be linear and would entangle with other molecules and organelles. The outer surface of the complex is ready for binding to bacterial or plant cofactors needed for nuclear import of the ssDNA-VirE2 complex. Indeed, VirE2 was shown to interact with an *Arabidopsis* protein, VIP1, that allows nuclear import in yeast or animal cells (15). Recently, it was shown that VIP1 mediates interaction between VirE2 and karyopherin alpha, a component of the host cell nuclear import machinery (16). Then, once in the nucleus, targeted proteolysis mediated by another virulence factor, VirF, would degrade VirE2 and VIP1 (17). Therefore the T-DNA is free for conversion to double-stranded intermediates and then integrate in the genome, possibly into double-stranded breaks (18), (19).

Natural hosts of *Agrobacterium* are dicotyledonous plants (20), and efforts to broaden its host range succeeded: now *Agrobacterium* is used to infect monocots (21), yeast (22), fungi (23,24) and it was even shown to be able to infect human cells (25).

The binding of VirE2 is not sequence-specific, any DNA sequence can be transferred provided the 25bp border sequences are present. The *Agrobacterium* became the primary tool for plant genetic engineering (26) and artificial systems have been developed where the T-DNA can be up to 150kb long (27,28), provided some Vir proteins such as VirG, VirE1 and VirE2 were over expressed. *In vitro* prepared T-DNA complexes (VirE2/VirD2 in complex with ssDNA) can be also be used as an artificial DNA delivery system, making the VirE2-ssDNA complex an attractive candidate for clean gene transfer to eukaryotic cells (29). *Agrobacterium* T-DNA transfer is an extremely powerful tool to engineer transgenic organisms and the system is still improving, namely regarding its host range, efficiency and targeting.

In this paper we investigated the kinetics, force generation and mechanics of VirE2 protein binding to naked ssDNA in order to further characterize the properties of the central VirE2-ssDNA complex with optical tweezers. Our studies reveal a new and fundamental function of VirE2 and have found that the cooperative binding of VirE2 on T-DNA could allow a fast and powerful active transfer of the T-DNA into the infected cytoplasm.

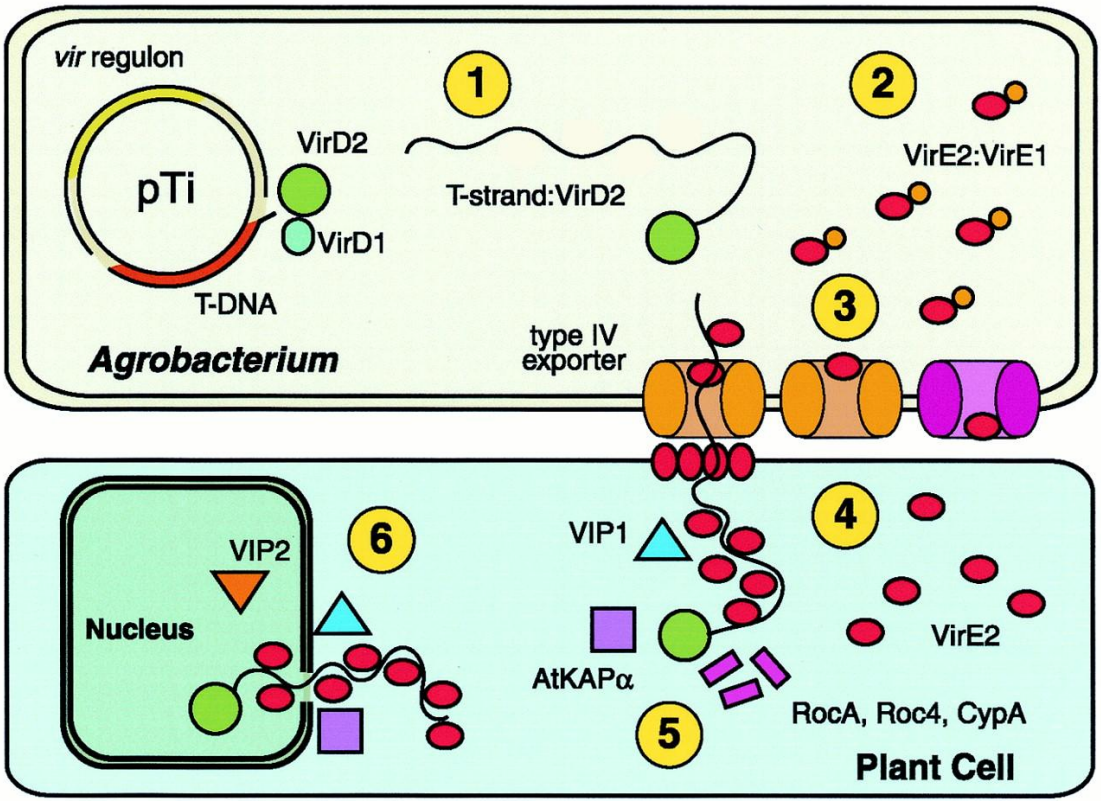

Figure 1. *Hypothetical model for T-DNA transfer from an Agrobacterial cell into a plant cell* (30).

3.3 Materials and Methods

DNA handles

Two types of DNA molecules were used for this study.

Type 1: DNA molecules were prepared by PCR amplification of the pPIA plasmid (15071 bp) using 5'-Thiol-TAT CGT CGC CGC ACT TAT GAC TGT-3' and 5'-TAT GTC GAT GTA CAC AAC CGC CGA-3' as forward and reverse primers (Microsynth, Balgach CH), respectively. The resulting 14107 bp PCR fragment was digested with EagI (New England Biolabs). After digestion, the longest fragment (13883~bp) was end-filled with Klenow Exo$^-$ (New England Biolabs) with two dGTPs and two biotin-14-dCTPs (Invitrogen). Type 2: a PTYB1 plasmid (7477 bp) was digested with BSA1 (New England Biolabs) and ligated at one end with small Thiol-modified double stranded DNA (dsDNA) extensions (24 bp) that had an overhang (4 bp) compatible with the restriction site of BSA1 in PTYB1. The obtained

product (7497 bp) was finally end-filled with Klenow Exo$^-$ using one biotin-14-dATP and two dGTPs and two biotin-14-dCTPs (31).

DNA of type 1 and 2 were then covalently coupled to 2.17 µm amino-modified beads (Spherotech, Libertyville IL) using a similar procedure as described by Hegner (32).

Purification of VirE2-His6 proteins

We used similar purification conditions as described in Dumas *et al.* (33), with the addition of glycerol (final proportion 20 % w/v) to the sample buffer (50 mM NaH_2PO_4 pH 8, 300 mM NaCl) before storage of the protein at – 80 ºC.

Transmission electron microscopy (TEM)

2 µL of M13ssDNA (New England Biolabs) at 60 µg/ml were heated to 65 °C for 10 minutes, centrifuged 10 minutes at 18,000xg at 4 °C and then cooled 10 minutes on ice. 4 µL of VirE2 protein at 0.1 mg/ml were then added and the mixture was incubated overnight at room temperature. The sample was diluted 1/5 before applying 3 µL onto a glow-discharged TEM microscopy grid (200 mesh/inch, gold-plated copper grid). After 45 s, the grids were blotted and washed on three droplets of water. A blotting step followed each wash. The grids were then negatively stained on two droplets of 2 % (w/v) uranyl acetate and blotted. The negatively stained grids were examined using a Hitachi 7000 TEM. Images were recorded on a SO163 film (Kodak). The negatives were scanned on a Primescan D 7100 (Heidelberger Druckmaschinen AG, Kiel, Germany) at a resolution of 4 Å/pixel.

Optical tweezers

The experimental apparatus for optical tweezers experiments has been published earlier (34). DNA-modified beads were trapped by the laser beam and the free biotinylated DNA end was subsequently attached to a 2.20 µm streptavidin bead (Spherotech, Libertyville IL), which was held by suction on a micropipette. The bead-to-bead distance was determined from both the movement of the micropipette (controlled with a closed-loop piezoelectric element) and the deflection of the laser (monitored by a two dimensional position sensitive detector). The pipette bead was moved away from the trap bead at a constant velocity of 0.8 nm/ms. At this rate, it took a few seconds to get a complete force curve. Forces were obtained from the

direct measurement of the change in light momentum flux. All signals (distance, force) were low-pass filtered at 159 Hz. If not mentioned otherwise in the text, force curves were measured in assembly buffer [50 mM pH 8.0 NaH_2PO_4, 150 mM NaCl and 5 % w/v glycerol]. Prior to injection, VirE2 proteins were centrifuged at 14,000xg for 20 min. The supernatant was kept at 4°C and injected at a concentration ranging from 6 to 20 µg/ml in assembly buffer. Experiments were performed at room temperature.

3.4 Results and discussion

3.4.1 Translocation of the ssDNA from the bacteria to the plant cell

After docking of the bacteria to the plant cell a DNA and protein export machinery is activated to allow successful infection of the plant host cell as described in the introduction. The focus of our research was on VirE2 protein a central player on DNA transport through the cytosol of the plant cell. VirE2 exits *Agrobacterium* via the type IV exporter independently (35). VirE2 has to be associated with VirE1 protein to allow export from the bacteria cell. It has been shown that VirE2 monomers transferred first into host cell. Such a pre-infection of molecules is required to allow subsequent protection of the infectious T-DNA and further efficient DNA transport through the cytosol. The size of VirE2 monomer probably is too small to activate the host immune system. To study the effects which might arise in the cytosol of VirE2 proteins interacting with T-DNA we studied the formation process of the nucleo-protein complex. This step represents the first step in a series of actions provided by the bacteria to shuttle the T-DNA into the host plant cell. VirD2 is covalently attached to the 5' end of the DNA and helps to protect the first piece of DNA which protrudes through the import channel. A free 5'-end would give exo-nucleases access to nucleic acid degradation. It has been shown in other studies that VirE2:ssDNA complexes are resistant to 3' or 5' exonucleases as well as endonucleases. Our studies revealed that the formation of the complex occurred very fast. It is known that VirE2 binds ssDNA regardless of sequence and therefore no selection of nucleic material has to occur upon entry in to the host cell. Using optical tweezers we measured the speed of formation of the VirE2:ssDNA complex by clamping naked ssDNA of 4.8 µm length in-between two polystyrene spheres and then kept the externally applied force during

formation of the nucleoprotein complex constant. The ssDNA strand was fully coated with VirE2 and compaction of the ssDNA due to protein polymerization was observed in fraction of seconds. Figure 2 shows the dependence of the polymerization rate on the externally applied force.

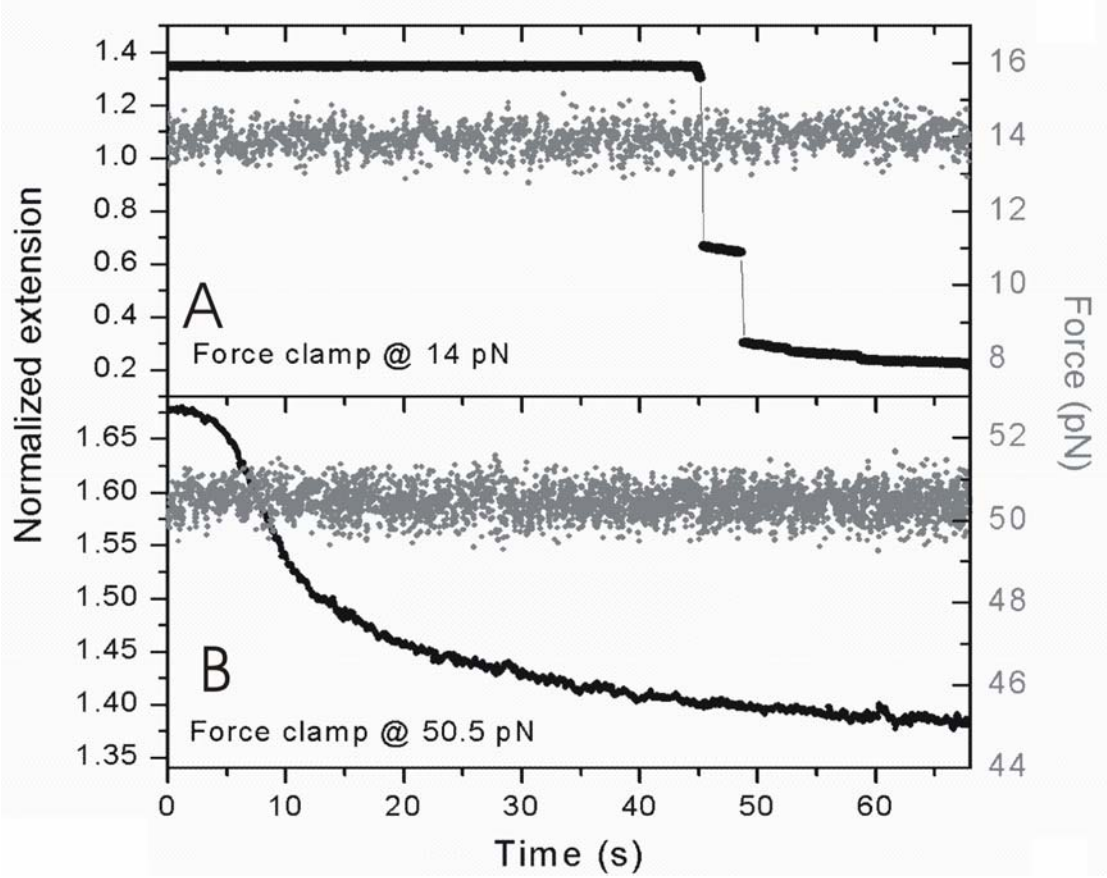

Figure 2. *Experimental time traces of single ssDNA molecules upon VirE2 injection obtained in a force-feedback optical tweezers operation mode (black solid line). Upper panel A) force-clamp at 14 pN. Lower panel B) force-clamp at 50.5 pN. The time at which VirE2 proteins start to polymerize ssDNA depends on the injection speed. Therefore, all curves have been offset along the horizontal axis. Extension normalized to the contour length of dsDNA is shown. Depending on the force-setpoint applied, different behaviors are observed. At low forces (smaller than ~30 pN), time traces show abrupt changes that evidence for a cooperative binding mode of VirE2. At higher forces, the larger inter-nucleotide distance decreases VirE2-VirE2 interactions and a non-cooperative binding mode is favored. For clarity, the force signal is also shown (gray solid line).*

In figure 2A a constant force experiment is shown where the force was kept at ~ 14 pN at which force we observe a polymerization speed of ~ 6 ± 1 μm/s. As shown the VirE2 coating was compacting the naked ssDNA almost instantaneously. In figure 2B the force was kept at ~ 50 pN and then the compaction speed was drastically reduced but VirE2 monomers were still able to bind to the extended ssDNA conformation. Because we lowered protein-protein interactions at higher force F > 50 pN (simply because ssDNA is forced to remain in an extended form), polymerization and compaction could not occur in a cooperative manner. In this case, polymerization was mainly governed by the probability for a VirE2 monomer to find an available state for binding. Although this probability was high at low forces, it dramatically decreased as the externally applied force increased. The fact that the VirE2 monomer was able to bind at forces up to 45 pN indicated that the binding sites of the ssDNA were still in register with the needs of the protein binding cleft. This indicated that the distance from base to base was almost perfect over a large scale and compaction was not disturbed at forces < 10 pN reaching an upper value for compaction at forces up to 50 pN. The base to base distance at 50 pN was calculated to be ~0.58 nm a distance comparable to the sugar pucker in ssDNA which starts out as C3' endo also to distance found to be ~0.59 nm (36). When we set the force feedback point of the experiment higher than 50 pN then no VirE2 protein binding was observed, which implied that the phosphate to phosphate distance plays an important role in defining the contact points of the ssDNA with the VirE2 protein monomer. We observed two force regimes, first at forces < 10 pN the polymerization and compaction seemed to reach an optimal speed of ~6 ± 1μm/s which was not affected by the externally applied forces. When higher forces were applied then we observed a decrease in polymerization/compaction speed.

3.4.2 Rate of Polymerization

The rate of polymerization is a quantity that is not accessible when performing experiments on an ensemble of molecules. In single-molecule experiments, one circumvents the need for synchronization of many molecules at a time and such dynamical properties are straightforward to probe. Force-clamp experiments (i.e. force-feedback) are an appealing route to investigate the dynamics of polymerization. As seen in Fig. 3, the rate of polymerization decreased as a function of the tension

applied on the filament. This feature demonstrated that the rate-limiting step for complete formation of VirE2:ssDNA solenoidal complexes is force dependent.

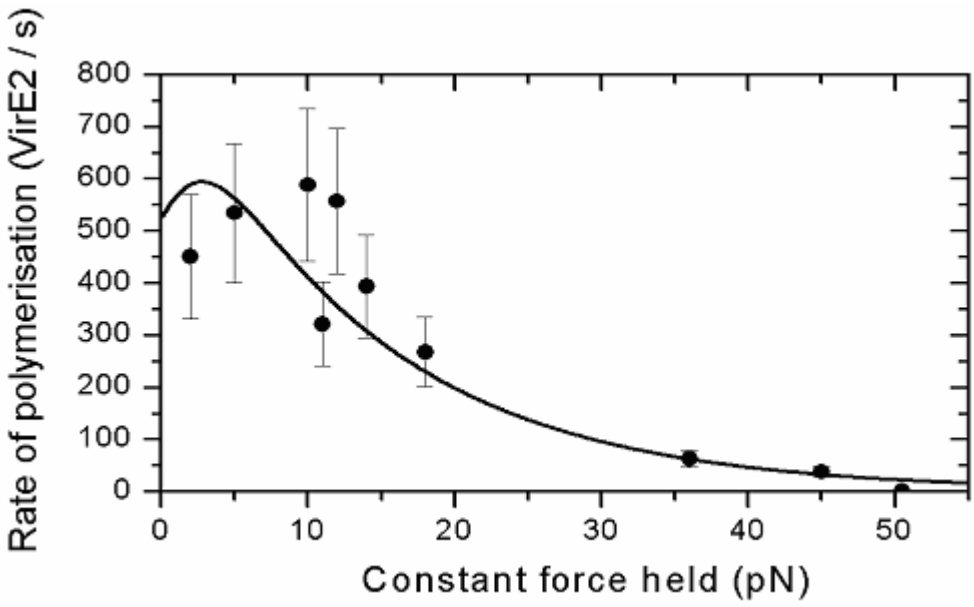

***Figure 3**: Rate of polymerization k(f) and compaction of VirE2 on ssDNA as a function of the applied tension measured with force-clamp experiments. Shown is rate of polymerization k(f) as the function of the force set point. k(f) is expressed in VirE2 per ms. The conversion factor [microns/ms (as obtained from the experimental curves) to VirE2/ms] is 1/(0.68X19)=7.7x10^{-2} assuming that the base to base distance of ssDNA is 0.68 nm and that VirE2 binds 19 nucleotides. The curve can be fitted with an Arrhenius law (solid line). A local model taking into account the change in conformation of ssDNA upon VirE2 binding accounts for the observed force-dependence of k(f) (solid line). In this local model, the only free parameter is a constant pre-factor k_0. Other parameters are derived from known structural parameters of ssDNA (i.e. (i) angular fluctuations of non-coated ssDNA segments in a freely jointed polymer chain model in the presence of an external force (ii) compacted form of fully coated ssDNA obtained from HR-TEM measurements).*

The curve in figure 3 can be fitted with the force dependence of *k* modeled using an Arrhenius law (37):

$k(f) = k_0 \exp(- < w(f) > / k_B T)$ where <*w(f)*> represents the time average of the work produced during binding of the protein to nucleotides. If the nucleotides are

tightly bound to the protein in the final state (bound) and assuming – in a first approximation - that the adjacent nucleotides (not bound) are unhindered by VirE2 binding, we have (38):

$$< w(f) >= fL_{SS}\left[\left(\coth\frac{2A_{SS}f}{k_BT}-\frac{k_BT}{2A_{SS}f}\right)-\frac{L_V}{L_{SS}}\right] \qquad [1]$$

where the averaged angular variations in between two nucleotides in a pure ssDNA form are derived from the freely jointed polymer chain model. For the persistence length and the local contour length of ssDNA, we used: A_{ss} = 0.7 nm and L_{ss} = 0.68 nm at 150 mM salt concentration. L_V can be estimated from the recent HR-TEM analysis of SSDNA-VirE2 filaments (13): over the helical pitch of 5.15 nm there are 82 DNA bases (4.25 VirE2) with a local contour length of 32.6/82 = 0.4 nm (13), the only unknown parameter in *k(f)* is k_0, which represents a constant pre-factor. The good agreement between the overlay and the experimental data point (Fig.3) validates the approach we used. In particular, this confirms that VirE2 binds 19 nucleotides (82 bases / 4.25 VirE2).

Polymerization showed cooperative behavior, the polymerization speed was not affected at forces up to ~ 12 pN this indicated that till this force the bases to base distance was optimal and the externally applied force is not preventing the final 3D compaction of the filament. At forces higher than 12 pN the formation of the final nucleoprotein complex slowed down but was still able to nucleate and polymerize up to ~50 pN external force. The base to base distance was longer at these forces and the external strain on the structure prevented the needed protein-protein contacts for final compaction. When such ssDNA strands were relaxed after the constant force experiment at force > 50 pN where no formation of filaments was observed the force versus distance curve showed the mechanical properties of naked ssDNA during relaxation but immediate alteration of the mechanics upon subsequent elongation.

To gain additional insight into the polymerization process we performed a constant length experiment. First the forces acting on the elongated ssDNA to be covered have to be defined. dsDNA is exhibiting a base to base distance in B-form of 0.34 nm, in naked ssDNA the base to base distance upon full extension measures 0.68 nm. Because we used different DNAs that have different lengths, the curve were normalized to the contour length of dsDNA (4720 nm for DNA of type 1, 2540 nm for DNA of type 2). Since we performed force versus extension experiments

subsequently on ssDNA we defined its contour length stretched to its full extension as 2.0 normalized by the length of the original dsDNA. dsDNA and ssDNA can be regarded as entropic springs which are defined by their mechanical properties which are dominated by the persistence length.

Now we revisit the effect of protein polymerization on the naked ssDNA but we kept the length of the extended ssDNA at a normalized contour length of ~0.3 of the total expansion possible of 2.0. From the previous experiments we knew that the polymerization at forces ~ < 12 pN was not affecting the speed of compaction. Another fact to be considered performing this experiment was that an ssDNA kept at ~0.3 of the total length was subjected to entropic forces which kept the ssDNA extended at a force of ~4 pN. At this force we measured a fast polymerization / compaction of ~ 6 μm/s. A typical experiment where the length had been kept constant at ~0.3 of its normalized length is shown in figure 4.

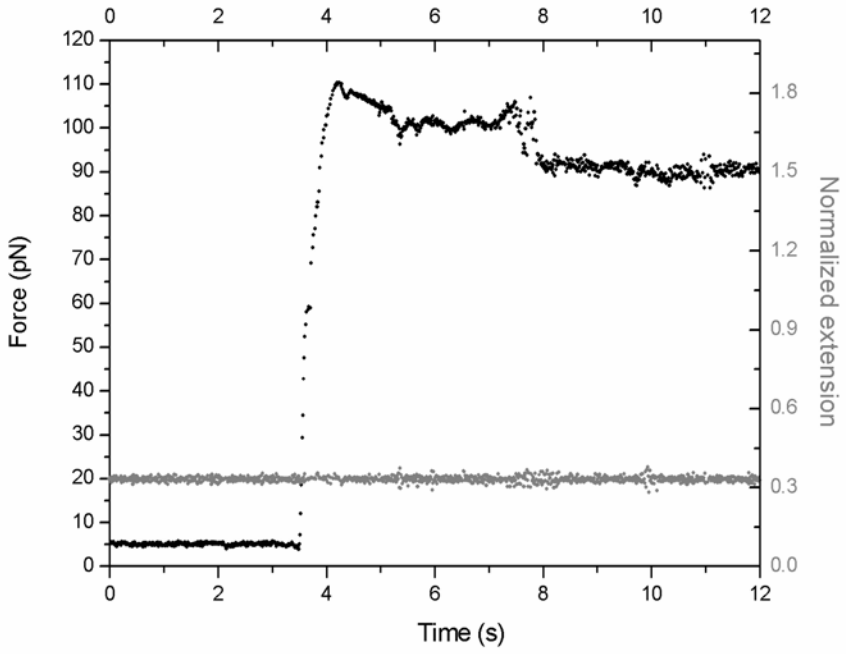

Figure 4. *Constant length feedback experiment. Experimental time traces of single ssDNA molecules upon VirE2 injection obtained in a distance-feedback, optical tweezers operation mode (black traces). The time at which VirE2 proteins start to polymerize ssDNA depends on the injection speed. Therefore, all curves have been offset along the horizontal axis and are extension normalized to the contour length of dsDNA. VirE2 proteins polymerizing on ssDNA are capable of producing high forces (up to ~100 pN) when the distance setpoint is set to ~0.3. This force value is in good*

agreement with the force-extension curves (Fig. 2). For clarity, the distance signal is also shown (gray traces).

In figure 4, an abrupt change in force from ~0 to ~100 pN is observed upon VirE2 addition when the tethered length of ssDNA is set to a normalized extension of ~0.3. In this model, the free energy gained upon protein binding allows a re-organization of adjacent VirE2 proteins in a helicoidal structure that subsequently generates a force. Because of the high rigidity of VirE2 domains, extracting relevant mechanical parameters of fully coated ssDNA filaments (e.g. persistence length *A*) from a worm-like-chain (WLC) model is a difficult task. Similarly, a mechanical model based on the helical structure of VirE2 would underestimate both the persistence length *A* and stretch modulus.

Our measurement clearly show that during this time the force on the construct did not exceed ~5 pN then after complete coverage within ~ 0.3 seconds the force which is measured on the ssDNA covered with VirE2 protein gradually increases to ~ 110 pN and then jittering around ~ 100 pN. We attribute this to two different regimes of which the first one describes the diffusion limited binding of monomers during the initial covering of the ssDNA and thereafter some rearrangement within the filament which underwent some conformational change which stabilized the final structure. Please note that during the initial coverage the forces remain below ~ 5 pN and thereafter the formation of the solenoidal compact form of the final VirE2-ssDNA complex was dominated by protein-protein interactions along the contour of the VirE2 solenoid but additional contacts in-between the individual turns might contribute to the buildup of the forces measured.

One thing which was clearly observed was that the binding of the VirE2 protein to the naked ssDNA was not only actively compacting the ssDNA but also was able to buildup considerable forces upon fully forming the solenoidal form of the final product which will reach a energy minima upon completed compaction. Such fast binding and active compaction will bias the local motion of the naked ssDNA on its way through the plant cell membrane. The capability of generation of forces up to ~ 110 pN would also significantly remove any local hairpins within the ssDNA which might prevent efficient sliding through the membrane. This behavior was the first one to be observed which generated forces in this range without the aid of additional motor proteins or energy conversions involved. The forces arising only were

generated by the protein-ssDNA complex which underwent conformational changes during the time the complex was formed. Such force generations as observed in length clamp experiments have to be regarded as static forces and are induced by the conformational change of the nucleoprotein complex. The polymerization at constant force and the distance feedback experiment showed that the VirE2 protein could bind ssDNA which was presented in various configurations. The base to base distance was not strictly defined during the first binding of the protein to the ssDNA we could elongate the ssDNA base to base distance by a factor of two and the proteins monomer were still able to bind to the target. Since we divided the polymerization and the final solenoidal filament formation in two steps maybe the first initial binding was not affected by external forces but as has been shown in figure 4 (constant length) experiment the compaction into the final solenoidal structure (second step) was severely interfered if the length was kept above the final compaction distance or at forces > 12 pN. This might imply that the ratio of 4.2 protein units per turn as visualized per SEM is a given quantity but the DNA/protein ratio of ~ 19 bases (ssDNA) per protein monomer as suggested by SEM imaging which occurred under equilibrium condition and without externally limiting factors the ratio might be a variable quantity.

3.4.3 Force curves at low protein concentration

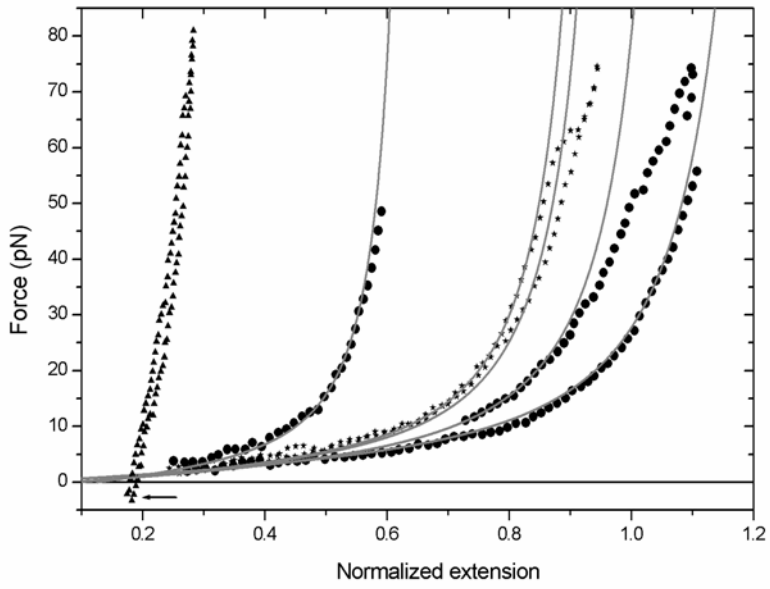

Figure 5. *Force versus extension curves of fully (triangles) and partially coated (circles, stars) ssDNA-VirE2 filaments. Experimental curves have been normalized to*

the contour length of dsDNA. The gray lines are non-extensible WLC fits assuming that partially coated fragments consist of two domains (fully coated ssDNA and non-coated ssDNA with VirE2) that have well different rigidities. Due to the incubation mode of ssDNA in our experiment and because VirE2 is a non-sequence specific ssDNA binding protein, we observe a non-perfect coating of ssDNA (i.e. multiple nucleation sites lead to different helical domains that might not be in register). This is evidenced by the presence of abrupt jumps (cooperative release of VirE2 domains, see circles) in the force-extension curves when the filaments are pulled. At full coverage, VirE2-ssDNA filaments consist in highly rigid biological objects that can resist compression forces up to ~3.5 pN (arrow).

In this section, we discuss experiments where - after injection of VirE2 proteins - the end-to-end distance of the beads was kept at a normalized extension of 0.2 (~ 1000 nm for DNA of type 1) or below and subsequent force curves were measured. Choosing different VirE2 concentrations or decreasing (at a given concentration) the speed at which proteins are injecting in the chamber allows studying initial stages of the polymerization. We point out that such experiments [where the initial end-to-end distance is chosen different from the final filament length as visualized by SEM (13)] do not probe the final completely packed native state of VirE2-ssDNA filaments. This contrasts with force-clamp experiments (discussed in the previous section) for which the pipette is free to move to always keep the same tension on the molecule upon protein injection. Nevertheless, a thorough comparison of the results obtained for these two types of experiments allows getting a clear picture of the mechanics of VirE2-ssDNA filaments at various stages of the filament formation. Although force curves show some variability, all of the curves measured at low VirE2 concentration display common and reproducible features before a stable state is reached (complete polymerization). As seen in Fig. 5, the obtained force-extension curves show - at low force - a high flexibility, which is to some point comparable to that of ssDNA. Interestingly, the obtained force-curve can be well fitted with an inextensible WLC model using the persistence length of bare ssDNA (i.e. ~ 0.8 nm) and a contour length L_c equal to:

$$L_c = \delta \cdot l_{ssDNA} + \frac{1}{5.8}(1-\delta) \qquad [2]$$

where $0 \leq \delta \leq 1$. Here we assume that VirE2 compacts ssDNA by a factor $2*5.8$ (39). Depending on the experiment, we found different values of δ as well as different curvatures at higher forces. Such a fitting procedure shows that the mechanical properties of partially coated VirE2 filaments are mainly determined by the high flexibility of ssDNA. In other words, it looks like the filaments are composed of two different domains showing a well different rigidity to bending. A flexible domain of length $L_c = \delta * l_{ssDNA}$, which is composed of bases not coated with VirE2 proteins; and a rigid domain of length $(1/5.8)(1 - \delta)$ fully coated with VirE2. According to this analysis, the factor $1 - \delta$ represents the fraction of ssDNA coated with VirE2 proteins.

As seen in figure 5, two types of features were observed at low protein concentrations: (i) an hysteresis at forces ranging from ~ 50 to ~ 70 pN (black triangles) (ii) an abrupt jump in the force curves (black dots). The hysteresis is a common feature of all curves that have VirE2 coverage below $0.55 = 1- \delta$. Force *versus* extension curves often showed abrupt changes in force upon pulling (black dots). In some cases, a sawtooth pattern was sometimes observed (data not shown). Sawtooth patterns have been already seen in titin (40), nucleosomes (41,42). In these experiments, the sawtooth pattern was attributed to the unfolding or rupture of one individual element [immunoglobulin domains (40), histones (41,42)] the breaking of interaction in between dimmers so far has not been observed in other biological nucleoprotein assemblies. As discussed below, the occurrence of such abrupt jumps in the force-extension of VirE2 filaments is likely to be due to the cooperative un-peeling of several VirE2 proteins forming a long domain. Although the binding of VirE2 is extremely fast and highly cooperative (12) (*i.e*. the binding of VirE2 catalyzes the additional binding of proteins), VirE2 as observed in SEM preparations certainly does not form a perfect and extended decoration [a solenoidal structure (14)] along the hole ssDNA molecule (as shown in figure 5). A function which could be attributed to such a cooperative unbinding under external environmental changes could be the deprotection in a nucleus environment to integrate subsequently the genetic material to be transfer into the host genome. We attribute the jumps or sawtooth like observations in our force versus distance experiments to either disruption of individual domains linked with naked ssDNA forming hairpin like structures or to release of complete stretches of ssDNA in one shot. We observed complete unbinding (conversion to naked ssDNA) only under harsh environmental

changes as when the pH was raised to pH 14 by injecting 10 mM sodium hydroxide in the fluid chamber. In nature such a deprotection is proposed instead to be performed by proteolytic activity in the nucleus.

VirE2 is a non-sequence specific DNA binding protein (43) and therefore, there can be different nucleation sites on the DNA that lead to different helical domains (not in phase). At the interface in between non-registered domains, proteins have to re-arrange in a stable structure. Most likely, such conformation will consist in a tetrameric organization of VirE2 in a ring-like structure, which could be one binding mode of VirE2 in the absence of DNA (39). This explains why such rings are usually located at breaks in the helices. According to Asmahan *et al.* (13) the typical distances in between breaks is about 30 to 100 nm starting with a ssDNA template in a relaxed configuration as observed in SEM investigations.

3.4.4 Mechanical properties of fully formed VirE2-ssDNA filaments

After the T-DNA is being transported through the plants membrane is encountered directly by VirE2 which coats the naked ssDNA immediately, to protect it from nuclease degradation. One protein (VirD2) already attached to the ssDNA strand at the 5' end of the ssDNA and therefore prevents exo-nuclease activity. The coverage of the remaining naked ssDNA helps to prevent endo-nucleases to attack the ssDNA and in addition is able to contract and compact the ssDNA considerably which allows efficient subsequent transport through the cytoplasm. Next we studied the mechanics of the VirE2 covered ssDNA. Such a nucleoprotein complex could be covered with various amounts of VirE2 proteins as revealed by TEM imaging shown in figure 6.

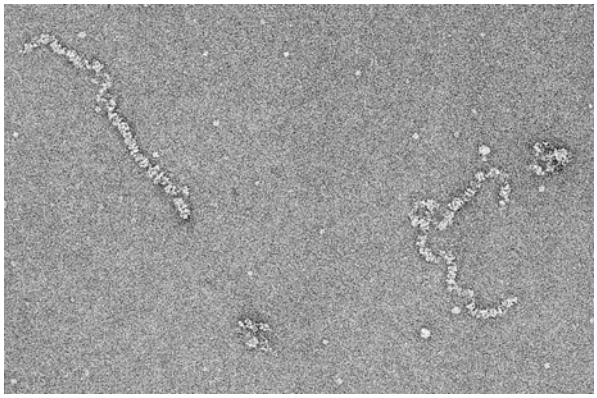

Figure 6. *TEM images of VirE2 coated ssDNA filaments (conditions during coating experiment are described in the methods section).*

Upon entry into the host cell the ssDNA would immediately be protected if VirE2 molecules have been previously exported from the bacteria into the host cell. In such a case all newly protruding ssDNA would be covered and therefore protected and conditions in which partial coating occurs would not take place if enough monomers have been imported during pre-infection of the host cell.

After pulling several force curves (having VirE2 monomers in the surrounding), all VirE2-ssDNA filaments adopt a final stable and reproducible conformation that consists of an almost rigid rod (triangles in figure 5). It seems as if the transition into the stiff rod like configuration is observed like longer stretches of nucleo-protein fragments locking into each other upon subsequent pulling. After a final mechanics is obtained no unbinding by applying forces > 100 pN are able to release protein subunits from the nucleoprotein complex. The nucleo-protein complex which originated from our pulling experiments shows distinct transitions to become a perfect VirE2-ssDNA complex.

Due to the high stiffness of such filament, it is difficult to estimate its persistence length with a WLC fit. As visible in figure 5, the mechanics of the filament doesn't obey the WLC theory. Interestingly, our ssDNA-VirE2 filaments of ~ 820 nm can be compressed without any buckling up to a force of about 3.5 pN (arrow in figure 5). Given that the critical force F_B for buckling reads: $F_B = 4\pi^2 A k_B T / L^2$ (44), a persistence length of ~14.5 μm was calculated in the case of ssDNA-VirE2 fragments, similar to that of F-actin (45). This length corresponds to a ssDNA molecule of about 21,000 bases. The VirE2:ssDNA shows even a mechanical behavior which allows to exert negative forces (i.e. pushing forces). Such mechanics has been observed on microtubules which allow pushing forces without buckling up to 10 pN.

Persistence length

We use a procedure similar to the one presented in (46). The persistence length A of a protein helix with pitch P, Young modulus E, moment of inertia I and inclination angle α reads:

$$\frac{A}{k_B T} = \frac{\pi P E I}{\left[(2\pi R)^2 + P^2\right]^{0.5}} \left(2(2+\sigma)\cos\alpha + 2\sin\alpha\right)^{-1}$$

For a cylinder with radius r, I is equal to $\pi r^4/4$. From (47), we have P = 5.15 nm, I =17.6 nm^4, R = 5.7 nm and α = 9.1 degrees. Using typical values of E = 3.4x10^3 pN·nm $^{-2}$ (46,47) and σ = 0.5 for a protein, we find A = 1250 nm.

Stretch modulus

Similarly, the stretch modulus S of the protein helix can be obtained using:

$$S = \frac{PEI}{R^2\left[(2\pi R)^2 + P^2\right]^{0.5}}\left(\sin^2\alpha + (1+\sigma)\cos^2\alpha\right)^{-1}$$

For VirE2 filaments we found S = 180 pN,

The procedure we use here represents only a lower estimate of both A and S. First, interactions in between proteins and the DNA template are not taken into account. Second, HR-TEM observations (13) have evidenced for axial interactions (neglected in the present model) in between adjacent protein turns that can considerably stiffen up the mechanical arrangement of the complex.

3.5 Conclusion

3.5.1 Biological relevance of the findings of the tweezers

In the optical tweezers setup, the time scale of an experiment is in minutes as compared to the overnight incubation time of the electron microscopy work. The optical tweezers showed that the kinetics of binding is extremely fast; what might be needed to protect the naked, linear ssDNA from nucleases as it enters the eukaryotic cell. Without protein covering, linear ssDNA is degraded 10 to 20 fold faster than circular ssDNA or dsDNA, pointing to exonucleases as the main processing activities responsible for degradation of exogenous DNA (29). In this same study, the presence of VirD2 and /or VirE2 on the ssDNA was shown to protect the ssDNA and allow integration of preserved, complete T-DNA. Indeed, upon cell entry, the VirD2 protein protects the 5' end from exonuclease activity, and as the ssDNA exits its entry port into the eukaryotic cell and is free for interaction, the VirE2 proteins would coat and protect it. As there is only a limited number of incoming T-DNA, it has to be noted that there is an excess of VirE2, even if the VirE2 level needed in plants is low (48). The concentration of VirE2 in the plant is not known, but transgenic plants expressing VirE2 can complement VirE2 deficient *Agrobacterium*, even if the level of VirE2

protein produced by the plant is not detectable by Western. The lower the VirE2 concentration, the less nucleating points, the more regular is the complex, but the waiting time until protection of the ssDNA is achieved is also longer.

3.5.2 Transport through cytosol

Moreover, to move in the crowded cytoplasm, a more flexible structure might be more likely to move than a rigid structure. A 7249 bases T-DNA coated with VirE2 is 425 nm long with a diameter of ~16 nm, to be compared with the size of a plant cell (about 100 µm in length). The complex should is able to enter the nucleus through the nuclear pore complex as recent structural data show that the nuclear pore complex can translocate cargos with a diameter of up to 35-40 nm in a nuclear localization signal dependant, receptor mediated manner (49). So, there is no need for elongation of the telephone-cord structure, the VirE2-ssDNA complex will be able to pass even if it is further decorated by the factors involved in nuclear import such as VIP1 and karyophilin alpha. Indeed, this means that the stiff final state of the complex that could be measured can pass as such through the nuclear pore complex.

Our model that identifies VirE2 as the key factor for pulling T-DNA into the plant cytoplasm relies on the following assumptions: (i) VirE2 does not bind ssDNA in *Agrobacterium* (ii) the presence of VirE2 proteins in the plant cell. This is in agreement with the findings of Cascales and Christie (35) (who have shown that *Agrobacterium* separately exports the VirD2-T-strand and VirE2 proteins and that VirE2 binds T-DNA in the plant cytosol) as well as the observations of Citovsky *et al.* (50) (who have found that transgenic plants expressing VirE2 allow successful transfection of *VirE2*-null-*Agrobacterium* T-DNA). T-DNA-VirD2 is exported from *Agrobacterium* to the plant cell membrane through the Type IV secretion. Such secretion system cannot however account for the transfer of a long ssDNA piece as the recognition signal is located on VirD2 (51). Once the T-DNA-VirD2 complex enters the plant cell, a VirE2 protein binds non-specifically to the T-DNA and catalyses the subsequent binding of additional VirE2 proteins. Because the stable conformation of VirE2-DNA consists in a compact helical structure, binding of VirE2 will actively pull T-DNA in the plant cytosol (Fig. 7). The generation of forces without the need for external energy sources might be a more general mechanism in nature when nucleic acids are trans-located across membranes of different

compartments (say A and B) and the importing compartment (B) contains proteins that compact nucleic acids.

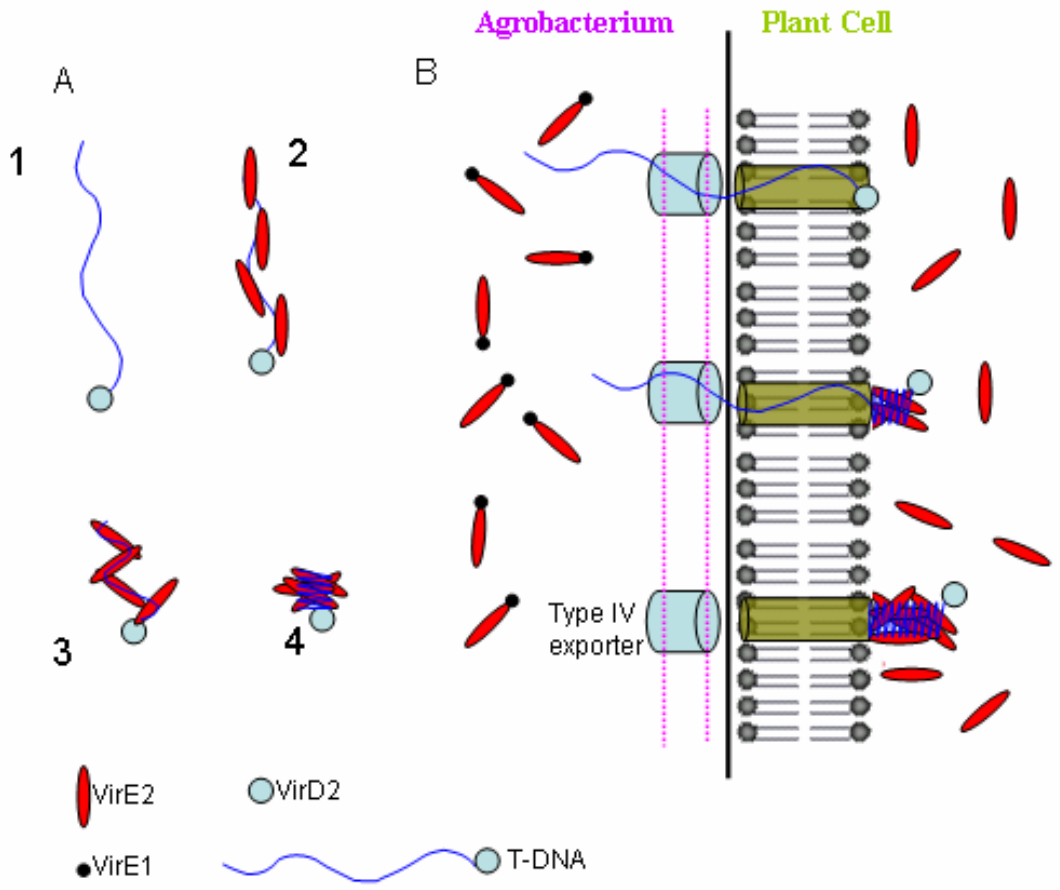

Figure 7. *A simple model explaining the generation of forces on ssDNA upon VirE2 binding. Left panel (A): A VirE2-VirE1 protein doesn't bind to ssDNA in the Agrobacterium [1] but favors rapid and subsequent cooperative binding of additional proteins in plant cell cytoplasm as presence of VirE2 alone [2]. Because, the stable and energy minimal conformation of VirE2 molecules bound to ssDNA consists in a compacted helicoidal structure (13) [3-4], the re-arrangement of protein monomers gives rise to a force that can allow pulling of DNA. In this model, the gain in free energy upon VirE2 binding to ssDNA is solely responsible for the generation of a force. Right panel (B): VirE2 does not interact with ssDNA in Agrobacterium with complex formation with VirE1 and uncoated VirD2-TDNA filaments are trans-located through a Type 4 secretion system. Note that the fast coating of DNA by VirE2 allows an efficient protection of the T-DNA from exonucleases upon entry in the plant cytoplasm.*

3.6 References

1. Chilton, M.D., Drummond, M.H., Merio, D.J., Sciaky, D., Montoya, A.L., Gordon, M.P. and Nester, E.W. (1977) Stable incorporation of plasmid DNA into higher plant cells: the molecular basis of crown gall tumorigenesis. *Cell*, **11**, 263-271.
2. Tzfira, T.a.C., V. (2000) From host recognition to T-DNA integration: the function of bacterial and plant genes in the Agrobacterium-plant cell interaction Mol. Plant Pathol., **1**, 201-212.
3. Gelvin, S.B. (2003) Agrobacterium-mediated plant transformation: the biology behind the "gene-jockeying" tool. *Microbiol. Mol. Biol. Rev.*, **67**, 16-37.
4. Tzfira, T., Li, J., Lacroix, B. and Citovsky, V. (2004) Agrobacterium T-DNA integration: molecules and models. *Trends. Genet.*, **20**, 375-383.
5. Durrenberger, F., Crameri, A., Hohn, B. and Koukolikova-Nicola, Z. (1989) Covalently bound VirD2 protein of Agrobacterium tumefaciens protects the T-DNA from exonucleolytic degradation. *Proc. Nat. Acad. Sci. U S A*, **86**, 9154-9158.
6. Herrera-Estrella, A., Chen, Z.M., Van Montagu, M. and K., W. (1988) VirD proteins of Agrobacterium tumefaciens are required for the formation of a covalent DNA-protein complex at the 5' terminus of T-strand molecules. *EMBO J.*, **7**, 4055-4062.
7. Ward, E.R. and Barnes, W.M. (1988) VirD2 protein of Agrobacterium tumefaciens very tightly linked to the 5' end of T-strand DNA. *Science*, **242**, 927-930.
8. Young, C. and Nester, E.W. (1988) Association of the virD2 protein with the 5' end of T strands in Agrobacterium tumefaciens. *J. Bacteriol.*, **170**, 3367-3374.
9. de la Cruz, F. and Lanka, E. (1998) Function of the Ti-plasmid Vir proteins: T-complex formation and transfer to the plant cell. *In H. Spaink, P. Hooykaas, and A. Kondorosi (ed.), The Rhizobiaceae. Kluwer Academic Publishers, Dordrecht, The Netherlands.*, 281-301.
10. Llosa, M., Gomis-Ruth, F.X., Coll, M. and de la Cruz Fd, F. (2002) Bacterial conjugation: a two-step mechanism for DNA transport. *Mol. Microbiol.*, **45**, 1-8.
11. Gietl, C., Koukolikova-Nicola, Z. and Hohn, B. (1987) Mobilization of T-DNA from Agrobacterium to plant cells involves a protein that binds single-stranded DNA. *Proc. Nat. Acad. Sci. U S A*, **84**, 9006-9010.
12. Citovsky, V., Wong, M.L. and Zambryski, P. (1989) Cooperative interaction of Agrobacterium VirE2 protein with single- stranded DNA: implications for the T-DNA transfer process. *Proc. Nat. Acad. Sci. U S A*, **86**, 1193-1197.
13. Abu-Arish, A., Frenkiel-Krispin, D., Fricke, T., Tzfira, T., Citovsky, V., Wolf, S.G. and Elbaum, M. (2004) Three-dimensional reconstruction of Agrobacterium VirE2 protein with single-stranded DNA. *J. Biol. Chem.*, **279**, 25359-25363.
14. Citovsky, V., Guralnick, B., Simon, M.N. and Wall, J.S. (1997) The molecular structure of agrobacterium VirE2-single stranded DNA complexes involved in nuclear import. *J. Mol. Biol.*, **271**, 718-727.

15. Tzfira, T., Vaidya, M. and Citovsky, V. (2001) VIP1, an Arabidopsis protein that interacts with Agrobacterium VirE2, is involved in VirE2 nuclear import and Agrobacterium infectivity. *EMBO J.*, **20**, 3596-3607.
16. Citovsky, V., Kapelnikov, A., Oliel, S., Zakai, N., Rojas, M.R., Gilbertson, R.L., Tzfira, T. and Loyter, A. (2004) Protein interactions involved in nuclear import of the Agrobacterium VirE2 protein in vivo and in vitro. *J. Biol.Chem.*, **279**, 29528-29533.
17. Tzfira, T., Vaidya, M. and Citovsky, V. (2004) Involvement of targeted proteolysis in plant genetic transformation by Agrobacterium. *Nature*, **431**, 87-92.
18. Chilton, M.D. and Que, Q. (2003) Targeted integration of T-DNA into the tobacco genome at double-stranded breaks: new insights on the mechanism of T-DNA integration. *Plant Physiol.*, **133**, 956-965.
19. Tzfira, T., Frankman, L.R., Vaidya, M. and Citovsky, V. (2003) Site-specific integration of Agrobacterium tumefaciens T-DNA via double-stranded intermediates. *Plant Physiol.*, **133**, 1011-1023.
20. de Cleene, M.a.d.L., J. (1976) *Bot Rev*, **42**, 389-466.
21. Ishida, Y., Saito, H., Ohta, S., Hiei, Y., Komari, T. and Kumashiro, T. (1996) High efficiency transformation of maize (Zea mays L.) mediated by Agrobacterium tumefaciens. *Nat. Biotechnol.*, **14**, 745-750.
22. Piers, K.L., Heath, J.D., Liang, X., Stephens, K.M. and Nester, E.W. (1996) Agrobacterium tumefaciens-mediated transformation of yeast. *Proc. Natl. Acad. Sci. U S A*, **93**, 1613-1618.
23. de Groot, M.J., Bundock, P., Hooykaas, P.J. and Beijersbergen, A.G. (1998) Agrobacterium tumefaciens-mediated transformation of filamentous fungi. *Nat. Biotechnol.*, **16**, 839-842.
24. Gouka, R.J., Gerk, C., Hooykaas, P.J., Bundock, P., Musters, W., Verrips, C.T. and de Groot, M.J. (1999) Transformation of Aspergillus awamori by Agrobacterium tumefaciens-mediated homologous recombination. *Nat. Biotechnol.*, **17**, 598-601.
25. Kunik, T., Tzfira, T., Kapulnik, Y., Gafni, Y., Dingwall, C. and Citovsky, V. (2001) Genetic transformation of HeLa cells by Agrobacterium. *Proc. Nat. Acad. Sci. U S A*, **98**, 1871-1876.
26. Tzfira, T. and Citovsky, V. (2003) The Agrobacterium-plant cell interaction. Taking biology lessons from a bug. *Plant Physiol.*, **133**, 943-947.
27. Frary, A. and Hamilton, C.M. (2001) Efficiency and stability of high molecular weight DNA transformation: an analysis in tomato. *Transgenic Res.*, **10**, 121-132.
28. Hamilton, C.M., Frary, A., Lewis, C. and Tanksley, S.D. (1996) Stable transfer of intact high molecular weight DNA into plant chromosomes. *Proc. Nat. Acad. Sci. U S A*, **93**, 9975-9979.
29. Pelczar, P., Kalck, V., Gomez, D. and Hohn, B. (2004) Agrobacterium proteins VirD2 and VirE2 mediate precise integration of synthetic T-DNA complexes in mammalian cells. *EMBO Rep.*, **5**, 632-637.
30. Ward, D.V. and Zambryski, P.C. (2001) The six functions of Agrobacterium VirE2. *Proc. Natl. Acad. Sci. U S A*, **98**, 385-386.
31. Husale, S., Grange, W. and Hegner, M. (2002) DNA mechanics affected by small DNA interacting ligands. *Single Mol.*, **3**, 91-96.
32. Hegner, M. (2000) DNA Handles for Single Molecule Experiments. *Single Mol.*, **1**, 139-144.

33. Dumas, F., Duckely, M., Pelczar, P., Van Gelder, P. and Hohn, B. (2001) An Agrobacterium VirE2 channel for transferred-DNA transport into plant cells. *Proc. Nat. Acad. Sci. U S A*, **98**, 485-490.
34. Grange, W., Husale, S., Güntherodt, H.-J. and Hegner, M. (2002) Optical tweezers system measuring the change in light momentum flux. *Rev. Sci. Instr.*, **73**, 2308-2316.
35. Cascales, E. and Christie, P.J. (2004) Definition of a bacterial type IV secretion pathway for a DNA substrate. *Science*, **304**, 1170-1173.
36. Cantor, C.R. and Schimmel, P.R. (1980) Biophysical Chemistry I(ISBN: 0716711907). **III**.
37. Wuite, G.J.L., Smith, S.B., Young, M., Keller, D. and Bustamante, C. (2000) Single-molecule studies of the effect of template tension on T7 DNA polymerase activity. *Nature*, **404**, 103-106.
38. Goel, A., Frank-Kamenetskii, M.D., Ellenberger, T. and Herschbach, D. (2001) Tuning DNA "strings":Modulating the rate of DNA replication with mechanical tension. *Proc. Natl. Acad. Sci. U.S.A*, **98**, 8485-8489.
39. Asmahan, A.-A., Frenkiel-Krispin, D., Fricke, T., Tzfira, T., Citovsky, V., Grayer Wolf, S. and M., E. (2004) *J. Bio. Chem.*, **279**, 25359-25363.
40. Rief, M., Gautel, M., Oesterhelt, F., Fernandez, J.M. and Gaub, H.E. (1997) *Science*, **276**, 1109-1112.
41. Cui, Y. and Bustamante, C. (2000) Pulling a single chromatin fiber reveals the forces that maintain its higher-order structure. *Proc. Nat. Acad. Sci. U S A*, **97**, 127-132.
42. Brower-Toland, D., Smithdagger, C.L., Yeh, R.C., Lis, J.T., Peterson, C.L. and Wang, M.D. (2002) From the Cover: Mechanical disruption of individual nucleosomes reveals a reversible multistage release of DNA. *Proc. Natl. Acad. Sci. USA*, **99**, 1960-1965.
43. Christie, P.J., Ward, J.E., Winans, S.C. and Nester, E.W. (1988) The Agrobacterium tumefaciens virE2 gene product is a single-stranded-DNA-binding protein that associates with T-DNA. *J. Bacteriol.*, **170**, 2659-2667.
44. Manning, G.S. (1986) Correlation of polymer persistence length with Euler buckling fluctuations. *Phys. Rev. A*, **34**, 4467-4468.
45. Liu, X. and Pollack, G.H. (2002) Mechanics of F-actin characterized with microfabricated cantilevers. *Biophys. J.*, **83**, 2705-2715.
46. Hegner, M., Smith, S.B. and Bustamante, C. (1999) Polymerization and mechanical properties of single RecA-DNA filaments. *Proc. Natl. Acad. Sci. USA*, **96**, 10109-10114.
47. Mickey, B. and Howard, J. (1995) Rigidity of microtubules is increased by stabilizing agents. *J. Cell Biol.*, **130**, 909-917.
48. Jacob, S. and Hohn, B. personnal communication.
49. Panté, N. and Kann, M. (2002) Nuclear Pore Complex Is Able to Transport Macromolecules with Diameters of ~39 nm. *Mol. Biol. Cell*, **13**, 425-434.
50. Citovsky, V., Zupan, J., Warnick, D. and Zambryski, P. (1992) Nuclear localization of Agrobacterium VirE2 protein in plant cells. *Science*, **256**, 1802-1805.
51. Vergunst, A.C., Lier, M.C.M.v., Dulk-Ras, A.d., Stüve, T.A.G., Ouwehand, A. and Hooykaas, P.J.J. (2005) Positive charge is an important feature of the C-terminal transport signal of the VirB/D4-translocated proteins of Agrobacterium. *Proc. Natl. Acad. Sci. U.S.A*, **102**, 832-837.

4. Single-molecule studies of dsDNA denaturation induced by NaOH and force–mechanical pulling

4.1 Abstract

Single molecule techniques such as the optical tweezers give access to the 'melting' of hydrogen bonds by mechanical forces or alkali denaturation (NaOH) of double stranded DNA in real time. Various feedback experiments allow to extract the rate (bp/sec) at which melting of hydrogen bonds occur and show that denaturation of dsDNA molecules follows a first order transition. ssDNA exhibits different mechanical conformations when immersed in NaOH or NaCl. Force extension experiments reveal the difference in free energy for ssDNA in these salt environments. The mechanical stability and the transition of dsDNA to ssDNA was investigated at different ionic strength. Fluorescent images of single λ DNA molecules labeled with SYBR® Green were observed at forces ≥ 65 pN and indicate a S –DNA transition.

4.2 Introduction

Denaturation or dehybridization of DNA is the process in which strands of DNA melt to form two separate strands. DNA can be denatured by either heat, alkali (e.g. NaOH) or formamide. Thermal denaturation of DNA is achieved by increasing the temperature to its melting temperature (depending on nucleic acid composition and / length). Thermal energy disrupts hydrogen bonds and other interactions, alters the hydration shell, leading to variations in base stacking. NaOH denatures DNA and RNA by breaking hydrogen bonds in–between base pairs. High pH deprotonizes groups on nucleic acid bases that are involved in base pairing, thus eliminating or altering H-bonding and alters the hydration of DNA which affects the base stacking.

The denaturation of dsDNA is subject of study since four decades in statistical physics. Most efforts devoted to establish a solid theory for thermal denaturation of DNA. A theoretical model of DNA denaturation was first introduced by Poland and Scheraga (1). This model showed a continuous phase transition in both two and three dimensions. But it was in conflict with the experiments performed by UV spectrometry (2). Such temperature induced DNA melting experiments showed sharp

jumps in the UV spectra's which corresponded to a sudden breaking of large numbers of base pairs and therefore was described as a first order phase transition.
On the basis of polymer networks theory, Kafri *et al.* extended the classical Poland-Scheraga (PS) model and predicted that DNA denaturation obeys a first order transition (3). Compared to real DNA data, approximations of this model were in debate and were recommended experiments at single molecule level (4,5). Carlon *et al.* defined a model taking the different binding energies of base pairs and stiffness into account (6). They showed that model exhibits a first order phase transition whereas experimental evidence or simulation melting curves of known DNA sequences are missing to verify with their model.

DNA thermal denaturation has been studied by UV absorption, circular dichroism, differential scanning calorimetry, temperature gradient gel electrophoresis, fluorescence emission and nuclear magnetic resonance (7). Whereas little work focused on the denaturation of DNA by pH shifts (e.g. NaOH). Accurate prediction of DNA denaturation or melting curves is important for several molecular biological techniques such as primer design, DNA control during PCR, mutation analysis (8,9), Southern blotting (10) and sequencing by hybridization (11).

In earlier experiments UV–light absorption studies were used to observe the melting curves of DNA molecules containing specific length and sequence. On the basis of sharp jumps in the thermal melting curves it was reported that the transition from bound to unbound is first order. Here we studied dsDNA strand separation by NaOH exposure with the help of optical tweezers and also observed a first order transition.
First, Smith *et al.* were able to use optical tweezers to study the elasticity of single DNA molecules at high forces (12). The main observation of these experiments was an overstretching transition of dsDNA at forces ~65 pN and requiring only ~ 2pN to undergo an elongation of 1.7 times its contour length. It has been experimentally shown that the two strands do not separate at the end of overstretching transition (13,14), and forces ~150 pN were needed to detach the one strand. Molecular dynamics simulations predicted that dsDNA remains in double stranded form (15-18) during this transition. Rouzina *et al.* and Williams *et al.* reported that these studies were unable to reproduce the experimental data and described a new model indicating

that the overstretching transition of dsDNA underlies a force induced melting transition (19-21). Our experiments provide new insights and verify the conformational changes during the overstretching transition of dsDNA.

We report the rate of alkaline melting of hydrogen bonds (bp/sec) of dsDNA in real time. Subsequently we monitored the mechanical changes during exchange of NaOH to NaCl which shows a sigmoidal curve indicating a highly cooperative nature. This paper is divided in three parts, the first part describes the denaturation kinetics of dsDNA in presence of NaOH. The conformation of ssDNA in two different salt environments is discussed in the second part. And in the third part, we revisit the denaturation of dsDNA by mechanical pulling and provide additional information on the overstreching behavior of DNA.

4.3 Materials and methods

DNA preparation: We used a 5623 bp DNA segment of the plasmid pTYB1 (New England Biolabs), which was PCR amplified. Forward (thiol modification at the 5 prime end) and reverse primer were ordered from Microsynth (Balgach). 5623 base pair fragments were amplified using the expand long template PCR protocol from Roche utilizing a unique blend of Tag and PWO polymerases. Finally the 3' overhangs generated by Hind III digestion were filled in with biotinalyted nucleotide using Klenow exo$^-$ DNA polymerase.

The thiol modified dsDNA was coupled to amino modified polystyrene beads with the help of a bifunctional cross linker (22). After the coupling, DNA–beads were stored in a buffer containing 150 mM NaCl, 10 mM Hepes pH 7.5, 1 mM EDTA and 1 mM NaN_3 (chamber buffer).

For fluorescent imaging of DNA, we used λ DNA. The 5' overhangs of λ DNA (48502 bp) were biotinylated with Klenow exo$^-$ enzyme and subsequently linked to two individual streptavidin spheres as discussed in (12,22).

Measurement of force extension curves

We used a dual laser beam system to trap DNA modified polystyrene beads inside a fluid chamber ~100 μm away from the chamber walls. The biotinylated end of the DNA was ‘fished’ by streptavidin bead which was previously sucked on a

micropipette. The force acting on the bead was calibrated by force versus displacement measurements, viscous drag method as well as by recording the corner frequency of the power spectral density as reported previously (23). Any movement of the trapped bead is changing the light momentum flux and is directly recorded as a force acting on the sphere. The distance in between two beads was measured by the CCD camera. The position of the trapped bead was also detected on photodetector with the help of a laser of different wavelength. Movement of the pipette away from the trap (stretching of the molecule) or towards the trap (relaxing) can be determined with ~2 nm accuracy by using a feedback compensated piezoelectric translation stage (517.3 CL, Physik Instruments, Germany), operated with a LabVIEW software. During stretching experiments the pipette was moved in 20 nm steps, after each step the force was measured 100 times and averaged.

DNA imaging by OT combined with confocal fluorescence spectroscopy:

Images of λ DNA labeled with SYBR® Green (10000x dilution), were obtained by an electron multiplying CCD camera (IXON, Andor, 512x512 pixels), SYBR® Green has its excitation maximum at 498 nm and emission maximum at 522 nm. We used 488 nm Argon-ion laser (Spectra Physics, CA) to excite SYBR® Green molecules which binds to the grooves of dsDNA (24). It binds to dsDNA as well as ssDNA. Image acquisition time used was 0.16 sec.

4.4 Results

4.4.1 Kinetics of dsDNA denaturation with NaOH

To study the structural transitions of dsDNA to ssDNA in presence of NaOH, we carried out different constant distance or force feedback experiments. A schematic of a distance feedback experiment is shown in fig.1. We kept the distance ‘D’ in between two beads (length of DNA) constant throughout the experiment. Then we monitored all the changes in force only.

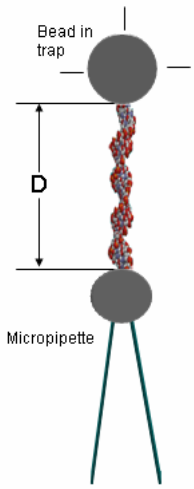

Figure 1. *Schematic of constant distance feedback experiment. Where D is the elongation of the molecule.*

The mechanics of individual ds and ssDNA molecules has been investigated in great detail (12). In figure 2, the mechanics of naked dsDNA (black squares) and ssDNA (blue) in chamber buffer @ 150 mM NaCl is shown. The force versus extension curve of the same ssDNA in 150 mM NaOH is indicated in red circles. NaOH is dehybridizing dsDNA and converting to ssDNA.

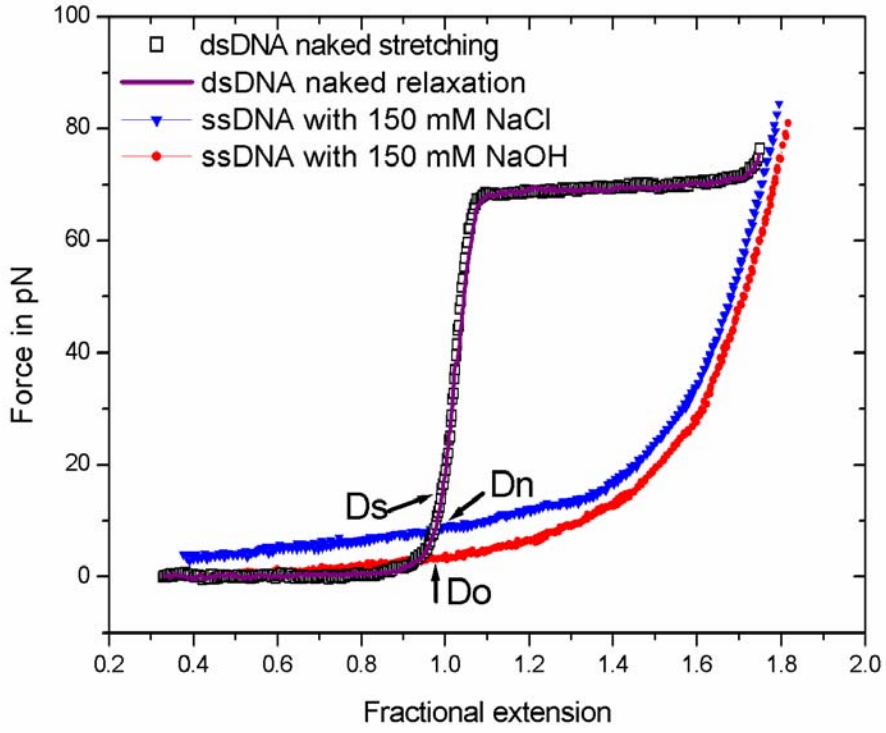

Figure 2. *The black curve shows the stretching of dsDNA, the red curve shows the*

stretching of ssDNA in presence of 150 mM NaOH, and the blue curve shows the stretching of ssDNA in 150 mM NaCl.

The denatured ssDNA seems to relax in the basic environment and exhibits minimum forces during pulling which are close to the forces measured in dsDNA. It indicates that the ssDNA in NaOH environment is not able to form hairpins and that the entropic forces are greatly reduced. The position shown by the arrows Ds, Dn and Do represents the values of force observed in the distance feedback experiment at fractional extension of ~1. Ds depicting the force on dsDNA, which dropped to force Do due to the formation of ssDNA in NaOH. Dn represents the force raised again due to the exchange of NaOH by NaCl.

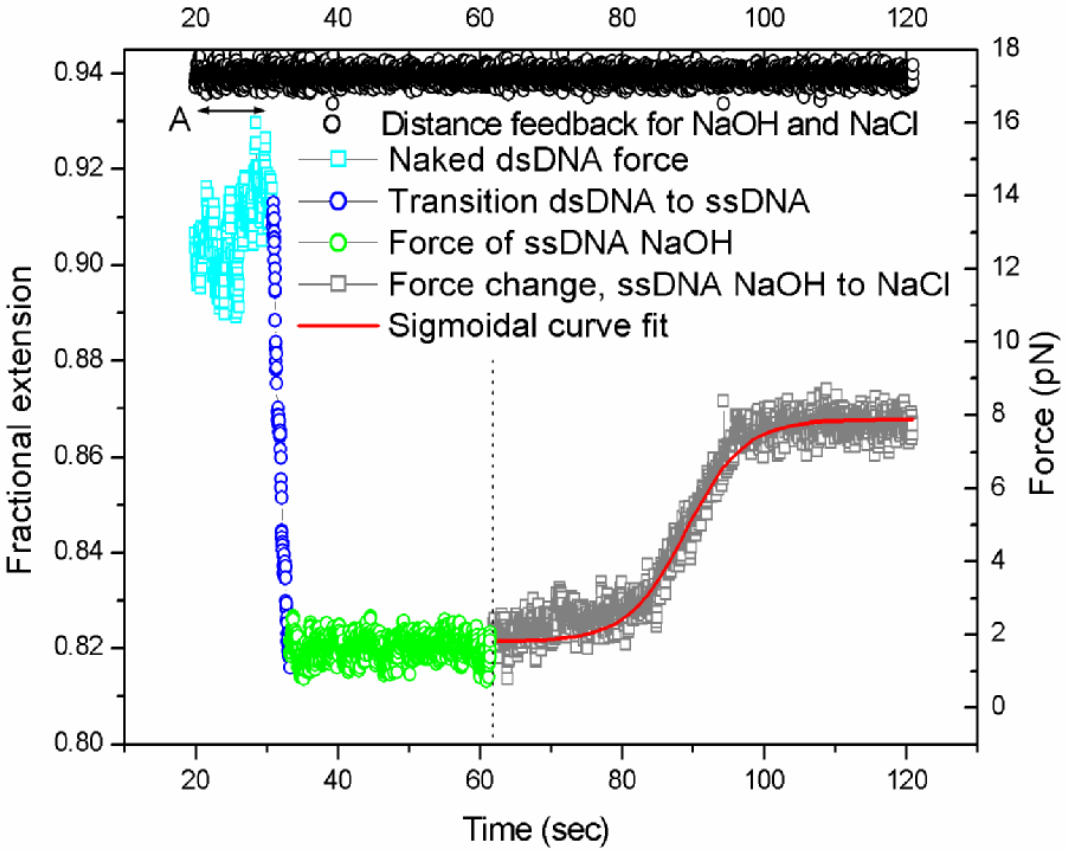

Figure 3. *Curve with cyan squares shows the changes in force on naked dsDNA, ssDNA in presence of 150mM NaOH (green circles) and 150 mM NaCl (gray squares). Red line curve shows sigmoidal fit of force change due to the replacement of NaOH by NaCl.*

In figure 3 the left side separated by the dotted line shows the transition of dsDNA to ssDNA due to the effect of breaking of H bonds by NaOH while right part shows the conformational changes of the ssDNA by exchanging NaOH by NaCl (using the same flow speed during injection). Black circles show the distance feedback. Region 'A'

shows the force (cyan squares) on the double stranded DNA. A drop in force (blue circles) indicates the start of breaking of H bonds of DNA and therefore the denaturation or dehybridization of dsDNA. After ~30 sec. the NaOH reduces the force on dsDNA and we observe a discontinuity in the recorded force (blue). The sharp changes in force (i.e. decrease in force) can be attributed to the generic features of a first order transition. The dsDNA contains 5623 bp and the breakage of all the hydrogen bonds (i.e. dsDNA to ssDNA conversion) took a total ~2 sec.→ ~ 2800 bp/sec indicating the change in force from ~ 14 pN to 2 pN due to the presence of 150 mM NaoH. The transition is occurring in multi step like denaturation which could be attributed to AT rich sequences. This conversion rate depended on the concentration of NaOH. At concentration 50 mM, we observed a dsDNA to ssDNA conversion rate of 375 bp/sec (data not shown). The region highlighted in green indicates the stable conformation of ssDNA in NaOH. After the conversion to ssDNA the force stabilized at ~ 2 pN in presence of NaOH. During the replacement of the surrounding buffer from 150 mM NaOH to 150 mM NaCl a mechanical change is detected. This transition (indicated in gray) can be fitted with a sigmoidal curve following the equation 1.

$$F = \left(FS_{OH} - FS_{Cl}\right) \Big/ \left[1 + e^{(t-t_0)/dt}\right] + FS_{cl} \qquad [1]$$

where FS_{OH} is the force on ssDNA in NaOH, FS_{Cl} force on ssDNA in NaCl, t is the time in seconds, t_0 is the mid point of the conformational transition and dt is the time constant or slope factor which is given by $F' = \left(FS_{OH} - FS_{Cl}\right) \Big/ 4\,dt$.

After the complete exchange, the ssDNA reaches a stable conformation in the presence of NaCl.

4.4.2 Force clamped experiments

In these experiments we investigate the melting transition by keeping the forces at constant value. As visible from figure 2 depending on where we place the force setpoint the final ssDNA length can be shorter or longer than the initial dsDNA length.

Fig. 4 shows the increase in elongation of dsDNA held at a constant force of 18 pN which then indicates the transition upon NaOH of dsDNA to ssDNA. Point P

indicates the start of the denaturation of dsDNA while Q shows end of the transition from dsDNA to ssDNA induced by 150 mM NaOH. The arrow shows individual jumps or fast increases in distance during the transition. We attribute this breaking of hydrogen bonds to AT rich stretches at single molecule level which denaturate more rapidly and comparable to the steps observed in the length clamp experiments. Previously this phenomenon was observed by measuring the UV absorption rate in DNA melting experiments which corresponded to a sudden breaking of large number of base pairs indicating also a first order transition (2).

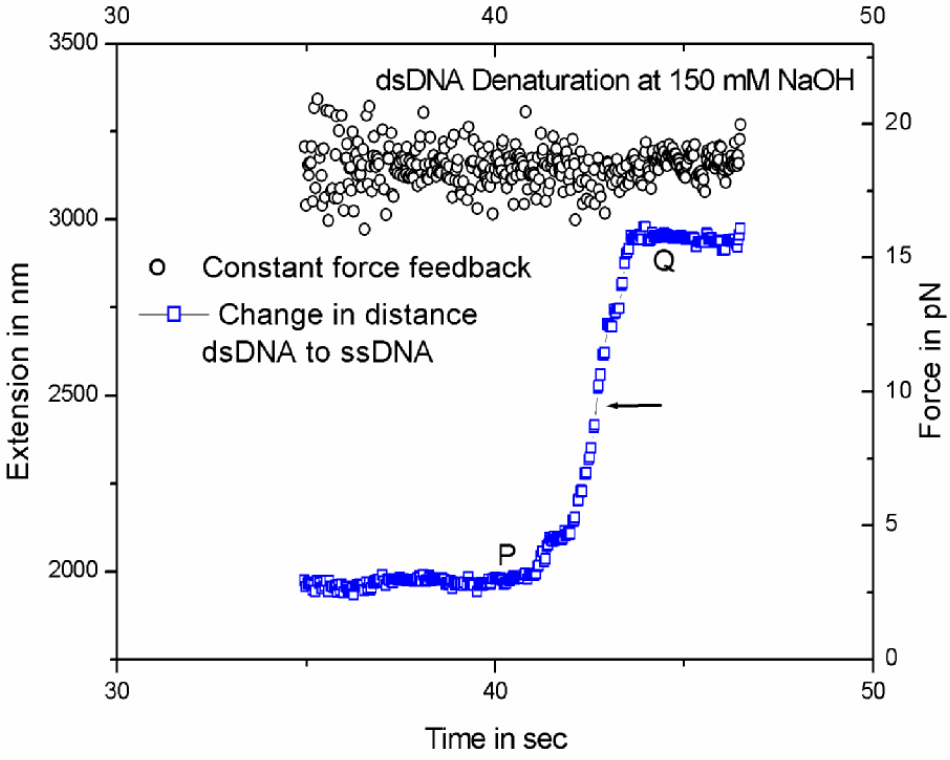

Figure 4. *Black circles show the clamping force of the molecule. The curve with blue square shows the changes in elongation of the DNA molecule. P indicates the start of the elongation of dsDNA due to ssDNA conversion while Q shows the final elongation of ssDNA at constant force of 18 pN.*

We observed real time decrease in force due to the change in phase of dsDNA at force~14 pN. The spontaneous increase in length at certain force (F_{tr}) or increase in force at certain distance corresponds to the increase in free energy of the molecule (25).

$$G(x_3) = G(x_1) + \int_{x_1}^{x_2} F\,dx + F_{tr} \bullet (x_3 - x_2) \qquad [2]$$

4.4.3 Kinetics of dsDNA denaturation by mechanical pulling

The transition of dsDNA to ssDNA can also be induced by the mechanical pulling of dsDNA to high force (~150 pN) at 150mM concentration of salt. As in the previously discussed experiments the dsDNA molecules have to be anchored through one strand (i.e. from the 5' to the 3' end) to the interfaces of the polystyrene spheres. No single stranded breaks are allowed and best quality of dsDNA was achieved by amplifying the long dsDNA by PCR reactions. When such molecules are subjected to external forces, a transition from dsDNA to ssDNA (denaturation) can take place as indicated by an arrow in figure 5. This arrow indicates the transition point where one strand of dsDNA gets completely separated from the double helix. We observed that this transition point was sensitive to ionic conditions during pulling and decreased with decreasing concentration of salt. A single strand will get separated only when the free energy of the ssDNA will be less than the initial energies in the dsDNA (26). The black curve in fig.5 shows the stretching and denaturation of dsDNA in 60 mM salt and black arrow shows the transition of dsDNA to ssDNA under these conditions at a force of ~120 pN.

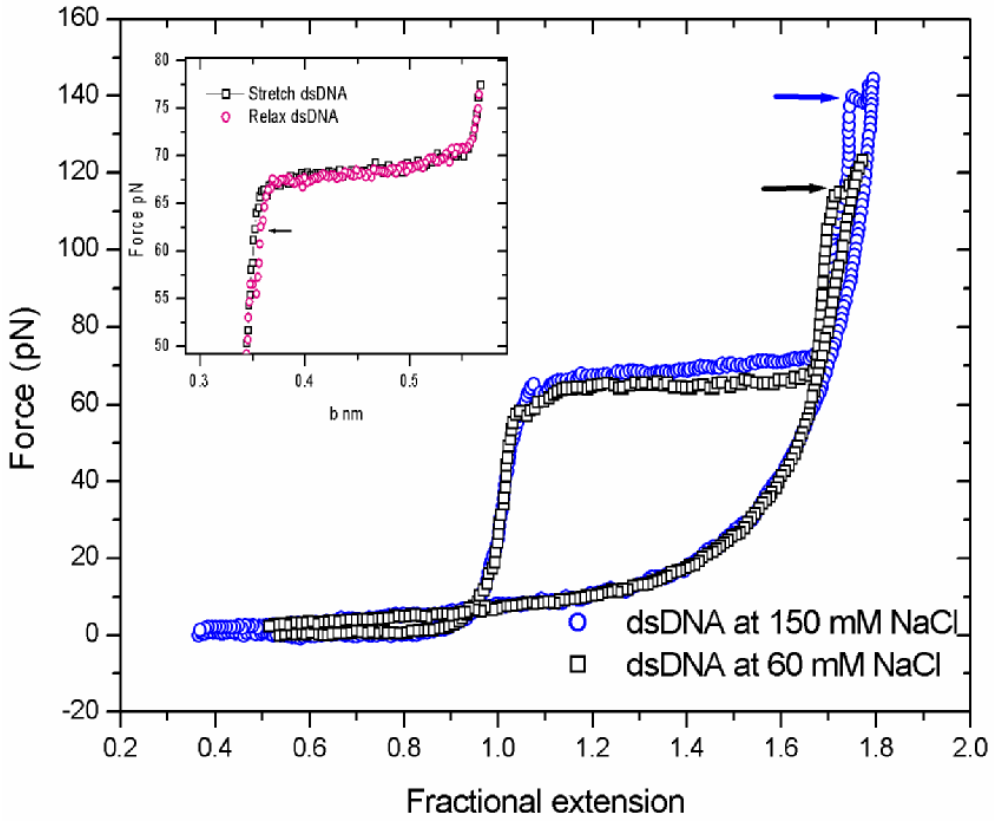

Figure 5. *The denaturation of dsDNA by mechanical pulling. Blue circles show the stretching of dsDNA to ssDNA in 150 mM NaCl. Black squares represent the curve of*

dsDNA to ssDNA at 60 mM NaCl. The arrow in blue and black indicate the melting and detachment of one strand into the solution, i.e. breaking all base pairs and holding of one strand only, indicates the structural transition from dsDNA to ssDNA. The inset displays the pulling and relaxation of dsDNA to ~78 pN which doesn't induce melting. No hysteresis during relaxation is observed.

The inset of fig.5 shows the tethering of dsDNA at 150 mM, NaCl. The force versus extension during the stretching path (black squares) and relaxation (pink circles) of the molecule are shown. The horizontal black arrow indicates that only minimal hysteresis was observed during relaxation. This small hysteresis could be due to the stretching of double helix to forces higher than the overstretching force, eventually inducing S–DNA (skew ladder) which needs time to rearrange or it represents the mechanical fraying of the ends of the dsDNA only which rehybridize. Note that PCR generated dsDNA showed almost no hysteresis during relaxation whereas λ dsDNA revealed huge hysteresis during relaxation from overstretched dsDNA (data not shown). During the overstretching transition the extensible wormlike chain model is not valid and DNA shows a 70% increase in its contour length. The overstretching transition of DNA was experimentally and theoretically thought to unwind to form a unstacked parallel ladder-like structure (12,15). Our results of dsDNA transitions at high forces are consistent with the previous work reported by (13,14). We didn't observe any hysteresis during relaxation with shorter 1.9 μm DNA (i.e. 5623 bp), pulled up to ~ 80 pN, indicating S–form dsDNA.

Usually melting phenomenon in lower salt concentration (~55 mM) can be visualized with the stretching curves as shown in figure 6. The stretching curve of partial dsDNA along the direction ABC (black squares) indicates that the molecule investigated is composed of some double stranded DNA as well as ssDNA. Pulling of complete naked dsDNA shows a force plateau of a length of around 70% of its contour length during overstretching transition (purple line). In figure 6 we measure a shorter plateau (black squares) of about ~35 % of its naked dsDNA contour length only. This suggests that during extension was composed of 50 % of dsDNA as well as ssDNA. The blue curve visualizes the relaxation of the molecule (the path labeled by the letters CDEA). Form point C to D, we observe hysteresis which indicates that the melted base pairs needed time to rejoin themselves. Up to point D the relaxation curve

lied on the path of the partial dsDNA (~ 50 % dsDNA) but exhibits an additional abrupt increase in force of 26 pN from point D to E during relaxation of 351 nm lasting 112 ms. A 351 nm relaxation corresponded to 1034 base pairs of (~100 helical turns) dsDNA or 517 bases of ssDNA which we interpreted as the rejoining of base pairs.

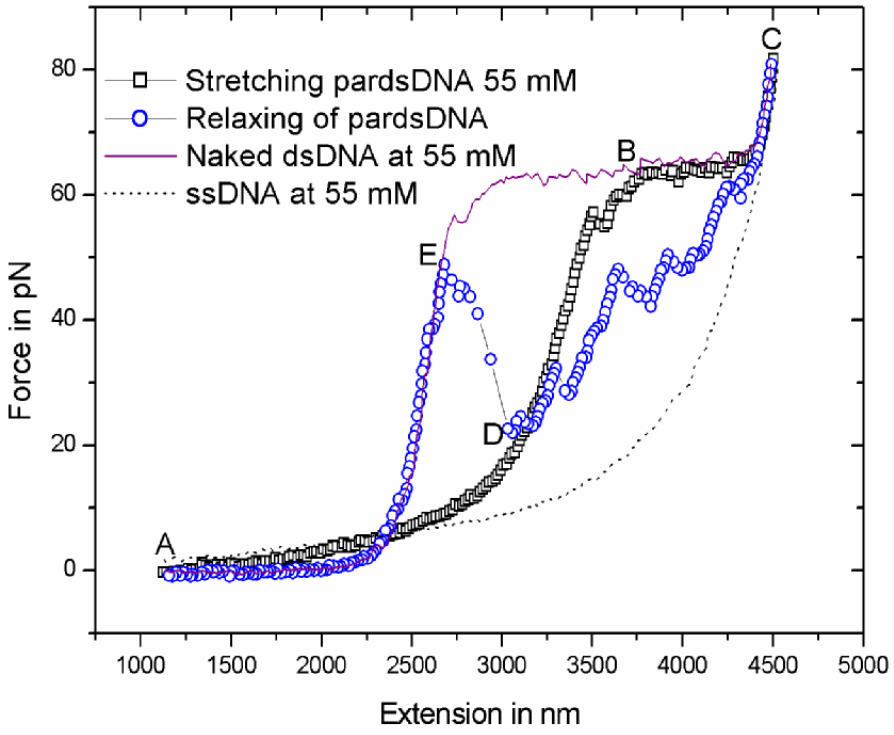

Figure 6. *Stretching of partial ssDNA in ~55 mM NaCl (black squares) while the relaxation of the molecule is shown by the curve with blue circles. During the first pull stretching cycle, the mechanics measured was like 'normal' dsDNA (purple line) but during the relaxing cycle the investigated molecule was converted to partial ssDNA form. Part of the melted ssDNA strand in the first pull could not completely rejoin or hybridize during relaxation. It might be hanging somewhere or recoiled unfavorable for cooperative rehybridization. During the second pull we observed again the partial mechanics of ssDNA during the overstretching transition. During the second relaxation cycle we observed a complete reanneling of base pairs at an external load of 48 pN. This two pulling cycles show that the molecule was melted during the overstretching transition and reanneled to form again a complete dsDNA. At an external force of 48 pN near to contour length, the molecule again wraps back*

to form a complete helical structure (B form). From point E to A we again observe the mechanics of naked form of dsDNA having same persistence length P and stretch modulus S as the starting dsDNA molecule of P = 50 nm and S = 1200 pN.

Here we assumed that some melting process started from the ends of our molecule. One strand is held in between two beads and a part of the other complementary strand was melted off due to overstretching of the dsDNA and was released into the solution. This part was unable to rehybridize during the first relaxation with partial dsDNA formed in the first pull. A subsequent second stretching allowed the molecule to fray back (almost a complete detachment of the second strand). Relaxing of the molecule reoriented melted strand and allowed rehybridization which is a reversible process and highly cooperative. Such melting was depending on the quality of DNA. A complete reannealing is only possible if the initial strands are nick free. Here we demonstrated by means of mechanical pulling or relaxing that one can change the conformation of the single DNA molecule.

The entropy change, ΔS, to convert ssDNA (partially) into dsDNA at any given force at stable temperature can be obtained from the areas under the experimental force – extension curves, that is:

$$T\Delta S(F) = n\left[\int_0^{x_{ss}(F)} F_{ss}\, dx - \int_0^{x_{ds}(F)} F_{ds}\, dx\right] \qquad [3]$$

where $F_{ds,ss}$ are the experimental forces required to extend the chains by an amount x, n adjacent sugar-phosphate units from single- to double-stranded geometry (27).

The re-formation of partial ssDNA to ds DNA is very difficult process if the strand is released into the solution. We observed the re-formation of the complete form of dsDNA from the partial ssDNA in a cooperative and fast manner indicating that the strand was not released completely into the solution. As visible in figure 6, < 10 % of the DNA molecule was in a dsDNA configuration but enabled complete reformation of dsDNA during relaxation. The entropy gain by partial removal of bonds, separating the melted domain, can be compensated by the binding energy upon ‘re-zipping’. We observed it as a transition from bound (dsDNA) to unbound (ssDNA) and then to the bound state again.

dsDNA started to melt as it was pulled through the overstretching transition. Our data at lower salt concentrations (~55 mM) is consistent with the force induced melting model described by Williams *et al*. (21) but in contrast to our data at physiological conditions (150 mM NaCl) which are not concordant with their findings. We observed, at low salt, that separation of parts of dsDNA was inducible in the force regime from 60 – 80 pN.

4.5 Discussion

4.5.1 ssDNA conformations

Our experimental approach allows to study the helix- to -coil change transformations, the effect of NaOH on base pairing, base pair stacking, electrostatic interactions and to probe different conformations of DNA molecules.

ssDNA, a linear chain of nucleotides with high flexibility, is more contractile than dsDNA at low forces. It can be stretched to a longer length at high force up to 60 pN because it has no helix form. Pulling of ssDNA- 150 mM NaCl from 10 pN up to 80 pN shows a stretching of 0.36 nm/bp to 0.59 nm/bp (sugar phosphate pucker) whereas ssDNA- in 150 mM NaOH shows 0.44 and 0.60 nm/bp respectively.

Once all hydrogen bonds of the base pairs are broken in our experimental setup, one strand gets released into the solution while the other remains attached in between two beads. Constant distance experiments (fig.3) indicate the transition by a drop in the measured force. In constant force experiments we observe a change in length which suggests a change in conformational properties of ssDNA. OH^- renders ssDNA softer to stretching while Cl^- stiffens the molecule. Previous single molecule studies reported that the force-extension characteristics of a single stranded DNA is closely related to the ionic concentration of the solution and DNA sequence composition (27-29).

We observed that an experimental curve at low salt (1.5 mM) ssDNA-NaCl showed same force versus extension behavior as ssDNA- 150 mM NaOH up to 34 pN (data not shown). But deviate from the low salt curve at forces higher than 34 pN. At force ~ 80 pN we measured a stretching of ssDNA in low salt and NaOH of 0.76 nm/bp and 0.78 nm/bp respectively. ssDNA is a highly negatively charged polyelectrolyte. At low salt conditions, electrostatic interactions dominate the conformation. The long range electrostatically repulsive potential between segments may largely influence the conformations of stretched ssDNA and at low forces the molecule is attaining a relaxed conformation due to ionic repulsion. In high salt conditions, it has been

reported that secondary structures of ssDNA appear in more easily aligned and form hairpin like structures. External stretching causes a hairpin-coil structural transitions, which are continuous for ssDNA made of random sequences (30). Whereas Y. Zhang reported that designed sequences such as poly(dA-dT) and poly(dG-dC), with a stacking potential between base pairs encourages the aggregation of base pairs into bulk hairpins and makes the hairpin coil transition discontinuous (first order) (31). We observed that at high salt conditions, more force is needed to pull the molecule as compared to low salt or a NaOH environment. In high salt secondary structures (hairpins) can be formed more easily. Ionic shielding enable that segments of ssDNA can bend onto themselves and its complementary bases could connect to form base pairs. Therefore a slightly larger external force is needed to open hairpin ssDNA under the high salt condition at forces ≥ ~17 pN.

The experimentally measured mechanics of ssDNA in 150 mM NaCl (as shown in fig.2) can be fitted by the WLC model (using the correct sugar-phosphate distance without addition of stretch modulus) or FJC model (modified with stretch modulus) but neither could produce a perfect fit in all force regimes. This indicates that the actual flexibility of a ssDNA molecule described using a model is most likely between these two limiting regimes of polymer flexibility, which has some intermediate rotational-isomeric flexibility (32) and further theoretical and experimental work is necessary here (28).

4.5.2 Free energy of ssDNA (submersed in NaOH or NaCl) subject to an external force

We used the experimental curves in figure 2 to calculate the effect of an applied force *f* on the two different conformations of ssDNA. All the values of energies in the subsequent paragraph are calculated per base pair. The free energy at a given extension is equal to the work done by the force to stretch the molecule to a fixed length *x* and can be given as

$$F(x) = \int_0^x f(x')\,dx' \qquad [4]$$

The difference in work done by the stretching of ssDNA in 150 mM NaCl, $F_{sc}(x)$ and 150 mM NaOH, $F_{so,}$ can be given by

$$\Delta W(x) = F_{sc}(x) - F_{so}(x) = \int_0^x [f_{sc}(x') - f_{so}(x')]\,dx' \qquad [5]$$

Equation 5 indicates the factor by which the energy of attraction of different segments of ssDNA in NaCl differs from the one of ssDNA in NaOH environment.

Force dependent free energies of ssDNA in 150 mm NaCl and NaOH are shown in figure 7 by empty squares and circles respectively. The solid filled squares represent the difference of force dependent free energies of the two configurations of ssDNA. We observe an increase in difference of free energies upto ~17 pN, which is the value required to open hairpins within the ssDNA. These data compare to experiments performed with scanning force microscopy but with a much higher force resolution. They measured the opening of a DNA hairpin required forces up to 10-15 pN and this pulling force was strongly dependent on DNA sequence and solution conditions (33). It was also shown that ssDNA with the higher GC content required a few pN stronger stretching force (29).

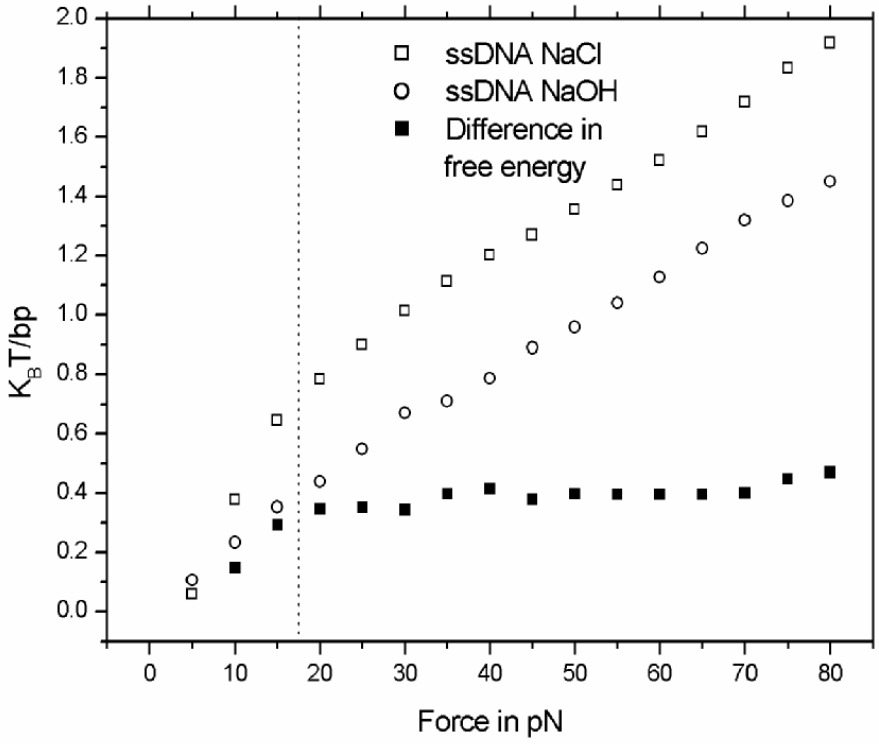

Figure 7. *Force dependent free energy curves (analogues to helmoltz free energy). Empty circles and squares indicate the free energies of ssDNA in presence of NaOH and NaCl respectively. The filled black squares represent the difference in free energies.*

At forces higher than ~17 pN, we extract a constant difference of free energies. To pull up to 15 pN ssDNA-150 mM NaCl requires ~0.3 K_BT/bp more energy as compared to ssDNA-150 mM NaOH. This indicates formation of secondary structures in high salt (i.e. formation of hairpins).

4.5.3 Melting curves

The progress of breaking of base pairs can be followed in single molecule experiments. The number of single stranded bases, N_{ss}, remaining at time t can be written as

$$N_{ss}(t) = \frac{x_{meas}(F,t) - x_{ds}(F)}{x_{ss}(F) - x_{ds}(F)} * N_{tot} \qquad [6]$$

where x_{meas} is the end-to-end distance of the molecule at force F, $x_{ds,ss}(F)$ are the end-to-end distances of fully double or single-stranded DNA at that force, and N_{tot} is the total number of bases dsDNA (13,27). Thus the rate of breaking of base pairs in real time can be monitored as a differential curve of dN_{ss}/dT versus time T.

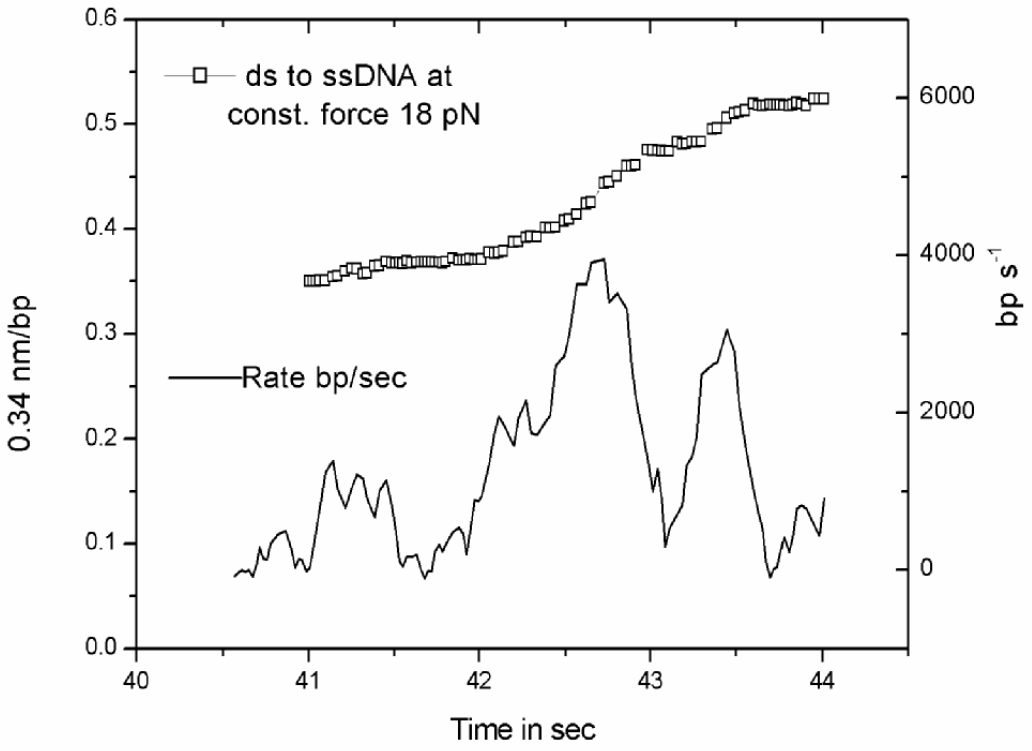

Figure 8. *Force feedback experiment; fractional length per base pair of DNA (square curve). Rate of bp/sec versus temp is the differential melting curve (plot of distance derivative of the fraction of broken base pairs versus time) i.e. dN/dT vs. T. it is*

obtained by differentiation of the N_{ss} data values after adjacent averaging of 6 data points.

In figure 8 the black line represents the melting characteristics of 5623 bp dsDNA. We observe the sudden breaking of a large numbers of base pairs, indicating again a first order phase transition (under basic conditions) of which switching from a bound to an unbound state is one of the characteristics (3). We observe different peaks (bp/sec) which correlates to a multistep melting behavior. The characteristics of melting curves of intermediate length of dsDNA are consistent with previous rates observed with the UV absorption during the dsDNA denaturation (2). The asymptotic description of the melting of base pairs was in debate for lengths of few thousand base pairs (~5000 bp) (4,5). Our melting curve may help to clarify recent dsDNA denatruration models or could greatly improve the predictive power of theoretical treatments (3,6).

4.5.4 Importance of the chemical dsDNA denaturation

We studied the kinetics of chemical denaturation processes and observed end points where no more hydrogen bonds are present to break. Our method may help to improve the design of PCR primers, Southern blotting, DNA chips and theoretical traditional thermal framework. There are different types of proteins which bind specifically to ssDNA and have great importance in DNA recombination, replication and repair (e.g single stranded binding protein, RecA protein etc.), the dsDNA to ssDNA conversion can be influenced by such process.

4.5.5 Melting and overstretching transition of dsDNA

DNA replication is very complex procedure and is carried out by a variety of proteins. The separation of strands by mechanical pulling is quite similar to the some of the steps occurring in vivo by the action of helicase (34,35) and is important in the studies of the initial steps in DNA replication and RNA transcription. The enzyme which associates with DNA needs to open few base pairs in close vicinity. In the case of replication this opening take place near one of the ends. During transcription it can be anywhere after the promoter site on the DNA. Our data with 5'–3' pulling of short dsDNA in physiological buffer shows no hysteresis during the overstretching transition of dsDNA. Small PCR constructs of DNA are completely nick free. At

physiological conditions high forces up to ~ 150 pN are required to completely melt off one strand (as shown in fig.5).

Melting of dsDNA observed at ~55 mM as shown in fig.6, is due to the low ionic strength. DNA is a polyanionic molecule, the salt 'shields' the negative charge of each phosphate group. At low salt concentrations dsDNA becomes more negatively charged resulting in greater strand-strand repulsion. When the charges are not able to be shielded, the electrostatic repulsion renders it energetically more favourable to separate the strands.

4.5.6 Prediction of melting force

The force dependent stretching free energy $\Delta\Phi(F)$ can be calculated directly from the experimental curves as

$$\Delta\Phi(F) = -\int_0^F [b_{ss}(F) - b_{ds}(F)]dF$$

where b_{ss}(F) and b_{ds}(F) are the lengths of ssDNA and dsDNA respectively (21).
The prediction of the melting force can be verified from the relation $\Delta\Phi(f_{tra}) = -\Delta G^{\circ}$. Where $-\Delta\Phi(f_{tra})$, is the absolute value of the destabilizing free energy at force *f* and $\Delta G^{\circ} = G^{\circ}_{ss} - G^{\circ}_{ds}$ is the free energy of melting transition without force. In table I we compare the values reported previously by Rouzina *et al.* (19) with our results (second row).

DNA μm	T_m °c	ΔG°kcal/mol	$-\Delta\Phi(f_{tra})$* kcal/mol
16.5 (19)	87	1.7	0.65** 1.3**
1.91	~86.4	1.65	1.56

Table I. *shows the comparison of free energy.*

* is the transition force at which dsDNA melts. In our case it was ~144 pN while Rouzina *et.al.* considered the overstretching force ~ 65 pN as a melting force (19).

** Represent values of DNA melting into a state with one or two single strands under tension respectively (19).

Although the values from table I shows that our data of the energy at the transition is close to the predicted melting force, we can not rule out that the overstretching

transition in dsDNA (from B– to S–DNA) @ 68 pN is a melting phenomenon (19,20). Additional experiments are needed to clarify the debate on the overstretching transition.

4.5.7 Fluorescently labeled imaging of λ DNA at transition force ≥ 65 pN

Recent studies predicted that DNA melting starts at overstretching transition (19-21). We carried out few experiments with lambda DNA to check the melting and fraying of the strands in solution at physiological conditions. The molecule was attached to the trapped bead by only one of its two strands and was picked up by the micropipette bead at the complementary strand. Earlier experiments by Hegner *et al.* (13) using an analytical ultracentrifuge and visualizing the size distribution of the λ–DNA melted with NaOH showed DNA with nicks providing only a minimal amount of λDNA–ssDNA of full length (i.e. 48502 bp). We pre-incubated lambda DNA with SYBR® Green or allowed it to interact with naked λ DNA in situ. Consecutive fluorescent images (~0.17 sec/image) during λ DNA stretching were captured with an EM-CCD camera (DV887AC-FI, Andor, Ireland).

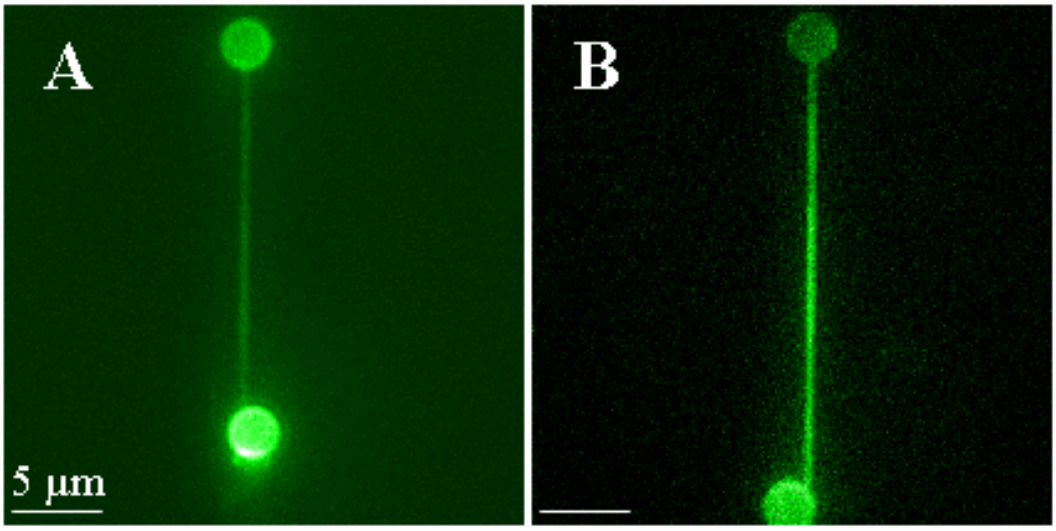

Figure 9. *Video microscopy on single dsDNA molecules during overstretching form of dsDNA. The lambada DNA is fluorescently labelled with SYBR® Green. Figure shows the overstretched form of dsDNA,* ***A****) applied force = ~ 66 pN;* ***B****) applied force = ~ 68 pN.*

Our experiments didn't reveal any release of melted strands into the solution, even when we pulled to a fully overstretched form at physiological conditions. We recorded several images of DNA labeled with SYBR® Green molecules. Rupturing of

molecules was noticed may be due to the breakage of biotin streptavidin bond at high forces or photo bleaching (photo induced cutting) of the DNA. Figure 9A shows the stretching of DNA at a force of ~ 66 pN (F = overstretch, ~1.3 fractional extension) while figure 9B shows the overstretched conformation of DNA (F > overstretch, ~ 1.7 fractional extension). We stretched the molecule more than 1.7x its contour length to forces up to ≤ 150 pN. If there were nicks, one of the melting strand should fray back from both sides of the nick and be release into solution. A melted region should become visible since SYBR® Green binds to ssDNA also (65 pN≤ F ≥120 pN). In all the experiments we observed both strands were attached together and no melted portion of one strand became visible. This may be due to i) no melting but dsDNA could form skewed ladder or unwinding helical structure of the two strands to form an unstacked parallel ladder or ii) it is melting and both strands remain close to each other, at a force F = overstretch. It is difficult to get more insights into the S-DNA transition video experiments due to limitations arising from the changes in mechanics of dsDNA, efficiency of binding molecules (i.e. SYBR® Green binding to ds and ssDNA is not equal), surrounding free molecules, auto fluorescence of polystyrene beads etc.

We believe that at physiological conditions, dsDNA doesn't melt at an overstretching force of 65 pN (assuming no nicks for small plasmid DNA or PCR products) but that the strands start to melt at higher forces (transition point, as shown in the fig.5). Forces acting on the molecule during overstretching to past overstretched form are in between ~ 70 pN to 120 pN. However the present force pulling curves with simultaneous video microscopy are not sufficient to explain the conformational changes of DNA in detail on a load scale. To explore what is happening on local scale, studies with single fluorophors attached to individual single DNA strands and subsequent monitoring FRET signal is required. Then the FRET signal stability during the force transition can precisely elucidate the conformational changes of DNA during the overstretching transition at the local scale while applying external forces.

4.6 Conclusion

We have described how optical tweezers single molecule technique can be used to study the structural changes in dsDNA induced by the chemical denaturation and mechanical pulling.

1. Denaturation of DNA (melting of hydrogen bond) by NaOH shows a first order transition. The resulting data provide additional details for the verification of current DNA denaturation theories.

2. Exchange of salt from 150 mM NaOH to 150 mM NaCl shows sigmoidal curves indicating cooperative nature.

3. The kinetics of force induced melting and reannealing process has been investigated in situ at the single molecule level.

4. Overstretching transition and denaturation of dsDNA at physiological conditions has remained elusive even though it can be visualized by video microscopy.

Acknowledgement

Financial support is acknowledged from the Swiss National Foundation (SNF) grant (3152-67919.02) and by the National Centre of Competence in Research 'Nanoscale Science' (NCCR).

4.7 References

1. Poland, D. and Scheraga, H.A. (1966) Occurrence of a phase transition in nucleic acid models. *J. Chem. Phys.*, **45**, 1464-1469.
2. Wartell, R.M. and Benight, A.S. (1985) Thermal denaturation of DNA molecules: A comparison of theory with experiment. *Phys. Rep.*, **126**, 67-107.
3. Kafri, Y., Mukamel, D. and Peliti, L. (2000) Why is the DNA Denaturation Transition First Order? *Phys. Rev. Lett.*, **85**, 4988-4991.
4. Hanke, A. and Metzler, R. (2003) Comment on " Why is the DNA Denaturation Transition First Order?" *Phy. Rev. Lett.*, **90**, 159801.
5. Kafri, Y., Mukamel, D. and Peliti, L. (2003) Kafri,Mukamel,and Peliti Reply. *Phy. Rev. Lett.*, **90**, 159802.
6. Carlon, E., Orlandini, E. and Stella, A.L. (2002) The role of stiffness and excluded volume in DNA denaturation. *Phy. Rev. Lett.*, **88**, 198101-198104.
7. Bloomfield, V.A., Crothers, D.M. and Tinoco, I. (2000) Nucleic Acids Structures, Properties and Functions. *University Science Books, Mill Valley*.
8. Lyon, E. (2001) Mutation detection using fluorescent hybridization probes and melting curve analysis. *Expert Rev. Mol. Diagn.*, **1**, 92-101.
9. Saiki, R.K., Gelfand, D.H., Stoffel, S., Scharf, S.J., Higuchi, R., Horn, G.T., Mullis, K.B. and Erlich, H.A. (1988) Primer-directed enzymatic amplification of DNA with a thermostable DNA polymerase. *Science*, **239**, 487-491.
10. Southern, E.M. (1975) Long range periodicities in mouse satellite DNA. *J. Mol. Biol.*, **94**, 51-54.
11. Fodor, S.P.A., Rava, R.P., Huang, X.C., Pease, A.C., Holmes, C.P. and Adams, C.L. (1993) Multiplexed biochemical assays with biological chips. *Nature*, **364**, 555 - 556.

12. Smith, S.B., Cui, Y. and Bustamante, C. (1996) Overstretching B-DNA: the elastic response of individual double-stranded and single-stranded DNA molecules. *Science*, **271**, 795-799.
13. Hegner, M., Smith, S.B. and Bustamante, C. (1999) Polymerization and mechanical properties of single RecA-DNA filaments. *Proc. Natl. Acad. Sci. USA*, **96**, 10109-10114.
14. Clausen–Schaumann, H., Rief, M., Tolksdorf, C. and Gaub, H.E. (2000) Mechanical Stability of Single DNA Molecules. *Biophys. J.*, **78**, 1997-2007.
15. Lebrun, A. and Lavery, R. (1996) Modelling extreme stretching of DNA. *Nucl. Acids Res.*, **24**, 2260-2267.
16. Ahsan, A., Rudnick, J. and Bruinsma, R. (1998) Elasticity Theory of the B-DNA to S-DNA Transition. *Biophys. J.*, **74**, 132-137.
17. Konrad, M.W. and Bolonick, J.I. (1996) Molecular dynamics simulation of DNA stretching is consistent with the tension observed for extension and strand separation and predicts a novel ladder structutre. *J. Am. Chem. Soc.*, **118**, 10989-10994.
18. Kosikov, K.M., Gorin, A.A., Zhurkin, V.B. and Olson, W.K. (1999) DNA stretching and compression: Large scale simulations of double helical structures. *J. Mol. Biol.*, **289**, 1301-1326.
19. Rouzina, I. and Bloomfield, V.A. (2001) Force-Induced Melting of the DNA Double Helix 1. Thermodynamic Analysis. *Biophys. J.*, **80**, 882-893.
20. Rouzina, I. and Bloomfield, V.A. (2001) Force-Induced Melting of the DNA Double Helix. 2. Effect of Solution Conditions. *Biophys. J.*, **80**, 894-900.
21. Williams, M.C., Rouzina, I. and Bloomfield, V.A. (2002) Thermodynamics of DNA Interactions from Single Molecule Stretching Experiments. *Acc. Chem. Res.*, **35**, 159-166.
22. Hegner, M. (2000) DNA Handles for Single Molecule Experiments. *Single Mol.*, **1**, 139-144.
23. Grange, W., Husale, S., Güntherodt, H.-J. and Hegner, M. (2002) Optical tweezers system measuring the change in light momentum flux. *Rev. Sci. Instr.*, **73**, 2308 - 2316.
24. Husale, S., Grange, W. and Hegner, M. (2002) DNA mechanics affected by small DNA interacting ligands. *Single Mol.*, **3**, 91-96.
25. Tinoco, I.J. and Bustamante, C. (2002) The effect of force on thermodynamics and kinetics of single molecule reactions. *Biophysical Chemistry*, **101-102**, 513-533.
26. Danilowicz, C., Coljee, V.W., Bouzigues, C., Lubensky, D.K., Nelson, D.R. and Prentiss, M. (2002) DNA unzipped under a constant force exhibits multiple metastable intermediates. *Proc. Natl. Acad. Sci. U S A*, **100**, 1694-1699.
27. Wuite, G.J.L., Smith, S.B., Young, M., Keller, D. and Bustamante, C. (2000) Single-molecule studies of the effect of template tension on T7 DNA polymerase activity. *Nature*, **404**, 103-106.
28. Bustamante, C., Smith, S.B., Liphardt, J. and Smith, D. (2000) Single-molecule studies of DNA mechanics. *Curr. Op. Struct. Biol.*, **10**, 279-285.
29. Maier, B., Bensimon, D. and Croquette, V. (2000) Replication by a single DNA polymerase of a stretched single-stranded DNA. *Proc. Natl. Acad. Sci.*, **97**, 12002-12007.
30. Montanari, A. and Mezard, M. (2000) Hairpin Formation and Elongation of Biomolecules. *Phy. Rev. Lett.*, **86**, 2178-2181.

31. Zhang, Y., Zhou, H. and Yang, Z.C.O. (2001) Stretching Single -Stranded DNA: Interplay of Electrostatic, Base-Pairing,and Base-Pair Stacking Interactions. *Biophys. J.*, **81**, 1133-1143.
32. Grosberg, A.Y. and Khokhlov, A.R. (1994) Polyelectrolytes. Trans. Atanov, Y. A. *Statistical Physics of Macromolecules*, **5**, 217-220.
33. Rief, M.H., Clausen–Schaumann, H. and Gaub, H.E. (1999) Sequence-dependent mechanics of single DNA molecules. *Nat. Struct. Biol.*, **6**, 346-349.
34. Murphy, M.C., Rasnik, I., Cheng, W., Lohman, T.M. and Ha, T. (2004) Probing Single-Stranded DNA Conformational Flexibility Using Fluorescence Spectroscopy. *Biophysical Journal*, **86**, 2530-2537.
35. Lohman, T.M. (1993) Helicase-catalyzed DNA unwinding. *J. Biol. Chem.*, **268**, 2269-2272.

5. Development of optical tweezers combined with single molecule fluorescence detection

5.1 Abstract

The application of mechanical load (force) on single biomolecules and simultaneous monitoring of their conformational changes using local fluorescent probes provides new opportunities to explore models which explain the physical and chemical properties of biomolecules. We have successfully combined force measuring optical tweezers with single molecule fluorescence detection (SMF). Here we present details related to the setup which consist of a dual beam optical trap (fixed, λ = 830 nm), movable trap (λ = 1064 nm) and single molecule fluorescence detection (λ = 350-700 nm). The high detection efficiency was achieved by choosing the emission wavelengths of the fluorescence reporter molecules in a band pass window different from the trapping and excitation wavelengths. Spectral separation was achieved by the judicious choices of dichoric mirrors and optical filters of the instrument. Our preliminary results show the detection of single quantum dots, alexa dyes covalently coupled to λ DNA and fluorescent images of λ DNA.

5.2 Introduction

5.2.1 Fundamentals of Single-molecule fluorescence detection (SMF) studies

In 1852, the term “fluorescence” was first introduced by George Stokes, who suggested that fluorescent dyes can be used for the detection of organic substances. The first successful optical detection of a single molecule (with multiple fluorescent labels) in a liquid was reported by Hirschfeld (1). Attaching fluorophores to biological macromolecules (protein or nucleic acids) allows investigators to image individual molecules by fluorescence microscopy. During the last ten years it became possible to detect single chromophores and to measure some of their physical and chemical properties. In short, SMF monitors the microscopic location or movement of individual labeled proteins fused to fluorescent dyes. The single molecule is illuminated or excited by laser light and the emitted fluorescence is collected by using an objective lens (high NA) coupled to a sensitive detector such as an electron-multiplying charge coupled device (EMCCD), an avalanche photodiode or photomultiplier tube.

5.2.2 Advantages of SMF

The advantages of single molecule fluorescence detection studies in comparison to ensemble measurements are (i) SMF offers individual dynamic information instead of averaged population behavior, (ii) SMF allows reduction in cost of materials used and shows possible applications in single molecule array technology.

5.2.3 What can fluorescence detection tell us?

1. It reports the chromophores location, that it is there, and individual compounds can be labelled separately.
2. The polarization response can reveal the rotational motion of the host molecule.
3. The emission brightness can change due to reactions with the surrounding media.
4. Fluorescence resonance energy transfer (FRET) can be applied to measure distance changes (between two dyes, donor and acceptor) on the nanometer scale which is a relevant length scale for many biomolcules.

5.2.4 Fluorescence

Fluorescence can be explained with the Jablonski diagram, as shown below:

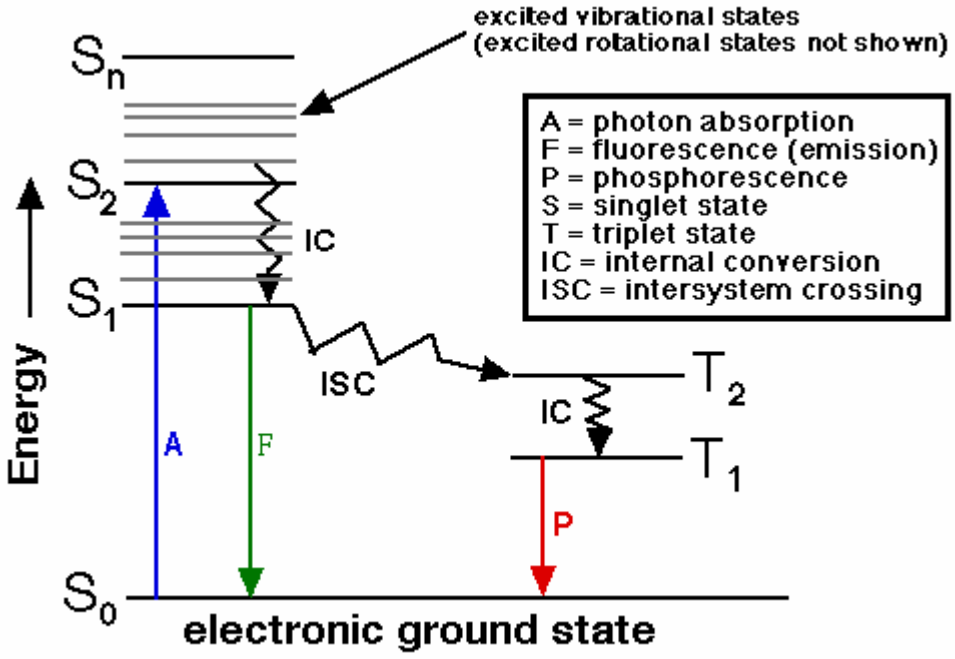

Figure1. *Jablonski diagram.*

Once a fluorophore molecule has absorbed energy in the form of electromagnetic radiation, there are a number of routes by which it can return from its excited to the ground state. The photon emission shown by the downward pointing green line (short wavelength) occurs between states of the same spin (S_1- S_0) and is called as

fluorescence. It is the emission of light caused by the electronic excitation and subsequent relaxation of the molecule. The lifetime of this phenomenon is very short (1×10^{-5} to 10^{-8} seconds).

If the spin state of the initial and final energy levels are different (e.g. $T_1 \longrightarrow S_0$), the emission (loss of energy) is called phosphorescence. In the diagram this is depicted by a red line (longer wavelength). Lifetime of phosphorescence is longer than fluorescence (1×10^{-4} seconds to minutes or even hours). All the initially excited molecules by absorption (step A) do not return to the ground state S_0 by fluorescence emission (step F).

Internal conversion (IC), intersystem crossing (ISC) and vibrational relaxation are the three nonradiative deactivation processes. Internal conversion is the radiationless transition between energy states of the same spin state. Intersystem crossing is a radiationless transition between different spin states (compares to phosphorescence). Vibrational relaxation, the most common of the three–for most molecules, occurs very quickly (~1×10^{-12} seconds).

5.2.5 FRET

Fluorescence or Förster resonance energy transfer (FRET) describes an energy transfer mechanism between two fluorescent dye molecules (2). A fluorescent donor is excited at its specific fluorescence excitation wavelength. By a long-range dipole-dipole (as dipole is a pair of electric charges or magnetic poles of equal magnitude but opposite polarity, separated by a small distance) coupling mechanism, this excited state is then nonradiatively transferred to a second molecule, the acceptor. The donor returns to the electronic ground state. The described energy transfer mechanism is termed as FRET (2).

Figure 2A *shows two conformational states of a model of folding and unfolding of an RNA molecule hairpin ribozyme with a donor and an acceptor attached to the ends of two arms (3). The right side (open form) shows little energy transfer due to the fact that the two dyes are far from each other. Such a conformation indicates that the donor excitation by the laser results primarily in donor emission. On the left side (closed form) the two dyes are close to each other resulting in a strong energy transfer. Here the acceptor fluorophore is excited by the donor and emits strongly and*

the donor shows weak emission. Figure 2B displays the energy transfer efficiency versus distance between two dyes.

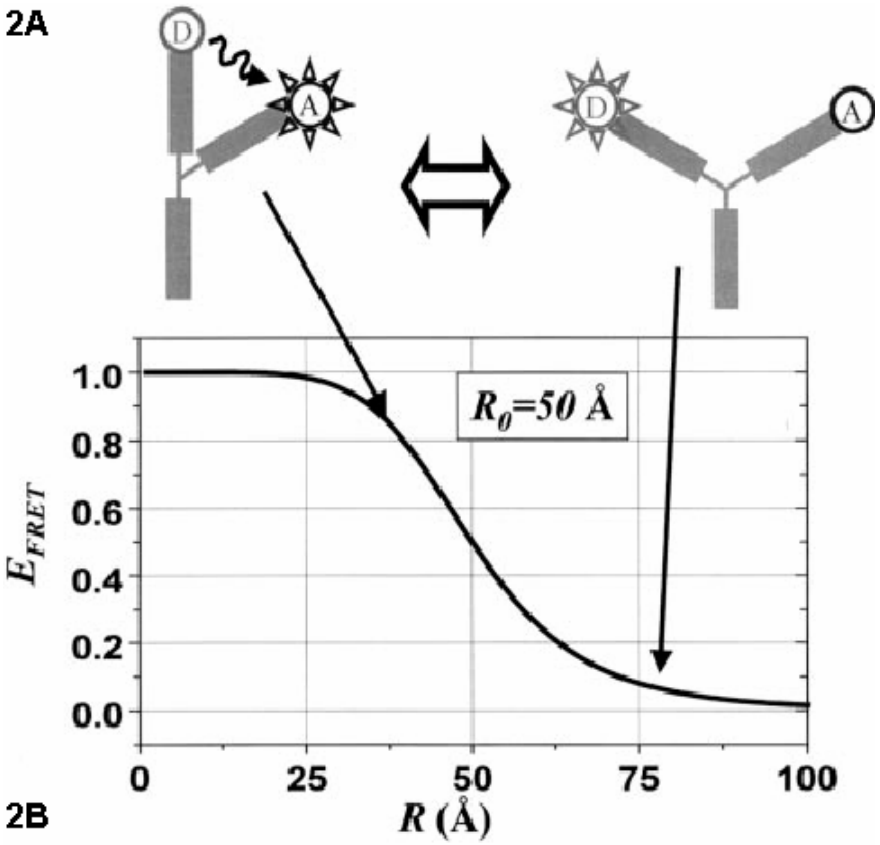

The efficiency of energy transfer is strongly depending on the separation of the two fluorophores. Therefore it can be used as a molecular ruler on the 1-10 nm scale which is ideal for the study of biological molecules as they are comparable in size (e.g. proteins).

The efficiency E is defined as the fraction of energy (in photons) absorbed by the donor that is subsequently transferred to the acceptor (4).

$E = \frac{R_0^6}{R_0^6 + R^6}$ where R_0 = Förster distance, R= the distance between the centers of the fluorophore dipole moments.

More relevant for experimental proof of the existence of FRET is the following expression: $E = 1 - \frac{F_{DA}}{F_D}$

where F_{DA} depicts fluorescence intensity of the donor in the presence of the acceptor and F_D the fluorescence intensity of the donor when the acceptor is far away.

This indicates that when the acceptor is close to the donor F_{DA} should be low and the efficiency should be close to one. When the acceptor is far away then $F_{DA} = F_D$ and efficiency equals to zero.

Among fluorescence technique applications, FRET is particularly popular because it is sensitive to local distance changes in host biomolecules. FRET measures interatomic distances (10 -75 Å) such as conformational changes in biological molecules in real time by monitoring the transfer of energy in–between different fluorophores (donor-acceptor) (3). Many pairs of organic fluorophore dyes have been used successfully for various biological systems spanning DNA, RNA and protein investigations (5-7).

5.3 Motor Proteins / Proteins studied with OT or SMF

Many models used in physics, chemistry and biology are often based on the description of single-molecule properties. The optical tweezers (OT) technique was first introduced by Ashkin *et al.* in the mid eighties (8). The radiation pressure produced by single-beam or double beam near-infrared lasers is applied to trap and manipulate molecular handles to which single molecules are attached. In the last two decades OT technique emerged as a powerful technique for biophysical research and proved its capability in the manipulation and investigation of single biomolecule properties. With precise control of position sensitive sensors one can elucidate forces and displacements in the piconewton and nanometer range. These tools have been used to explore the molecular mechanics of biological motors (to measure the force and movement produced by molecular motors as they convert the chemical energy from hydrolysis of a single molecule of ATP into mechanical work) (9,10), DNA protein binding (11), receptor-ligand binding (12-14), and biopolymer physics (15-18). The comprehensive work done with OT in biology has been reported in chapter one of this thesis.

Previously, muscle motor proteins have been extensively studied with the use of SMF, as it is possible to relate the mechanism of motion directly to changes in fluorescence. Following are the examples of studies performed with SMF or optical trap techniques. The first study of a single turnover of an enzyme molecule in an aqueous environment was of myosin hydrolyzing a fluorescent ATP analog (19). Optical studies of the

turnovers of single enzyme molecules have indicated that the behavior of some enzymes might depend upon their previous state (20,21).

Single-molecule fluorescence has also been used to observe discrete sub-states during protein folding (22,23). Cell biologists have shown particular interest in the studies of the behavior of individual molecules inside living cells (24-26). Single myosin molecule mechanics, muscle contraction driven by the motor protein myosin (27), kinesin molecules involved in intracellular trafficking, individual stepping motion of them was observed (by optical trapping) (28), dynein responsible for movement of eukaryotic cilia and flagella (29), RNA polymerase responsible of transcribing a DNA template into messenger RNA (30). The individual fluorescently labelled kinesin molecules moving along a fixed microtubule confirmed the need for both heads of the kinesin protein for processive motion to occur (stepping of motor molecules) (31). Molloy *et al*. used OT to reveal a working stroke from chymotryptic fragments of myosin II longer than expected from many conventional structural models (32). The stepping of motor molecules such as myosin (33) was observed at the single-molecule level.

Single molecules of Green fluorescent protein (GFP) have been observed in an aqueous enviroment (34). GFP is a naturally fluorescent protein derived from the jellyfish Aequorea Victoria. It has been proven useful to study static and dynamic aspects of proteins within living cells. The GFP sequence can be co–expressed as an attached probe to a particular protein. Moerner and co-workers have reported a blinking behavior of GFP on the timescale of several seconds (35).

Polymerases incorporate individual nucleotides into a polynucleotide sequence. Single RNA polymerase molecules have been observed directly by Harada *et al.* (36). In their experiment dsDNA was suspended between two optical traps, and the motion of a fluorescently labeled RNA polymerase along the DNA was observed. Their results suggest that the protein preferentially bound to AT as opposed to GC rich regions of the DNA (36). The Bustamante group has also employed optical traps to study the motion of polymerases, their work has produced valuable insights into the functioning of DNA and RNA polymerases (37).

ATP synthases are the primary proteins responsible for the production of cellular ATP. The F1-ATP synthase has been studied at single-molecule level by Kinosita and

coworkers (38). They attached a fluorescently labelled actin filament to a surface-attached ATP synthase to observe the stepwise rotation of these molecular machines.

Single-molecule fluorescence resonance energy transfer experiments have revealed complex catalytic dynamics of staphylococcal nuclease (39) and co-localization of multiple ligands on a single receptor (phospholipids membrane protein) (40).
The study of Cholesterol Oxidase by Lu *et al*. provided the first strong evidence for dynamic disorder in enzyme activity (41). It is described in terms of a variation in the turnover rate for an individual enzyme, with the slow variation in rate attributed to slow conformational changes of the entire enzyme. The experiments to study fluorescence during enzyme activity were also conducted by Wiess and co-workers in 1999. They observed ligand binding and unbinding events and characterized these events through the fluctuations in FRET efficiency and fluorescence polarization anisotropy (42).
The first demonstration that fluorescence resonance energy transfer can be used to track the motion of a single molecule undergoing conformational changes was presented by Chu and co-workers in 1999 (43). A three-way RNA junction was labeled with two dyes on two of the arms of the junction, and conformational changes monitored upon binding of both proteins and Mg^{2+}. Recently the same group has published work on a surface-immobilised, FRET–labelled catalytic RNA. Large changes in FRET efficiency during the catalytic cycle allowed a detailed interpretation of the fluctuations present. This experiment enabled the direct observation of the catalytic folding step of this ribozyme and presented evidence for a previously unseen folding pathway of this RNA (please refer to figure 2 of this chapter) (44).
All above examples indicate that most of research work is centered on the use of optical tweezers and SMF to study the biomolecules and dominated the field of single molecule research ever since they were independently developed over 15 years ago.

5.4 Combining fluorescence and force measurement

The above mentioned (OT and SMF) powerful techniques were first combined sequentially but not simultaneously by Funatsu *et al*.(the kinetics of myosin binding to ATP using Cy3-labelled fluorescent ATP analogs) and Ishijima *et al*. (19,45). In

their experiment, they (45) showed the coordination between the binding of ATP to myosin and the mechanical motion of the actin filament. It was done by attaching beads to the end of actin filaments and monitoring the fluorescent ATP molecules on a myosin motor interacting with the actin filament. Binding, hydrolysis and release of a fluorescently labelled nucleotide to a surface-attached myosin were monitored. A delay between force generation and ADP release was observed, suggesting that there was no tight coupling between the enzyme-ligand state and force production (45).

Another example of combined optical trap force and fluorescence measurements comes from the diminished binding of RNA polymerase to DNA when the polymer length was increased (36).

Recently Lang *et al.* successfully combined these two techniques (single beam optical trap and single molecule fluorescence) and mechanically unzipped the DNA hybrid (46). In their experiment, they used complementary DNA strands labeled with tetramethylrhodamine molecules. One of the DNA strands was attached to a polystyrene bead and the other to a glass coverslip. The bead was trapped by the laser beam and the stage moved so as to 'unzip' the DNA strands. As soon as the two strands were ripped apart, the fluorophores were separated, releasing a short burst of light.

As compared to single beam optical trap setups which work in the vicinity of transparent interfaces, our setup (dual beam optical trap) is more complicated as the interfaces are located in the middle of a fluid chamber (>150 μm away from the interfaces) and the tweezers are consisting of dual beam optical trap and steerable third trap. It was a challenging task to combine such an instrument with single molecule fluorescence detection. Here, we demonstrate the single molecule fluorescence detection capability obtained from a quantum dot and alexa fluorophors which were covalently coupled to λ DNA.

5.5 Construction of the setup

5.5.1 Motivations

1. It is obvious that the combination of optical trapping and single-molecule fluorescence detection would offer a powerful approach to monitor spatial or conformational changes at the single molecule level. Both techniques suffer some specific limitations such as optical tweezers alone can not determine precisely the

local conformational changes (e.g. overstretching of dsDNA) imposed by external load. These conformational changes can be pinpointed with SMF, by attaching fluorophores to specific locations and monitoring their subsequent motions.

2. Aiming that the combination of OT and SMF experiments provide the ability to manipulate a macromolecule in an area optimized for fluorescence excitation. Thus, correlations between fluorescence and mechanical signals generate information related to molecular binding events observed by fluorescence and structural changes perturbed by external load.

3. Despite the developments in molecular biology and genetics in the last decade many questions remain unanswered, for example: can we visualize exactly how a protein performs its task? How do biological molecules interact? How do proteins fold? If experimental setups are further developed the answers to these questions are helpful to understand the functions of biological machinery or the biomolecules involved. We except the combination of the two techniques may shed light on such open questions.

5.5.2 Experimental setup

I. Dual beam optical trap

Dual beam optical trap is formed by the two diode lasers D1 and D2 (wavelength of 832 nm) which is fixed in 3D space. The diode laser beam shaping and cleaning were done by the optical elements P1, F1, L1-L2, P which represents the anamorphic prisms 06GPA004, Melles Griot, Irvine, CA (produce square shaped beam), Optical isolators IO-5-830-LP, Optics for Research, Caldwell, NJ (to prevent back reflections and reduce mode hopping of the laser), achromat doublet lens and pinhole (spacial filtration of the beam) respectively. Shutters (S) provide automatic control of the trapping laser beam, used to pass or block the laser lights. Quarter wave plates (QW) are used to change the state of polarization (circular) at the location of the trap. Position beam splitter (PS) directs the light to objective lens as well as after the trap to the detectors. D and D1 are the linear position sensitive detectors used to read out the light intensity and to detect the position of the trapped bead respectively. The focal plane of the objective lenses illuminated by LED λ = 380 nm was imaged on the chipset of a CCD camera (VCB-3424, MSM Trading, Switzerland) with the help of planoconvex lens (f = 300 mm) or Achromat lens. F4, F5 (Schott, Feldbach,

Switzerland) and additional low-pass filters used to eliminate unwanted infrared and blue laser wavelengths (stray lights).

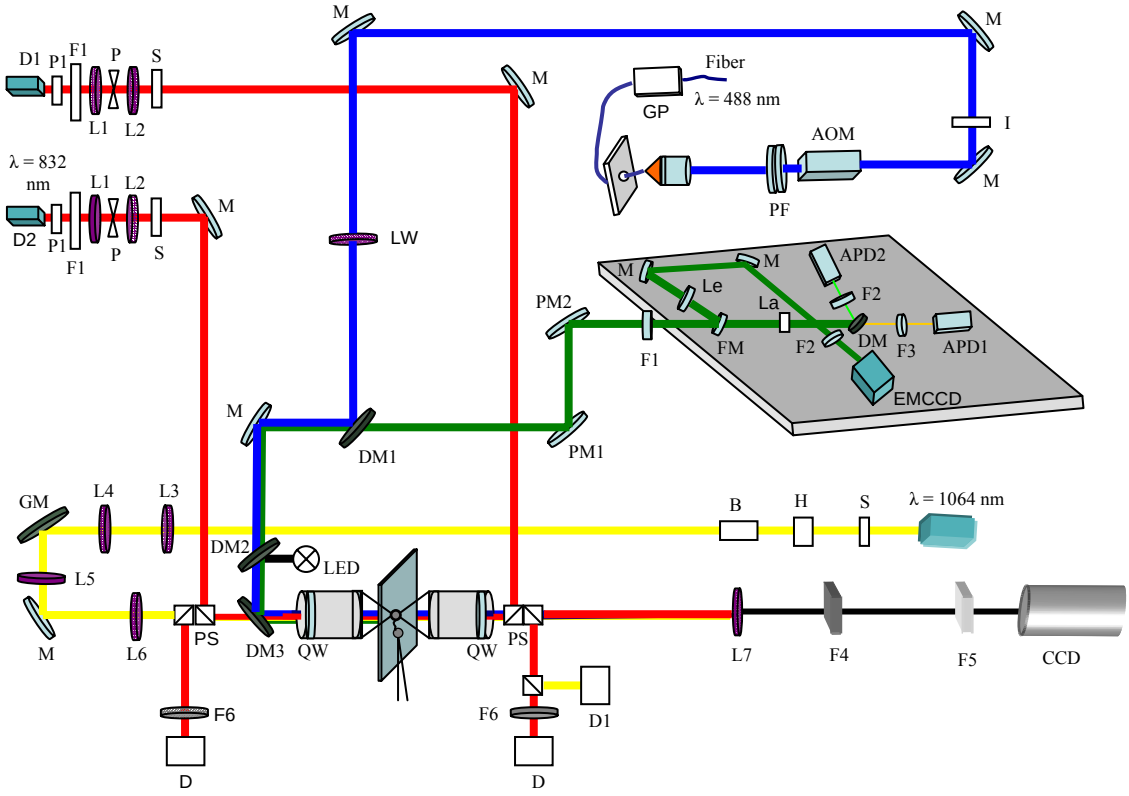

Figure 3. *The schematic layout of experimental setup. The thick red lines show the light pathways of the dual beam trapping lasers, front laser and back laser whereas front laser is also used as a position detection laser. Remaining light pathways are indicated for the LED transillumination in black, movable third trap (yellow), fluorescence excitation lasers (dark blue) and fluorescence emission (green).*

II Third Trap

Laser light coming from the Nd:YAG laser (λ =1064 nm) is shown in yellow. H depicts the height adjustment prior to the dual beam trap position. Beam expander B, is used to expand the beam such that it overfills the back aperture of the objective lens. Lenses L5 and L6 form the afocal system. Gimbal mirror GM is used to move the location of trap in x-y plane. Steering of beam along z axis was achieved with the lenses L3 and L4. This part of the experimental setup has been previously reported in ref. (47).

III. Injection of Excitation laser (λ = 488 nm)

To excite fluorescent molecules we used an Argon-ion (177–G02, Spectra physics, CA) blue laser (λ = 488 nm). The output of the laser was coupled into a glass fiber.

1. The fiber was inserted on the top of the device, drop in polarization controller-PolaRITE (General Photonics).

2. A single-mode fiber coupler (F-915, submicron resolution, Newport) and a objective lens (60x, Numerical aperture 0.85, working distance 0.3 mm, Newport) was used to decouple and colliminate the laser light from the fiber. After the objective lens, we measured a beam size of ~ 0.7 mm. A Melles Griot rotation mount was used to mount the laser line filter (488 nm, XL06, Omega optical, transmission ~ 70%) and the sheet polarizer (5511, New Focus, transmission 80%) which was used to get linear polarized light parallel to the optical table.

3. Mechanical shutters with switching times in the range of milli second were not sufficient to synchronize both events simultaneously, the mechanical pulling and the fluorescence measurement. Acousto optic modulators (1205-C2, Isomet) are the best option to solve such problems, they can operate with μsec interval time. The first order diffracted light is deflected by an angle that depends on the acoustic frequency through $\Delta\theta = \lambda f / v$, where λ is the optical wavelength, v velocity and f frequency of the acoustic wave. It was mounted on the precision rotation platform (PR01/M, Thorlabs) which has a backlash free micrometer adjustment to provide rotation with high precision. If the platform dial is in an unlocked state, continuous smooth rotation can be measured with the 1° graduation marks. When locked, the dial is adjusted by the ±7° micrometer drive system, offering 5 arc min. resolutions from the side vernier.

4. Mirrors, M (BB1-E02, Thorlabs) are the broad band mirrors having excellent reflectivity.

5. An Iris I is used (home made) to cut excess stray light (except the first order reflection from AOM).

6. Coated plano convex lenses (LW) of different focal lengths (300, 500, 750 mm BK7 material, Thorolabs) were mounted on a 6 station empty filter wheel, 01" (FW1AB, Thorlabs). A selection of different lenses offers the options in selection of power density per illumination area near the focus of the trap. Considering all the power losses in the optical path, we got the following values of power densities i) without lens = 4.5 kW/cm^2, illumination diameter = 4.5 ± 0.8 μm ii) with 750 mm lens = 0.7 kW/cm^2, illumination diameter = 11±1 μm, iii) 500 mm lens = 0.4 kW/cm^2, illumination diameter = 15±1 μm and iv) 300 mm lens = 0.25 kW/cm^2, illumination diameter = 19± 4 μm. For the in–coupling of the blue laser into the objective lens

(injection of beam), we used three dichoric mirrors such that we ended up with ~ 80 % of the incident power of the laser light.

7. Dichoric mirrors

i) DM1, XF2010 (Omega filters), which reflects incoming light @ 488 nm = 95% and transmits @ 560 nm = 99%, @ 830nm =10 %, @1064nm: 72 %.

ii) DM2, XF2007 (Omega filters): It is introduced to allow 99 % reflection of light emitting diode (Marubeni) at 380nm. This wavelength was used for the normal imaging of pipette and beads. In addition this dichoric transmits @ 488 nm = 82%, @ 560 nm = 99%, @ 830nm = 90 % and @1064nm = 86 %.

ii) DM3, 750dcxxr (Chroma Technology): It is the main dichoric mirror which transmits wavelengths 830 nm (90%) and 1064 nm (85%) to the objective lens while 380 nm (99%), 488 nm (95%) and 560nm (95%) from the SMF detection path are reflected into and from the objective lens.

IV. Imaging of fluorescent signal:

All the emitted light from fluorescent material was collected by the APD (avalanche photodiode, measures photons) or the EMCCD (2D imaging of the focal plane) (DV887AC-FI, Andor, Ireland) through the path DM3, DM2, M, DM1, PM1 and PM2 (green line) where PM1 and PM2 are periscope mirrors which are used for height adjustment. F1 is the filter which transmits wavelengths of 505-755 nm and cuts 488 nm, 830 nm and 1064 nm. The flipper mirror FM is used to select either EMCCD imaging or photon counting on APD. An EMCCD camera was used for visualization of fluorophores. An achromat lens (Le), LAC191-A (focal length =1000 mm, Thorlabs) was placed to get the emitted fluorescence in a confocal setting onto EMCCD. Filter F2 (ABSP 660, Omega filters) was placed in front of EMCCD to pass wavelengths of 420-680 nm and to reject 830 nm and 1064 nm. A dichoric mirror, DM, 560DCLP (Omega filters) is used to separate two wavelengths, the emission of the donor from the emission of the acceptor, first it reflects up to ~ 550 nm and second transmits from 605 nm. Optical filters used in FRET detection have the big advantage that one can cut off the excitation light very efficiently. We placed filter F2, XF3084 (transmits 510-570 nm, Omega filters) to pass emission of Alexa 488 dye to APD2 (Single-photon counting module, SPCM-AQR14, Perkin Elmer) whereas filter F3, XF3081 (which transmits at 610-700 nm, Omega filters) was placed in front of APD1 to detect emission signal from Alexa 594 dye. This allows only photons of specific fluorescence emission to reach the detector. The active area was calculated

from the relation $\frac{f_{la}}{f_{ob}} = \frac{A_a}{A_r}$ where f_{la} is the focal length of the lens in front of APD, f_{ob} is the focal length of objective lens, A_a is the active area of APD and A_r is the final value of the selected area projected on the APD.

5.6 Results

5.6.1 Single molecule visualization with SYBR® Green stained dsDNA molecules

Fluorescent images allow discrimination two single dsDNA molecules or one dsDNA strand.

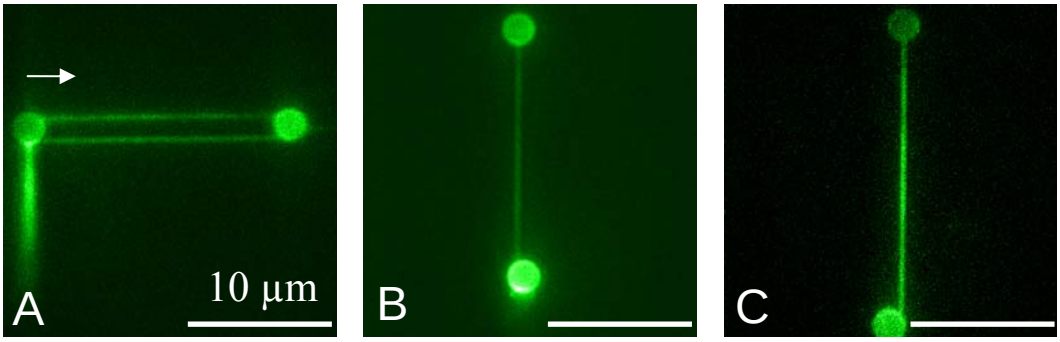

Figure 4 *EMCCD imaging of single dsDNA molecules labeled with SYBR® Green.*

Figure 4A shows two double stranded DNA molecules in between two polystyrene beads. The arrow indicates the direction of flow of the buffer. Fig.4B and 4C display subsequent images of a single DNA molecule (having same molecular contour length) observed during mechanical overstretching (B–DNA→S–DNA transition). We observed that the fluorescence life time can be increased by aligning trapped molecules in the focal plane and gating of the excitation laser by short pulses.

5.6.2 Fluorescent images of single quantum dots and alexa dyes

i) Visualization of quantum dots

Quantum dots are a unique class of nanoscale semiconductors, ranging from 2-10 nanometers in diameter. They have great importance as their electrical conductivity can be greatly altered via an external stimulus such as voltage, photon flux, etc. Quantum dots can be excited by one common wavelength (e.g. 488 nm) and their emission wavelength is tuned by their respective size. We have coupled streptavidin modified quantum dots (Q dot 605, Hayward CA) to one 5' end of λ DNA. The image acquisition rate of 15.67 Hz was used to generate movies. The rectangle in figure 5A shows the location of fluorescent emission of a quantum dot whereas 5B, 5C and 5D are the consecutive images obtained during recording of a movie (image rate 50 ms). Fig.5E represents the variation in light intensity (light maximum versus time in ms)

which can be attributed to the known blinking of the visualized quantum dot attached to the end of a lambda dsDNA molecule freely floating in the stream of chamber buffer. The average max. and min. of the light intensity is indicated by the dotted red and blue lines respectively.

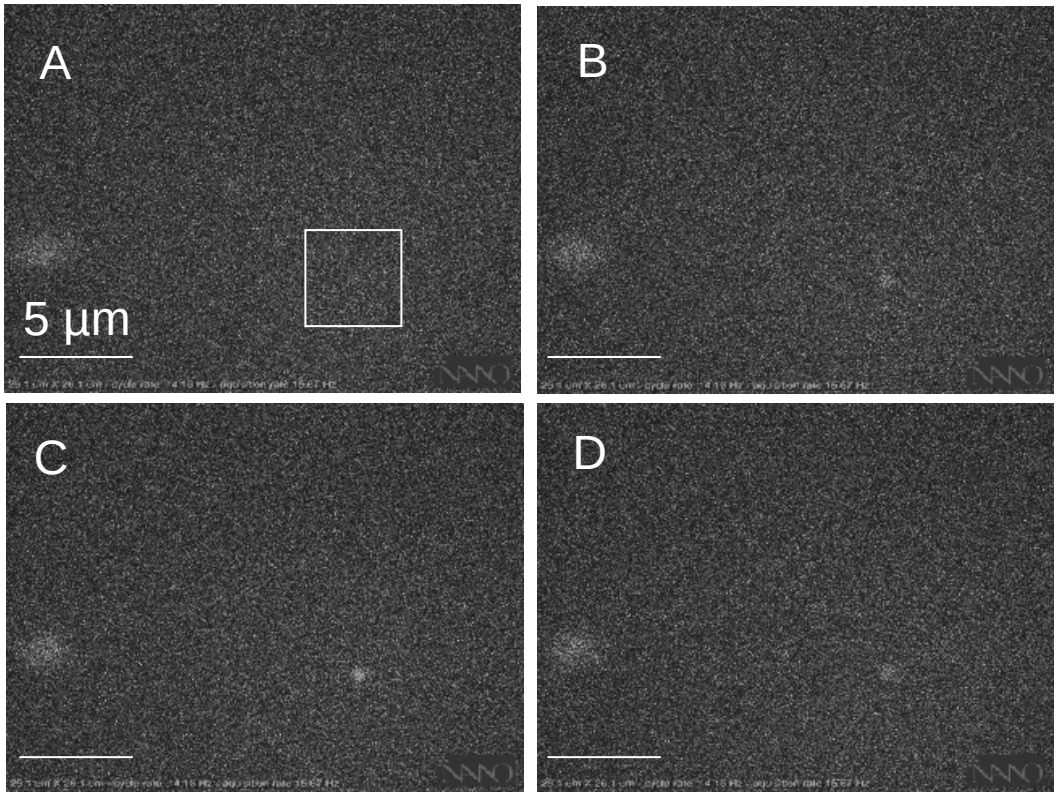

Figure 5A–D *Consecutive images (rate every 50 ms) of a Q–dot attached via streptavidin to a biotinylated λ DNA and bars are of 5 µm.*

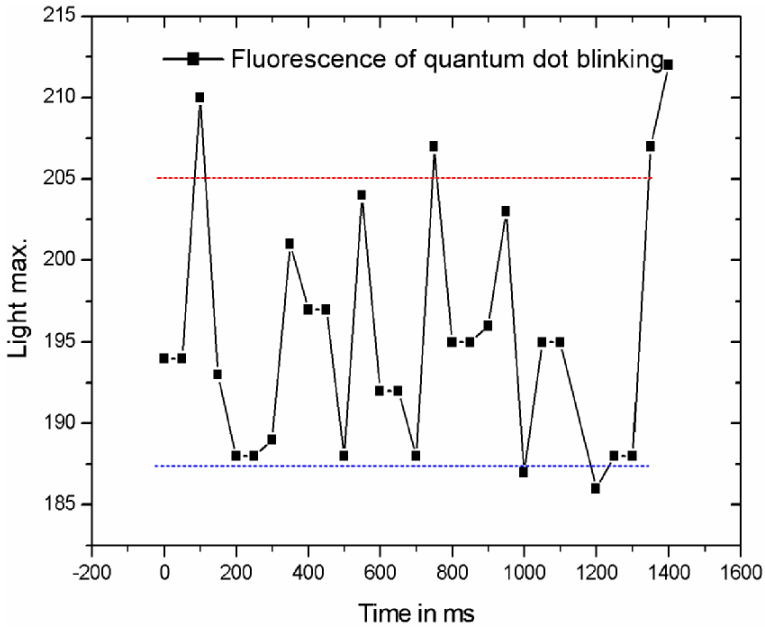

Figure 5E. *Intensity variation during image recording from the region of interest (ROI) containing the blinking quantum dot.*

ii)Visualization of single alexa dyes.

Fig.6A-D show the fluorescent images and subsequent bleaching of individual Alexa−488 fluorophors coupled to the end of λ DNA. Fig. 6E shows the response of alexa dye (light max versus time) exposed to blue laser (Argon ion) 488 nm. The decrease in light intensity overtime indicates the photo bleaching of the organic fluorophore alexa in solution.

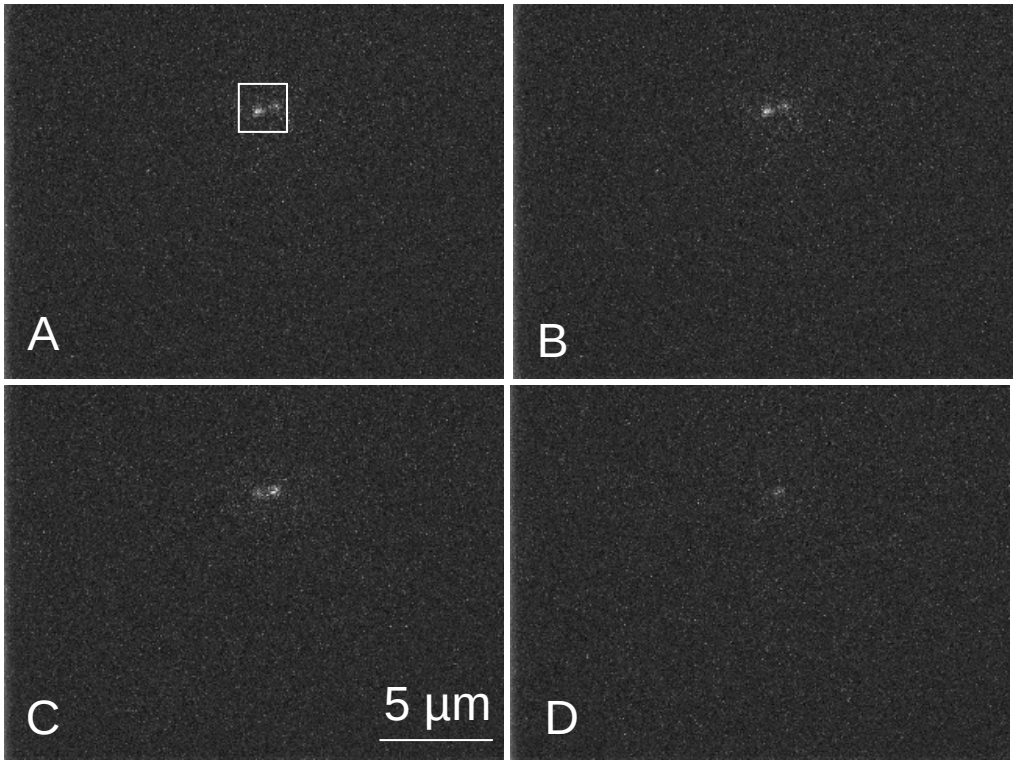

***Figure 6A–D**. consecutive imaging of individual Alexa−488 dyes attached to lambda DNA.*

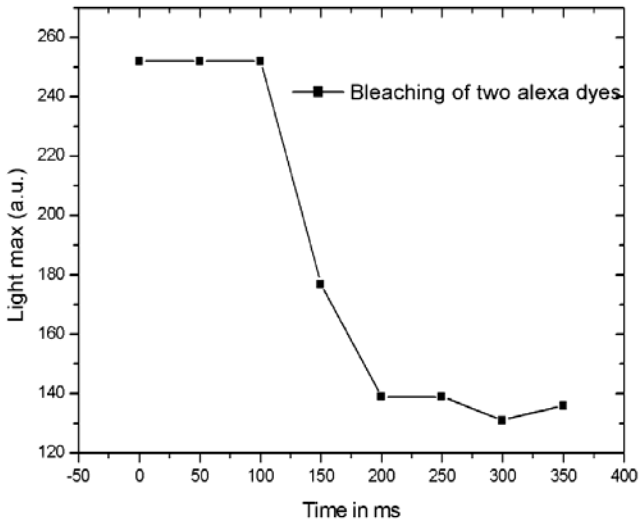

***Figure 6E**. Emission intensity of observed Alexa−488 dyes versus time. The decrease indicates the photobleaching.*

We observed as expected that the semiconductor quantum dots are much brighter/nm^2 and more photo–stable than the organic fluorophores. It is important to have bright fluorophores which allow easier observation of single–molecule experiments in living cells. Long-lasting fluorophores may reveal both, fast and slow processes in molecules so that slow changes in kinetic properties of a biomolecule may be studied in detail. It is important to note that the Q–dots have a bigger absorption cross section than organic dyes and require different excitation intensity.

5.6.3 Trapping and manipulation of mitochondria

Figure 7A–D shows fluorescence images of trapping and manipulation of mitochondria labeled with GFP. In collaboration with the group of Prof. W. Voos at the University of Freiburg, we investigate the transmembrane transport (import) of proteins in mitochondria. A first step as shown here in Figure 7A–D is the manipulation and immobilization of complete mitochondria organelles on polystyrene spheres.

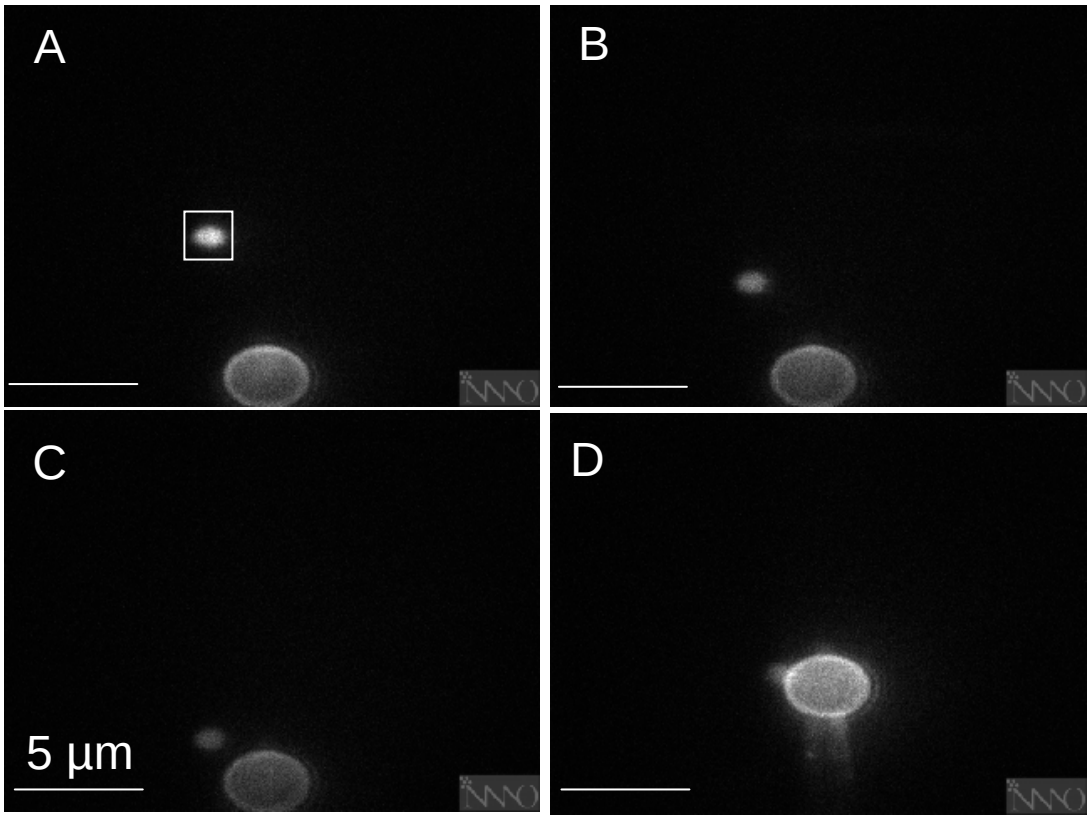

Figure 7. *Manipulation and attachment of functional mitochondria to aldehyde activated polystyrene spheres.*

5.7 Conclusion and Outlook

The key to our developed setup was to find the right combination of dichoric mirrors, dyes, filters and automation of the instrument. An appropriate selection was found and allow now to obtain high detection efficiency of fluorescent signals in combination to optical trapping manipulation.

We believe that the combined optical trap and single-molecule fluorescence detection method will enhance the traditional single-molecule studies of proteins such as the molecular motors kinesin and myosin etc. Force-induced mechanical transitions are challenging to interpret, due to difficulties in determining the precise location at which an applied force produced a conformational change. The combined approach will shed light on the information about the structure and mechanics of a single macromolecule by pinpointing the locations of structural transitions.

This instrument is ready to monitor the intramolecular distances by FRET. Plenty of new fluorescence measurements, on an optically trapped macromolecule, can be performed which were previously not feasible. In order to use FRET to monitor distance changes (particularly for conformational changes), the rotational freedom of the attached fluorescent dyes is one of the challenge and must be understood in greater detail. In our instrument the biomolecule should be in focus with the objective lens (focal plane) to allow efficient information collection. Molecules out of focus are not able to report on the molecular scale.

Applications

There are lots of models and hypotheses which can now be tested with the combined setup. The effects of applied external mechanical load on single–enzyme turnovers, biomolecular interactions and conformational changes can now be studied with nanometer precision and millisecond time resolution. Following are the some examples listed where one can use OT and SMF at the same time.

1. Pairs of fluorescent tags can be inserted at the target sites on the biomolecule (e.g. DNA) to probe the conformational changes induced by force spectroscopy (B–to S–DNA transition).

2. Protein folding and unfolding (individual domains or binding sites) can be studied by monitoring the changes in relation to end to end distances detected by optical trap and to reveal the external forces exerted during conformational changes.

3. Conformational changes of chaperonin complexes (opening or closure of the lid) may be monitored by attaching a fluorescent tags to it whereas the force exerted on a bound protein can be measured with optical tweezers.

4. Molecular motors: conformational changes and force production of motor proteins during ATP hydrolysis, coupling between the biochemical and mechanical events can be observed. In such experiments, simultaneous recording of motor motions detected with the optical trap and the binding and unbinding of fluorescent substrates can supply information about the relative timing of events.

5. Displacements of enzymes (e.g. polymerases) and conformational changes can be followed by applying different loads (forces) with nanoscale biochemical changes.

6. Helicases are the proteins responsible for the unwinding of double-stranded DNA in the replication during cell duplication. By individually fluorescent labeling both strands of DNA with a FRET pairs, the change in energy transfer efficiency can be monitored as the double-stranded sequence is unwound by the helicase (48).

5.8 References

1. Hirschfeld, T. (1976) Optical microscopic observations of single small molecules. *Appl. Opt.*, **15**, 2965-2966.
2. Förster, T. (1965). *Modern Quantum Chemistry (Sinanoglu, O., Ed.)*, **37**, 93-137.
3. Ha, T. (2001) Single-Molecule Fluorescence Resonance Energy Transfer. *Methods*, **25**, 78-86.
4. Lakowicz, J.R. (1999) Principles of Fluorescence Spectroscopy. 367 -371.
5. McKinney, S.A., Declais, A.-C., Lilley, D.M.J. and Ha, T. (2003) Structural dynamics of individual Holliday junctions. *Nat. Struct. Biol.*, **10**, 93 - 97.
6. Zhuang, X.W., Kim, H., Pereira, M.J.B., Babcock, H.P., Walter, N.G. and Chu, S. (2002) Correlating structural dynamics and function in single ribozyme molecules. *Science*, **296**, 1473-1476.
7. Ha, T., Rasnik, I., Cheng, W., Babcock, H.P., Gauss, G.H., Lohman, T.M. and Chu, S. (2002) Initiation and re-initiation of DNA unwinding by the Escherichia coli Rep helicase. *Nature*, **419**, 638 - 641.
8. Ashkin, A., Dziedzik, J.M., Bjorkholm, J.E. and Chu, S. (1986) Observation of a single-beam gradient force optical trap for dielectric particles. *Opt. Lett.*, **11**, 288-290.
9. Schnitzer, M.J., Visscher, K. and Block, S.M. (2000) Force production by single kinesin motors. *Nat. Cell Biol.*, **2**, 718-723.
10. Veigel, C., Coluccio, L.M., Jontes, J.D., Sparrow, J.C., Milligan, R.A. and Molloy, J.E. (1999) The motor protein myosin-I produces its working stroke in two steps. *Nature*, **398**, 530-533.

11. Hegner, M., Smith, S.B. and Bustamante, C. (1999) Polymerization and mechanical properties of single RecA-DNA filaments. *Proc. Natl. Acad. Sci. USA*, **96**, 10109-10114.
12. Kawaguchi, K. and Ishiwata, S. (2001) Nucleotide-dependent single-to double-headed binding of kinesin. *Science*, **291**, 667-669.
13. Miyata, H., Yasuda, R. and Kinosita, K.J. (1996) Strength and lifetime of the bond between actin and skeletal muscle-actinin studied with an optical trapping technique. *Biochim. Biophys. Acta*, **1290**, 83-88.
14. Nishizaka, T., Miyata, H., Yoshikawa, H., Ishiwata, S. and Kinosita, K.J. (1995) Unbinding force of a single motor molecule of muscle measured using optical tweezers. *Nature*, **377**, 251-254.
15. Sun, Y.L., Luo, Z.P. and An, K.N. (2001) Stretching Short Biopolymers Using Optical Tweezers. *Biochem. Biophys. Res. Commun.*, **286**, 826-830.
16. Wang, M.D., Yin, H., Landick, R., Gelles, J. and Block, S.M. (1997) Stretching DNA with optical tweezers. *Biophys. J.*, **72**, 1335-1346.
17. Smith, S.B., Cui, Y. and Bustamante, C. (1996) Overstretching B-DNA: the elastic response of individual double-stranded and single-stranded DNA molecules. *Science*, **271**, 795-799.
18. Cui, Y. and Bustamante, C. (2000) Pulling a single chromatin fiber reveals the forces that maintain its higher-order structure. *Proc. Natl. Acad. Sci. U S A*, **97**, 127–132.
19. Funatsu, T., Y, H., Tokunaga, M., Saito, K. and Yanagida, T. (1995) Imaging of single fluorescent molecules and individual ATP turnovers by single myosin molecules in aqueous solution. *Nature*, **374**, 555-559.
20. Xie, X.S. and Lu, H.P. (1999) Single-molecule enzymology. *J. Biol. Chem.*, **274**, 15967-15970.
21. Edman, L. and Rigler, R. (2000) Memory landscapes of single-enzyme molecules. *Proc. Natl. Acad. Sci. U S A*, **97**, 8266-8271.
22. Deniz, A.A., Laurence, T.A., Beligere, G.S., Dahan, M., Martin, A.B., Chemla, D.S., Dawson, P.E., Schultz, P.G. and Weiss, S. (2000) Single-molecule protein folding: diffusion fluorescence resonance energy transfer studies of the denaturation of chymotrypsin inhibitor 2. *Proc. Natl. Acad. Sci. USA*, **97**, 5179-5184.
23. Jia, Y.W., Talaga, D.S., Lau, W.L., Lu, H.S.M., DeGrado, W.F. and Hochstrasser, R.M. (1999) Folding dynamics of single GCN4 peptides by fluorescence resonant energy transfer confocal microscopy. *Chem. Phys.*, **247**, 69-83.
24. Sako, Y., Minoghchi, S. and Yanagida, T. (2000) Single-molecule imaging of EGFR signalling on the surface of living cells. *Nat. Cell. Biol.*, **2**, 168-172.
25. Harms, G.S., Cognet, L., Lommerse, P.H.M., Blab, G.A., Kahr, H., Gamsjager, R., Spaink, H.P., Soldatov, N.M., Romanin, C. and Schmidt, T. (2001) Single-molecule imaging of L-type Ca2+ channels in live cells. *Biophys. J.*, **81**, 2639-2646.
26. Mashanov, G.I., Tacon, D., Knight, A.E., Peckham, M. and Molloy, J.E. (2003) Visualizing single molecules inside living cells using total internal reflection fluorescence microscopy. *Methods*, **29**, 142-152.
27. Finer, J., Simmons, R. and Spudich, J. (1994) Single myosin molecule mechanics: piconewton forces and nanometer steps. *Nature*, **368**, 113-119.

28. Svoboda, K., Schmidt, C.F., Schnapp, B.J. and Block, S.M. (1993) Direct observation of kinesin stepping by optical trapping interferometry. *Nature*, **365**, 721-727.
29. Sakakibara, H., Kojima, H., Sakai, Y., Katayama, E. and Oiwa, K. (1999) Innerarm dynein c of Chlamydomonas flagella is a single-headed processive motor. *Nature*, **400**, 586-590.
30. Yin, H., Wang, M.D., Svoboda, K., Landick, R., Block, S.M. and Gelles, J. (1995) Transcription against an applied force. *Science*, **270**, 1653-1657.
31. Vale, R.D., Funatsu, T., Pierce, D.W., Romberg, L., Harada, Y. and Yanagida, T. (1996) Direct Observation of Single Kinesin Molecules Moving Along Microtubules. *Nature*, **380**, 451-453.
32. Molloy, J.E., Kendrick-Jones, J., Veigel, C. and Tregear, R.T. (2000) An unexpectedly large working stroke from chymotryptic fragments of myosin II. *FEBS Lett.*, **480**, 293-297.
33. Iwane, A.H., Funatsu, T., Harada, Y., Tokunaga, M., Ohara, O., Morimoto, S. and Yanagida, T. (1997) Single-Molecular Assay of Individual ATP Turnover by a Myosin-GFP Fusion Protein Expressed in Vitro. *FEBS Lett.*, **407**, 235-238.
34. Dickson, R., Norris, D., Tzeng, Y. and Moerner, W. (1996) Three-Dimensional Imaging of Single Molecules Solvated in Pores of Poly(Acrylamide) Gels. *Science*, **274**, 966-968.
35. Dickson, R.M., Cubitt, A.B., Tsien, R.Y. and Moerner, W.E. (1997) On/off blinking and switching behaviour of singlemolecules of green fluorescent protein. *Nature*, **388**, 355-358.
36. Harada, Y., Funatsu, T., Murakami, K., Nonoyama, Y., Ishihama, A. and Yanagida, T. (1999) Single-Molecule Imaging of RNA Polymerase-DNA Interactions in Real Time. *Biophys. J.*, **76**, 709-715.
37. Wuite, G.J.L., Smith, S.B., Young, M., Keller, D. and Bustamante, C. (2000) Single-molecule studies of the effect of template tension on T7 DNA polymerase activity. *Nature*, **404**, 103-106.
38. Noji, H., Yasuda, R., Yoshida, M. and Kinoshita, K. (1997) Direct observation of the rotation of rotation of F_1-ATPase. *Nature*, **386**, 299-302.
39. Ting, A.Y., Ha, T.J., Liang, J., Caldwell, W.B., Deniz, A.A., Chemla, D.S., Schultz, P.G. and Weiss, S. (1999) Single-Molecule Fluorescence Spectroscopy of Enzyme Conformational Dynamics and Cleavage Mechanism. *Proc. Natl. Acad. Sci. USA*, ***96***, 893-898.
40. Schutz, G.J., Trabesinger, W. and Schmidt, T. (1998) Direct Observation of Ligand Colocalization on Individual Receptor Molecules. *Biophys. J.*, **74**, 2223-2226.
41. Lu, H.P., Xun, L.Y. and Xie, X.S. (1998) Single-Molecule Enzymatic Dynamics. *Science*, **282**, 1877-1882.
42. Ha, T., Ting, Y.A., Liang, J., Caldwell, W.B., Deniz, A.A., Chemla, D.S., Schultz, P.G. and Weiss, S. (1999) Single-molecule fluorescence spectroscopy of enzyme conformational dynamics and cleavage mechanism. *Proc. Natl; Acad. Sci.*, **96**, 893-898.
43. Ha, T., Zhuang, X., Kim, H.D., Orr, J.W., Williamson, J.R. and Chu, S. (1999) Ligand-induced conformational changes observed in single RNA molecules. *Proc. Natl. Acad. Sci. U S A*, **96**, 9077-9082.

44. Zhuang, X., Bartley, L.E., Babcock, H.P., Russell, R., Ha, T., Herschlag, D. and Chu, S. (2000) A Single-Molecule Study of RNA Catalysis and Folding. *Science*, **288**, 2048-2051.
45. Ishijima, A., Kojima, H., Funatsu, T., Tokunaga, M., Higuchi, H., Tanaka, H. and Yanagida, T. (1998) Simultaneous Observation of Individual ATPase and Mechanical Events by a Single Myosin Molecule During Interaction with Actin. *Cell*, **92**, 161-171.
46. Lang, M.J., Fordyce, P.M. and Block, S.M. (2003) Combined optical trapping and single-molecule fluorescence. *Journal of Biology*, **2**, 6.1-6.4.
47. Grange, W., Husale, S., Güntherodt, H.-J. and Hegner, M. (2002) Optical tweezers system measuring the change in light momentum flux. *Rev. Sci. Instr.*, **73**, 2308 - 2316.
48. Murphy, M.C., Rasnik, I., Cheng, W., Lohman, T.M. and Ha, T. (2004) Probing Single-Stranded DNA Conformational Flexibility Using Fluorescence Spectroscopy. *Biophys. J.*, **86**, 2530-2537.

6.1 Conclusion

We have presented a series of experiments with small molecules binding to dsDNA that culminated in the ultimate goal of measuring mechanical changes of single dsDNA or ssDNA induced by DNA binding agents. Most of the results obtained in these experiments are generally applicable and suggest further experiments. The investigated fundamental mechanical properties can be used for the discrimination and identification of different binding modes of the ligands and, furthermore, may be relevant for various processes such as nucleosome packing, medical applications like cancer or gene therapy. In the near future, scientists might achieve more efficient gene transfer with the recommended compounds evaluated in our studies.

Single molecule studies of dsDNA denaturation (melting of hydrogen bond) by NaOH show a first order transition which provides additional details for the verification of current DNA denaturation theories. Whereas overstretching transition and denaturation of dsDNA at physiological conditions has remained elusive even though it can be visualized by video microscopy. The results obtained offer interesting details not only from the point of view of biology, but also from a statistical physics standpoint.

The main goal of single-molecule manipulations is to access the machinery of a living cell. We investigated the molecular machinery of VirE2 protein involved in bacterial infections in plant cells. New details such as the single molecule kinetics showed that VirE2 proteins act as powerful machinery, capable of producing work up to 50 pN external load while coating ssDNA at a rate larger than 500 VirE2 per second. ssDNA-binding VirE2 proteins could be solely responsible for pulling ssDNA into the host cell cytoplasm. Our experiments shed light on the unknown questions in the field of single molecule biophysics and biochemistry and support the ongoing investigations of this protein.

With the implementation of combined OT and SMF, it is possible to look at complex molecular systems at a single molecule level and reveal behavior which would be neglected due to averaging in traditional biochemistry experiments. This instrument is

ready to monitor the intramolecular distances on a local scale by FRET. Plenty of new fluorescence measurements, on an optically trapped macromolecule, can now be performed which were previously not feasible. The results will undoubtedly yield new insights into structural, energetic and kinetic aspects of the functioning of a wide variety of biological machines such as the molecular motors – e.g. DNA polymerases and kinesin.

On the other hand, single molecule fluorescence investigation of the structural dynamics based on the mechanical activity, has not been studied in great detail here. Much still remains to be done in this field and some examples are listed here.

Future biological experiments

1. Pairs of complementary fluorescent tags can be inserted at the target sites on the biomolecule (e.g. DNA) to probe the conformational changes induced by force spectroscopy (B– to S–DNA transition).
2. Protein folding and unfolding (individual domains or binding sites) can be studied by monitoring the changes in relation to end to end distances detected by optical trap and to reveal the external forces exerted during conformational changes.
3. Conformational changes of chaperonin complexes (opening or closure of the lid) may be monitored by attaching a fluorescent tags to it whereas the force exerted on a bound protein can be measured with optical tweezers.
4. Molecular motors: conformational changes and force production of motor proteins during ATP hydrolysis, coupling between the biochemical and mechanical events can be monitored. In such experiments, simultaneous recording of motor motions detected with the optical trap and the binding and unbinding of fluorescent substrates can supply information about the relative timing of events.
5. Displacements of enzymes (e.g. polymerases) and conformational changes can be followed by applying different loads (forces) with nanoscale biochemical changes.
6. Helicases are the proteins responsible for the unwinding of double-stranded DNA during replication and cell duplication. By individually fluorescent labeling both strands of DNA with a FRET pairs, the change in energy transfer efficiency can be monitored as the double-stranded sequence is unwound by the helicase.

In conclusion with combined OT and SMF, biologists will be able to manipulate single biomolecules (non-invasively) with nanometer precision, sub-piconewton resolution with single molecule fluorescence. All these things can now be performed with a single instrument which promises revolutionary advances across many disciplines.

6.2 Appendix A: DNA modifications for OT experiments

6.2.1 Preparation of λ DNA (biotinylation)

Sample	Stock conc.	Volume	Final conc.
Lambada DNA	0.25µg/µl	40 µl	10 µg
Biotin 14 dCTP	0.4mM	12.5 µl	50 µM
Biotin 14 dATP	0.4 mM	12.5 µl	50 µM
dGTP	1mM	10 µl	100 µM
dTTP	1 mM	10 µl	100 µM
Klenow exo$^-$	5 unit/µl	5 µl	2.5 units/µg DNA
Neb 2 buffer	10x	10 µl	1x
		100 µl	

Steps

First incubate the DNA sample at 65° C for 20 min. Then decrease the temperature of tube upto 37°C and add the remaining recipe. Incubate this for 30 min and hold finally at 4°C. Since EDTA prevents the activity of degrading enzyme, refill the tube with chamber buffer 150 mM NaCl, 10 mM HEPES, 1 mM EDTA, 1.5 mM sodium azid or add EDTA 1mM.

Spin the sample 7 times with sartorius column 10K or 5K at rpm 4K to clean the excess of biotinylated nucleotides. 5K coloumn is the best choice for the recovery of DNA sample.

6..2.2 Alexa 488 streptavidin dye coupling to λ DNA

Sample	Stock conc.	Volume	Final conc.
Lambda DNA	112 pM	55µl	82 pM
Alexa 488	4 nM	20µl	1 nM
		70 µl	

6.2.3 Coupling of Quantum dot to lambda DNA

Sample	Stock conc.	Volume	Final conc.
Lambda DNA	116 pM	24 µl	93 pM
Qdot	2 nM	3 µl	200 pM
Chamber buffer (150 mM NaCl)		3 µl	
		30 µl	

Incubation for 40 minutes, use shaker 2.

Since there are 12 biotins on the sticky ends of the lambda DNA, we choose to have only 2 Qdot per DNA.

Resuspend the smaple with 500µl of 150 mM chamber buffer therefore the final concentration of the DNA will be 5.6 pM.

6.2.4 λ DNA preparation for fluorescence experiments

Nice fluorescence images of lambda DNA were achieved with the SYBR® Green.

Following are the steps to perform experiment with SYBR® Green.

1. Make sure the attachment of lambada DNA in between two beads.
2. Flow 5 to 10 µl of 0.1x Sybrgreen. (10000 dilution).
3. Flow the chamber buffer which consist of antibleaching buffer (each at 1x concentration) as given below.

Glucose (100x- 2.3 g in 10 ml, 1.27 M), Glucose oxidase (100x- 10 mg/ml, 5mg + 250µl H_20 + 250µl Glycerol), Catalase (100x- 3.6 mg/ml, 3.8mg + 5.28ml H_20 + 5.28ml Glycerol), 2-mecapthoethanol (75x, 1.5 M).

6.2.5 Modification of DNA with the help of PCR amplification technique

1. To Modify DNA (for stretching experiments with Optical tweezers) by DNA amplification technique (PCR).
2. Use company plasmid PTYB1 (7477 bp) (brought from New England Biolabs) as a template to design forward and reverse primers for the amplification process.
3. Design a primer such that one primer must be complementary to one strand of the double helix while the other primer should complementary to the other strand.
4. According to our design, forward primer is 5' Thiol_TGT AAC TCG CCT TGA TCG TTG GGA 3' (start at 607) and reverse primer 5' AGC GGA TAC ACC AGG ATT TGT CGT 3' (start at 7194) (ordered from Microsynth company).
5. Carry out the three parts of the polymerase chain reaction in the same tube, but at different temperatures. In the first part of the process separate the two DNA strands of the double helix. Do it simply by heating the tube to 94°C for 10 sec.
6. To bind the primers to the DNA strands, cool the tube to 57° C. At this temperature, the primers bind (anneal) to the ends of the DNA strands. This takes about 30 seconds.

7. The final step of the reaction is to make a complete copy of the templates. Since the enzyme, expand long template PCR works best at around 68°C therefore raise the temperature of the tube to 68°C. The Expand long template PCR enzyme adds nucleotides to the primer and makes a complementary copy of the template. The working of enzyme is as follows. If the template contains an A nucleotide, the enzyme adds a T nucleotide to the primer. If the template contains a G, it adds a C to the new chain, and so on till the end of the DNA strand. This completes one PCR cycle which takes approximately six minutes (rate ~ 1000 bp/min).

At the end of a cycle, each piece of DNA in the tube will be duplicated to 6587 base pairs and repeat the cycle to 25 times. After amplification of DNA, cut it asymmetrically with Hind III enzyme to have 4 base pair overhangs (AGCT). Then use the Klenow exo$^-$ enzyme to fill the overhangs with biotinylated nucleotides (dUTP, dCTP, dATP) and dGTP. Final length of DNA should be 5623 bp. The thiol group at 5 prime end will help to couple DNA to amino modified polystyrene beads.

6.2.5.1 Rciepe for the preparation of PCR DNA (5623bp):
Template pTYB1 and enzyme is expand long template PCR.

Sample	Stock conc.	Volume	Final conc.
Buffer 1	10 x	50 µl	1x
pTYB1-pcr_ forward primer	10 µM	15 µl	300 nM
pTYB1-pcr_ reverse primer	10 µM	15 µl	300 nM
dNTPs (A,C,G,T)	1 mM	175 µl	350 µM
Template pTYB1	0.2 µg/µl	1 µl	200 ng
*Hotstart “expand long template”		3.75 µl x2	
H_2O		236 µl	
		500 µl	

* We split the above sample in two tubes each of 250 µl. The enzyme was added at the temperature of 94^0C.

Following are the cycles performed in PCR.

(0) 2min for 94^0C, (1) 10x { 94^0C for 10 sec, 57^0C for 30 sec, 68^0C for 5 min.}, (2)7x { 94^0C for 15sec, 57^0C for 30 sec, 68^0C for 6 min.}, (3) 8x { 94^0C for 15 sec, 57.5^0C for 30 sec, 68^0C for 7 min.}, (4) 7 min for 68^0C.

Digestion of above sample with Hind III enzyme

Sample	Stock conc.	Volume	Final conc.
Ptyb1_sample (above)		500 µl	15 µg
Neb buffer2	10x	57 µl	1x
HindIII	20 units/µl	8 µl	10 units/µg DNA
H_2O		5 µl	
		570 µl	

HindIII digestion at 37^0C for 5 hours, heat shock at 65^0C for 20 minutes.
Keep 40 µl of above sample for electrophoresis gel to check the quality of final product. Use the PCR columns two times to get rid of excess nucleotides.

After digestion the overhangs is AGCT, we use Klenow exo$^-$ to incorporate the biotin nucleotides.

Sample	Stock conc.	Volume	Final conc.
pTYB1_sample (digested)		33 µl	10 µg
Ecopol Buffer	10x	6 µl	1x
Biotin dCTP	400 µM	3 µl	20 µM
Biotin dUTP	400 µM	3 µl	20 µM
Biotin dATP	400 µM	1.5 µl	20 µM
dGTP	1 mM	2 µl	33 µM
dATP	1 mM	0.6 µl	10 µM
Klenow exo$^-$	5 unit/µl	10 µl	5 u/µg of DNA
		60 µl	

Incubation at 37^0 for 40 min plus heat shock at 65^0 for 20 minutes.

Use 10K column to clean the excess of biotin from the above product. 7x is the optimal cleaning. Final product contains 5623bp as well as 900bp small extensions. That's why subtract the 15% amount from the final quantity to get the concentration of DNA.

6.2.6 Coupling of PCR_pTYB1 DNA to 2.18 amino beads

Scheme $RNH_2^- + Sulfo - SMCC + HS - DNA \rightarrow RNH - Maleimides - HS - DNA$
Chemical reaction is as shown below,
Steps
1. Cleaning of 20 µl beads with HEPES 20 mM pH 7.5, 3 times.
2. Activation in 300 µl HEPES 20 mM pH 7.5 for 1 hour.
Weight of sulfo-SMCC = 3 mg in 450 µl total = 15 mM.
Concentration of (NH_2) groups = $\frac{20}{300} x360\ \mu M = 24\mu M$

(concentration of sulfo-SMCC is 625 times more than the concentration of NH_2 groups).
3. Cleaning of excess of SMCC or stop the reaction with the buffer MES 1 mM at pH 6.0, total 7 times.
4. Preparation of coupling buffer 7X: 700 µl 5 M NaCl, 280 µl HEPES pH 7, 0.25 M, 35 µl EDTA of 0.2 M pH 8, 1 µl of TCEP (3 mg in 100ul , 5 µl of it in 145 µl).
5. Final volume of coupling is

14 µl of DNA + cleaned 2 µl bead (from step 3) + 2 µl 7x coupling buffer.

Approximately ratio is 1400 DNA/bead.

Important notes

Most of the beads from companies are delivered with anti microbacterial compound, that's why clean it with HEPES pH 7.5.

For pH = 7.5, efficiency of NH_2:NH_3 is 1:1000, use high concentration of crosslinkers use ~1000 cross linkers per amino group.

Some cross linkers are not bind in tube reaction, to stop reaction use buffer 1mM MES, pH = 6. Store it on ice because maleimides is not very active at this temperature. To break S-H bond use TCEP.

TCEP is unstable with water (that's why not to be prepared in advance)

TCEP in H_2O is stable @ neutral pH 6.5 –7.5 for 20 min.

Keep coupling volume of the final reaction small to enhance the probability HS-DNA colliding with active bead.

Note: If you ligate small fragments to big fragment, avoid excess of small fragments in this reaction relative to big fragment. 250 small per one big fragment is optimal concentration. Highest concentration of big molecules should not exceed 10 nM.

Use elutrap to separate the small extension then change buffer to coupling buffer. Å

Use column filter (5K or 10K) to get rid of nucleotide. Don't reduce the number of cleaning cycles, these reactions are performed @ mM concentrations. The activating substances have to be reduced by cleaning to pM or fM to not compete later or inactivate the nM DNA targets before successful coupling.

*Hints to calculate the molarity of NH_2 groups: e.g.

Bead surface area = $4\pi r^2 = 32.15 x 10^{-12}\ M$

Area of reactive group = $134\ Å^2 = 134\ x\ 10^{-20}\ M$

Groups/beads = $\frac{32.15 x 10^{-12}}{134 x 10^{-20}} = 0.239 x 10^8$

Beads/liter = $2.3 x 10^{12}$

Total beads x groups/ liter = 2.3 x 10^{12} x 0.239 x 10^{8} = 0.55 x 10^{20}

Molarity = $\frac{0.55 x 10^{20}}{6.023 x 10^{23}} = 91.6 \mu M$

6.2.7 DNA Modification Procedure 2

Target:

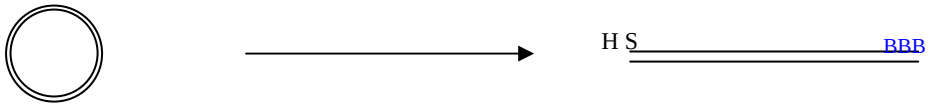

DNA Plasmid Modified DNA

Step 1. Digestion

Cut the plasmid (PTYB1, 7447 bp) asymmetrically with BsaI enzyme

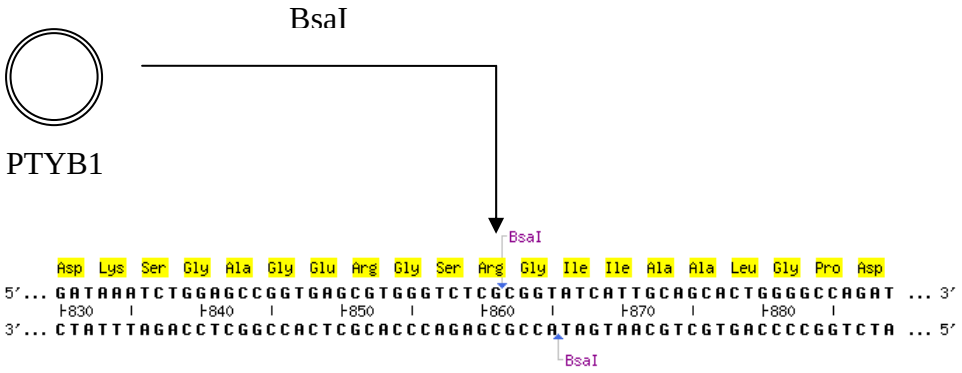

Two overhangs are (a) ———— CTCG…….3'
———————— GCCA.....5'

Note: useful for ligation of small fragment.

(b) CGGT———————————— .....5'
TAGT ———————————.....3'

Note: useful for biotinylation.

Step 2. Preparation of small extension:

Hybridisation of BamlangI with IV

Bamlang I GCCGAACTACCCCACGGAAG……..3'

Bamlang IV CGGTCTTCCGTGGGGTAGTTCGGC…..3'

Hybridization

CGGTCTTCCGTGGGGTAGTTCGGC……3'
GAAGGCACCCCATCAAGCCG …...5'

Step 3. Ligation of small fragment to big [note: To overhang (a)]

5`——————— CTCG CGGTCTTCCGTGGGGTAGTTCGGC……3'
3`——————————— GCCAGAAGGCACCCCATCAAGCCG …...5'

Step 4. Biotinylation with Klenow exo$^-$

Note: Fill in biotin at 3' end of overhang (b)

CGGT ——————————— .....5'
GCCA TAGT——————————— .....3'
B B B

6.2.7.1 Recipe for DNA modification procedure 2

Digestion of pTYB1 plasmid with BSA I

Sample	Stock conc.	Volume	Final conc.
pTYB1 plasmid	0.185 µg/µl	40 µl	7.4 µg
Buffer 3	10x	5.5 µl	1x
BSA I	5 unit/µl	7.5 µl	5 unit/µg DNA
H_20		2 µl	
		55 µl	

Incubation at 50°C for 4 hours, heat shock at 65°C for 20 minutes, final hold at 4°C.

Hybridization of two oligos:

Sample	Stock conc.	Volume	Final conc.
Bamlang I (THI)	82 µM	249 µl	50 µM
Bamlang IV	408 µM	50 µl	50 µM
NaCl	5 M	4.1 µl	50 mM
H_20		104	
		408 µl	

Ligation of small extension (oligos) to digested pTYB1

Sample	Stock conc.	Volume	Final conc.
pTYB1 digested	30 nM	50 µl	4.3 nM (7.4µg)
NaCl	5 M	3.5 µl	50 mM
pTYB1small extension	50 µM	30 µl	4.3 µM
Buffer ligase	10 x	35 µl	1x
Enzyme ligase (NEB)		3 µl	
H_20		228.5 µl	
		350 µl	

Gel and Elutrap: to separate small extensions from big and to recover sample from gel. Sample recovered from elutrap ~1 ml, reduce it to 57 µl by using 10k column.

Incorporation of biotinylated nucleotides: Klenow exo$^-$ reaction

Sample	Stock conc.	Volume	Final conc.
pTYB1 (after elutrap)	3 µg	57 µl	9 nM
Eco pol buffer	10x	7 µl	1x
Klenow exo-	5 unit /µl	3 µl	5u/µg DNA
14 dCTP biotin	400 µM	1.5 µl	8.5 µM
14 dATP biotin	400 µM	1.5 µl	8.5 µM
dGTP	1 mM	0.5 µl	7 µM
		70 µl	

Clean with 10 K column 7 times.

6.3 Appendix B

Optical Tweezers: Operators Instruction Manual

1. Turn on the three electrical switches (brown buttons) those are located on the back of optical table.
2. Turn on the power supply battery plus toggle switch (named EIN on NI-130 board) of LED, detector and air pressure bottle sensor.
3. Switch on PXI 1002.
4. Switch on the PC and TV screen.
5. Launch Lab view 6.1, open D/Tweezers/ Init/initialisation.vi and run it.
6. Open GPIB/High_resolution/Press+PI.vi run it. First press 04 button of the joystick for ventilation. Then turn on the air pressure. There are three options PI, Shutter and Pressure. PI is basically for the movement of micropipette. Position no. 1, 2 and 3 are for the movement in X, Y and Z directions respectively. Limit of Z direction is 0 to 20 µm. Keep always at 10, which is the initial position. By pressing shutter select your desired operation. Press pressure option for the selection of respective valve of your buffer solution. To apply pressure use Joystick buttons. 02 to apply pressure, 03 for vacuum and 04 for ventilation. Toggle switch (like throat) is for the movement of micropipette in X and Y direction.
7. Then turn on the power and output of temperature controller as well as laser diode driver of front and back laser. Do not to go high i.e. 250mA, instead it use 220 mA current supply.
8. Place the chamber on Piezo-Platform (Thorlabs). Put the water inside two lenses. Remove the filter schott A, 375Df50 and approach with the front objective to see the laser spot (which on the sliding rail in front of IR ccd camera).
9. Open Detector/detector.vi and run it. Use it a) for the adjustment of pinhole to get the maximum power. At start maximum average power for front laser is 58 mW and for the back laser is 65 mW. b) Press Front and back detectors option and try to get red spot (indicating position of the respective, front or back laser on the detector) to centre with the help of X axis, Y axis plus and minus options available on vi. For the alignment first trap a bead with back laser

only, check the focus with IR ccd camera, then make red spot to centre, open dual trap, close back laser, correct the focus of bead with the help Z axis black screw of the Piezo table (Thorlabs, position is directing towards the ccd camera), now again open dual trap and press align button for the alignment. Repeat this procedure at least thrice for the perfect alignment. Check red spot of position detector is in the centre or not, if not then make it on centre as like front laser should be.

10. Switch the laser power supply plus pumping of 3rd laser. Open Newport-Gimbal/gimbal.vi and run it. Press Move to mean (relative) button then position on Newport universal motion controller should be 5.649999.
11. Check the focus of trapped bead of front laser and third laser is having same focus or not. If not then open Stage/stage.vi and run it by choosing the speed and direction options one can make same focus of trapped bead by front laser.
12. To check the Flow force open Detector/Lambda.vi and run it.
13. To measure the forces and counts, open Measure2/Main.vi and run it. Press Configure Data acquisition to select the desired parameters. Then press set region of interest, draw rectangle, stored the image, test it and press return. Press start acquisition for the measurement.
14. For fluorescence excitation switch on blue laser 488 nm, go to full power.
15. Turn on the power supply of acosto-optic modulator such that voltage should be 28 volt and current 0.48 amp. Power of Blue laser before polarizer and after objective lens is around 4.3 mW and power of 1st order at the beginning after iris is 1.5 mW. For information lenses on circular lens holders are on position 4 focal length is 300 mm, on position 5 - 500 mm and on position number 6 - 750 mm.
16. To see the first order blue laser and fluorescence on camera launch iXon then go to hardware/ shutter control option.
17. For selection of valve open Hamilton/Hamilton_new.vi and run it. Positions of valve of Hamilton one or two are shown by black, white, pink balls in the vi indicating number 1,2, 3 etc. starting from left.
18. Before filter schott A, 375Df50 there are two lenses one is Achromat LAC 181A 250 mm to know the exact position of trapped bead and blue laser spot and another is 300 mm uncoated to get the good image.

6.4 Appendix C: Curriculum vitae

Name: Husale Sudhir Charudatta

Nationality: Indian

Date of Birth: 05.07.1975

Languages known: English, Hindi, Marathi.

Present address: Vogesenstrasse 80, Basel- 4056, Switzerland.

Permanent address: Po: Deolalipravara, Tal: Rahuri, Dist: Ahmednagar, Pin: 413716, Maharashtra, India.

Email: **schusale@yahoo.com**

Sex: Male

Educational Qualifications:

Graduation: B.Sc. (Physics), 1995.
R.B.N.B. College, Shrirampur, Pune University, India.

Post Graduation: M.Sc. (Physics), 1998.
Ahmednagar College, Pune University, India.

M. Phil. (Biophysics): 2001.
Department of Physics, Pune University, India.
Project: "Development of Single beam Optical Tweezers".

PhD in Experimental Biophysics: 2005.
"**Single biomolecule studies using optical tweezers**".
Institute of Physics, University of Basel, Switzerland.

6.5 Appendix D: list and full text of published papers

1. Husale, S., Grange, W. and Hegner, M. (2002) DNA mechanics affected by small DNA interacting ligands. *Single Mol.*, **3**, 91-96.
2. Grange, W., Husale, S., Güntherodt, H.-J. and Hegner, M. (2002) Optical tweezers system measuring the change in light momentum flux. *Rev. Sci. Instr.*, **73**, 2308 - 2316.
3. Hegner, M., Gerber, C., Arntz, Y., Zhang, J., Bertoncini, P., Husale, S., Lang, H.P. and Grange, W. (2003) Biological Single Molecule Applications and Advanced Biosensing. *J. Chromatogr. Lib.*, **68**, 241-263.
4. Grange, W., Husale, S., Duckely, M., Engel, A. and Hegner, M. (2005) Mechanical properties and molecular machinery of VirE2-ssDNA filament investigated by optical tweezers. *To be submitted.*
5. Husale, S., Grange, W. and Hegner, M. (2005) Single-molecule studies of dsDNA denaturation induced by NaOH and force-mechanical pulling. *To be submitted.*
6. Husale, S., Grange, W., Bürgi, S., Giese, B. and Hegner, M. (2005) Effect of surfactant molecules binding to single dsDNA investigated by optical tweezers. *To be submitted.*

Single Mol. **3** (2002) 2-3, 91-96

DNA Mechanics Affected by Small DNA Interacting Ligands

Sudhir Husale, Wilfried Grange and Martin Hegner

NCCR Nanoscale Science, Institute of Physics
University of Basel
Klingelbergstrasse 82
CH-4056 Basel, Switzerland

Correspondence to
PD Dr. Martin Hegner
Institut für Physik
Universität Basel
Klingelbergstrasse 82
CH-4056 Basel, Switzerland
phone **41-61-267 37 61*
fax **41-61-267 37 84*
email *Martin.Hegner@unibas.ch*

submitted *15 Apr 2002*
accepted *22 Jun 2002*
published *29 Jun 2002*

keywords: Optical Tweezers, DNA mechanics, DNA modification, Force Spectroscopy, DNA ligands

Abstract

We have investigated the mechanics of individual DNA strands exposed to DNA binding ligands. The interaction of these agents with individual dsDNA strands measured by optical tweezers clearly indicates the ligand-DNA binding mode. As expected, if the compound is intercalating then an increase of contour length is detected. Groove binders affect the overstretching capabilities of the formerly "naked" dsDNA strand. We interacted SYBR® Green I with naked dsDNA. The binding mode of this compound, which is used for nucleic acid gel staining, is not known. The mechanics of the interaction of SYBR® is revealed by optical tweezers experiments. The force extension curves on single dsDNA fragments show a groove-binding mode, which does not affect the contour length of the molecule but significantly alters the overstretching behaviour of the dsDNA.

Introduction

Small nucleic acid binding agents are used as DNA staining reagents in molecular biological techniques [1]. These agents bind to the DNA in different manners: intercalation between the base pairs, within the minor or major grooves, and by non-classical modes [2]. For typical DNA staining experiments (e.g. gel electrophoresis), the binding properties of these compounds affect the fluorescence signal to noise ratio significantly. For instance, it is known that Ethidium Bromide (MW 394.32; CAS 1239-45-8), which has to intercalate between the individual stacked base pairs, cannot be used if the amount of DNA is typically less than tens of nanograms. In contrast, other compounds such as SYBR® Green I (Molecular Probes, Eugene, OR), which bind to dsDNA with great specificity, are able to reveal DNA amounts of two orders of magnitudes lower weight.

In addition, small DNA binding ligands have great importance in treatment of genetic, oncogenic and viral diseases [3]. They can for instance act as probes for nucleic acid damage and structure [4]. The activity of a variety of naturally occurring and man-made antibiotics has been linked to their ability to bind the minor groove of DNA. Sequence-specific DNA-binding small molecules that can permeate human cells potentially could regulate transcription

 1438-5163/02/2-307-0091$17.50+.50/0

Single Mol. **3** (2002) 2-3

of specific genes. For instance Dickinson et al. [5] showed that these synthetic ligands specifically inhibit DNA-binding of transcription factors, and therefore provide a general approach for regulation of gene expression, as well as a mechanism for the inhibition of viral replication.

There are different approaches to get insight into the binding interaction, affinity and specific amount of molecules bound per base pair among which are x-ray diffraction and NMR studies [6,7]. In a recent study, Coury et al. [8] presented a procedure to detect these properties by measuring the contour length of the dsDNA molecule by scanning force microscopy. They incubated the bare DNA molecules with the specific agent and subsequently deposited the modified molecules onto a mica surface and investigated the amount of extension relative to the contour length. For their studies it was shown that the fraction of bound molecules could be estimated and an affinity could be determined by subjecting the DNA to various amounts of ligands. Such an approach reveals some of these parameters, but has the drawback that molecules have to be placed onto a surface in order to be accessible to the SFM imaging. It was shown [9,10] that the deposition of DNA onto mica is allowing the dsDNA molecule to adhere to the surface in a equilibrated manner, but in the subsequent study [10] it was experimentally explored that the dsDNA is partially changing its conformation from B-form DNA to A-form. A significant influence of the surface vicinity onto the binding behavior of the small reagents to DNA has to be included, and therefore, such measurements using the SFM can only reveal general trends upon reagent binding. If agents are investigated which bind to the grooves of the DNA, then an increase of contour length is not occurring. The specific binding of the groove-binding compound has to be examined by competition experiments with intercalating agents to prove an interaction.

Also, force spectroscopy was performed with SFM to discriminate small molecule DNA binding mode [11]. It was shown that the mechanical properties are greatly affected

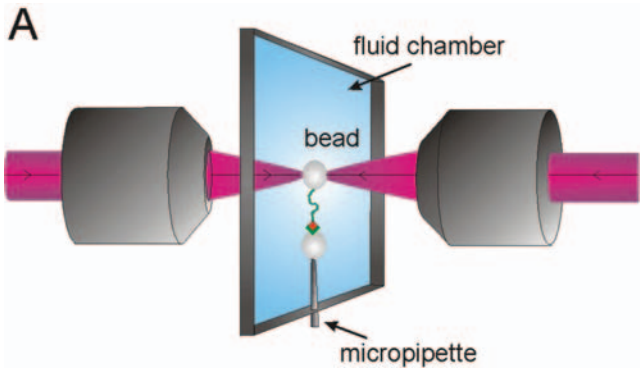

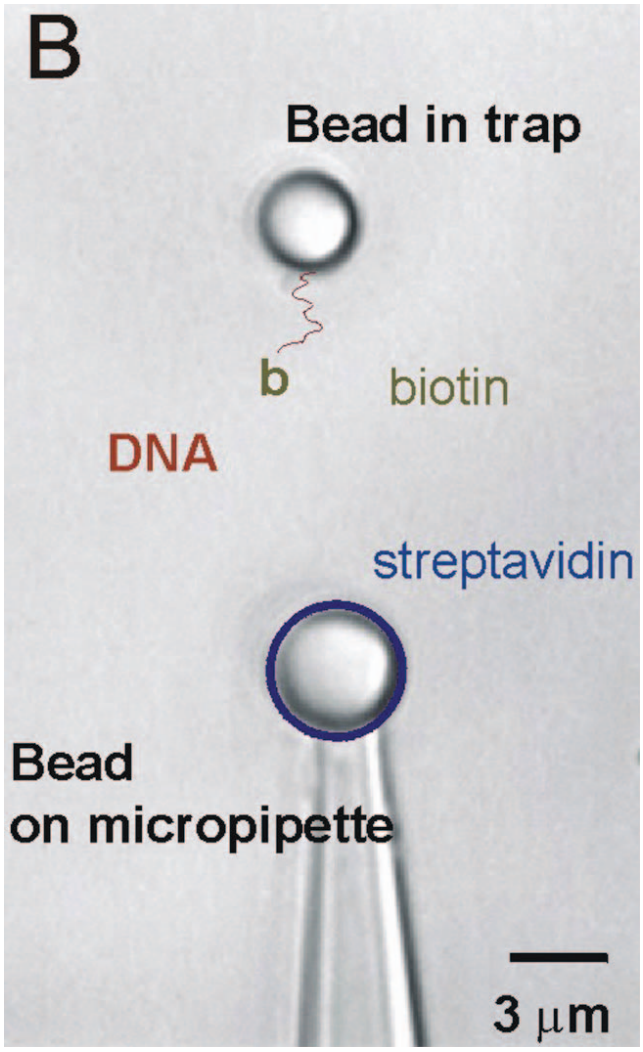

Fig. 1. A) *Scheme of the double beam optical tweezers showing the counter propagating laser beams (λ = 830 nm) and the beads held by the micropipette and the OT within the fluid chamber.* **B)** *A typical picture obtained during the optical tweezers experiment. A bead (3.1 microns in diameter) coated with streptavidin receptors is held by suction on a micropipette. A second bead (in the center of the image, 2.9 microns in diameter) is trapped in three dimensions using two counter propagating laser beams. Single dsDNA molecules are covalently attached to this latter bead and have a free biotinylated 3' end (schematically shown (not to scale)). For a typical experiment, the micropipette is moved with nanometer accuracy close to the streptavidin bead till some deflection of the laser beam on a position detector is observed. In this case, the dsDNA single molecule is linked to the streptavidin receptor through a streptavidin-biotin bridge.*

when small molecules interact with DNA. The force versus extension curves show typical and different behaviours for cross-linking (cisplatin), minor groove binder (bernil), and intercalating [ethidium bromide (EtBr)] molecules. Thus, it was emphasized that force spectroscopy could be used as a fast and reliable tool for screening purposes.

To further investigate the binding mode of such small interacting molecules, we present in this paper OT experiments. While SFM is best suited when overall mechanical properties have to be investigated, OT is a technique of choice to reveal small changes in mechanics (persistence length, stretch modulus). In this study, we show experiments performed on both EtBr and SYBR® green (i.e. a compound of which the binding mode is not clearly indicated). In agreement with SFM [11], we observe characteristic changes for each DNA binding molecule. Both the persistence length and the stretch modulus of DNA show a significant decrease upon interaction with such agents. Moreover, by applying a constant force feedback while injection of the agents, we were able to determine binding kinetics.

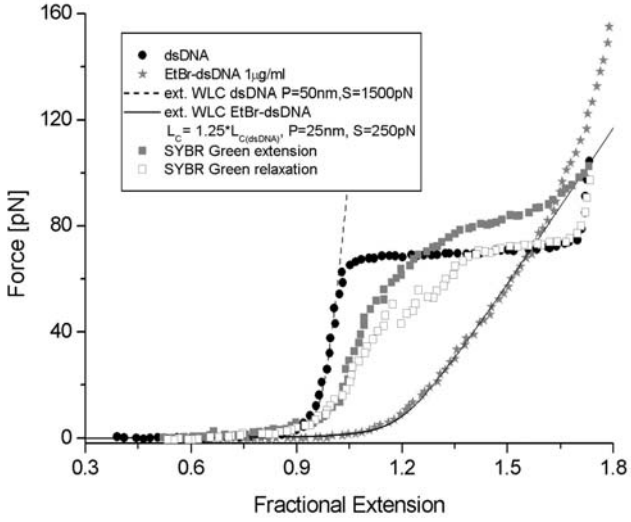

Fig. 2. *Typical force versus fractional extension x/L curves obtained for bare dsDNA (circles); and EtBr (stars). SYBR® Green I dsDNA (squares, full square extension, hollow squares relaxation), Also shown is the fit to the data using an extensible worm like chain model (Eq. 1) (dashed lines). From this fit; relevant enthlapic parameters (stretch modulus) are obtained.*

Experimental Section

Modification of dsDNA and Coupling to Beads

For typical optical tweezers experiments, a micron-sized bead (BangsLabs, Fishers IN) is generally coated with some receptor (e.g. antibodies or streptavidin) and placed onto a micropipette that can be moved using a piezoelectric element. Then a second set of microspheres is injected in the fluid chamber and one of them is trapped. These spheres have single dsDNA molecules attached with one end to the chemically activated surface, exposing on the other dsDNA end a ligand (e.g. biotin) into the solution. The experiment then just consists of approaching the pipette close enough to the bead in the trap till some force is felt onto a detector (Fig. 1 A and B). Due to the high affinity of biotin-streptavidin (KD $> 10^{-14}$ M^{-1}) the molecular recognition of this ligand-receptor interaction is easy to achieve. In contrast, an efficient site directed coupling of single molecules to beads is generally more demanding. Although there are different approaches to attach DNA molecules to chemically modified beads, the best is certainly to use a site directed covalent coupling for one end only because it allows making stock solutions of material and to reach high forces while applying external tension. For instance, an antigen-antibody bridge will rupture at forces above ~50 pN (in typical slow pulling tweezers experiments). Site directed covalent coupling of dsDNA to amino beads was performed using a procedure similar to the one described in [12]. In brief, we use a commercial dsDNA circular plasmid (pTYB1, 7477 base pairs (NEB, Beverly, MA)). The plasmid DNA was then digested with a restriction enzyme (BSA1), which cuts only once in a non symmetrically manner. In other words, two different non-palindromic overhangs are obtained after a single enzymatic digestion that can be subsequently modified in two different ways. At one end of the digested plasmid DNA, biotinylated nucleotides (Invitrogen, Basel CH) were incorporated using the Klenow exo--polymerase enzyme (NEB, Beverly, MA). On the other end small thiol modified dsDNA extensions (Microsynth, Balgach CH) were ligated. After intensive cleaning, we end up with modified dsDNA molecules with biotin groups at their 3' end and a thiol group at the 5' end. Covalent coupling of as-modified dsDNA molecules to amino-beads (BangsLabs, Fishers IN) was achieved through a standard SMCC cross linker (Pierce, Rockford, IL) as described in [12].

Optical Tweezers

The implementation and description of the optical tweezers instrument used to perform the experiments have been presented in details in [13]. Basically, it consists of a dual beam apparatus, i.e. two counter propagating laser beams which share coincident foci. In contrast to single beam optical tweezers,- our instrument directly measures the change in light momentum flux when a trapped object experiences a force. This instrument, therefore, has to be calibrated once since local parameters do not affect the force readings. In

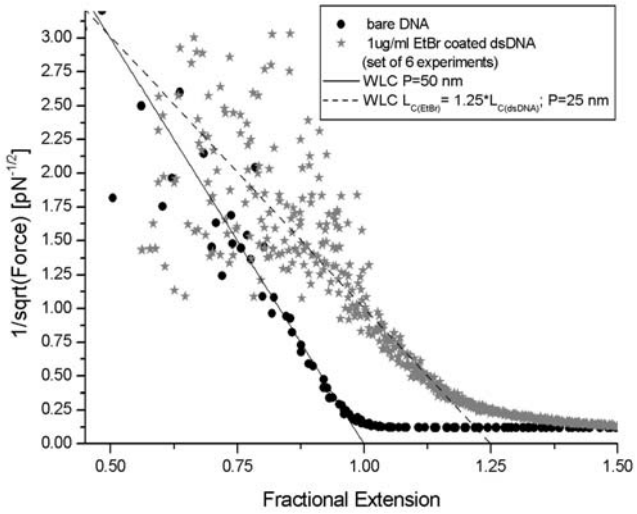

Fig. 3. *The inverse of the square root of the force F as function of the fractional extension x/L (squares, bare dsDNA. circles; dsDNA after EtBr intercalation). The linear dependence observed for forces below ~10 pN is typical of a non-extensible worm like chain (WLC) behavior. The persistence length (contour length) is deduced from an extrapolation a zero extension (force). Because the point where the DNA is attached onto the streptavidin bead is unknown; the contour length has to be adjusted according to the length of the linearized dsDNA plasmid. The jittering observed above ~1.5 indicates where thermal noise fluctuations dominate the signal.*

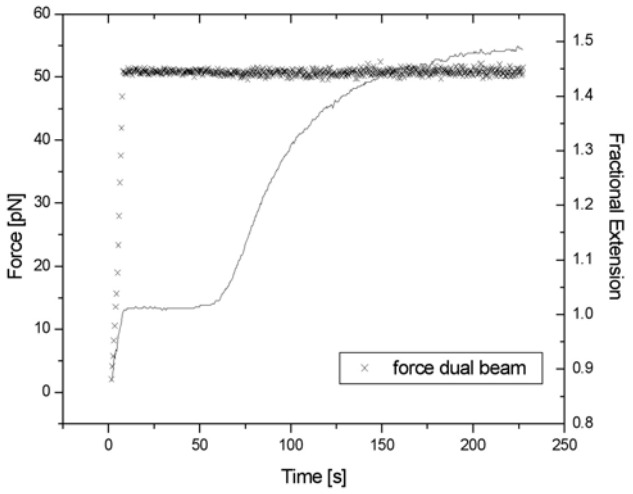

Fig. 4. *Incorporation of EtBr into a dsDNA single molecule followed in real time. For this experiment, a bare dsDNA was first pulled beyond its entropically regime up to 50 pN (0 to 5 seconds) along the X-axis (as defined in our experiment). Then, a flow of EtBr (2.5 μM) was applied in the chamber (15 pN along the Y direction, i.e. perpendicular to the pulling direction) and the force along the X-axis was kept constant at 50 pN. When EtBr arrives in the vicinity of the single dsDNA molecule (after 50 seconds), the bead end to end distance starts to increase, indicating intercalation of EtBr into adjacent DNA base pairs. After 150 seconds, the bead end-to-end distance does not show any significant dependence, which reveals maximum incorporation of EtBr. Crosshairs, force (pN); line, fractional extension.*

addition the dual beam optical tweezers has a high trapping efficiency, which is typically three times larger than in a conventional single beam optical tweezers setup.

Results

Although AFM based techniques have been applied in the past to investigate mechanical properties of single polymers [14,15], intrinsic relevant parameters such as the persistence length are not accessible to this technique, mainly because of the large thermal noise of commercial AFM cantilever. Optical tweezers have, however, typical force resolution of about 0.3 pN and overcome limitations of standard AFM devices. This is of prime importance in our study since only slight changes are expected while interacting small DNA binding molecules.

Mechanics of dsDNA

To check the integrity of our bare dsDNA, we show in Fig. 2 a typical force F versus extension x curve (150 mM NaCl, Hepes buffer pH 7.5). As expected, the dsDNA (circles) shows an overstretching plateau at 68 pN (S-transition), in excellent agreement with previous studies [16]. Although the origin of the transition is subject of some debate [16,17], the force versus extension curve for forces below 60 pN can be well described by an extensible worm like chain model (WLC) [18], using:

$$x / L = 1 - 0.5(k_B T / FA)^{1/2} + F / S \qquad (1)$$

where A is the persistence length, S the stretch modulus of the molecule, L the contour length, and k_BT = 4.1 pN·nm at room temperature. At small forces (typically smaller than 5 pN), only entropy should contribute to the observed mechanics of DNA and we can - to a good approximation - neglect any enthalpic elastic terms (S) in Eq. 1. In this case, a linear fit of $F^{-1/2}$ (Fig. 3) as a function of the extension gives a robust estimate of the persistence length A. We find an A value of 50 nm, consistent with previous studies [16,18]. Knowing this latter parameter and the contour length of the molecule, the stretch modulus of the dsDNA can be easily

obtained from a fit of the force versus fractional extension using Eq. 1. We obtain an S value of 1500 pN using our standard chamber buffer.

Mechanics of dsDNA Interacting with Small Molecules

In the previous paragraph we measured the individual properties of "naked" dsDNA in order to have a molecular "ruler", to which we can compare the subsequent experiments. Next, we investigated the interaction of the bare dsDNA with ethidium bromide (EtBr). For such agents that directly intercalate between adjacent base pairs we expect to observe great changes in the mechanical properties. Therefore, by measuring the end-to-end distance of the molecule, while maintaining a constant force, we can directly follow the uptake kinetics of DNA binding agents. This way we ensure that the DNA molecule is covered to its maximum binding capabilities at a specific concentration of reagent. We present in figure 4 the results of such a force feedback experiment at ~50 pN. The flow force of EtBr for this experiment was 15 pN in the orthogonal direction [2.5 mM], not affecting the force feedback on the dsDNA molecule. Incorporation of EtBr is completed after ~150 s for 2.5 μM at the chosen flow rate.

In figure 2 the mechanical properties of such an EtBr intercalated dsDNA molecule is shown (stars). A fitting procedure identical to the one describe above reveals values of 25 nm and 250 pN for the persistence and stretch modulus respectively. In addition, we observe a change of contour length of about 25 % due to the intercalation of EtBr. According to [19], the increase of length per EtBr molecule is 0.34 nm. Observing the increase of length directly from the measurement, we can conclude that, on average, every fourth base pair has intercalated EtBr, which ican be difficult to access using scanning force spectroscopy measurement. Furthermore, from the parameters extracted, we see that the intercalation of dyes is greatly affecting the mechanics of bare dsDNA. Namely the decrease of persistence length by factors two and the reduction of the stretch modulus of six. We should mention that an applied tension on the double strand DNA during the intercalation did not bias the amount of uptake of binding agents. For instance, feedback on the force at 50 pN or at 0 pN does not change any mechanical properties.

Additionally, in figure 2 the force versus extension of a dsDNA coated with SYBR® Green I is shown (squares). As visible in the graph, the interaction of the SYBR® Green I with dsDNA doesn't alter the contour length of the molecule, but slightly decreases the persistence length (40 nm) and the stretch modulus (500 pN) of the DNA molecule during the extension cycle. During the relaxation of the molecules in presence of SYBR®, we repeatedly observe hysteresis of the force versus extension experiment. The overstretching plateau of the interacting dsDNA is affected during extension and during relaxation. Extension of the molecule shows a short overstretch plateau occurring at higher force values ~80 pN but almost no cooperativity as in the S-transition of bare dsDNA is observed. The force extension curve is then "merging" with the one from bare dsDNA after the S-transition. During relaxation of the SYBR® -dsDNA complex, again an overstretch plateau is observed which indicates either that some SYBR® molecules unbound during the high force applied to the dsDNA molecule or that intermolecular forces in-between SYBR® molecules have been ruptured, which frees parts of the bare backbone of the underlying dsDNA molecule. During the next pulling cycle, the force versus extension curve follows on a comparable path and shows the same hysteresis.

Conclusion

Using optical tweezers experiments, we were able to measure directly the kinetics of binding of small ligands to dsDNA. By recording a force versus distance experiment, we are able to extract the mechanical parameters of the modified dsDNA molecule directly. The parameters obtained indicate the way of binding, if intercalation occurs, then the contour length is affected. Additionally, we can determine the occupancy of the ligand on the DNA from such measurements and see how the native mechanics of the molecule is altered. If compounds bind to dsDNA which aren't intercalating, then the binding is directly revealed in the way the modified dsDNA is going through its overstretch transition. Such experiments can give direct insight into the binding of small ligands to DNA and can be of great importance for a general only screening of other compounds.

Acknowledgement: This work was supported by grants from the Swiss National Science Foundation and the support from the NCCR Nanoscale Science is gratefully acknowledged.

References

[1] Haugland R.P., Handbook of fluorescent probes and research chemicals. Molecular Probes, Inc., Eugene OR, 1996.
[2] Lipscomb L. A., Zhou F. X., Presnell S. R., Woo R. J., Pee, M. E., Plaskon R. R. Williams L. D. Biochemistry **35** (1996) 2818-2823.
[3] Haskell C.M., Cancer Treatment, Saunders, Philadelphia 1990.
[4] Williams, L. D., Goldberg, I. H. Biochemistry **27** (1988) 3004-3011.

[5] Dickinson L. A., Gulizia R. J., Trauger J. W., Baird E. E., Mosier D. E., Gottesfeld J. M. Dervan P. B. Proc. Natl. Acad. Sci. USA, **95** (1998) 12890- 12895.
[6] Coste F., Malinge J. M., Serre L., Shepard W., Roth M., Leng M., Zelwer C. Nucleic Acids Res. **27** (1999) 1837-1846.
[7] Gelasco, A., Lippard, S. J., Biochemistry **37** (1998) 9230-9239.
[8] Coury J.E., McFail-Isom L., Williams L.D., Bottomley L.A. Proc. Natl.Acad.Sci. USA **93** (1996) 12283-12286.
[9] Rivetti C., Guthold M., Bustamante C., J. Mol. Biol. **264** (1996) 919-932.
[10] Rivetti C., Codeluppi S., Ultramicroscopy **87** (2001) 55-66.
[11] Krautbauer R., Pope L.H., Schrader T.E., Allen, S. H.E. Gaub Febs Lett. **510** (2002) 154-158.
[12] Hegner M., Single Mol. **1** (2000) 139-144.
[13] Grange W., Husale S., Güntherodt H.-J., Hegner M., Rev. Sci. Instr. **73** (2002) 2308-2316
[14] Rief M., Clausen-Schaumann H., Gaub H.E., Nature Struct. Biol. **6** (1999) 346-349.
[15] Fisher T. E., Marszalek P.E., Oberhauser A.F., Carrion-Vazquez M., Fernandez J.M. J. Physiol.-London **520** (1999) 5-14.
[16] Smith S. B., Cui Y., Bustamante C., Science **271** (1996) 795-798.
[17] Rouzina I., Bloomfield V.A. Biophys J. **80** (2001) 882-893
[18] Hegner M., Smith S.B., Bustamante C., Proc. Natl. Acad. Sci. USA **96** (1999) 10109-10114.
[19] Lerman L.S. J. Cell. Comp. Physiol. **64** (1964) 1-18.

Optical tweezers system measuring the change in light momentum flux

Wilfried Grange, Sudhir Husale, Hans-Joachim Güntherodt, and Martin Hegner[a)]
Institute of Physics, National Center of Competence in Research (NCCR) Nanoscale Science, University of Basel, Klingelbergstrasse 82, CH-4056 Basel, Switzerland

(Received 19 October 2001; accepted for publication 13 March 2002)

This article describes the design of a dual-beam optical tweezers (OT) instrument which, in contrast to conventional single-beam OT, directly measures the change in light momentum flux when a trapped object experiences a force. Consequently, no local calibration is needed to measure the force acting on a trapped particle. The instrument has a high trapping efficiency and forces up to 200 pN can be measured. In addition, the above-mentioned system operates in conjunction with a three-dimensional steerable single-beam OT. © *2002 American Institute of Physics.*
[DOI: 10.1063/1.1477608]

I. INTRODUCTION

It was first demonstrated in 1970 by Ashkin that light could be used to trap and accelerate dielectric micron-sized particles.[1] For these experiments, a stable optical potential well was formed using two—slightly divergent—counterpropagating laser beams. This pioneer study established the groundwork for the well-known optical tweezers (OT) technique, where a single laser beam is focused by a high numerical aperture (NA) objective lens to a diffraction-limited spot.[2] At the focal point, not only dielectric spheres can be trapped, but also biological organisms such as cells, virus, or bacteria, as shown in 1987 by Ashkin and co-workers.[3,4] The considerable interest of biologists for the OTs technique comes from the fact that minute forces can be also measured with sub-pN accuracy on the trapped object.[5] Since such small forces are not accessible by conventional techniques such as scanning-force-microscopy-based techniques (in liquid and at room temperature), OT has become a major investigation tool in biology (see Refs. 6 and 7 for recent reviews).

In the ray-optics regime, known as the Mie regime, the origin of optical forces can be understood easily. Since a bundle of light rays is refracted when passing through a dielectric object, existing rays have a different direction than incoming rays. This results in a change in the light momentum. By conservation of momentum, the change in the light momentum causes a change in the momentum of the trapped particle. As a result, the particle will feel a force. Optical forces are, however, very small, since ~100 mW of power at the focus produces only forces of tens of pN. It can be shown that stable trapping occurs along the optical axis when the *gradient force* (which is, to a good approximation, proportional to the spatial gradient of the light) overcomes the *scattering force* (caused by Fresnel reflections at the surface and directly proportional to the intensity of the light). This explains why (i) high-NA objective lenses have to be used and (ii) the back aperture of the objective lens has to be overfilled. In principle, the change in the direction of the refracted rays can be observed on a detector. In this case, a collecting lens, such as a condenser lens, is placed after the objective lens and converts angular deflections into transverse deviations $X(Y)$. An important point is that the deviations $X(Y)$ are directly proportional to the change in light momentum flux (the force), if and only if all rays are collected[8] (the proportionality constant depends on the known instrument parameters, see Sec. II A). For a single-beam OT, this latter condition is never fulfilled because of the light scattering at the back aperture of the objective lens that introduces marginal rays. Therefore, an OT instrument has to be calibrated by some means. One of the most accurate calibration procedures consists in determining (i) the light lever stiffness (in $\mathrm{pN\,nm^{-1}}$) from the thermal power spectrum and (ii) the detector sensitivity (in $\mathrm{V\,nm^{-1}}$, to relate nanometer displacements of the particle in the trap with volts). Since both the trap stiffness and the detector sensitivity depend on local parameters (laser power, size or index of refraction of the particle, local fluid viscosity, etc.), they have to be determined for each new experiment. This is certainly an important drawback of the OT technique. To overcome these limitations, one has to collect all the rays and, therefore, to underfill the back aperture of the objective lens. In this case, the spatial gradient of the light will be too small to overcome the scattering force and trapping cannot be stable. An appealing route to have a stable trapping without overfilling the back aperture of the objective lens is to use two counterpropagating laser beams that focus on the same point.[9] As a result, scattering forces, which act only in the direction of the beam, will compensate each other and stable trapping is possible. To our knowledge, Smith and coworkers first describe in 1996 the use of a dual-beam OT instrument to investigate the mechanical properties of single molecules.[10] This work studied the response of a ds-DNA single molecule stretched beyond its entropically regime and revealed, thanks to the high trapping efficiency of dual-beam OTs, the existence of an overstretching plateau at 68 pN. Latter, dual-beam OTs have lead to fascinating progress in single-molecule studies. For instance, dual-beam OTs have been used to investigate (i) the folding–unfolding transitions

a)Electronic mail: Martin.Hegner@unibas.ch

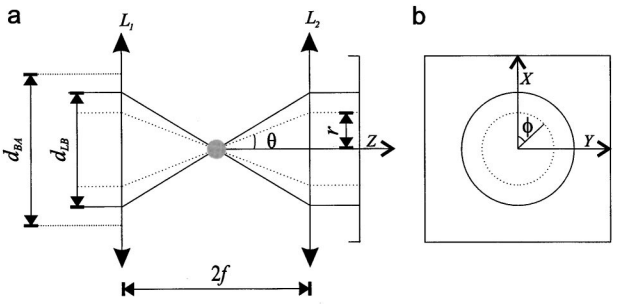

FIG. 1. Schematic representation of the lens system and definition of angular coordinates. (a) A laser beam (full diameter d_{LB} enters a objective lens L_1 (back aperture diameter d_{BA}). The focused rays are collected by a condenser lens, identical to the objective lens. We assume $d_{\mathrm{LB}} \leqslant d_{\mathrm{BA}}$ so that no scattered rays are present. A ray (dotted line), exiting a particle (gray sphere) at an angle θ with respect to the optical axis (Z direction), hits the detector at a radial height $r = nf \sin\theta$. (b) Scheme of the detector. Also are introduced the angle ϕ and the unit vectors $\hat{\imath}$ and $\hat{\jmath}$ (X and Y directions, respectively). Note that the two lasers should focus at different locations along the Z direction (see Ref. 9).

of single Titin molecules,[11] (ii) the polymerization of individual RecA-DNA filaments,[12] (iii) the activity of polymerase enzymes,[13] (iv) the unfolding of single RNA molecules,[14] and (v) the package of DNA in viruses.[15]

Although dual-beam OTs have been used over the past six years, a detailed description about the possible implementation of such instruments has not been yet given. In this article, we describe a dual-beam OT instrument, based on the principles mentioned above, and which does not suffer from the limitations of conventional single-beam OTs. In particular, it will be shown that this new instrument acts as a force transducer by measuring directly (i.e., without any local calibrations needed) the change in light momentum flux. The trapping efficiency of this instrument is larger than single-beam OTs, which is of prime importance for biological investigations. In addition, a third trap (fully steerable in three dimensions) is implemented and allows us to handle micron-sized objects with ~40 nm accuracy in the specimen plane (Sec. III).

II. DUAL-BEAM OPTICAL TWEEZERS

A. Theoretical considerations

We consider the following experimental setup (shown in Fig. 1), where a laser beam is focused by an objective lens L_1 and is collected with a condenser lens L_2.[16] We furthermore assume that (i) the diameter of the laser beam is much smaller than the back aperture of the objective lens, (ii) L_1 and L_2 are identical and corrected for infinity (i.e., a collimated laser beam is focused at the focal length of the lens), and (iii) L_1 and L_2 form an afocal system (i.e., a collimated laser beam emerges as a collimated beam). In the following, f will denote the focal length of the two lenses, d_{BA} the diameter of the back aperture, and d_{LB} the full diameter of the laser beam. For simplicity, we will now assume that the diameter of the particle d is larger than the wavelength λ so that a ray optics picture is sufficient to calculate the trapping force (i.e., we vector sum the momentum of all light rays).

The force F exerted by the laser light onto a particle is simply the difference in light momentum flux between the rays entering the particle and the rays exiting the particle. For a bundle of rays, the momentum flux is given by nW/c, where n is the index of refraction of the surrounding medium, W the power of the light (in watts), and c the speed of light. Using angular coordinates, F can be written as[8]

$$F = \frac{n}{4\pi c} \oint I(\theta,\phi)(\hat{\imath}\sin\theta\cos\phi + \hat{\jmath}\sin\theta\sin\phi + \hat{k}\cos\theta)\, d\gamma, \tag{1}$$

where θ and ϕ are defined in Fig. 1, $I(\theta,\phi)$ is the intensity in watts per steradian [$I(\theta,\phi)$ is negative for rays entering the particle], and $d\gamma$ is an element of the solid angle ($d\gamma = \sin\theta d\theta d\phi$). A detector placed after L_2 converts angular deviations into transverse deviations. Therefore, one can rewrite Eq. (1) as[17]

$$F^{\star} = \frac{1}{cf} \oint E(r,\phi)(r[\hat{\imath}\cos\phi + \hat{\jmath}\sin\phi])\, dA. \tag{2}$$

In the above equation, $F^{\star}$ denotes the transverse force felt by the particle, r is the radial height of a ray exiting the particle with an angle θ ($r = nf\sin\theta$), $E(r,\phi)$ is the intensity per unit area on the detector (in $\mathrm{W\,m^{-2}}$), and dA is an element of area on the detector ($dA = r\,dr\,d\phi$). It is natural to decompose Eq. (2) into two components F_X and F_Y for the X (along the $\hat{\imath}$ axis) and Y (along the $\hat{\jmath}$ axis) directions, respectively,

$$F_X = \frac{1}{cf} \oint E(r,\phi)(\hat{\imath} r\cos\phi)\, dA, \tag{3a}$$

$$F_Y = \frac{1}{cf} \oint E(r,\phi)(\hat{\jmath} r\sin\phi)\, dA. \tag{3b}$$

The right-hand sides of Eqs. (3a) and (3b) are quantities that can be measured with a position sensing detector (PSD). Indeed, a two-dimensional PSD allows a separation of the X and Y components and can be designed to give output currents I_X and I_Y that are related to the weighted component of the light intensity as follows:

$$I_X = \alpha \int E(X,Y)\frac{X}{R}\, dX\, dY, \tag{4a}$$

$$I_Y = \alpha \int E(X,Y)\frac{Y}{R}\, dX\, dY, \tag{4b}$$

where $2R$ is the effective length of the PSD (i.e., the distance between the two electrodes), and α is a factor describing the efficiency of the detector ($\mathrm{V\,W^{-1}}$ at the trap). Identifying Eqs. (3) and (4) gives the simple result:

$$F_X = \frac{I_X R}{c\alpha f}, \tag{5a}$$

$$F_Y = \frac{I_Y R}{c\alpha f}. \tag{5b}$$

In conclusion, the force acting on a particle can be determined without any local calibration since the quantities R, α, and f depend only on instrument parameters that do not vary

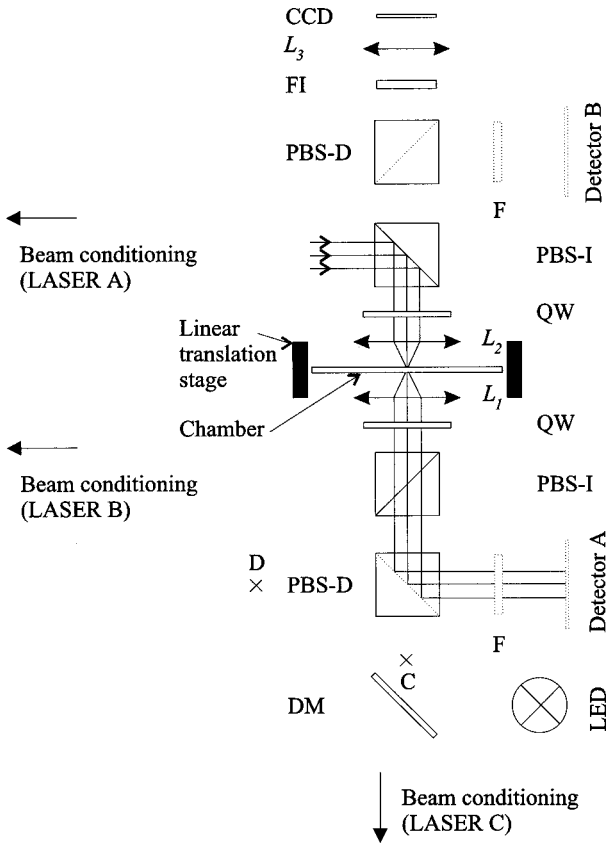

FIG. 2. Experimental setup required for the injection and detection of the two counterpropagating laser beams. Dotted lines show elements that are not in the plane of the optical table. L_1 (L_2), injection and detection lens; PBS, polarized beam splitter; QW, quarter-wave plate; and F, low-pass filter. Note that L_2 is placed onto a piezoelectric element (gray rectangle). Also shown is the imaging part: LED, light-emitting diode (480 nm); DM, dichroic mirror; and FI, low-pass filters for imaging. L_3 is a planoconvex lens used to image the focal plane of L_2 on a CCD camera. The chamber is placed on an independent piezoelectric element (gray rectangle). See Secs. II B 1 and II B 4 for explanations.

with the experimental conditions. It is obvious that Eqs. (5a) and (5b) hold only in the case where all light rays are collected. Therefore, a dual-beam instrument is needed (Sec. I). Let us finally mention that Eqs. (5a) and (5b) have been derived using ray optics theory. In the following sections, we will see, however, that the instrument we have built still works properly when the latter approximation is *a priori* not fulfilled.

B. Instrument design

1. Injection and detection of the lasers

Since two counterpropagating laser beams are used to trap a single particle, it is important to be able to detect transverse deviations for one laser (say, *A*) without any perturbation (e.g., loss of power) on the other laser (say, *B*). This problem is solved by the use of polarized beam splitters (PBS) (03PBS064, Melles Griot, Irvine, CA) and quarter-wave (QW) plates (QWPO-830-08-4-R10, CVI, Albuquerque, NM), as described in detail below.

Figure 2 shows the experimental setup used to (i) inject the two lasers and (ii) detect transverse deviations (i.e., forces). As described previously (Sec. II A), this experimental setup consists of two identical water immersion lenses [UPLAPO 60X/W/IR, Olympus, Zürich, Switzerland (NA $=1.2$, $d_{\mathrm{BA}}=7.2$ mm, 285 μm working distance)] that form an afocal optical system.[18,19] Before entering a lens, the collimated laser, which has been conditioned to have a (1, -1,0,0) polarization state (vertical *p* state in Stokes notations)[20] is reflected by a PBS element (PBS-I). When passing through the two lenses and the two QWs, the state of light polarization is first changed to (1,0,0,1) and then to (1,1,0,0) (horizontal *p* state). Therefore, the next PBS (PBS-I) transmits the laser beam. Finally, a third PBS (PBS-D) redirects the laser beam to a two-dimensional PSD detector (detector *A*) (DL-10, UDT, Hawthorne, CA). Since this setup is fully symmetric, laser *B* [incoming polarization state (1,-1,0,0)] can be also injected and detected without any significant loss of power on detector *B*. For laser *A*, parasite reflections measured at points *C* and *D* are smaller than 2% (see Fig. 2). Similar values have been obtained for laser *B*.

As shown in Sec. I, the two counterpropagating lasers *A* and *B* have to be superimposed (i.e., they should nearly focus at the same point) to allow a high trapping efficiency. For this reason, lens L_2 is placed onto a *XYZ* flexure stage (MDT631, Thorlabs, Newton, NJ) operated by a three-axis piezocontroller (MDT690, Thorlabs, Newton, NJ).

2. Beam shaping and conditioning

Since we underfill the back aperture of microscope lenses L_1 and L_2, trapping along the *Z* axis with a single laser beam is far from being stable. However, we need—for alignment procedures—to be able to trap with a single beam, at least when small forces ($<$20 pN) are applied. For this reason, beam shaping and conditioning have to be done carefully and have to minimize as possible optical aberrations and wave-front distortions (see Fig. 3 for a schematic representation of the experimental setup).

Each single-mode diode laser [5431-G1, SDL, San Jose, CA ($\lambda=830$ nm, maximum power 200 mW)] is driven with an external module (laser diode driver model 505, Newport, Irvine, CA) and is temperature controlled (temperature controller model 325, Newport, Irvine, CA).[21] The collimated delivered beam is Gaussian TEM_{00} mode and rectangular shaped ($\sim 5.2\times 1.7$ mm). The diode laser has been mounted to deliver a (1,0,1,0) polarized beam. Beam shaping is achieved using anamorphic prisms (06GPA004, Melles Griot, Irvine, CA) that produce a square-shaped beam ($\sim$5.2 mm, full length). To prevent back reflections and reduce mode hopping of the laser, we use optical isolators (IO-5-830-LP, Optics for Research, Caldwell, NJ). Note that the electric field experiences a 45° rotation when passing through this latter optical element. Therefore, the state of polarization is now (1,-1,0,0). Finally, the beam is spatial filtered using two identical achromat doublets (focal length: 100 mm) and a 40 μm pinhole [mounted on an *XYZ* lens positioner (LP-1-XYZ, Newport, Irvine, CA)]. After this filtering, the laser beam shows a clean Gaussian profile with an isotropic circular shape ($d_{\mathrm{LB}}\sim 5$ mm) and can be finally injected through the microscope lenses.

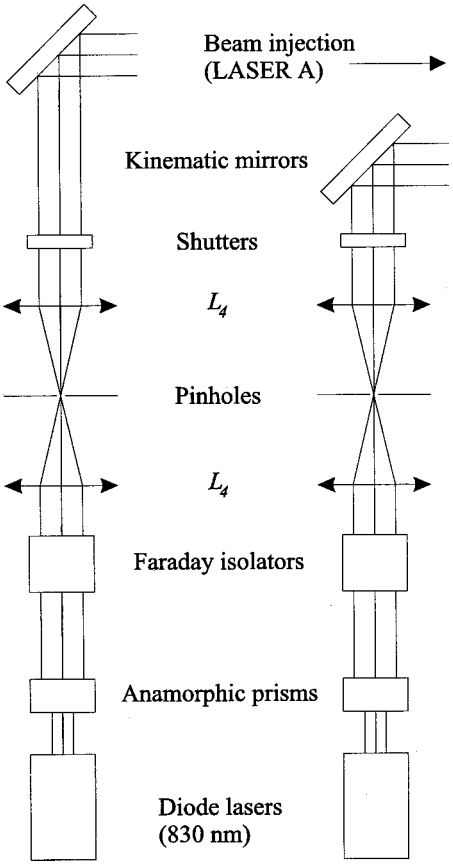

FIG. 3. Double-beam conditioning. A description of parts can be found in the text (Sec. II B 2). Note (i) that the separation between the two lenses L_4 (focal length f_4) is chosen as $2\,f_4$ and (ii) kinematic mirrors are used to redirect the beam onto the PBS (Fig. 2).

The above-described arrangement has been found to allow for precise conditioning and to minimize loss of power through the different optical element. For a maximum output power of 200 mW of the laser diode, we measure a value of ~75 mW at the trap focus.

3. Detector

For each laser, a two-dimensional PSD detector directly measures the quantities I_X and I_Y (in volts) that appear in Eqs. (4a) and (4b) and that are relevant to determine the force [Eqs. (5a) and (5b)]. In addition, a voltage, directly proportional to the light intensity, is readout from each PSD. To reduce noise, the electronic circuit (needed for proper signal conditioning) is placed in a shielded box next to the detector.

4. Chamber, imaging, flow system

The chamber and flow system we use is similar to the ones described in Ref. 22. Typically, the chamber itself consists of two parafilm layers sealed on two microscope coverglass No. 1. Prior to sealing, the parafilm layers are cut to define a channel ($50\times3.5\times0.3$ mm) for fluid injection and a ~100 μm glass tube (inner diameter) is inserted between the parafilm layers. Two holes are drilled within the chamber to define an inlet and an outlet for liquid. The ~300-μm-thick chamber is then placed on an aluminum holder. A glass micropipette is pulled from a glass capillary (outer diameter ~80 μm) to obtain a <1 μm diam on one side. The micropipette is finally inserted inside the ~100 μm tube and connected to a manual syringe to allow suction of micron-sized beads. An important point is that the nearly coincident focus of the two counterpropagating laser beams defines a fixed location in space (Sec. II B 1). For this reason, the chamber has to be placed on an element that allows movements in three-dimensions, independently of the *XYZ* flexure stage used to align the lasers. This element is composed of two one-dimensional translation stages (TSX-1D, Newport, Irvine, CA) that have a 25 mm travel range in the *Z* direction. These stages hold a three-axis piezoelectric flexure scanner (517.3CL, Physik Instrumente, Waldbronn, Germany) that has a maximum extension of 100 μm for the *X* and *Y* directions and 20 μm along the *Z* axis, respectively (Fig. 2). Each axis is operated by a voltage signal (0–100 V) provided by an amplifier module (E-503.00, Physik Instrumente, Waldbronn, Germany). This voltage is controlled by an analog signal (0–10 V) applied to the standard coaxial inputs of the amplifier. For accurate movements (closed-loop operation), a servocontroller (E-509.C3, Physik Instrumente, Waldbronn, Germany) is also used.

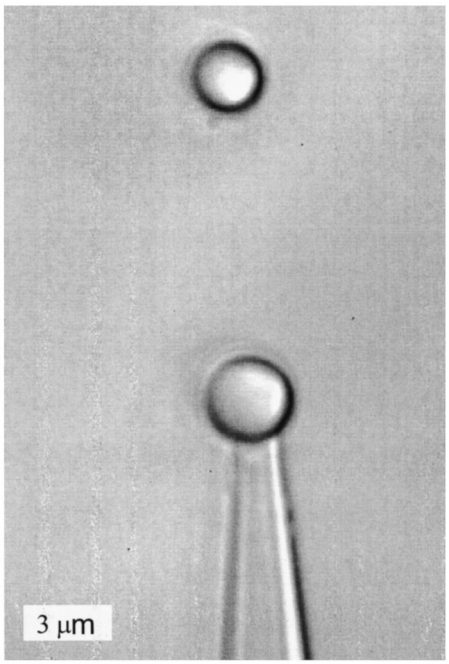

FIG. 4. Typical image of the micropipette (aperture <1 μm) holding a polystyrene bead (diameter, 3.10 μm). The polystyrene bead in the upper part of the image (diameter, 2.90 μm) is trapped by the two counterpropagating laser beams. For a typical stretching experiment, a single molecule is placed between the two beads and the micropipette (placed onto a piezoelectric element) is moved with nanometer accuracy.

For a typical experiment, the pipette and the trapped bead have to be imaged onto a charge-coupled-device (CCD) camera (Fig. 4). A planoconvex lens L_3 is, therefore, used to image the specimen plane (the focus of the objective lenses) onto the chipset of the CCD camera (VCB-3424, MSM Trading, Basel, Switzerland). Light is provided by a light-emitting diode (LED) ($\lambda = 480$ nm), which is first reflected by a dichroic mirror (600DRLP, Omega Optical, Brattleboro,

VT) and then injected into L_1 (Fig. 1). The pipette is brought to the specimen plane using both manual translation stages and a piezoelectric device (see above). Note, finally, that additional low-pass filters [labeled FI in Fig. 2 (Schott, Feldbach, Switzerland)] are used to eliminate unwanted IR radiation on the CCD.

Fluid delivery is controlled using pressure bottles and an automatic valve system (MVP, Hamilton, Reno, NV). Pressure bottles are used either to contract or expand the air on the different buffer solutions, which are afterwards injected in the chamber by the valve system.[22] The flow rate in the chamber is directly proportional to the difference in height between the liquid in the buffer solution and the waste solution (connected to the outlet of the chamber) times the applied pressure (vacuum). In contrast to peristaltic pumps, such a system has no mechanical parts and, therefore, produces steady flow streams with pN accuracy.

5. Automation

We use Labview (National Instruments, Austin, TX) to fully control and operate our instrument. Two cards [PCI-6031E and PCI-6704, 16 bits resolution, 100 kSamples/s (National Instruments, Austin, TX)] allow us (i) to output voltages on the different piezoelectric elements, (ii) to acquire analog signals from the detectors and the pressure sensors, and (iii) to control the shutters (846HP, Newport, Irvine, CA). In addition, the valve system is controlled via the serial port of the PC through a PXI-1002 chassis (National Instruments, Austin, TX). Finally, we use a frame grabber (PCI-1408, National Instruments, Austin, TX) to process images acquired on the CCD camera.

C. Results

We already have emphasized that the main advantage of the dual-beam OT lies in the fact that we measure directly the difference in light momentum flux (Secs. I and II A). Therefore, we are able to determine the force acting on the trapped particle without any knowledge of the trap stiffness. In other words, the instrument should always give a correct measure of the force acting on the particle even if some local parameters (e.g., power of the laser, index of refraction, etc.) change. In this section, we first briefly describe the calibration procedure needed to determine the force from output detector signals. As a benchmark test, we pull a dsDNA single molecule beyond its entropically regime. Then, we demonstrate that the calibration is independent of local variables (laser power, size of the trapped particle). Finally, the performances of the instrument are highlighted.

1. Calibration procedure and overstretching of dsDNA

The calibration only needs to be done once since only the quantities α [the detector efficiency, $\mathrm{V\,W^{-1}}$ (at the trap)] and R (the effective radius of the detector, m) have to be known to get the force [Eqs. (5a) and (5b)]. Other quantities (i.e., focal length) are obtained from the manufactures. α can be easily determined using a power meter, and R using a collimated laser mounted on an XY translation stage.

To test this calibration, we have recorded the force as a function of the displacement of a trapped particle (in the specimen plane), while gradually increasing the speed of the flow in the chamber. From the slope of the force versus displacement plots,[23] the value of the trap stiffness K can be determined (Table I). Alternatively, the stiffness of an optical trap (i.e., for a low Reynolds number) can be estimated from the power spectral density $S_{\mathrm{FF}}(f)$ of the thermal force fluctuations using[5]

$$S_{\mathrm{FF}}(f)=\frac{2kT\gamma f^2}{\pi(f^2+f_c^2)}, \tag{6}$$

where γ is the viscous drag, f_c the corner frequency [$f_c=(2\pi\gamma)^{-1}$ K], and $kT=4.1$ pN nm at room temperature. For our experiment, spherical particles are used and are trapped far away from the chamber walls. Therefore, the viscous drag is easily computable. As a consequence, the trap stiffness can be determined, independently of the calibration procedure.[5]

TABLE I. Stiffness of the optical trap (pN $\mu\mathrm{m}^{-1}$) determined from (i) force vs displacement measurements ($K^{\star}$) and (ii) the corner frequency of the power spectral density of the force fluctuations (Sec. II C 1) ($K^{\bullet}$). Stiffnesses have been measured for different bead sizes and different laser powers at the focus. Also shown is the percentage of light collected by the microscope lenses.

Diameter (μm)	$K^{\star}$ (pN $\mu\mathrm{m}^{-1}$)		$K^{\bullet}$ (pN $\mu\mathrm{m}^{-1}$)		Light collected (%)
	150 mW	80 mW	150 mW	80 mW	
7.00	57±5	29±3	61±3	31±3	>99
3.10	144±9	73±6	144±4	74±3	>99
1.87	265±12	140±10	256±5	138±4	>99
0.60	140±10	72±6	154±5	80±5	97

As seen in Table I, the stiffness values measured using (i) a robust and widely used calibration method (thermal fluctuations) and (ii) the change in light momentum flux are in good agreement. This comes from the fact that nearly all the rays are collected with our high-NA condenser lens, even when diffraction effects are expected to be important (i.e., $\lambda \leqslant d$). This last result undoubtedly demonstrates the validity of the calibration procedure.

As a typical benchmark test, we show in Fig. 5 a typical overstretching curve of a single 10 kbp ds-DNA molecule. For this experiment, a micron-sized polystyrene bead (Bangs laboratories, Fishers, IN)—coated with Streptavidin receptors—was first trapped by the lasers. The micropipette was approached close enough to the bead and suction was applied with a syringe to hold this 3.10-μm-diam bead on the clear aperture of the micropipette (Fig. 4). The micropipette was then retracted away from the trap and a second bead (coated with one ds-DNA, 2.90 μm in diameter) was injected in the chamber and trapped. The activation of this latter bead follows the procedure described in Ref. 24. Briefly, it consists of (i) chemically activating the microsphere and covalently attaching a thiol-modified 5′-end of the dsDNA to the surface of the bead and (ii) attaching a Biotin ligand group to the other 3′-end. Since Biotin and Streptavidin have a strong affinity, the experiment consists of moving the micropipette around the trapped bead until a hookup is felt on the detectors.

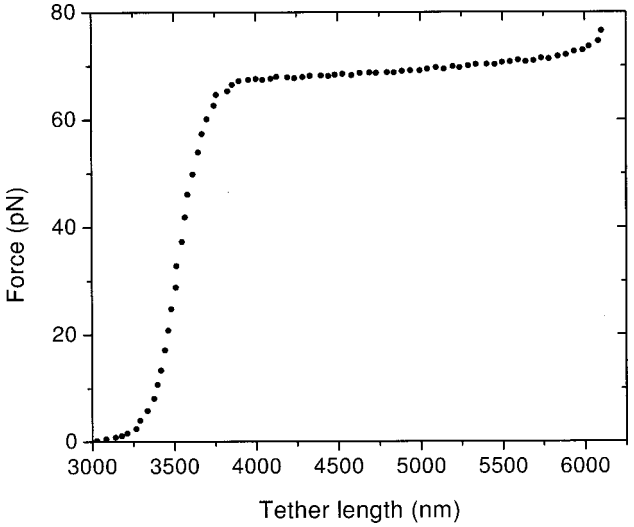

FIG. 5. Typical overstretching curve obtained on a single 10 kbp ds-DNA molecule [150 mM NaCl, Hepes buffer *p*H 7.5]. Note that the length of the dsDNA was inferred from the distance of the two beads (see Ref. 23).

The DNA overstretching curve (Fig. 5) shows, as expected, a plateau at 68 pN (*S* transition) [150 mM NaCl, Hepes buffer *p*H 7.5], in excellent agreement with previous experiments.[10,12,25]

2. Power and bead size dependence

Figure 6 shows the force acting on a polystyrene microsphere (3.10 μm in diameter) as a function of the speed of flow. For a total power of 150 mW, the force shows—as expected—a linear behavior as a function of the applied pressure. Decreasing the total power of the laser should not affect the force acting on the trapped particle but should dramatically decrease the trapping efficiency. In other words, the stiffness of the light lever is modified when the power of the lasers is changed (see the inset of Fig. 6) and a new calibration should be performed for a single-beam OT instrument to accurately determine the force acting on the trapped particle. With our instrument we, however, directly measure the change in light momentum flux. Therefore, the force versus applied pressure plots measured for different laser powers show a unique linear dependence.

We now demonstrate that the momentum flux sensor is independent of the bead size. For this purpose, different bead sizes were trapped by the lasers and the detector outputs were recorded as a function of the fluid velocity [Fig. 7(A)]. According to Stokes law, the slopes S_{Stokes} of the obtained curves should be proportional to the diameter of the trapped particles. As a result, the quantity $F/v_{\mathrm{flow}}=S_{\mathrm{Stokes}}$ (i.e., the frictional force divided the fluid velocity) should be a linear function of the bead diameter. This is exactly what is obtained in our measurements [Fig. 7(B)].

3. Thermal noise and trapping efficiency

The thermal noise level ($\mathrm{pN}^2/\mathrm{Hz}$) of the instrument has been obtained from the power spectrum measured with a 16 bit card over a large bandwidth (10–50 kHz).[5] For a 3.10-μm-diam bead, the noise level is constant (white noise) for frequencies below 785 Hz (corner frequency f_c) and about

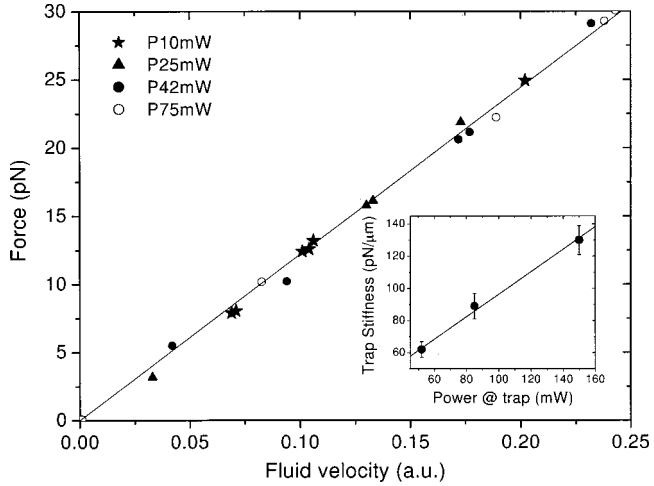

FIG. 6. Force as a function of the fluid velocity (3.10-μm-diam bead). Empty circles, 150 mW; filled circles, 84 mW; triangles, 50 mW; stars, 20 mW. Solid line, linear fit to the data. In the inset is shown the dependence of the trap stiffness as a function of the total laser power (i.e., for the two laser beams). Note that the trap stiffness can be easily obtained from a fit of the power spectrum with a Lorentzian function (Sec. II C 1).

$4\gamma kT=4.7\times10^{-4}$ $\mathrm{pN}^2/\mathrm{Hz}$ [Eq. (6)]. This noise is mainly of thermal origin since other sources of noise have been minimized. The noise drops rapidly for frequencies above f_c and reaches a value of about 1×10^{-7} $\mathrm{pN}^2/\mathrm{Hz}$ for frequencies above 40 kHz. As mentioned above (Sec. II C 1), this behavior is characteristic of a particle that has a low Reynolds number and that moves in a parabolic potential well.[5] Note, finally, that for a typical experiment the detector signal is low-pass filtered to cut high frequencies and to prevent aliasing.

The performance of the instrument can be discussed in terms of a dimensionless factor *Q*, known as the trapping efficiency. *Q* is related to the maximum trapping force F_{trap} and the laser power *P* through the following relation:

$$F_{\mathrm{trap}}=nQP/c. \tag{7}$$

The Stokes law calibration (Sec. II C 2) allows us to determine F_{trap}. We found values of 200, 145, and 36 pN, for bead diameters of 3.10, 1.87, and 0.60 μm, respectively. This gives *Q* values of 0.30, 0.22, and 0.05, respectively. Clearly,

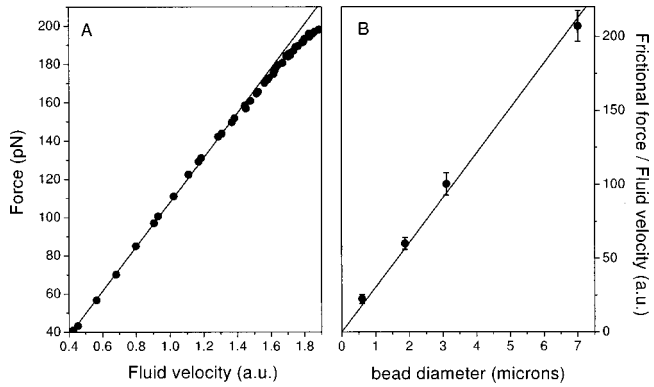

FIG. 7. (A) Force as a function of the applied pressure (3.10-μm-diam bead). Note that the force readings start to be nonlinear at ~170 pN (Sec. II D). (B) Ratio of the frictional force and the fluid velocity as a function of the bead diameter. Solid lines, linear fits to the data.

the momentum flux sensor shows a high trapping efficiency and reaches high forces as compared to single-beam OTs. For instance, the maximum force that can be applied on a micron-size bead with single-beam OTs is only of about 60 pN.[19,26]

D. Discussion

In the previous sections, we have shown that the calibration procedure is independent of both the power of the lasers and the size of the particle. But, we also have checked that the calibration of the instrument is independent of other local parameters such as the index of refraction of the particle or the surrounding buffer, and the shape of the trapped particle (not shown).[8]

An important assumption made for the derivation of Eqs. (5a) and (5b) is that all the rays are collected. If this would not be the case, then the detector readings would be inaccurate. For all bead sizes investigated (0.60, 1.87, 3.10, and 7.00 μm), the percentage of light collected by the condenser lens was larger than 97. This, therefore, indicates the validity of the approach we have used. We emphasize that the use of low-NA lenses (smaller than 1), possible with dual-beam OTs,[8] is not recommended when using bead sizes comparable to the wavelength of the laser. Indeed, scattering effects are important in this case. As a consequence, the percentage of light collected after the condenser lens will be probably smaller than 90%, which reduces the accuracy of the instrument. Moreover, the force readings can be inaccurate for a high-NA lens when the force is so high that part of the laser spot hits the back aperture of the lens. For our lens ($d_{\mathrm{BA}}=7.2$ mm, $f=3$ mm), and the size of the laser ($d_{\mathrm{LB}}\sim 5$ mm), the force readings start to be inaccurate for forces greater than $\sim$170 pN at full laser power [Fig. 7(A)], well above any reported force involved in biological transitions or molecular motor processes.[6,7]

Let us finally point out that dual-beam OTs, if much more powerful than single-beam OTs, suffer also from limitations. Among them, optical drift is a real nuisance in the experiment and has to be corrected [e.g., by the use of a piezoelectric element placed on one of the microscope objectives (Sec. II B 1)]. This procedure has been automized in our instrument.

III. THIRD TRAP

As seen the previous sections, lasers *A* and *B* share a common focus, which defines a fixed location in space for the trap. As a consequence, the trapped bead cannot be steered (with the above-described setup) in three-dimensions. We now describe the implementation of a single-beam OT (used as a handle) that allows movements of another trapped object with a $\sim$40 nm accuracy in the specimen plane. In the following sections, we will use the same notations as in Sec. II.

A. Requirements for a steerable trap

Because a single-beam OT is used to steer the trap, the back aperture of the microscope has to be overfilled (Sec. I). Moreover, the incoming laser beam (laser *C*) should pivot around the objective entrance aperture to ensure a stable trapping when moving the trap. In their review paper, Svoboda and Block[5] have presented many experimental setups that fulfill this latter requirement. Among them, the use of a piezoelectric gimbal mirror, which is placed in a plane conjugate to the back aperture of the microscope, is certainly best suited (see below).[27] Indeed, such an arrangement allows fast steering of the trap[28] and has less constraints (in terms of distances between the different optical elements) than usual steering setups.

1. Steering in the specimen plane (X, Y directions)

To steer the beam in the specimen plane, we need to image the back aperture of the microscope lens (e.g., L_1, Fig. 2) onto a device that has angular movements only (e.g., a gimbal mirror). To accomplish this, two lenses [say, L'_{xy} (focal length f'_{xy}) and L''_{xy} (focal length f''_{xy})] have to be inserted between the back aperture of the microscope lens and the gimbal mount. Moreover, the relationship between the distances d_{gs} [between the plane of rotation of the gimbal mount and L'_{xy} (the lens closest to the gimbal)] and d_{sb} (between L''_{xy} and the back aperture of the microscope) should be given by[27]

$$d_{gs}=\frac{f'_{xy}}{f''_{xy}}\left[f'_{xy}+f''_{xy}-\frac{f'_{xy}}{f''_{xy}}d_{sb}\right], \tag{8}$$

where we have assumed—for simplicity—that L'_{xy} and L''_{xy} are forming an afocal system. Under this condition [Eq. (8)], a tilt of θ of the gimbal mirror will induce a displacement of $\sim 2\,ff'_{xy}\theta/f''_{xy}$ in the specimen plane (i.e., *X* and *Y* directions).

2. Steering along the Z direction

As outlined by Fällman and Axner,[27] the beam can also be steered along the *Z* direction if two additional steering lenses [say, L'_z (focal length f'_z) and L''_z (focal length f''_z)] are placed in front of the gimbal mirror. When (i) L''_z (the lens which is closest to the gimbal) is placed at a distance of f''_z away from the gimbal and (ii) the distance between L'_z and L''_z is about $f'_z+f''_z$, a movement of L'_z along the *Z* direction will change the divergence of the beam without changing the size of the beam on the gimbal mirror (i.e., the degree of overfilling of the microscope lens). In this case, a translation of L'_z along the *Z* direction induces a change δz_{trap} of the focus (the specimen plane) along the *Z* direction equal to[27]

$$\delta z_{\mathrm{trap}}=\left(\frac{ff'_{xy}}{f''_{xy}f''_z}\right)^2\delta_z. \tag{9}$$

Let us point out that the *Z* steering is of peculiar importance in our instrument since lasers *A* (*B*) and *C* do not have the same divergence.

B. Instrument design

For the third beam, we use a diode laser emitting at 1064 nm (LCS-DTL-322, Laser 2000, Wessling, Germany). The beam has a TEM_{00} beam diameter of $\sim$1.5 ($1/e^2$) and is linear polarized (maximum output power: 1 W). The laser

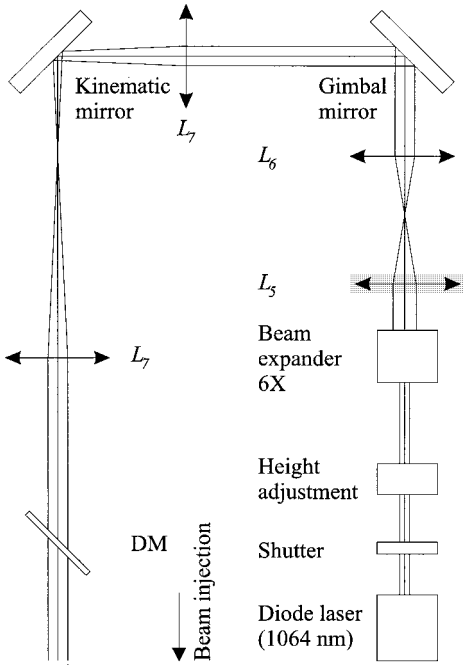

FIG. 8. Setup for the steerable third trap. Note that (i) the dichroic mirror (DM) is the same as the one shown in Fig. 2 and (ii) lens L_5 is placed on a translation stage (gray rectangle). The back aperture of the microscope lens L_1 (Fig. 2) is imaged onto the plane of rotation of the gimbal mirror with the use of two identical lenses L_7 that form—in our instrument—an afocal system.

beam is first brought at a correct height (similar to that of lasers *A* and *B*) using an *X*-beam steerer, composed of two 45° mirrors (Fig. 8). To achieve proper overfilling of the microscope back aperture (lens L_1), a 6× beam expander (S6ASS0106, Sill Optics, Wendelstein, Germany) is then implemented within the path. For *Z* steering (Sec. III A 2), we use two lenses L_5 (focal length: 80 mm) and L_6 (focal length: 62.9 mm). These two lenses form an afocal arrangement and L_5 is placed onto a piezoelectric element (MDT631, Thorlabs, Newton, NJ), which is operated by a piezocontroller (MDT690, Thorlabs, Newton, NJ) and an additional dc-stepper motor. The *XYZ* flexure stage (used only in the *Z* direction) has a piezoelectric translation of 15 μm and a manual translation of 2 mm. This results in a maximum change in depth of focus of ~35 nm and ~4.6 μm for the piezoelectric and dc operations, respectively [Eq. (9), see below for the specifications of the *XY*-steering lenses].

Beam steering along the *X* and *Y* directions (in the specimen plane) is achieved by pivoting a gimbal mount (U200-G, Newport, Irvine, CA). For precise movements of the gimbal, we use closed-loop dc actuators (CMA-12CCL, Newport, Irvine, CA) driven by a ESP300 platform (Newport, Irvine, CA). With such a configuration, the minimal incremental angular motion of the gimbal is 7×10^{-6} rad, yielding a minimal incremental motion of ~42 nm in the specimen plane (Sec. III A 1). The *XY*-steering lenses [labeled L_7 (focal length: 175 mm) in Fig. 8] also are placed in an afocal arrangement and follow the requirements (in terms of position) mentioned in the preceding section.

After proper conditioning of the laser, the laser beam passes through a dichroic mirror (see Figs. 2 and 8) and enters microscope lens L_1. At the entrance back aperture of L_1, we measured a $1/e^2$ diameter of ~7.1 mm. It is important to note that the PBS used to inject lasers *A* and *B* transmits most of the 1064 nm laser beam. However, parasitic back reflections of the 1064 nm laser beam can interfere with the output readings of the detectors *A* and *B* (Fig. 2). To prevent this, we use low-pass filters [labeled *F* in Fig. 2 (Schott, Feldbach, Switzerland)].

C. Discussion

The steering system presented in the previous sections is found to allow precise three-dimensional movements of the trap in the specimen plane with minimal loss of the light when pivoting the laser beam around the entrance back aperture of the microscope lens. Moreover, it allows micron-sized movements of the trap in all three dimensions. We checked, also (by measuring the escape force on detector *A* and *B* as a function of the flow speed), that this third trap has a reasonable trapping efficiency, comparable to that of single-beam OTs. The third trap will enable the local probing with sub-pN resolution of biological interactions along a filamentous molecule attached between the pipette and the dual-beam tweezers. Among these interactions are protein-DNA interactions[13] and filamentous proteins (e.g., actin or tubulin) interacting with other proteins (the targeting molecule will then be attached to the third bead). This third possibility is of great relevance for localization of individual targets of the investigated systems which might differ on the specific location of the interacting biological systems.

ACKNOWLEDGMENTS

This work was supported by the Swiss National Science Foundation (Grant Nos. 31-61497.00 and 2160-056392.99), the Treubel Foundation, and the National Competence Center for Research (NCCR) ''Nanoscale Science'' network. The authors would like to acknowledge Steven B. Smith for fruitful discussions.

[1] A. Ashkin, Phys. Rev. Lett. **24**, 156 (1970).
[2] A. Ashkin, J. M. Dziedzic, J. C. Bjorkholm, and S. Chu, Opt. Lett. **11**, 288 (1986).
[3] A. Ashkin and J. M. Dziedzic, Science **235**, 1517 (1987).
[4] A. Ashkin, J. M. Dziedzic, and T. Yamane, Nature (London) **330**, 769 (1987).
[5] K. Svoboda, and S. M. Block, Annu. Rev. Biophys. Biomol. Struct. **23**, 247 (1994).
[6] A. D. Mehta, M. Rief, J. A. Spudich, D. A. Smith, and R. M. Simmons, Science **283**, 1689 (1999).
[7] C. Bustamante, J. C. Macosko, and G. J. L. Wuite, Nat. Rev., Mol. Cell Biol. **1**, 130 (2000).
[8] S. B. Smith, Ph.D. thesis, University of Twente, The Netherlands (1998).
[9] Due to Fresnel reflections of incident light rays at the surface of the trapped particle, the focus of two lasers should be slightly different along the *Z* direction.
[10] S. B. Smith, Y. J. Cui, and C. Bustamante, Science **271**, 795 (1996).
[11] M. S. Z. Kellermayer, S. B. Smith, H. L. Granzier, and C. Bustamante, Science **276**, 1112 (1997).
[12] M. Hegner, S. B. Smith, and C. Bustamante, Proc. Natl. Acad. Sci. U.S.A. **96**, 10109 (1999).
[13] G. L. J. Wuite, S. B. Smith, M. Young, D. Keller, and C. Bustamante, Nature (London) **404**, 103 (2000).
[14] J. Liphardt, B. Onoa, S. B. Smith, I. Tinoco, Jr., and C. Bustamante, Science **292**, 733 (2001).

[15] D. E. Smith, S. J. Tans, S. B. Smith, S. Grimes, D. L. Anderson, and C. Bustamante, Nature (London) **413**, 748 (2001).
[16] The denomination used here (objective lens, condenser lens) is to some extend arbitrary since lenses L_1 and L_2 play the same role.
[17] This integral runs over the detector, which only measures the change in light momentum flux for exiting rays. Since the momentum flux for incident rays is independent of the force, it represents only a constant offset value in Eq. (1).
[18] Until recently, high-NA water immersion lenses were not commercially available. Therefore, oil immersion lenses had to be used. Although such lenses produce a steep spatial gradient, the difference in the index of refraction between oil and water (inside the chamber) dramatically increases spherical abberations, when the focus is brought away from the chamber wall. As a result, a single beam trap which uses oil immersion lenses can only trap within a distance of $\sim$20 μm away from the chamber wall. Nowadays, high-NA (1.2) water immersion lenses overcome such limitations. For instance, they allow a stable trapping at distances greater than $\sim$150 μm away from the surface.
[19] L. P. Ghislain, N. A. Switz, and W. W. Webb, Rev. Sci. Instrum. **65**, 2762 (1994).
[20] W. Bickel and W. Baile, Am. J. Phys. **53**, 468 (1985).
[21] The 830 nm wavelength is best suited for biological investigations due to the relative transparency of biological materials and water at this wavelength. K. C. Neuman, E. H. Chadd, G. F. Lion, K. Bergman, and S. M. Block, Biophys. J. **77**, 2856 (1999).
[22] G. L. J. Wuite, R. J. Davenport, A. Rappaport, and C. Bustamante, Biophys. J. **79**, 1155 (2000).
[23] For these measurements, video microscopy was used to track the location of the trapped bead in the specimen plane. The CCD camera was calibrated using a 10-μm-increments calibration grid (one pixel equals 48 nm). Using IMAQ libraries from Labview (National Instruments, Austin, TX) that have subpixel accuracy, movements as small as $\sim$7 nm can be easily detected.
[24] M. Hegner, Single Mol. **1**, 139 (2000).
[25] M. Rief, H. Clausen-Schaumann, and H. E. Gaub, Nat. Struct. Biol. **6**, 346 (1999).
[26] R. M. Simons, J. T. Finer, S. Chu, and J. A. Spudich, Biophys. J. **70**, 1813 (1996).
[27] E. Fällman and O. Axner, Appl. Opt. **36**, 2107 (1997).
[28] C. Mio, T. Gong, A. Terray, and D. W. M. Marr, Rev. Sci. Instrum. **71**, 2196 (2000).

Chapter No. 13

Biological Single Molecule Applications and Advanced Biosensing

M. Hegner[a]*, Ch. Gerber[a, b], Y. Arntz[a], J. Zhang[a], P. Bertoncini[a], S. Husale[a], H.P. Lang[a, b] and W. Grange[a]

[a]Institute of Physics, NCCR Nanoscale Science, University of Basel Klingelbergstrasse 82, CH - 4056 Basel, Switzerland

[b]IBM Zurich Research Laboratory, Säumerstrasse 4, CH- 8803 Rüschlikon, Switzerland

*Corresponding author: martin.hegner@unibas.ch

1. INTRODUCTION

1.1. Macroscopic versus microscopic measurements in biology

Macroscopic experiments yield time and population averages of the individual characteristics of each molecule. At the level of the individual molecules, the picture is quite different: individual molecules are found in states far from the mean population, and their instantaneous dynamics are seemingly random. Whenever unusual states or the rapid, random motions of a molecule are important, the macroscopic picture fails, and a microscopic description becomes necessary. Single-molecule experiments differ from macroscopic measurements in two fundamental ways: first, in the importance of the fluctuations in both the system and in the measuring instrument, and second, in the relative importance of force and displacement as variables under experimental control and subject to direct experimental measurements. In single-molecule experiments, the crucial parts of the measuring instruments themselves are small and subject to the same fluctuations as the system under study. Single-molecule experiments thus, give access to some of the microscopic dynamics that are hidden in the macroscopic experiments.

1.2. Force sensitive Methods

During the last decade, new force measuring devices have been developed which paved the way to explore the rich possibilities of mechanical measurements in the Pico Newton (pN) range of force generating motor-proteins and interacting biological macromolecules under physiological conditions.

One of them is the optical trapping scheme, which consists of bringing a beam of laser light to a diffraction-limited focus using a “good” lens, such as a microscope objective. Under the right conditions, the intense light gradient near

the focal region can achieve stable three-dimensional trapping of dielectric objects, varying in size from a few tens of nanometers up to tens of micrometers. The term optical tweezers (OT) was defined to describe this so called single-beam scheme.

Another force-measuring device is the scanning force microscope (SFM), which has evolved to a unique tool for the characterization of organic and biological molecules on surfaces. The SFM has proven its impact for biological applications, showing that it is possible to achieve sub nanometer lateral resolution on native membrane proteins in buffer solutions [1], to monitor enzymatic activity *in situ* [2] or to measure the unfolding of single proteins [3]. Up to now there is plenty of experimental information available regarding forces, which arise in biological systems. An overview upon force-measuring experiments carried out during the last few years to get information on biological systems is shown in figure 1.

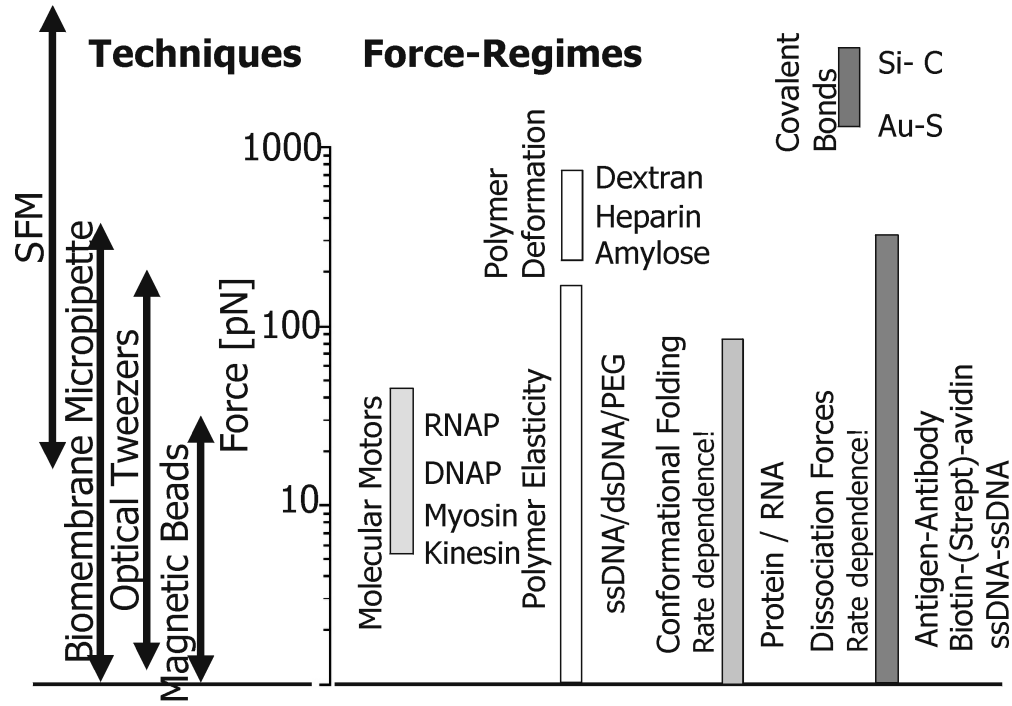

Figure 1: Overview on techniques, which are applied to assess information upon forces in biological systems. On the right a series of experiments in the various areas of motors proteins or molecular mechanics are shown. Some of the experiments like unfolding of individual proteins and dissociating (bio-molecular) bonds depend on the rate of the applied external force.

There is complementary biological information gathered by the various techniques. As visible in the graph, the force regime in which optical tweezers and scanning force microscopy are used overlap nicely. Optical tweezers preferably are applied in experiments on molecular motors and entropic elasticity of molecules and conformational folding of proteins and rupturing of bonds are mainly investigated by SFM.

In addition it has been shown during the last few years that the interaction of biomolecules on interfaces can be used as a tool for biosensing. The signal of the interaction of biomolecules on specific 'receptor' interfaces is transduced into a nanomechanical motion that is easily detected by the cantilever array technique a specific method evolved from the scanning force microscopy. It is the purpose of this review to give an insight into these fields of our research activities in the Physics Institute at the University of Basel.

2. OPTICAL TWEEZERS

As mentioned previously, optical tweezers (OT) are instruments, which allow to trap or levitate micron-sized dielectric particles using laser light. In addition, minute forces can be measured on the trapped particles with accuracy much better than what can be achieved with scanning force microscopy (in liquid and at room temperature). This explains why OT is nowadays considered as a technique of choice for the investigation of biomechanical forces. This section aims to give a basic introduction on this single-molecule technique (a single molecule can be attached to the handle and therefore its mechanical properties can be studied), describing technical details and possible implementation and calibration of OT instruments. Moreover, typical experiments performed with OTs will be highlighted.

2.1. Origin of Optical Forces

It was first demonstrated in 1970 by Ashkin that light could be used to trap and accelerate dielectric micron-sized particles [4]. For this experiment, a stable optical potential well was formed using two slightly divergent counter-propagating laser beams. This pioneer study established the groundwork for the Optical Tweezers (OT) technique, where a single laser beam is focused by a high numerical aperture (NA) objective lens to a diffraction-limited spot [5]. At the focus, not only dielectric particles spheres can be trapped but also biological organisms such as cells, virus, or bacteria [6, 7]. Although it is still challenging for theory to calculate typical optical forces [8, 9], the origin of optical forces can be understood easily (Fig. 2). Since a bundle of light rays is refracted when passing through a dielectric object, existing rays have a different directions than incoming rays. This results in the change in light momentum. By conservation of momentum, the change in the light momentum causes a change ΔP in the momentum of the trapped particle. As a result and due to Newton's second Law, the particle will feel a force F:

$$F = \frac{\Delta P}{\Delta t} = \frac{nQW}{c} \tag{1}$$

where n is the index of refraction of the surrounding medium, W the power of the laser, c the celerity of the light, and Q is a dimensionless factor, known as the trapping efficiency.

Optical forces are however very small, since 100 mW of power at the focus (10^{+7} W/cm^2) produces forces of only a few tens of pN on a micron-sized particle.

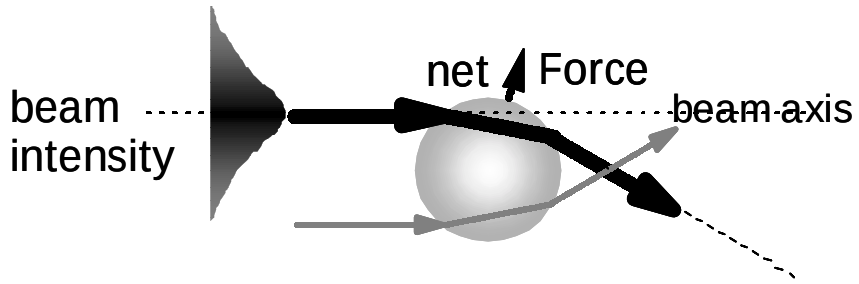

Figure 2: A transparent dielectric micron-sized particle with an index of refraction larger than the surrounding medium is pushed towards the largest intensity of the light. All light rays are refracted when entering the particle. Due to second Newton's law, the change in light momentum flux (the force) causes a reaction force on the particle. Center rays contain more photons than outer rays and exert therefore more force. The resulting net force is shown.

For biological applications, it is therefore imperative to choose a laser excitation, which (i) does not rise the temperature of the surrounding medium (say water) and (ii) prevents biological damage. It has been shown that near infrared excitation is always best suited, although the wavelength region between 700 and 760 nm should be avoided in typical OT experiments [10, 11].

As seen above, light exerts a pressure on dielectric particles. For practical applications, we need however to form a stable optical trap. In a simple picture, it can be shown that a stable trapping occurs when the scattering force is smaller than the gradient force. Basically, the scattering force (due to Fresnel reflections at the surface of the dielectric particle) is proportional to the power of the laser and acts only in the direction of propagation. As a consequence, this force does not trap. In contrast, the gradient force (proportional to the spatial gradient of the light) arises whenever the particle is out of the beam axis. This force acts therefore in 3-dimensions and tends to pull the particle towards the region of maximum spatial gradient (*i.e.* the focal point) if the index of refraction of the particle is larger than that of the buffer solution. This simple picture explains why a stable trapping is observed only when (i) high NA objective lenses are used (ii) the back aperture of the objective lens has to be overfilled (to produce a diffraction limited spot and therefore a maximum spatial gradient). Moreover, it suggests that handles with high refractive index (at least larger than the surrounding medium) have to be used.

2.2. Experimental Details

Knowing the origin of optical forces, we can build an optical trap. In principle, the design of such instruments should be easy since trapping requires only (i) a beam expander to overfill the back aperture of the microscope lens (ii) a good microscope lens with a high NA to produce a steep spatial gradient (iii) in addition when biological research is the focus of the experiment, lasers using wavelength in the near infrared should be used to avoid damage on the biological matter. Indeed, some rather simple modifications of a commercial inverted microscope are sufficient to build an OT [12]. Of course, whenever the following requirements have to be considered (beam steering, high mechanical stability, proper spatial filtering of the laser, reducing mode hopping the laser...), it is best to build an OT on a conventional optical table with custom optics and electronics [8]. Note finally that oil immersion microscope lenses are less suited for OTs due to the difference in index of refraction between oil and water (inside the chamber). The major microscope providers have nowadays a high numerical water-immersion lens in their program, which circumvent this drawback.

2.2.1. Calibration procedure

One of the main difficulties in OT experiments is to correctly estimate the force that acts on the trapped particle. We already have mentioned that an object changes the direction of the refracted rays when it experiences a force. In principle, such a change in the light momentum flux can be easily monitored onto a position sensitive detector (PSD) if we place after the objective lens a condenser lens (Fig. 3).

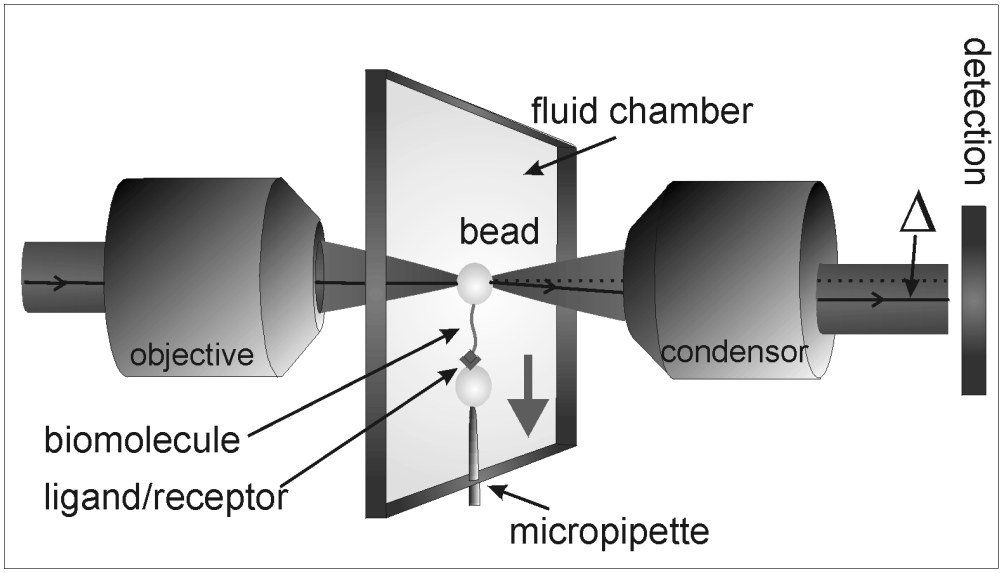

Figure 3: Schematic representation of an OT experiment. A microscope objective lens with a high NA is used to focus the laser light to a diffraction-limited spot. At the focus, where the spatial gradient is maximal, particle such as beads can be trapped. Light is collected with a condenser lens, which converts angular deflections into transverse deflections that can be monitored on a PSD. A single molecule can be attached between the trapped bead and a bead on a micropipette through a

receptor-ligand bridge. Mechanical properties of single molecules can be therefore investigated if the micropipette is placed onto a piezoelectric element. When the trapped bead experiences the force (arrow), it moves slightly away from its stable position. As in SFM, this leads to a deflection on the detector.

To relate deflections observed on the detector to forces, we need to calibrate the instrument. Many different approaches have been proposed in the past to perform such a calibration [8]. However, the thermal fluctuations calibration method is certainly the most widely used. Having an object in the trap, the stiffness K of the light lever can be estimated from the power spectral density $S(f)$ of the displacement fluctuations, using:

$$S(f) = \frac{k_B T}{\pi^2 \gamma \left(f^2 + f_c^2 \right)} \times A^2 \tag{2}$$

where γ denotes the viscous drag, $f_c = K(2\pi\gamma)^{-1}$ is the corner frequency (*i.e.* the frequency above which the particle does not feel the effect of the trap anymore), $k_B T = 4.1$ pN·nm at room temperature, and A is a factor describing the sensitivity of the detector ($V \cdot nm^{-1}$). Fitting the measured power spectral density with Eq. (2) gives a robust estimate of the corner frequency and consequently of the trap stiffness if the viscous drag is computable (*i.e.* for an object of known shape).

In addition, the detector sensitivity can be obtained from the area under the spectral density curve, knowing that the mean square displacement of the particle is related to both $S(f)$ and K through:

$$\left\langle x^2 \right\rangle = \int S(f) df = \frac{k_B T}{K} \times A^2 \tag{3}$$

Such a procedure shows that both the trap stiffness and the detector sensitivity (which are the only parameters needed to estimate the force) can be determined from a detector that is not absolutely calibrated.

2.2.2. State of the art instrumentation

In the previous section, we have seen that single beam OTs can easily measure forces. However, an important drawback of such instruments is that a new calibration has to be performed for each new experiment (each time some local parameters such as the shape or size of the trapped particle, the local fluid viscosity, or power of the laser are changed). Indeed, single beam OTs do not directly measure the change in light momentum flux because of the scattering at the interface of the microscope lens that introduces marginal rays. As shown by Smith [13], dual beam OTs overcome such limitations. Such instruments, although more expensive and more expensive than single beam OTs, need to be calibrated only once and have a very high trapping efficiency, which is of prime importance for biological investigations [14].

2.2.3. Thermal noise

At room temperature, Brownian motion of the trapped particle (OT) or the cantilever (SFM) limits the force resolution of this micromechnical experiments. As seen in the previous section, the power spectral density (*i.e.* thermal noise) is constant for frequency below the corner frequency and rolls off rapidly for frequency above f_c. However, *S(f)* usually extents to high frequencies. When the bandwidth f_s of the measurement is much smaller than the corner frequency or when low-pass filters are used, the minimum detectable force F_{min} reads (see Eq. (2) and (3)):

$$F_{\min} = (K / A)\sqrt{\langle x^2 \rangle} = \sqrt{4\gamma k_B T f_S} \tag{4}$$

In this case, the force resolution is independent of the trap stiffness [15]. To improve the sensitivity of micromechnical experiments, we can decrease (i) the temperature, (ii) the bandwidth of our measurement, or (iii) the drag viscosity. Alternatively, the resonance frequency of the SFM cantilever can be increased to reduce the noise at a give bandwidth. Certainly the best approach is to decrease the drag viscosity by reducing the size of the force-sensing device (the trapped bead or the cantilever) [15, 16]. This explains the need for small SFM cantilevers when high force sensitivity has to be achieved. Note that commercial SFM cantilevers have typical dimensions of 100 μm, whereas beads used for OT experiments have diameters of the order of 1 μm. For this reason, the force noise level of OT measurements (below 0.3 pN) is much smaller than that of SFM based techniques (10 pN, in liquid and at room temperature). However, the maximum force that can be measured with OTs is rather small as compared to SFM based techniques. For instance, dual beam OTs can measure forces only up to 200 pN [14].

2.3. Recent experiments

We do not attempt to give an exhaustive review of all experiments that have been performed with OTs (see [17, 18] for recent reviews). Rather, we would like to select and describe briefly typical applications of OTs in biology.

2.3.1. Molecular motors

Certainly, one of the most impressive applications of OTs is the study of molecular motors on a single molecule level. These molecular motors can be linear motors (Kinesin, Myosin) [19], DNA/RNA polymerase enzymes [20, 21] or DNA packaging viruses (bacteriophage ϕ29) [22].

Kinesin and Myosin are two ATPase motor proteins. Kinesin, which is used for organelle transport or chromosome segregation, moves along microtubules. In contrast, Myosin interacts with actin filaments and is used not only for muscle contraction but also is involved in many forms of cell movement. For these studies, OTs are used to interact single Kinesin or Myosin

in vitro with either a microtubule or an actin filament (Fig. 4.A). These experiments have revealed how much ATP has to be hydrolyzed and the forces generated at each step, demonstrating possible mechanisms involved in the movement.

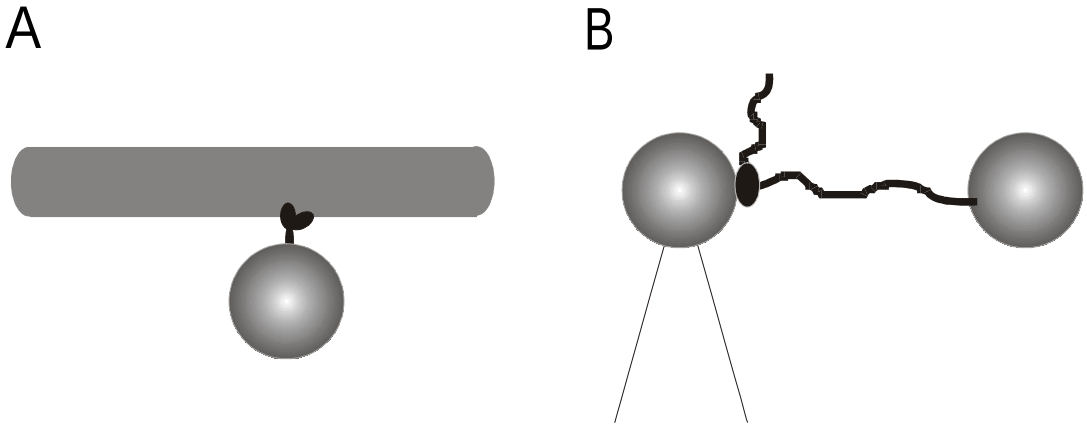

Figure 4: Possible experimental setups used for single molecule observation of molecular motors. (A) Beads coated with either Kinesin or Myosin are approached in the vicinity of a microtubule or an actin filament. For Kinesin studies, the microtubule is placed on a surface and the bead is hold by the OT. Kinesin can walk continuously for long distances (microns) before being released from the microtubule. In contrast, Myosin only binds weakly to actin and is released after a one step movement. For these experiments, the bead has therefore to be immobilized onto a surface and an actin filament is stretched and held by two optical traps. (B) A bead coated with an enzyme (black) interacting with a DNA molecule is held by suction on top of a micropipette in a continuous flow of buffer solution. A bead coated with a receptor recognizing the ligand-modified DNA molecule end is approached till the end is connected through the biomolecular interaction of the receptor with the ligand using OT. The enzyme runs then along the single DNA molecule and is used either to transcribe a dsDNA template into a messenger RNA (RNA polymerase) or to incorporate base pairs on ssDNA (DNA polymerase).

Other experiments investigated the function of motor enzymes used in DNA transcription or DNA polymerization. In this case a single DNA molecule is tethered between two beads (Fig. 4.B), and the rate of transcription or polymerization can be followed in real time by applying a constant tension (force feedback) and allowing the distance between the beads to change accordingly. Such studies have direct implications for the mechanism of gene regulation or force-induced exonuclase activity.

2.3.2. Mechanical properties of single molecules

Due to the high force sensitivity, OTs have been used to study (i) mechanical properties of DNA [23] (ii) protein or RNA unfolding [24-26] (iii) the polymerization of individual RecA-DNA filaments [27]. Again, these experiments provided new insights in biochemical processes on a single molecule and are of great relevance to biology. In a recent publication Husale et al. [28] showed that optical tweezers can easily be applied to investigate the influence of small ligands directly interacting with DNA to elucidate the binding mechanism of the ligands on the DNA.

3. SCANNING FORCE SPECTROSCOPY

3.1. Introduction to Dynamic Force Spectroscopy

It has long been known that only molecules with an excess of energy over the average energy of the population can participate in chemical reactions. Accordingly, reactions between ligands and receptors follow pathways (in a virtual energy landscape) that involve the formation of some type of high-energy transition states whose accessibility along a reaction coordinate ultimately controls the rate of the reaction. Until recently, chemists and biologists could only act on molecules if these were present in large quantities. Consequently, scientists could only access macroscopic thermodynamical quantities, e.g. the free energy of complex formation and/or dissociation.

Today, instruments offering a high spatial resolution and sensitivity down to the Pico- or Femto-Newton range allow one to study the adhesion of molecular bonds [29-41]. In particular, a novel type of force spectroscopy, the so-called dynamic force microscopy (DFS), has been developed. In figure 5 a setup of a scanning force microscope used for dynamic force spectroscopy is shown.

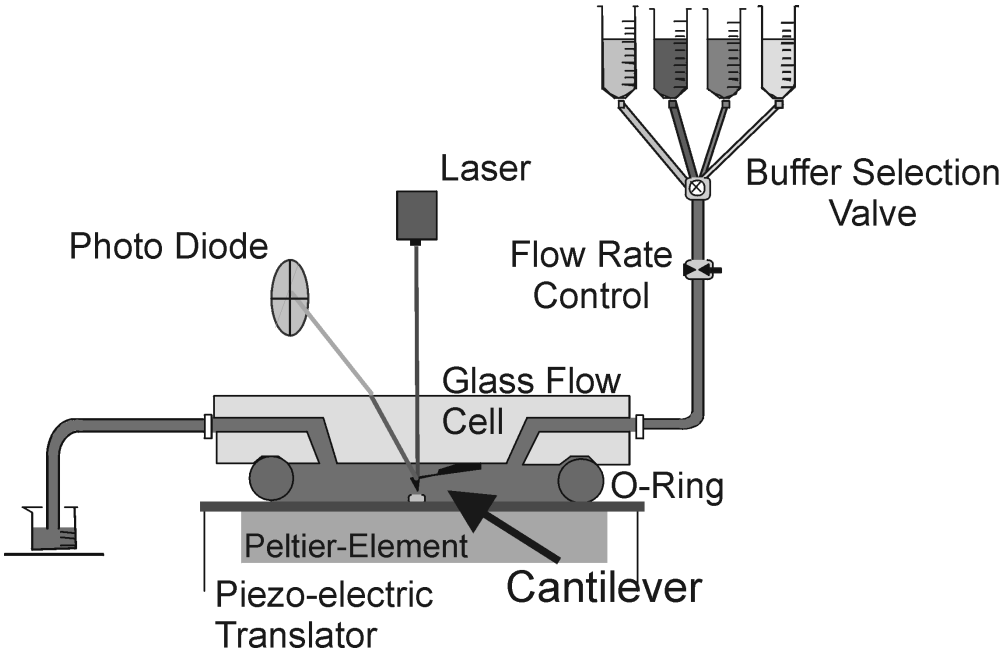

Figure 5: Setup of a scanning force microscope. The instrument is working in buffer media under ambient condition. A springboard type cantilever (dimensions ~300 X 20 X 0.5 μm, spring constant 0.01 N/m) is deflected when adhesive forces in-between the ligand-modified tip and the receptor-modified interface arises during retraction of the sample surface. The motion of deflection of the cantilever is detected using a laser beam, which is mirrored on the levers backside and projected onto a four-quadrant photosensitive diode. Various liquids can be injected and a peltier-element allows varying the temperature precisely.

In a DFS experiment, the dependence of the rupture force on the loading rate is investigated using a scanning force microscope (SFM), a bio-membrane

force probe (BFP), or eventually an optical tweezers setup. A rather detailed description of such experiments performed in our laboratory is given in this section [39-42]. For a typical DFS experiment using an SFM, a ligand is immobilized on a sharp tip attached to a micro-fabricated cantilever and the receptor is immobilized on a surface. When approaching the surface of the tip a bond may form between ligand and receptor. The bond is then loaded with an increasing force when retracting the surface from the tip. From these measurements, the energy landscape of a single bond can be mapped [43]. A typical force distance plot of these experiments is shown in figure 6.

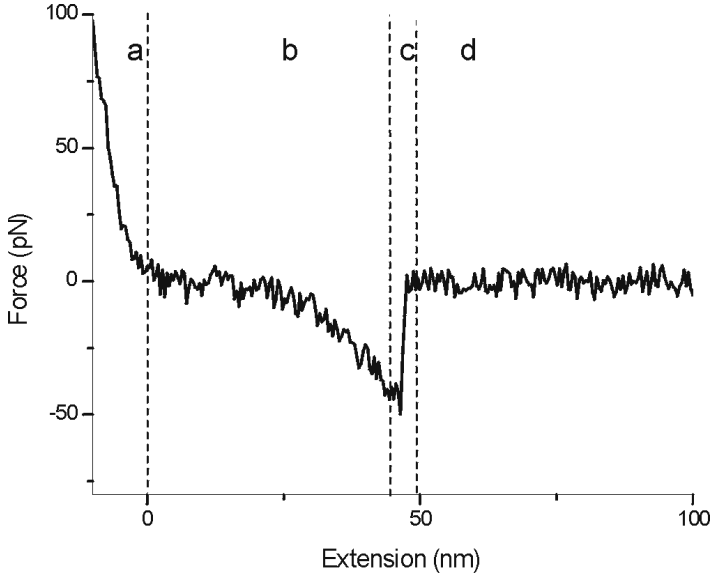

Figure 6: A typical force-distance curve obtained in a stretching SFM experiment (retraction cycle). A DNA strand (TATTAATATCAAGTTG) is immobilized by its 5′-end *via* a PEG linker on the SFM tip and its complement is attached in a similar fashion by its 5′-end to the surface. When the tip is approached close to the surface a specific bond between the two strands is formed (a). The SFM tip is then retracted from the surface at constant loading rate (b-[PEG stretching]). The sudden drop in the force curve reflects unbinding of the duplex (c-[specific DNA unbinding]). The loading rate *r* (retract velocity *v* times the elasticity *c*) is determined from the slope of the force-displacement curve before the unbinding event occurs.

This section is organized as follows. Part one introduces theoretical models that describe a chemical reaction when an external force is used to rupture a complex. Then, DFS experiments on complementary DNA strands are presented and illustrate the main ideas developed in part 3.1.

3.2. Theoretical Background

In this section, some thermo-dynamical models describing the rupture of a single bond will be briefly presented. More details can be found elsewhere [44-47].

Bell [45] first stated that the bond lifetime τ of an energy barrier reads:

$$\tau(F) = \tau_0 \exp[(E_0 - \Delta x F)/k_B T] \quad (5)$$

where T is the temperature, E_0 represents the bond energy (the height of the barrier), F is the external applied force per bond, Δx is the distance (projected along the direction of the applied force) between the ground state and the energy barrier (with energy E_0), and τ_0 is a pre-factor. Eq. (5) states that (i) a bond will rupture after a certain amount of time thanks to thermal fluctuations (ii) application of an external force dramatically changes the time it takes to overcome the energy barrier. Note finally that (5) can be re-written as:

$$k_{off}(F) = k_{off} \exp\left(F/F^0\right) \quad (6)$$

where k_{off} is the thermal off-rate of the barrier, and F^0 is a force-scale factor ($F^0 = k_B T/\Delta x$).

An important point is that the most probable force F^* needed to overcome an energy barrier should *a priori* depend on the loading rate, *i.e.* the velocity in a typical DFS experiment (typical values for velocities are in the range between 10 nm/s and 5000 nm/s). Indeed, when the loading rate decreases, F^* should decreases because of thermal fluctuations. In fact, a simple relation holds between F^* and the loading rate r ($r=k\nu$, where k is the stiffness of the DFS force sensor and ν is the retraction speed):

$$F^* = F^0 \ln\left(r/F^0 k_{off}\right) \quad (7)$$

By plotting F^* as a function of $\ln(r)$, one should therefore find different linear regimes, each of them corresponding to a specific region (a specific energy barrier) of the energy landscape. According to Evans [46], the kinetics runs as follows: application of an external force (i) selects a specific path (a reaction coordinate) in the energy landscape (ii) suppresses outer barriers (Eq. 5), and reveal inner barriers which start to govern the process. For instance, recent BFP and SFM experiments have revealed an intermediate state for the streptavidin (or avidin)-biotin complex [38, 41]. However, since each energy barrier defines a time-scale (a range of loading rate that has to be compatible with the time-scale of the experiment) only a specific part of the energy landscape can be mapped in a typical DFS experiment [47, 48].

3.3. Experimental

DFS measurements were performed with a commercial SFM instrument using some external data acquisition and data output capabilities in addition. The spring constants of all cantilevers (ranging from 12 to 17 pN/nm) were calibrated by the thermal fluctuation method [49] with an absolute uncertainty of 20%. For the temperature measurements presented below, the temperature was controlled using a home built cell where the buffer solution that immersed both

the probe surface and the SFM cantilever was in contact with a Peltier element, driven with a constant current source. Measurements at different points of the cell showed deviations of less than 2 °C.

The preparation and immobilization of all oligonucleotides follows the protocol described in Refs. 39 and 42.

3.4. Probability distribution and specificity of rupture forces

Unbinding events are caused by thermal fluctuations rather than by mechanical instability. Therefore unbinding forces show a distribution whose width σ is mainly determined by the force scale F^0, *i.e.* $\sigma=F^0(\Delta x)$.

When approaching the tip to the surface, many non-specific attachments may occur, even in the presence of treated surfaces or pure polymer samples. Therefore, it is imperative to test the specificity of the interaction (Fig. 7.).

Unspecific interactions can be minimized using linkers (e.g. poly(ethylene)glycol (PEG) linkers) that shift the region where unbinding takes place away from the surface. Finally, to quantify the most probable value for the unbinding force of a single complex, one has to work under conditions in which the probability that two or more duplexes are attached to the tip is low.

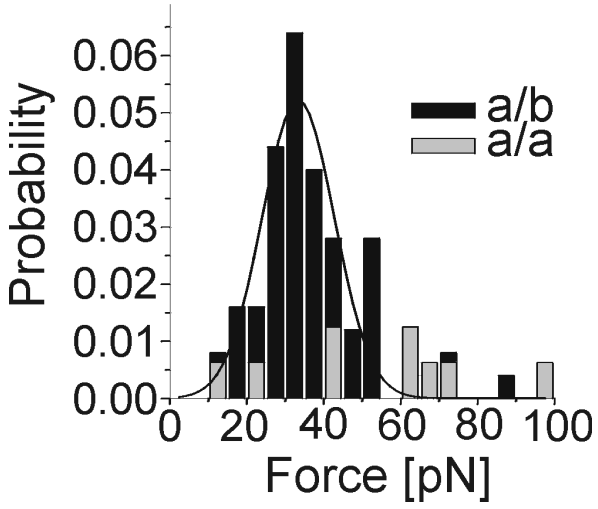

Figure 7: A typical probability distribution for the rupture force (about 500 approach/retract cycles, retract velocity 100 nm/s) [39]. For this experiment, an oligomer *a* (see text) was attached to the tip of the SFM-cantilever and its complement *b* was immobilized on the surface (complements were pulling apart at their opposite 5′-ends). Gray rectangles (*a* against *a*), black rectangles (*a* against *b*). To minimize unspecific interactions (e.g. *a* against *a*) and multiple unbinding events, 30-nm-long PEG linkers were attached to the 5′-ends. Note that the scale-force F^0 can be in principle determined from the width of the distribution.

These conditions are fulfilled for a low concentration and when the linkers have a length that is comparable to the diameter of the SFM-tip (about 50 nm). In this case, it is very unlikely that two or more linkers are extended to the same length when stretched. However, subsequent rupture events may be found. But still, the last rupture event will occur for an applied force equal to F^*.

3.5. Dynamic measurements

3.5.1. Base pair dependence

We now present DFS measurements performed on complementary DNA strands of different length [10, 20, and 30 base pairs (bp)] and pulled apart at their opposite 5'-ends. The base sequences of the oligonucleotides were designed to favor the binding to its complementary oligonucleotides in the ground state with respect to intermediate duplexes in which the strand is shifted relative to its complement. We have chosen the oligomer **a** (5'-G-G-C-T-C-C-C-T-T-C-T-A-C-C-A-C-T-G-A-C-A-T-C-G-C-A-A-C-G-G-3'), which contains 30 bases and in which every three base motive occurs only once in the sequence. For this sequence, self-complementarities are avoided because the complement of each three-base motive is not contained in the sequence. **a** was tested against its complement **b** (30 bp) and against truncated components **c** (20 bp) and **d** (10 bp), respectively.

As expected, a F^* *versus* ln(v) plot shows a linear behavior for each duplex (Eq. 7, see Figure 8).

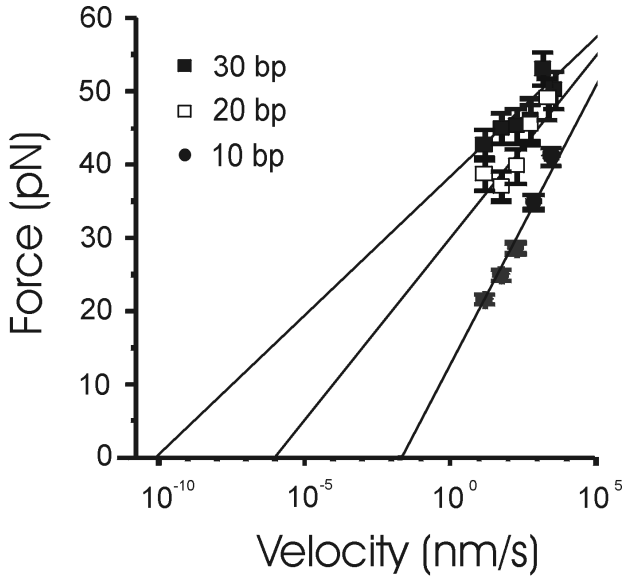

Figure 8: Velocity dependence of the most probable unbinding force [39]. Back squares (a-tip/b-surface, 30 bp), empty squares (a-tip/c-surface, 20 bp), circles (a-tip/d-surface, 10 bp). From a linear fit, both the force-scales $F^0 = k_BT/\Delta x$ and thermal off-rates can be determined.

For each duplex, the distance Δx from the ground state to the energy barrier and the thermal off rate k_{off} were determined according to Eq. 7. The Δx distance was found to follow the linear relation: $\Delta x = [(0.7 \pm 0.3) + (0.07 \pm 0.03) \times n]$ nm, where n is the number of base pairs. This increase of Δx with n clearly indicates cooperativity in the unbinding process. Measurements of k_{off} can be described by: $k_{off} \approx 10^{\alpha - \beta n} s^{-1}$, where $\alpha = 3 \pm 1$ and $\beta = 0.5 \pm 0.1$. The obtained k_{off} values are in good agreement with thermodynamical data [50]. Let us finally point out that an exponential decrease of the thermal off-rate with the number of

base pairs is expected because of the increase of the activation energy for dissociation (Eq. 5). However, the pre-factor τ_0 in Eq. 5 also strongly decreases with the number of base pairs because of the increasing number of degrees of freedom of the system.

3.5.2. Temperature dependence

In this section, temperature dependent DFS measurements are briefly discussed. The sequence **e** (5'-T-A-T-T-A-A-T-A-T-C-A-A-G-T-T-G-3') [51] attached to the tip and its complement **f** was immobilized on the surface. As previously, PEG linkers were used and DNA strands were pulled apart at their opposite 5'-ends. The specificity of the interaction was comparable to the one obtained in base-pair dependent measurements (Fig. 7).

As seen in Fig. 9, the slope of the F^* versus ln(r) plots changes as a function of temperature, which evidences for a strong temperature dependence of Δx. This result emphasizes the fact that for the DNA-duplex, the energy landscape is much more complicated than that of ligand-receptor bonds.

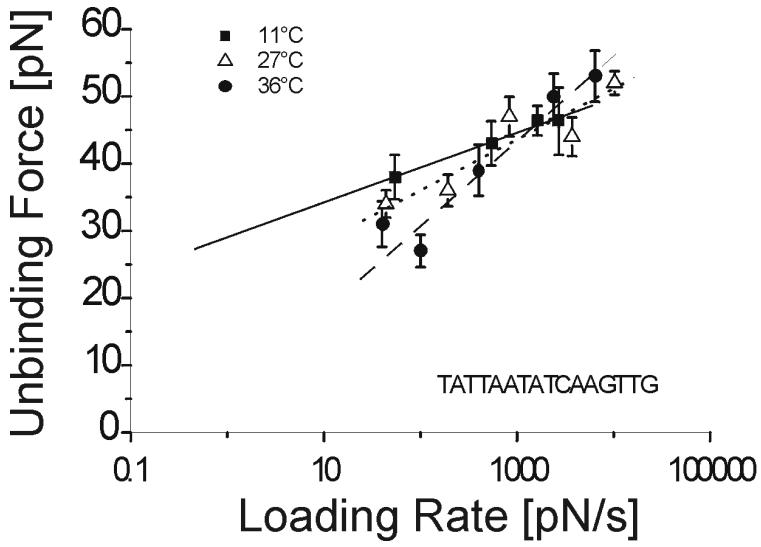

Figure 9: The most probable unbinding force as a function the loading rate (e-tip/f-surface, 16 bp) obtained at different temperatures. Squares (11 °C), triangles (27 °C), circles (36 °C).

As a consequence, the unbinding process may involve many different reaction paths. In this case, thermal fluctuations are expected to play a key role.

3.6. Future of dynamic force spectroscopy

Using DFS measurements, the energy landscape of molecular bonds can be mapped. Moreover, relevant parameters such as the location and height of the barriers and the thermal off-rates can be determined. Our measurements confirm that the most probable force for unbinding scales as the logarithm of the loading rate. From this dependence, both the natural thermal off-rate for dissociation K_{off} and the bond length x along the reaction coordinate were

determined. Our measured K_{off} values are in agreement with bulk temperature measurements indicating the validity of our measurements. The base pairs dependent measurements indicate that unbinding of DNA strands is a cooperative process. Temperature dependent measurements evidence for a decrease of Δx as the temperature increases [42]. This behavior, which is not expected in the case of one dimensional energy landscape with a sharp energy barrier, indicates the role played by entropic contributions when unbinding DNA and unfolding RNA or proteins. However, the linear decrease of x with the temperature is still an open question. It is obvious that the exact relationship between the bond length and the temperature is not straightforward and calculations are needed to explain the observed properties. Since the limited range of loading rates available in an SFM experiment does not allow one to map the whole energy landscape, such experiments should be combined in the future with other DFS setup such as bio-membrane force probe or optical tweezers setups. An additional solution is to apply small cantilevers, which allow faster pulling and exhibit less thermal noise; so smaller unbinding forces can be detected. These small cantilevers are still experimental [52] and great efforts are being made to commercialize them in the future. These developments will also ask for instrument development so it is expected to last a few years before they are widely used. One could envision that the dynamic force spectroscopy will be applied in the future to assess the binding affinity of biomolecules on bio-arrays but the experimentalists have to catch up to step in this direction.

4. ADVANCED BIO-SENSING USING MICRO MECHANICAL CANTILEVER ARRAYS

4.1. Introduction to micro-mechanical bio-sensors

During the last few years a series of new detection methods in the field of biosensors have been developed. Biosensors are analytical devices, which combine a biologically sensitive element with a physical or chemical transducer to selectively and quantitatively detect the presence of specific compounds in a given external environment.

These new biosensor devices allow sensitive, fast and real-time measurements. The interaction of biomolecules with the biosensor interface can be investigated by transduction of the signal into a magnetic [53] an impedance [54] or a nanomechanical [55] signal. In the field of nanomechanical transduction, a promising area is the use of cantilever arrays for biomolecular recognition of nucleic acids and proteins. One of the advantages of the cantilever array detection is the possibility to detect interacting compounds without the need of introducing an optically detectable label on the binding partners. For biomolecule detection the liquid phase is the preferred one but it has been shown that the cantilever array technique is also very appropriate for

the use as a sensor for stress [56], heat [57] and mass [58]. Recent experiments showed that this technique could also be applied as an artificial nose for analyte vapors (e.g. flavors) in the gas phase [59].

4.2. Nanomechanical cantilever as detectors

The principle of detection is based on the functionalization of the complete cantilever surface with a layer, which is sensitive to the compound to be investigated. The detection is feasible in different media (e.g. liquids or gas phase). The interaction of the analyte with the sensitive layer is transduced into a static deflection by inducing stress on one surface of the cantilever due to denser packing of the molecules [60] or a frequency shift in case of dynamic detection mode [61] due to changes in mass.

4.3. Overview of the two detection modes

4.3.1. Static mode

In static mode detection, the deflection of the individual cantilever depends on the stress induced by the binding reaction of the specific compounds to the interface. The interface has to be activated in an asymmetrical manner, as shown in figure 10. Most often one of the cantilever surfaces is coated with a metallic layer (e.g. gold) by vacuum deposition techniques and subsequently activated by binding a receptor molecule directly *via* a thiol group to the interface (e.g. thiol modified DNA oligonucleotides) or as in case of protein recognition by activating the fresh gold interface with a self-assembling bi-functional bio-reactive alky-thiol molecule to which the protein moiety is covalently coupled [62].

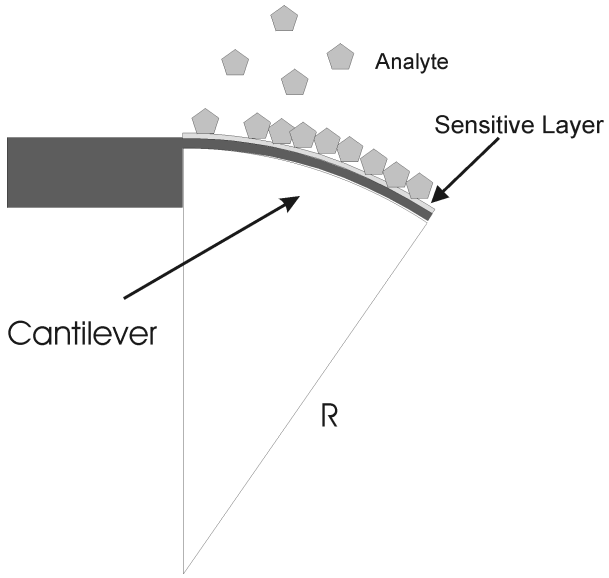

Figure 10: Interaction of the analyte (light gray pentagons) with the sensitive layer induces a stress on the interface and bends the cantilever (note the asymmetric coating of the individual cantilever surface).

The radius R of the curvature of the cantilever is given by the Stoney's law [63]

$$\sigma = Et_{Cant}^2 (6R(1-\gamma))^{-1} \quad (8)$$

where σ is the stress, γ is the Poisson ratio, E the Young's Modulus and t_{cant} the thickness of cantilever. The thickness of the lever is an important parameter, which can be varied to in─ or decrease the sensitivity of the device. By reducing the thickness a larger deflection due to stress change at the interface is possible. Note, that the interaction of the ligand with the receptor molecule has to occur in the vicinity of the interface. No flexible linking of the receptor molecule is allowed due to the fact that the induced stress will be diminished. IN addition the receptor molecules should be immobilized natively tightly packed on the interface to interact with the substances to be analyzed.

4.3.2. Dynamic mode

In the case of dynamic mode detection, the resonance frequency of the individual cantilever, which has to be excited, depends on the mass. The binding reaction of the analyte to the interfaces is increasing the mass and the resonance frequency is normally decreased. In figure 11 the scheme of dynamic cantilever detection is shown.

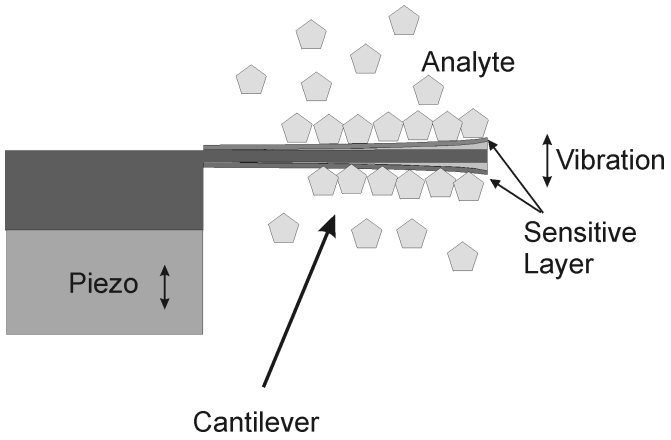

Figure 11: Interaction of analyte (light gray pentagons) with sensitive layers induces a change in the resonance frequency of cantilever.

The cantilever is excited by a piezo element. The change in mass (Δm) during the experiment due to an uptake of interacting biomolecules induces a change in the resonance frequency of cantilever, which can be described by the following formula [61]:

$$\Delta m = K\left(4n\pi^2\right)^{-1}\left(f_1^{-2} - f_0^{-2}\right) \quad (9)$$

where the resonance frequency prior and during experiment are f_0 and f_1, K is the spring constant of cantilever and n a factor depending on the geometry

of the cantilever. The uptake of mass due to specifically interacting molecules is doubled in this manner and the cantilever does not respond to temperature changes *via* a bimetallic effect. Additionally the preparation involves fewer steps as in the case of the static detection mode [57].

4.4. Setups

At the institute of Physics in Basel at the University of Basel in collaboration with the IBM Research Laboratory Zurich we developed cantilever array setups both for static and dynamic mode operation in liquids and in the gas phase.

The principal part of the setup is an array of 8 cantilevers, produced by classical lithography technology with wet etching. A typical picture of such a cantilever array is shown in figure 12.

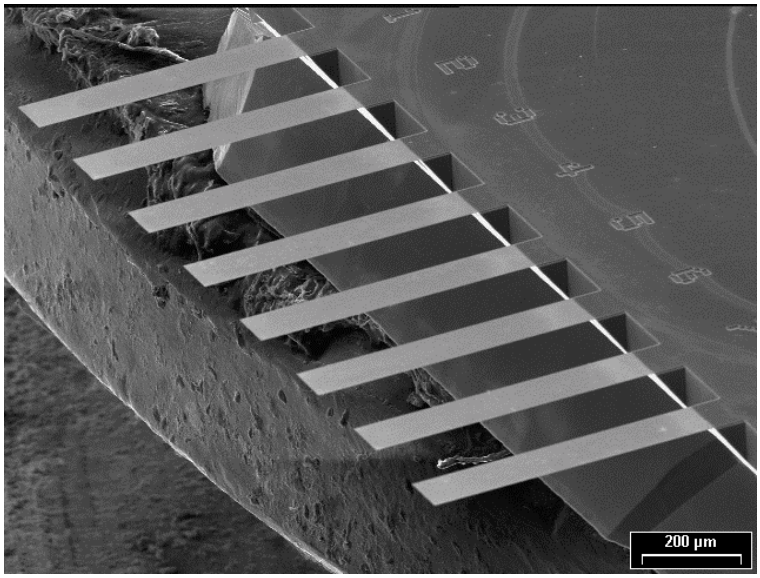

Figure 12: SEM picture of an array of 8 cantilevers. Dimensions: width 100 um, length 500 um, 0.5 um with a pitch of 250 um in-between.

The structure of an array is composed of 8 cantilevers. The etching process provides cantilever thickness ranging from 250 nm to 7 µm adapted for the individual application (*i.e.* static or dynamic mode).

A classical laser beam deflection optical detection for both the static and dynamic mode set up is used (see Fig. 13).

The laser source consists of an array of 8 VCELs (Vertical Cavity Surface Emitting Lasers, 760 nm wavelength, pitch 250 µm) and the position detection is obtained through a linear position sensitive detector (PSD). The array is mounted in a cell, which can be used for measurements in gas or a liquid environment.

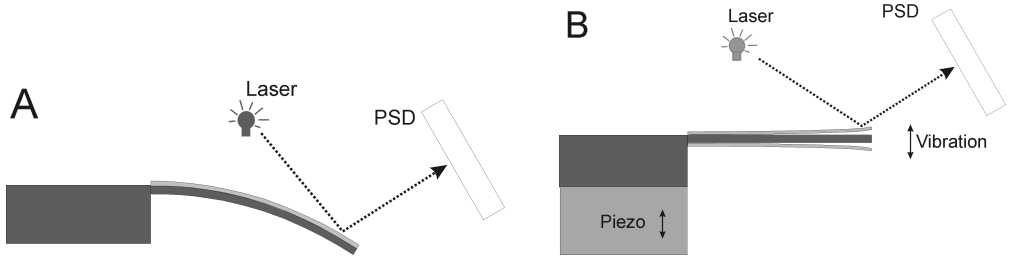

Figure 13: Optical detection used for static (A) or dynamic (B) mode detection of average cantilever position using a multiple laser source VCELs and a position sensitive device (PSD).

A scheme showing the setup is displayed in figure 14. The operation of our instruments is fully automatic. During the time course of a few hours up to eight different samples can be probed using the automatic fluid delivery. The instrumental noise of the static setup lies in the sub-nanometer range and the dynamic setup is able to detect mass changes in the order of picograms.

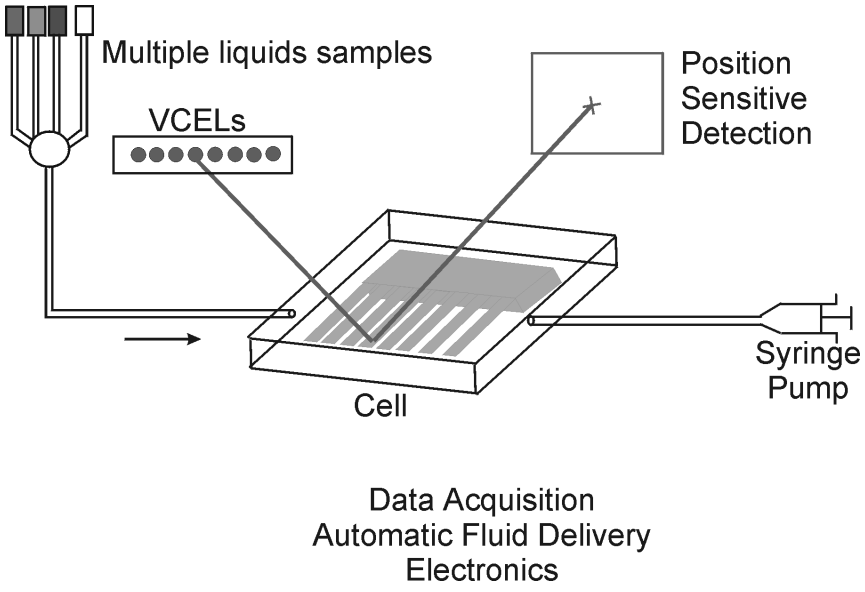

Figure 14 General structure of cantilever array setups for gas/liquid samples.

The key advantage to use cantilevers arrays is to offer the possibility of *in situ* reference and the simultaneous detection of different substances. The *in situ* reference is needed to avoid the thermo-mechanical noise especially in fluid phase detection. Changes in refractive index when the buffer changes will also contribute to a 'virtual' motion of the cantilever. As visible in figure 15 only the 'real' motion, which is the difference in-between the cantilevers on the same chip is originating from the specific biomolecular interaction.

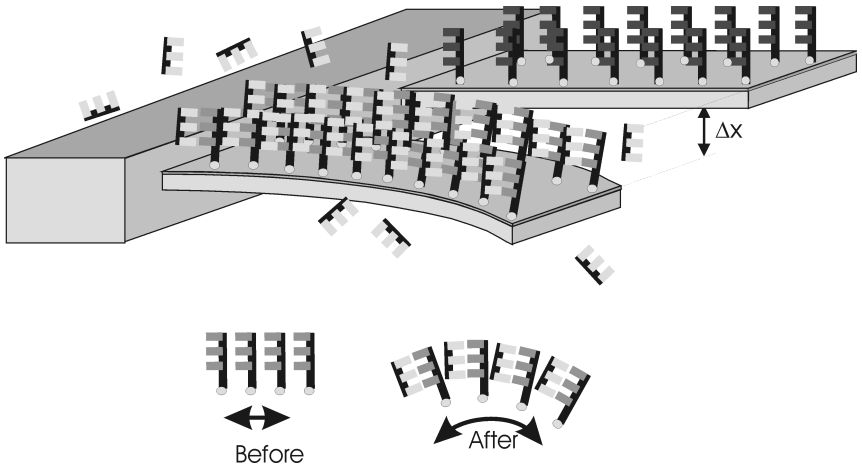

Figure 15: Static detection of biomolecular interaction. The cantilevers have to be equilibrated and then the biomolecule of interest is injected. Due to the specific interaction of the injected biomolecules (light gray) with the biomolecules on the cantilever shown in front stress builds up. A scheme is shown below. The interaction of the biomolecules with the receptor molecules induces stress at the interface, which deflects the individual cantilever specifically.

In figure 16 (A) A raw signal of the cantilever array is displayed. Since there will always be instrumental or thermal drift, the differential signal detection is mandatory. The figure shows an experiment with a set of three cantilevers (thickness ~500 nm). In this experiment we used two reference cantilevers with different coatings and one specific biorecognition cantilever. This cantilever is being stressed upon binding of the corresponding interacting biomolecule.

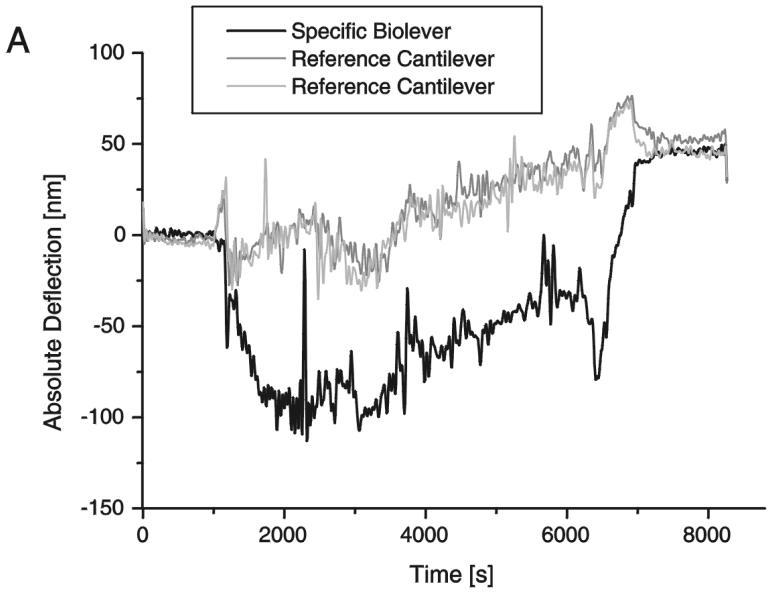

Figure 16 A: Raw data of a three-lever bio-array experiment. In the top traces (light gray, gray) the motion of the reference cantilevers is shown. In black color the motion of the biologically specific cantilever is

displayed. Upon injection of interacting biomolecules [~1000 s] turbulences of the liquid cause all levers to undergo some motion, which is stabilized immediately when the flow is stopped [~1200s]. The specific binding signal quickly builds up and remains stable. The interaction is fully reversible and can be broken by shifting the equilibrium of the binding reaction by injecting pure buffer solution [~6500s] into the fluid chamber. During the time course of two to three hours, we regularly see a drift of the cantilever arrays on the order of tens of nanometers even though the setup is temperature-stabilized (0.05°C).

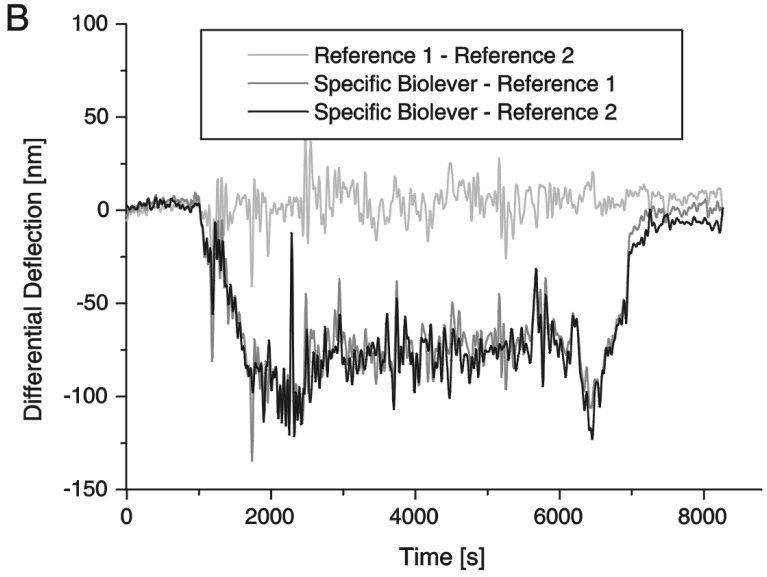

Figure 16 B: Differential data of the experimental set of figure 16 (A). The difference of in-between the two reference cantilevers is shown (light grey). Except for some small motions, no differential bending is observed, whereas in the color dark gray and black the difference of the specifically reacting cantilever with respect to the reference cantilevers is show. As shown after ~6500s pure buffer solution is injected and the differential signal collapses to values close to the starting point were no interacting biomolecules were present in the experiment.

As visible in figure 16 (B) the differential signal lacks of any external influences except for the specific biomolecular interaction which induces a differential signal of ~90 nm relative to the *in situ* reference. The experiment is reversible and can be repeated using different concentrations of analytes. In a recent work we presented data, which allow extracting of the thermodynamics of the interacting biomolecules (*i.e.* DNA) [64]. Deflection signals as small as a few nanometers are easily detected. Currently, the detection limit in static experiments lies in the range of nanomolar concentration [64] but can be significantly lowered by using cantilever arrays of thickness in the range of 250 – 500 nm in the future.

Great care has to be taken in the selection of the internal reference lever. In the case of DNA detection an oligonucleotide displaying a sequence, which does not induce cross talk binding reactions to the sequences to be detected is chosen. Coating with thin layers of titanium and gold using vacuum deposition modifies one side of the cantilever array. Onto this metallic interface a thiol-

modified oligonucleotide self-assembles in a high-density layer. Complementary and unknown oligonucleotide sequences are then injected and the specific interaction is directly visible within minutes. Stress at the interface is built up due to a higher density of packing (see figure 15). In protein detection, a protection of the asymmetrically coated cantilever has to be considered. Preparation of protein detecting cantilevers is a multi step procedure and requires surface chemistry knowledge. The side opposite to the biomolecular-modified side is generally protected by a poly-ethylene-glycol (PEG) layer. The bio-reference surface can be coated by using unspecifically interacting proteins (e.g. bovine serum albumin). In protein detection experiments larger 'fluctuations' of the cantilevers are observed (e.g. figure 16) than in the ssDNA-ssDNA experiments. A possible interpretation of this difference might be due to the fact that the proteins used [μM] absorb light within the visible spectrum and therefore induce some local changes in index of refraction. Specific signals are normally measured within minutes without problems. Usually some drift of few tens of nanometers is observed of the complete set of cantilevers during the time course of the experiment even though the instruments temperature is stabilized within ± 0.05 °C. But these effects are completely eliminated by using a differential read out on the very same cantilever array.

Cantilevers arrays are already applied as detector both in static and dynamic mode [60, 61]. Recent articles show the potential for detection of DNA hybridization [55, 64], cell capture or toxin detection [53]. Integrating cantilever arrays into micro-fluidic channels will significantly reduce the amount of sample required [65]. Attempts have been made to get data from single cantilever experiments for DNA [66] or antibody antigen reaction [67] or from a two-cantilever setup using different stiffness for the individual cantilevers [68]. We would like to point out that these approaches have serious drawbacks. Information extracted from these experiments, which often last multiple hours, cannot exclude unspecific drift of any kind. The signal in these experiments is interpreted as specificity on the biomolecular level but no correlation from one lever to the next is applicable if only one lever is used at the time. In a second approach, cantilevers with different stiffness are used to monitor the nanometer motions. Since the individual cantilever used show a difference of factor four in terms of stiffness, the response, which originates from specific interaction, is difficult to extract. The sensitivity of this approach is hampered due to the differences in stiffness, which is directly correlated to the thickness of the cantilever used (see Eq. 8). An interaction of the biomolecule with the stiffer reference cantilever might not be detectable if the stress signal lies within the thermal noise of that lever.

4.5. Future applications of cantilever arrays

The cantilever array technology explore a wide area of applications; all biomolecular interactions are in principle able to be experimentally detected using cantilever array as long as mass change or surface stress is induced due to the specific interaction. A few applications so far demonstrated promising results in the field of biological detection. The cantilever based sensor platform might fill the gap between the very expensive analytical instrumentation (e.g. mass-spectroscopy, HPLC, SPR), which are sensitive but costly and relatively slow and the chip technologies (e.g. gene-arrays) with its advantage of easy multiplexing capabilities, but the need of fluorescence labeling and with its restriction to higher molecular weight compounds like proteins and nucleic acids so far.

In comparison to the methods described above, the cantilever technology is cheap, fast, sensitive and applicable to a broad range of compounds. The cantilever arrays can be used repeatedly for successive experiments. The lack of multiplexing could be overcome by the application of large cantilever arrays with > 1000 Cantilevers/chip. There are now projects launched to introduce commercial platforms providing arrays of eight cantilevers for applications in the liquid or in the gas phase. A critical point for future developments in this field will be the access to the cantilevers arrays as it is in the 'normal' field biological applications using single cantilever scanning force microscopy. At the moment, there are no biological experiments published which use the dynamic mode detection. But as we believe the ease of preparation (symmetrically as pointed out above) and the fact that the sensitivity towards environmental changes is reduced, this might be the instrumental approach of choice for the future biological detection using cantilever arrays.

5. CONCLUSION

During the last decade single molecule experiments provided ample information in the field of biological basic research. We would like to point out again that these kinds of experiments do not probe an ensemble of molecules and therefore give access to information or properties of sub-populations of biomolecules. These experiments don't have to be synchronized and therefore no averaging occurs. In nature many cases, which define the status of an organism are depending on properties or activity of individual sub-populations (e.g. start of cancer in an individual cell). – It is a long way to go to have real implications of single molecule manipulation experiments on daily life, but the information revealed so far, show that the clues to some specific biological problems might lie in the detail [e.g. Ref. 22]. In addition, it is important to mention that single molecule experiments are always technically most demanding and the future results obtained on single molecule will mainly depend on instrumentation capabilities. One 'drawback' of single molecule

experiments is, that one experiment is not sufficient to elucidate the properties of a subpopulation. Enough experimental data has to be gathered, which is time consuming, to allow applying statistics.

A way out might be to combine the high sensitivity of these force measuring devices and sample a few thousand molecules at a given time as it is done by using cantilever arrays. This new array technology is not limited to genomic studies but can also detect protein-protein interactions [55], and will thus find applications in the fields of proteomics, biodiagnostics and combinatorial drug discovery where rapid, quantitative binding measurements are vital. The ability to directly translate biochemical recognition into nano-mechanical motion might have wide ranging implications, for example DNA computing applications or nanorobotics. The Nano-Newton forces generated are sufficient to operate micromechanical valves or microfluidic devices and *in situ* delivery devices could be triggered directly by signals from gene expression, immune response or single cells.

ACKNOWLEDGEMENT

Financial support of the NCCR "Nanoscale Science" the Swiss National Science Foundation and the ELTEM Regio Project Nanotechnology is gratefully acknowledged. We would like to thank our colleagues from Basel and IBM Rüschlikon for the great collaborative effort and for their valuable contributions to make progress in the field single molecules manipulation using OT and SFM and in the field of cantilever arrays. We are especially grateful to Ernst Meyer, Peter Vettiger, Felice Battiston, Torsten Strunz, Irina Schumakovitch and Hans-Joachim Güntherodt.

REFERENCES

[1] A. Engel and D.J.Müller, Nature Struct. Biol., 7 (2000) 715.
[2] M. Guthold, X.S. Zhu, C. Rivetti, G.L. Yang, N.H. Thomson, S. Kasas, H.G. Hansma, B. Smith, P.K. Hansma and C. Bustamante, Biophys. J., 77 (1999) 2284.
[3] M. Rief, M. Gautel, F. Oesterhelt, J.M. Fernandez, and H.E. Gaub, Science, 276 (1997) 1109.
[4] A. Ashkin, Phys. Rev. Lett., 24 (1970) 156.
[5] A. Ashkin, J.M. Dziedzic, J.C. Bjorkholm and S. Chu, Opt. Lett., 11 (1986) 288.
[6] A. Ashkin and J.M. Dziedzic, Science, 235 (1987) 1517.
[7] A. Ashkin, J.M. Dziedzic and T. Yamane, Nature, 330 (1987) 769.
[8] K. Svoboda and S.M. Block, Annu. Rev. Biophys. Biomol. Struct., 23 (1994) 247.
[9] N. Pam and H.M. Nussenzveig, Eur. Phys. Lett., 50 (2000) 702.
[10] K.C. Neuman, E.H. Chadd, G.F. Lion, K. Bergman and S.M. Block, Biophys. J., 77 (1999) 2856.
[11] G. Leitz, E. Fällman, S. Tuck and Ove Axner, Biophys. J., 82 (2002) 2224.
[12] R.S. Afzal and E.B. Treacy, Rev. Sci. Instrum., 63 (1992) 2157.
[13] S.B. Smith, PhD. Thesis, University of Twente, The Netherlands 1998.

[14] W. Grange, S. Husale, H.J. Güntherodt and M. Hegner, Rev. Sci. Instrum., in press (June 2002).
[15] F. Gittes and C.F. Schmidt, Eur. Biophys. J., 27 (1998) 75.
[16] M.B. Viani, T.E. Schaffer, A. Chand, M. Rief, H.E. Gaub, P.K. Hansma, J. Appl. Phys., 86 (1999) 2258.
[17] A.D. Metha, M. Rief, J.A. Spudich, D.A. Smith and R.M. Simmons, Science, 283 (1999) 1689.
[18] C. Bustamante, J.C. Macosko and G.J.L. Wuite, Nat. Rev., Mol. Cell Biol., 1 (2000) 130.
[19] G. Woehlke and M. Schliwa, Nat. Rev., Mol. Cell Biol., 1 (2000) 50.
[20] G.J. Wuite, S.B. Smith, M. Young, D. Keller and C. Bustamante, Nature, 404 (2000) 103.
[21] R.J. Davenport, G.J. Wuite, R. Landick and C. Bustamante, Science, 287 (2000) 2497.
[22] D.E. Smith, S.J. Tans, S.B. Smith, S. Grimes, D.L. Anderson and C. Bustamante, Nature, 413 (2001) 748.
[23] S.B. Smith, Y. Cui and C. Bustamante, Science, 271 (1996) 795.
[24] M.S. Kellermayer, S.B. Smith, H.L. Granzier and C. Bustamante, Science, 276 (1997) 1112.
[25] L. Tskhovrebova, J. Trinick, J.A. Sleep, and R.M. Simmons, Nature, 387 (1997) 308.
[26] J. Liphardt, B. Onoa, S. B. Smith, I. Tinoco Jr. and C. Bustamante, Science, 292 (2001) 733.
[27] M. Hegner, S.B. Smith and C. Bustamante, Proc. Natl. Acad. Sci. USA, 96 (1999) 10109.
[28] S. Husale, W. Grange and M. Hegner, Single Mol., (2002) in press (June 2002).
[29] G. U. Lee, L. A. Chrisley and R. J. Colton, Science, 266 (1994) 771.
[30] G. U. Lee, D.A. Kidwell and R. J., Colton, Langmuir, 10 (1994) 354.
[31] V.T. Moy, E.L. Florin and H.E. Gaub, Science, 266 (1994) 257.
[32] U. Dammer, O. Popescu, P. Wagner, D. Anselmetti, H.-J. Güntherodt, and G.N. Misevic, Science, 267 (1995) 1173.
[33] P. Hinterdorfer, W. Baumgartner, H.J. Gruber, K. Schilcher and H. Schindler, Proc. Natl. Acad. Sci USA, 93 (1996) 3477.
[34] U. Dammer, M. Hegner, D. Anselmetti, P. Wagner, M. Dreier, W. Huber and H.-J. Güntherodt, Biophys. J**.,** 70 (1996) 2437.
[35] S. Allen, X.Y. Chen, J. Davies, M.C. Davies, A.C. Dawkes, J.C., Edwards, C.J. Roberts, J. Sefton, S.J.B. Tendler and P.M. Williams, Biochemistry, 36 (1997) 7457.
[36] P.E. Marszalek, H. Lu, H.B. Li, M. Carrion-Vazquez, A.F. Oberhauser, K. Schulten and J.M. Fernandez, Nature, 402 (1999) 100.
[37] R. Ros, F. Schwesinger, D. Anselmetti, M. Kubon, R. Schäfer, A. Plückthun and L. Tiefenauer, Proc. Natl. Acad. Sci USA, 95 (1998) 7402.
[38] R. Merkel, P. Nassoy, A. Lueng, K. Ritchie and E. Evans, Nature, 397 (1999) 50.
[39] T. Strunz, K. Oroszlan, R. Schäfer and H.-J. Güntherodt, Proc. Natl. Acad. Sci USA, 96 (1999) 11277.
[40] F. Schwesinger, R. Ros, T. Strunz, D. Anselmetti, H.-J. Güntherodt, A. Honegger, L. Jermutus, L. Tiefenauer and A. Plückthun, Proc. Natl. Acad. Sci USA, 97 (2000) 7402.
[41] R. De Paris, T. Strunz, K. Oroszlan, H.-J. Güntherodt, and M. Hegner, Single Mol., 1 (2000) 285.
[42] I. Schumakovitch, W. Grange, T. Strunz, P. Bertoncini, H.-J. Güntherodt and M. Hegner, Biophys J., 82 (2002) 517.
[43] E. Evans, A. Leung, D. Hammer and S. Simon, Proc. Natl. Acad. Sci USA, 98 (2001) 3784.
[44] H.A. Kramers, Physica Utrecht, 7 (1940) 284.
[45] I. Bell, Science, 200 (1978) 618.

[46] E. Evans, Annu. Rev. Biophys. Biomol. Struct., 30 (2001) 105.
[47] E. Galligan, C.J. Roberts, M.C. Davies, S.J.B. Tendler and P.M. Williams, J. Chem. Phys.,114 (2001) 3208.
[48] B. Heymann and H. Grubmüller, Phys. Rev. Lett., 84 (2000) 6126.
[49] J.L. Hutter and J. Bechhoefer, Rev. Sci. Instrum., 64 (1993) 1868.
[50] D. Pörschke and M. Eigen, J. Mol. Biol., 62 (1971) 361.
[51] N. Tibanyenda, S. H. Debruin, C.A.G. Haasnoot, G. A. Vandermarel, J. H. Vanboom, C. W. Hilbers, Europ. J. Biochem., 139 (1984) 19.
[52] M.B. Viani, T.E. Schaffer, G.T. Paloczi, L.I. Pietrasanta, B.L. Smith, J.B. Thompson, M. Richter, M. Rief, H.E. Gaub, K.W. Plaxco, A.N. Cleland, H.G. Hansma and P.K. Hansma, Rev. Sci. Instr., 70 (1999) 4300.
[53] D.R. Baselt, G.U. Lee and R.J. Colton, Vac. Sci. Technol. B, 14(2) (1996) 789.
[54] H. Masayuki, Y. Yoshiaki, T. Hideki, O. Hideo, N. Tsunenori and Jun M., Biosensors and Bioelectronics 17 (2002) 173.
[55] J. Fritz, M.K. Baller, H.P. Lang, H. Rothuizen, P. Vettiger, E. Meyer, H.-J. Güntherodt, Ch. Gerber and J.K. Gimzewski, Science, 288 (2000) 316.
[56] R. Berger, E. Delamarche, H.P. Lang, Ch. Gerber, J.K. Gimzewski, E. Meyer and H.-J. Güntherodt, Science, 276 (1997**)** 2021.
[57] R. Berger, Ch. Gerber, J.K. Gimzewski, E. Meyer and H.-J. Güntherodt, Appl. Phys. Lett., 69 (1996) 40.
[58] T. Bachels, R. Schäfer and H.-J. Güntherodt, Phys. Rev. Lett., 84 (2000) 4890.
[59] M.K. Baller, H.P. Lang, J. Fritz, Ch. Gerber, J.K. Gimzewski, U. Drechsler, H. Rothuizen, M. Despont, P. Vettiger, F.M. Battiston, J.P. Ramseyer, P. Fornaro, E. Meyer and H.-J. Güntherodt, Ultramicroscopy, 82 (2000) 1.
[60] J. Fritz, M.K. Baller, H.P. Lang, T. Strunz, E. Meyer, H.-J. Güntherodt, E. Delamarche, Ch. Gerber and J.K. Gimzewski, Langmuir, 16 (2000) 9694.
[61] F.M. Battiston, J.P. Ramseyer, H.P. Lang, M.K. Baller, Ch. Gerber, J.K. Gimzewski, E. Meyer and H.-J. Güntherodt, Sensors and Actuators B, 77 (2001) 122.
[62] P. Wagner, M. Hegner, P. Kernen, F. Zaugg and G. Semenza, Biophys. J. 70 (1996) 2052.
[63] G.G. Stoney, Proc. R. Soc. London Soc. A 82 (1909) 172.
[64] R. McKendry, T. Strunz, J. Zhang, Y. Arntz, M. Hegner, H. P. Lang, M. Baller, U. Certa, E. Meyer, H.-J. Güntherodt and Ch. Gerber, Proc. Natl. Acad. Sci. USA (2002) in press.
[65] J. Thaysen, R. Marie and A. Boisen, in IEEE Int. Conf. Micro. Electro. Mech. Syst., Tech. Dig. Publisher: Institute of Electrical and Electronic Engineers, New York, 14th (2001) 401.
[66] K.M. Hansen, H.F. Ji, G.H. Wu, R. Datar, R. Cote, A. Majumdar and T. Thundat, Anal. Chem. 73 (2001) 1567.
[67] G.H. Wu, R.H. Datar, K.M. Hansen, T. Thundat, R.J. Cote and A. Majumdar, Nature Biotech. 19 (2001) 856.
[68] C. Grogan, R. Raiteri, G.M. O'Connor, T.J. Glynn, V. Cunningham, M. Kane, M. Charlton and D. Leech, Biosens. Bioelectron. 17 (2001) 201.